# ABSTRACT

Title of Dissertation: FUNCTIONAL NANOSTRUCTURE SYNTHESIS AND PROPERTIES

Qing (Edda) Liu, Doctor of Philosophy, 2012

Directed By: Michael R. Zachariah, Professor
Department of Mechanical Engineering and Chemistry

Studies of nano-scale systems have been going on for decades and are drawing more and more attention from scientists and engineers. Nanomaterials can be defined as materials with at least one dimension in the range of 1 to 100 nm. Nanoparticles possess high potential for novel materials and devices due to their unique properties. Besides merely regulating the size of particles, research on the shape of particles and their different intra-structures (porous, core-shell, hollow and capsule), has been conducted, regarding both synthetic methods and properties.

The focus of this dissertation is to address challenges in the synthesis of nanostructures, to explore the new characterization methods that helps better understand particle formation mechanisms and their properties, and to eventually apply the materials to engineering demands. The spray pyrolysis method is a comparatively new branch of synthesis method for nanoparticles. Due to some characteristics of it that conventional

methods do not embrace, it can realize some hypothetical structures and satisfy the application needs. 1) Porous magnetic material has been synthesized by it; different pore structures, crystallinity and magnetic properties were created by changing synthesis conditions. 2) As aerosol plays an important role in atmospheric visibility and global climate change, research on its optical properties attract worldwide attention. A new series of optical standards are demanded and generated to calibrate the optical instrumentation before the actual optical research; also, retrieving the refractive indexes of the new aerosol optical standards further help understand the complete properties of the material. 3) This method can generate potential materials to be used in lithium ion battery field, highlighted by their special structure which is difficult to obtain by traditional synthesis. 4) To support spray pyrolysis structure research, a new density/porosity measurement for aerosol particles were developed and studied. Based on this new characterization methodology, more interesting properties and the natures of these aerosol nanoparticles were revealed. 5) However, any synthetic approach has its own limitations, and thus an emulsion synthesis was employed in creating porous fluorescent silica nanoparticles as potential drug delivery, successful in combining the stable dye-fixing and one-step procedure with controllable porous structure.

# FUNCTIONAL NANOSTRUCTURE SYNTHESIS AND PROPERTIES

by

Qing (Edda) Liu

Dissertation submitted to the Faculty of the Graduate School of the
University of Maryland, College Park, in partial fulfillment
of the requirements for the degree of
Doctor of Philosophy
2012

Advisory Committee:

Professor Michael R. Zachariah, Chair
Professor Philip DeShong
Professor Bryan Eichhorn
Professor YuHuang Wang
Professor Sheryl Ehrman

# Dedication

To

My parents

Liu, Yi and Zhu, Liping

And all who were and are loving me.

This dissertation is lovingly dedicated to my respectable parents who have been my constant source of inspiration. Although they are not teaching me the chemistry, they have given me the drive and discipline to tackle any task with enthusiasm and determination. Although they may not be able to understand the work in the dissertation, I believe they must rejoice in this achievement no less than me.

I also dedicate this dissertation to everyone who was and is loving me. Their love transcends time and space, which brings me confidence, helps me concentrate and develops my ability each step of the way within my past 25 years.

# Acknowledgement

I owe my gratitude to all the people who have made this dissertation possible. First and the most important, I thank my advisor, Professor Michael Zachariah, who not only inspires me research ideas, but also mentors me how to develop research and what attitude professionals should have. It is such a fortune to study and work with him. He gives me both essential assistance and freedom in research; thus, this four-year training becomes my valuable experience for my entire life.

I would like to thank my other advisory committee members: Professor Philip DeShong , Professor Bryan Eichhorn, Professor Sheryl Ehrman and Professor YuHuang Wang; they started advising my professional career from my candidacy exam, lent me help whenever I met problems in projects, and spared a Friday afternoon from their busy schedule for my defense. In addition, Professor Chunsheng Wang has exposed me to the research of battery, which expanded my current study into this application. And Professor George Mulholland advised me on the optical standard project.

Last but not least, I would like to thank all my friends and colleagues, who I worked with and helped me with experiments from their personal time. Not only my group members, students, postdocs and their family in Professor Chunsheng Wang's group employ me the feeling of home, making my life in US warm and enjoyable. I would like to thank Fangyu Cao, who taught me how to resolve all kinds of detailed problems in laboratory; Xiao Zhang, a friend from Rutgers University, helped me conduct UV-Vis of solid sample, which, importantly, contributed to my first publication. I also appreciate the help from Xin Su and Ms. Sharon vonBergener for the dissertation editing in the very last short time, and the support from Weitian An during the last several months.

# Table of Contents

# List of Tables

# List of Figures

# List of Abbreviations

| | |
|---|---|
| AC | Altering Current |
| AFM | Atomic Force microscopy |
| AIBA | 2,2'-azobis (2-methylpropionamide) dihydrochloride |
| ALD | Atomic Layer Deposition |
| APM | Aerosol Particle Mass Analyzer |
| BET | Brunauer-Emmett-Teller Methodology |
| CMC (in Chapter 1) | Critical Micelle Concentration |
| CMC (in Chapter 5) | Carboxymethyl Cellulose |
| CPC | Condensation Particle Counter |
| CRD | Cavity Ring-Down |
| CRDS | Cavity Ring-Down Spectroscopy |
| CS | Carbon Sphere |
| CTAB | Cetyl trimethylammonium bromide |
| CV | Cyclic Voltammetry |
| CVD | Chemical Vapor Deposition |
| DLS | Dynamic Light Scattering |
| DMA | Differential Mobility Analyzer |
| EC/DEC | Ethylene Carbonate/Diethyl Carbonate |
| EDS | Energy-Dispersive X-ray Spectroscopy |
| EISA | Evaporation-Induced Self-Assembly |
| FTIR | Fourier Transform Infrared Spectroscopy |
| GITT | Galvanostatic Intermittent Titration Technique |
| IEP | Isoelectric Point |
| LC | Liquid Crystal |
| LCD | Liquid Crystal Display |
| LCT | Liquid Crystal Templating |
| LIB | Lithium-Ion Battery |
| MO | Metal Oxide |
| MRI | Magnetic Resonance Imaging |
| NIST SRM | National Institute of Standards and Technology Standard reference Materials |
| NMR | Nuclear Magnetic Resonance Spectroscopy |
| PAS | Photoacoustic Spectroscopy |
| PS | Polystyrene |
| P-S | Polymer-Surfactant |
| PSN | Porous silica Nanoparticles |
| PVD | Physical Vapor Deposition |
| PVP | Polyvinylpyrrolidone |
| SA | Self-Assembly |
| SAXS | Small-Angle X-ray Scattering |
| SEI | Solid-Electrolyte Interphase |

| | |
|---|---|
| SEM | Scanning Electron Microscopy |
| STM | Scanning Tunneling Microscopy |
| TEM | Transmission Electron microscopy |
| TEOS | Tetraethyl orthosilicate |
| TGA | Thermogravimetric Analysis |
| THF | Tetrahydrofuran |
| TLCT | True Liquid Crystal Templating |
| UV-Vis | Ultraviolet-Visible Spectroscopy |
| VSM | Vibrating sample magnetometer |
| XPS | X-ray Photoelectron Spectroscopy |
| XRD | X-ray Powder Diffraction |
| ZRA | Zero Resistance Ammeter |

# Chapter 1. Introduction

## 1.1 Nanoscale Systems

### 1.1.1 Development in the Nano Realm

Fundamentally, there is a hierarchy in the physical length scales: the macroscopic scale, the mesoscopic scale and the nanoscopic scale. The macroscopic scale, or bulk scale, is the length scale on which objects or processes are of a size that is measurable and observable by the naked eye, which is usually larger than one millimeter. The mesoscopic scale, an intermediate length scale, is between the size of a quantity of atoms and of materials measuring micrometers (100 nm-1000 nm). Thus, a few hundred nanometers is the approximate upper limit for a nanoparticle. Mesoscopic and macroscopic objects have in common that they both contain a large number of atoms. The difference is that, the average properties derived from its constituent materials and describing macroscopic objects usually obey the laws of classical mechanics; whereas a mesoscopic object is affected by fluctuations around the average, and is subject to quantum mechanics and statistical mechanics. A number of physical phenomena become more pronounced as the size of the system further decreases. Quantum effects become dominant for materials at the nano scale. The nanoscopic scale is sometimes marked as the point where the properties of a material change dramatically; below that point, while the type of atoms present and their relative orientations are still important, “surface area effects” of quantum effects become more apparent -- these effects are due to the geometry of the material, which can have a drastic effect on quantized states at such small dimensions.

What we call nanotechnology today was first used thousands of years ago. Since Roman period, nano-sized gold has been used to stain glass and ceramics. Modern scientific evaluation of colloidal gold did not begin until Michael Faraday's work in the 1850s, and then Thomas Graham introduced the term "colloid". Early 20th century witnessed the development in the photo-electric effect with the aid of quantum mechanics (1905, Albert Einstein), the invention of electron microscopes (1931, Ernst Ruska), and the discovery of tunneling phenomenon in semiconductor super lattices (1973 Nobel Prize for Leo Esaki). Nano research has been moving forward rapidly after Norio Taniguchi created the realm of "nanotechnology". For example, Alan J. Heeger, Alan G. MacDiarmid and Hideki Shirakawa shared the Nobel Prize in Chemistry for their discovery of conducting polymers by doping polyacetylene with oxidizers; Heinz Gerischer and Frank Willig first developed dye-sensitized solar cells laying the foundation for the development of the Grätzel cell in 1991. There followed research and discovery of nano-crystalline quantum dots, carbon nanotubes, and nanotube transistors. Nowadays, nano devices are used in a broad range of fields. At the same time, techniques for nanomaterial characterization are striking forward as needed, successful measurements with the scanning tunneling microscopy (STM), and other microscopies, such as atomic force microscopy (AFM), transmission electron microscopy (TEM), which made it possible to observe and analyze structures at the nanoscale. Recently, the 2010 Nobel Prize in Physics was awarded to the discovery of graphene, opening the new era for graphene nanoresearch.[1.1]

### 1.1.2 Synthesis Methods

Attracted by nanoparticles' unique properties, it is still challenging to prepare the ideal structures predicted by theoretical calculations, especially to isolate them as stable species. Due to the high surface energy and the large surface curvature, it is difficult to stabilize the surface of a nanoparticle unstable at such small scale. An understanding of the thermodynamic process and controlling of parameters for the growth of nanoparticles are indispensable for fabricating nanoparticles with the desired size and shape.

For homogeneous nucleation, the overall free energy change, $\Delta G$ for spherical particles can be expressed as,

$$\Delta G = -\frac{4}{V}\pi r^3 k_B T ln(S) + 4\pi r^2 \gamma \qquad (1.1)$$

Where $V$ is the molecular volume of the precipitated species, $r$ is the radius of the nuclei, $k_B$ is the Boltzmann constant, S is the saturation ratio, and $\gamma$ is the surface free energy per unit surface area.

$\Delta G$ is the sum of the free energy gain from the new volume formed (first term in Equation 1.1) and the free energy loss from the new surface created (second term in Equation 1.1). So the combination of volume free energy and interfacial energy determines the possibility of nanoparticle formation, as shown in Figure 1.1. When S>1, $\Delta G$ has a positive maximum ($\Delta G^*$) at a critical size ($r^*$). This maximum free energy is the activation energy for nucleation. Nuclei larger than the critical size will further decrease their free energy for growth and form stable nuclei that grow to form particles.

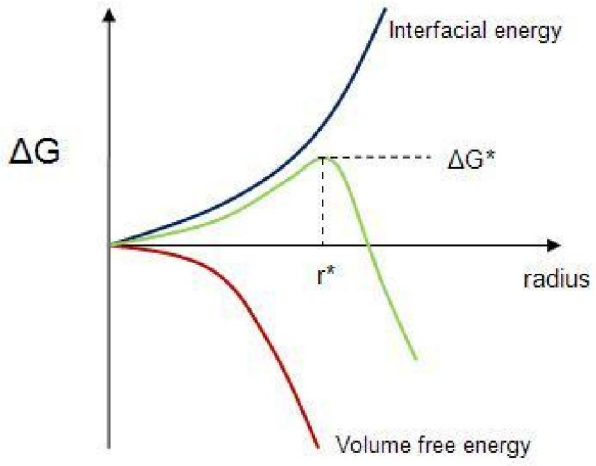


Figure 1.1. Interfacial, volume free and total energy plots as a function of particle size. (from http://en.wikipedia.org/wiki/Nucleation, accessed Aug 10, 2012)

Alternative nucleation processes are heterogeneous nucleation and secondary nucleation. Heterogeneous nucleation occurs much more often than homogeneous nucleation, because it is virtually impossible to achieve a solution completely free of foreign bodies. For example, common aqueous solutions prepared in the laboratory averagely contain more than $10^6$ solid particles per $cm^3$ with sizes less than 1μm, which may lead to spontaneous nucleation. Compared to homogeneous nucleation (with free energy $\Delta G_{hom}$), free energy of heterogeneous nucleation ($\Delta G_{het}$) includes a factor which is a function of the contact angle $\theta$:

$$f(\theta) = \frac{1}{2} - \frac{3}{4}cos\,\theta + \frac{1}{4}cos^3\,\theta \leq 1 \qquad (1.2)$$

Therefore, the impurity acts as a catalyst, lowering the nucleation free energy and accelerating the nucleation process.

$$\Delta G_{het} = \Delta G_{hom} \times f(\theta) \qquad (1.3)$$

The contact/wetting angle determines the easiness of nucleation. When $\theta$ is 0, it is perfectly wetting; strong attraction causes the free energy for nucleation to decrease to zero. When $\theta$ is 180°, it is perfectly non-wetting, which means there is no affinity

between the deposition molecules and the foreign solid sites, therefore this heterogeneous nucleation has the same energy barrier as homogeneous nucleation. At such preferential sites, the effective surface energy is decreased, thus facilitating nucleation and effecting the shape of the cluster, while the critical radius remains unchanged (Figure 1.2).

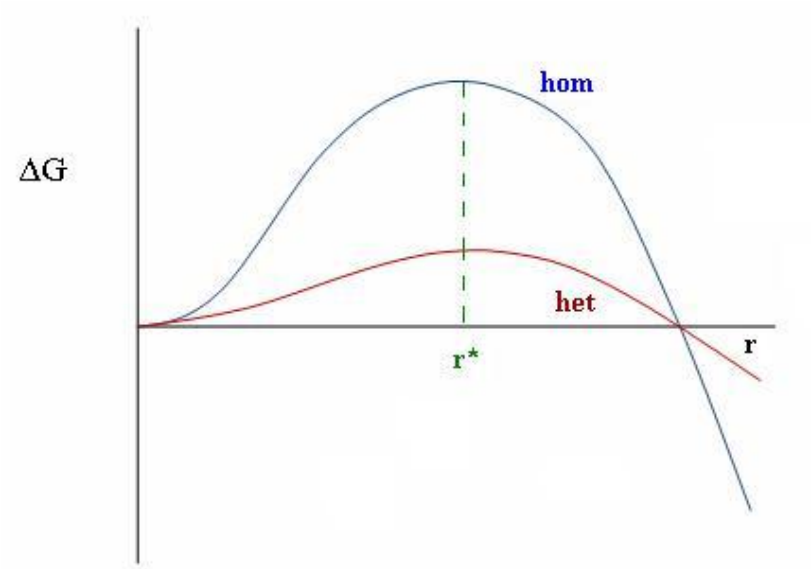


Figure 1.2. Free energy plots of homogenous and heterogeneous nucleation as a function of particle radius. (from http://en.wikipedia.org/wiki/Nucleation, accessed Aug 10, 2012)

Also, the size of the solid foreign bodies is important, and evidence suggests that the most active heteronuclei in liquid solutions lie within the range from 0.1 to 1μm. They form at preferential sites such as phase boundaries or impurities such as dust and require less energy than homogeneous nucleation.

While no crystals exist initially for primary nucleation (homogeneous/heterogeneous nucleation), secondary nucleation occurs much more readily at a lower supersaturation, when crystals of the solute are already present or deliberately added. For example, fluid shear of weak outgrowths or loosely bonded units from the crystal-solution interface in an agitated vessel is one of the secondary nucleation mechanisms, followed by

developing into stable nuclei in high supersaturation regions. Besides, crystal interactions or collisions sweep off newly introduced seed crystals or weak polycrystalline masses; growing crystals with dislocations, defects or inclusions lead to crack formation and the subsequent production of breakage fragments from internal stress. These are processes prone to secondary nucleation.[1.2]

#### 1.1.2.1 Sol Process

The sol process is a wet-chemical technique which is done in a liquid phase. The product particle size and size distribution is very temperature sensitive, so temperature control in the entire process is very important. A general scheme for preparing monodisperse nanostructures requires a short nucleation event followed by slower growth on the existing nuclei: rapid addition of reagents into a reaction vessel containing a hot solvent, followed by quick cooling for further growth/aging.[1.3] High temperature first decomposes the reagents and raises the precursor concentration above the nucleation threshold, then the concentration of these species in solution drops below the critical concentration for nucleation and a lower temperature is kept for particle growth to a more focused size distribution.

Temperature should be carefully adjusted to keep the rate at which the precursor reagents are supplied no more than the rate at which the material is consumed by the existing nuclei, ensuring that the supersaturated state is never revisited and only single nucleation occurs.

In addition to temperature, controls of other reaction parameters, such as reaction time, concentration, selection of reagents and surfactants if needed, are also important in terms of tuning the size, shape, quality and thus the properties of nanocrystals.[1.4]

#### 1.1.2.2 Sol-gel Process

The sol-gel process is also a very common wet-chemical technique. It is inorganic polymerization (oxides) starting from a colloidal solution (sol) that acts as the precursor for an integrated network (gel) of either discrete particles or network polymers. The major difference between the the sol-gel process and the sol process is that the sol-gel process undergoes various forms of hydrolysis and polycondensation. The solvent should be removed after the solution has been condensed to a gel (an inorganic network containing a liquid phase); therefore, drying and higher temperature calcination are used to remove the liquid from the gel, followed by final sintering to enhance mechanical properties. The size of the sol particles can be controlled by the solution composition, pH and reaction temperature. Porous structures of the final products are determined by the heating process and structural templates. Used in ceramics processing or metal oxides nanostructures, sol-gel research started growing to be very important in the 1990s; it fabricates materials for diverse applications in optics, electronics, energy, space, (bio)sensors, drug delivery, reactive materials and separation (*e.g.*, chromatography) technology.[1.5]

#### 1.1.2.3 Micelles

When the surfactant concentration exceeds the critical micelle concentration (CMC) in water, micelles can form spontaneously as a result of a balance between entropy and enthalpy. The bulk properties of the surfactant, such as osmotic pressure, turbidity, solubilization, surface tension, conductivity and self-diffusion, change around the CMC. The structure of micelles can be determined by the geometric factors of the surfactant at

the interface, headgroup area $\alpha_0$, alkyl chain volume $V$ and the maximum length $l_c$ to which the alkyl chain can extend. Packing considerations govern the geometry of aggregation by the following rules:

(a) Spherical micelles: $^{V}/_{\alpha_0 l_c} < {}^{1}/_{3}$

(b) Nonspherical micelles: $^{1}/_{3} < {}^{V}/_{\alpha_0 l_c} < {}^{1}/_{2}$

(c) Vesicles or bilayers: $^{1}/_{3} < {}^{V}/_{\alpha_0 l_c} < 1$

(d) Inverted (reverse) micelles: $1 < {}^{V}/_{\alpha_0 l_c}$

As the nanoscale reaction vessel, there are two general types of micelles which can initiate the reaction or confine the reactants, normal micelles and reverse micelles. Normal micelles are oil droplets in water, the hydrophobic hydrocarbon chains of the surfactants are oriented toward the interior of the micelle and the hydrophilic groups of the surfactants are in contact with the surrounding aqueous medium. Emulsion polymerization induces a marked increase in the local amount of reactants and supersaturation starts particle nucleation and growth. By tuning the reaction factors, different nanoparticle sizes and shapes (gold nanorods and silver nanoparticles/trangles) can be produced.[1.6]

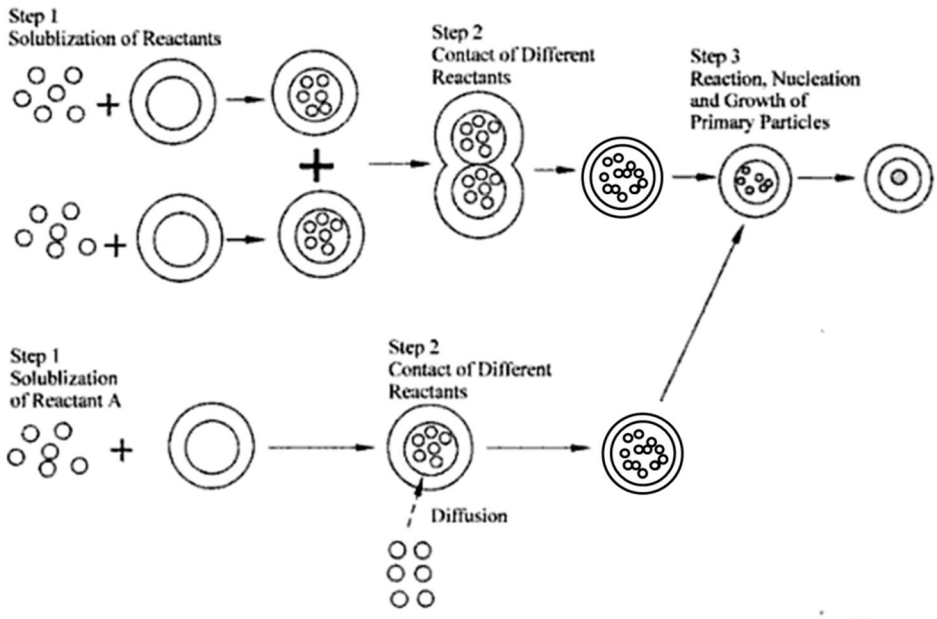


Figure 1.3. Two mechanisms of nanoparticle synthesis by reversed micelle method.[1.7]

Usually, reverse micelles can be formed by ionic surfactants with double-long alkyl chains alone (such as dioctyl sodium sulfosuccinate), or a mixture of ionic and nonionic surfactants. There are two general mechanisms for nanoparticle synthesis by the reverse micelle method (Figure 1.3). The first case involves the mixing of two reverse micelles. Due to the contact and coalescence of the reverse micelles, exchange of materials in the water droplets occurs, which causes a reaction between the cores, and nanoparticles are formed in the reversed micelles. The second case involves diffusion of a reactant into another reactant that is solubilized in the reversed micelles. By the reverse micelles method, metal nanoparticles (Pt, Ag, Au, Cu, *etc*.) can be prepared by reducing metal salts;[1.8] oxide nanoparticles ($ZrO_2$, $TiO_2$, $SiO_2$ and $\gamma$-$Fe_2O_3$)[1.9] can be prepared inside reverse micelles by the hydrolysis procedure where metal alkoxides dissolved in oil react with water inside the droplets; metal sulfate ($BaSO_4$)[1.10], metal carbonates ($BaCO_3$, $CaCO_3$, $SrCO_3$)[1.11] and silver halides[1.12] can also be produced by precipitation reactions

between reactants in reverse micelles. Interestingly, other shapes and structures such as nanowire[1.13] and core-shell nanocomposites[1.14] can also be synthesized by the reverse micelle method.

Different from normal micelles, the size of which is controlled by the length of the surfactant alkyl chain, the droplet size of reverse micelles and thus the particle size can be altered by changing the ratio of water and surfactant. Micelles are approximately spherical in shape. The shape and size of a micelle is also a function of the molecular geometry of its surfactant molecules and solution conditions such as surfactant concentration, temperature, pH, and ionic strength. Other phases, including shapes such as ellipsoids, cylinders, and bilayers, are also possible and useful in templating research.

1.1.2.4 Chemical Precipitation

Precipitation is the formation of a solid in a solution or inside another solid during a chemical reaction or by diffusion in a solid if the concentration of one solid is above the solubility limit in the host. The kinetics of nucleation and particle growth in homogeneous solutions can be adjusted by the controlled release of anions and cations, to synthesize monodisperse nanoparticles. Even though it is a straightforward and simple synthesis method, many factors can be engineered during the process. Combining temperature, pH, and components concentration control of solution by some organic molecules,[1.15] only one burst of nuclei will occur; particles of different sizes and complicated nanostructures can be constructed.[1.16] In addition, precipitation in solids is routinely used to synthesize nanoclusters propelled by proper temperature control, ion flux, and electron irradiation.[1.17]

1.1.2.5 Hydrothermal Synthesis

Hydrothermal synthesis is a method to synthesize mostly single crystals at high temperature and high water pressure. Water at elevated temperatures plays a catalytic role in the precursor material transformation because the assembly structure of the water is altered at elevated temperature; solubility and reactivity of reactants are also changed. Therefore, the unique pressure-temperature interaction of the hydrothermal solution allows preparation of phases that are difficult to prepare with other synthesis methods. Possible advantages of the hydrothermal method over other types of crystal growth include the ability to create anhydrous phases directly from solution, crystals that are not stable at their melting points and materials which have high vapor pressures near their melting points. For example, no method other than hydrothermal synthesis can be used to grow large $\alpha$-quartz single crystals due to the occurrence of several phase transitions at and above 574°C in this material.[1.18] Hydrothermal methods are also used for materials that melt incongruently because such materials cannot be grown with compositional and phase uniformity by the above synthesis methods.

Hydrothermal synthesis is performed in an apparatus consisting of a steel pressure vessel called an autoclave. The most used mechanism is that the gradient of temperature is maintained at opposite ends of the growth chamber so that the nutrient dissolves in the hotter zone and the saturated aqueous solution in the lower part is transported to the upper part by convective motion of the solution (Figure 1.4). However, the apparatus can be a disadvantage for this method because of its high cost and the impossibility of observing the crystal as it grows.[1.19]

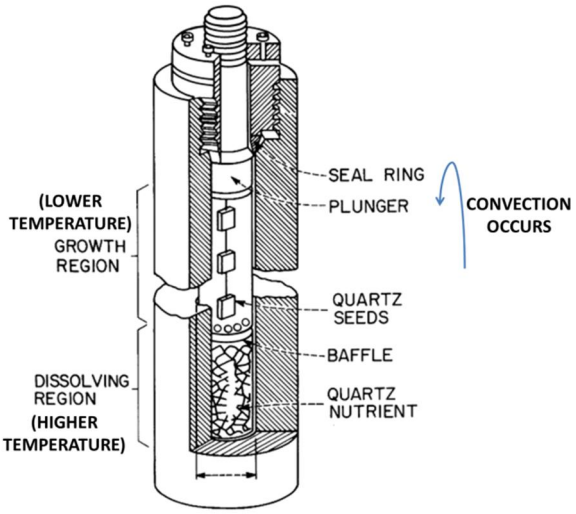

Figure 1.4. Schematic depiction of quartz growing autoclave.[1.20]

Some merits of hydrothermal methods are: product powders are highly reactive in sintering to improve some performance; powders possess better crystalline structures even without calcination or other post-treatments; reaction temperatures can be adjusted not that high to avoid high temperature process problems such as poor stoichiometry control due to volatilization of components (lead volatilization in lead ceramics) and stress-induced defects (micro-cracks) caused by phase transformations that occur as the ceramic is cooled to room temperature. Besides some parameter regulations like water pressure, temperature, reaction time, respective precursor to control particle size, morphology and crystallinity,[1.21] a major characteristic of hydrothermal synthesis is that the technology can be hybridized with myriad other processes (microwave, electrochemistry, ultrasound, mechanochemistry, optical radiation, hot-pressing, *etc.*) to gain advantages such as enhancement of reaction kinetics and the ability to create innovative materials.[1.22]

Except for utilizing a non-aqueous solvent media, solvothermal synthesis is similar to the hydrothermal process in precise control over the size, shape distribution, and

crystallinity of nanoparticles or nanostructures, by changing certain experimental parameters, including reaction temperature, reaction time, solvent type, surfactant type, and precursor type.

1.1.2.6 Vapor Deposition

Vapor deposition, including chemical vapor deposition (CVD) and physical vapor deposition (PVD), is the condensation of elements or compounds from the vapor state to form solid deposits. A variety of morphologies such as nanowires, nanorods, nanobelts, nanosheets, nanoribbons, and nanotubes have been synthesized using vapor deposition.[1.23]

In CVD, the vaporized precursors are introduced into a reactor, and then chemically adsorbed onto a substance held at an elevated temperature, which react or decompose on the substrate surface to produce the desired deposit. The process is often used in the semiconductor industry to produce thin films. The CVD process consists of three steps: (1) mass transport of reactants to the growth surface through a boundary layer by diffusion, (2) chemical reactions on the growth surface and (3) removal of the gas-phase reaction byproducts from the growth surface. Nucleation in the gas phase is homogeneous, whereas nucleation on the substrate is heterogeneous. Catalysts, such as Fe, Ni, Co, are also used in the CVD process.

PVD represents a variety of vacuum depositions, and this thin film coating method involves evaporation techniques (electron beam, thermal energy, sputtering, cathodic arc plasma and pulsed laser) followed by purely physical condensation, rather than involving a chemical reaction at the surface to be coated as in chemical vapor deposition. PVD is also a widely used manufacturing technique; its process consists of three steps: (1)

generating a vapor phase by evaporation or sublimation of the material, (2) transporting the material from the source to the substrate, and (3) formation of the particle and/or film by nucleation and growth.

1.1.2.7 Pyrolysis

Pyrolysis is a chemical process in which chemical precursors decomposes under suitable thermal treatment into one solid compound and unwanted waste evaporates away. Normally, the pyrolytic synthesis of compounds leads to powders with a wide size distribution in the micrometer range. To get a uniform nanosized material, some modifications or revisions of the pyrolytic preparation procedure and reaction conditions are used such as slowing the reaction rate or decomposing of the precursor in the inert solvent.

Three types of pyrolysis are usually used in synthesis, aerosol spray pyrolysis,[1.24] laser pyrolysis/photothermal synthesis,[1.25] and flame spray pyrolysis/combustion synthesis.[1.26] They are all gas phase processes, based on spraying, but using different heating methods. Spray pyrolysis is a droplet-to-particle conversion process, using a nebulizer to inject very small droplets of precursor solutions. The reaction takes place in solution in the droplets, followed by solvent evaporation. Spray pyrolysis is a process in which a thin film is deposited by spraying a solution on a heated surface, where the constituents react to form a chemical compound, or the aerosol is heated as it flows. There are four types of reaction: (1) the droplet resides on the surface as the solvent evaporates, leaving behind a solid that may further react in the dry state; (2) the solvent evaporates before the droplet reaches the surface and the dry solid impinges on the surface, where decomposition occurs; (3) the solvent vaporizes as the droplet approaches

the substrates, the solid then melts and vaporizes, and the vapor diffuses to the substrate, there to undergo a heterogeneous reaction (chemical vapor deposition); (4) the entire reaction takes place in the vapor state.

This thesis is focused on nanoparticle synthesis by aerosol spray pyrolysis, so the apparatus, parameter effects, particles produced by this method (morphology, properties, characterization and application) will be discussed in detail in later chapters.

1.1.2.8 Other Methods

There are some other energy sources to activate the reactions such as ultrasound or radiation, which can be cataloged into one of the methods above, sorting by reaction phases.

When a liquid is irradiated with high intensity sound or ultrasound, acoustic cavitation (the formation, growth, and implosive collapse of bubbles in liquids irradiated with sound) generally occurs. This is the phenomenon responsible for sonochemistry and sonoluminescence. During cavitation, the collapse of bubbles (hot spots) produces intense local heating (5,000–25,000 K) and high pressures (1000 atmospheres), with very short lifetimes (a few nanoseconds), so the heating and cooling rates are above $10^{10}$ K/s. Because high cooling rates hinder product crystallization, this method is used to prepare amorphous products. It is also used for deposition of nanoparticles on ceramic and polymeric surfaces and insertion of nano-materials into mesoporous materials by acoustic streaming (bulk movement of fluid powered by the propagation of acoustic waves).[1.27]

In sonochemical nano-synthesis, acoustic cavitation can break chemical bonds, so molecules undergo chemical reactions as a result of the application of powerful

ultrasound (20 kHz – 10 MHz). However, sonofragmentation is a physical method of fabricating nanoparticles from micrometer-sized feed (*e.g.*, 70–80 μm). High purity is its distinct advantage over other dry processes for nanoparticle fabrication.[1.28] Cavitation (low frequency) and acoustic streaming (high frequency) work together in all forms of ultrasonic processes, the relative contribution of which is a function of frequency. In the case of sonofragmentation, which is typically performed at low ultrasound frequencies (20–40 kHz), cavitation is clearly the principal driving force (mechanism is shown in Figure 1.5).

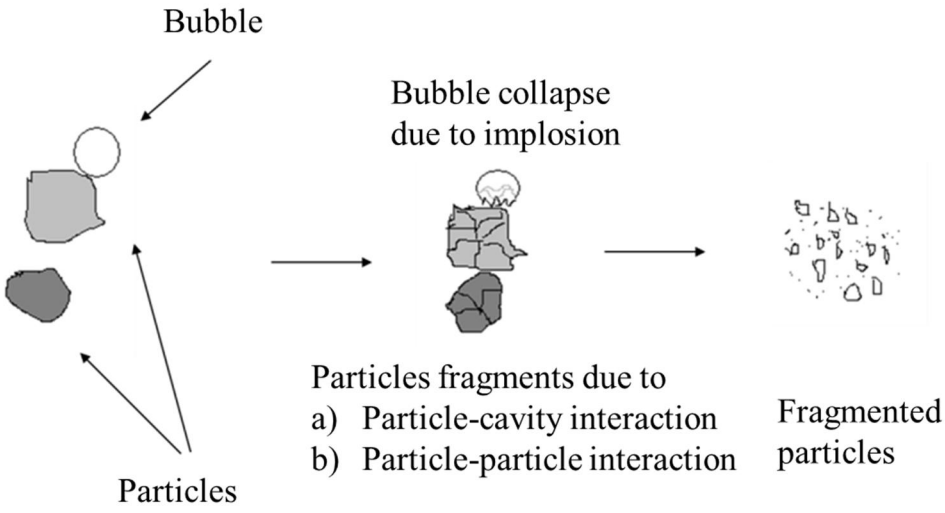


Figure 1.5. Two mechanisms responsible for ultra-sonic particle fragmentation.

Mechanical milling, especially commonly-used ball mills can induce reduction/oxidation/decomposition reactions, or grind brittle material to fine powder, as small as 5 nm. It rotates around a horizontal axis, partially filled with the material to be ground plus the grinding medium. Optimizing the grinding media parameters and combining them with other technologies,[1.29] are the current research direction of this grinding method.

### 1.1.3 Self-Assembly (SA)

Self-assembly is a process in which a set of components or constituents spontaneously forms an (ordered) aggregate through their global free-energy minimization. Important examples of SA in material science include the formation of molecular crystals, colloids, lipid bilayers, phase-separated polymers, self-assembled monolayers, as well as folding of polypeptide chains into proteins, folding of nucleic acids into their functional forms and molecular recognition.[1.30]

Distinctive features for self-assembly include:

- Building blocks

Building blocks, the basic elements in the SA process, may comprise not only atoms and molecules, but also a wide range of nano- and mesoscopic structures with different chemical compositions, shapes and functionalities. These nanoscale building blocks can in turn be synthesized through conventional chemical routes or by other SA strategies, *in situ* or prepared.

- Order

The self-assembled structure normally has a higher order than the isolated components. However, the well-structured array can be the highest level of disorder because each building block is surrounded by different units. This is different from chemical reactions within the entire system, which proceed towards a disordered state depending on thermodynamic parameters. In the self-assembly system, the spontaneous and reversible organization of units into ordered structures by non-covalent interactions maintains a low free energy in the process.

- Interactions

Another important aspect of SA is the key role of weak interactions (*e.g.*, Van der Waals forces, capillary forces, $\pi$–$\pi$ interactions, and hydrogen bonds) with respect to more "traditional" covalent, ionic or metallic bonds. Although typically less energetic ~10kcal/mol, these weak interactions play an important role in materials synthesis.

- Thermodynamic stability

The SA process always develops towards the thermodynamic minimum. Without intervention of external forces, the process must lead to a lower Gibbs free energy, thus self-assembled structures are thermodynamically more stable than the single, unassembled components. However, sometimes, that SA structure is not what is desired. Therefore, we must predict this minimum in self-assembled structures first. With knowledge of the SA mechanism, it might be possible to utilize blocking or enhancing mechanisms to facilitate a particular assembly process. This, combined with interactions between units, is responsible for the choice of controlling elements for synthesis, by means of reaction rate, morphology growth and terminal state regulation.

In present-day research, self-assembly is not necessarily “ordered”; instead it is a reaction which follows a path to a design of choice. Concluding from the above discussion, small fluctuations that alter thermodynamic variables might lead to marked changes in the structure, either during or after self-assembly. The weak nature of interactions is responsible for the flexibility of the architecture and allows for rearrangements of the structure in the direction determined by thermodynamics. Hence, self-assembly is reversible and adjustable and it is a process easily influenced by external

parameters. Therefore, it has the exciting advantage that a wide variety of infrastructures, outer configurations and functional groups on many size scales can be obtained.

While adjusting thermodynamic variables (such as the initial solvent, solute concentration, reaction temperature and additives) in SA systems, we need to consider the simultaneous presence of long-range repulsive forces, which can prevent aggregation, and short-range attractive forces, which are used to build assemblies. Then, predicted structures can be constructed, eventually the new properties of which can be applied to a broad range of engineering fields.

#### 1.1.3.1 Driving Force for Self-Assembly

Van der Waals, solvation, steric, electrostatic, magnetic dipolar, and capillary forces are always involved in reaction systems, some of which are comparatively weak so they are not discussed here. Three attractive interactions among building blocks are especially important in self-assembly mechanism research: electrostatic attraction, H-bridge, and subtle balance of intermolecular interactions of liquid crystal templating.

By strict definition, the van der Waals force is the totality of intermolecular forces (or between parts of the same molecule), including the attractive and repulsive forces, other than the forces due to covalent bonds, hydrogen bonds, or electrostatic interaction of ions with one another or with neutral molecules. So it usually represents forces between two permanent dipoles, a permanent dipole and a corresponding induced dipole, or two instantaneously induced dipoles' intermolecular forces. Solvation is an attraction interaction of a solute with the solvent, involving hydrogen bonding, ion-dipole, and dipole-dipole attractions or van der Waals forces, which leads to stabilization of the solute species in the solution. For example, as ions dissolve in a solvent they spread out

and become surrounded by polar solvent molecules which have a high dielectric constant. The polar molecules of these solvents can solvate ions because they can orient the appropriate partially charged portion of the molecule towards the ion in response to electrostatic attraction.

The original definition of the steric effect arises from the fact that each atom within a molecule occupies a certain amount of space. If atoms are brought too close together, there is an associated cost in energy due to overlapping electron clouds, and this repulsion may affect the molecule's preferred conformation and reactivity. For nanoparticle synthesis and stabilization, Steric forces between polymer-covered surfaces or in solutions containing a non-adsorbing polymer can modulate interparticle forces, producing an additional steric repulsive force or depleting the attractive force between them.

Together with steric stabilization, electrostatic stabilization is another mechanism for stabilization against aggregation, such as electrical double layer. Electrostatic force is the phenomenon that results from relatively stationary electrical charges. Besides interparticle repulsion in the colloid system, it can also be a cohesive force, which is the cause of particle growth, when the particles independently maintain positive and negative charges and react to each other accordingly.

Analogous to an electric dipole, a magnetic dipole is a pair of poles. As the dimensions of the source are reduced to zero while keeping the magnetic moment constant though, it is a closed loop. Magnetic dipole–dipole interaction refers to the direct interaction between two magnetic dipoles, where magnetic moment may come from two kinds of sources: (1) the motion of electric charges and (2) the intrinsic

magnetism of elementary particles. So there is always magnetic moment in an atom (the sum of all individual orbital angular momenta), in electrons (individual electron spins added to get a total spin), in the nucleus (depending on the spin of the individual nucleons), and in a molecule (the overall effects of all the above). Also, magnetic dipoles exist in nanoparticles, which can propel anisotropic self-assembly,[1.31] or work with the assistance of an applied external magnetic field.[1.32]

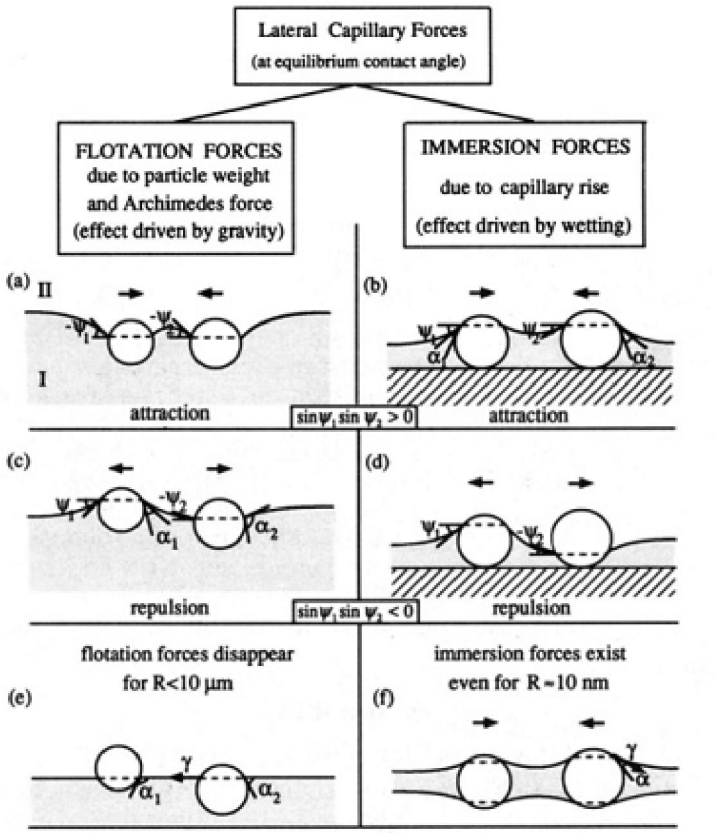


Figure 1.6. Comparison between the flotation (a, c, e) and immersion (b, d, f) lateral capillary forces. $\psi_1$ and $\psi_2$ are meniscus slope angles; $\alpha_1$ and $\alpha_2$ are contact angles; $\gamma$ is interfacial tension.[1.33]

Capillary force can also prompt self-assembly. The cause of the lateral capillary forces is the deformation of the liquid surface, which is supposed to be flat in the absence of particles. It has been observed that two similar particles floating on a liquid interface or partially immersed in a liquid layer, attract each other, however, by different

mechanisms. The origin of the flotation force is the particle weight plus the Archimedes force, to minimize the gravitational potential energy in such a way that particles approach and a liquid meniscus deforms. The deformation of the liquid surface in the partial immersion cases is related to the wetting properties of the particle surface. The flotation and immersion forces can be both attractive (Figure 1.6a, b) and repulsive (Figure 1.6c, d), determined by the signs of the meniscus slope angles: the capillary force is attractive when $sin\psi_1 sin\psi_2 > 0$ and repulsive when $sin\psi_1 sin\ \psi_2 < 0$($\psi > 0$ for convex meniscus).[1.33]

The larger the interfacial deformation created by the particles, the stronger the capillary interaction between them. For the spray pyrolysis system, a faster evaporation rate can facilitate faster moving of the molecules or colloidal particles, resulting in different structural assemblies.

Many factors can affect the above forces, and thus the nucleation and growth processes in fluid. For example, ionic strength of a solute is related to the system free energy; an appropriate solvent and stabilizing agent can form an extended layer for screening the attractions between particles; different surfactant concentrations create different micelles configurations; pH of the system controls the rates of hydrolysis and condensation; temperature determines diffusivity of growth units; addition of co-surfactants or additives such as alcohols or hydrocarbons change the structure and properties of micelles;[1.34] and there are other factors yet to be explored. More examples for SA driving forces will be discussed in detail in the section for Structure Manipulated Particles, such as driving force determined porous structure, of which pores come from bubble or template building blocks.

It is therefore important to develop synthetic methods with which the particles can be

stabilized to the size in demand, where repulsive and attractive forces between particles balance each other (controlled by free energy). Generally defining, Van der Waals force, H-bond and solvation effect are weak electrostatic interactions, and they are ubiquitous in systems. Combined with other effects, the mechanism research should consider balancing all repulsion and attraction effects.

1.1.3.2 Mechanisms

Mechanism research for SA can start from the study of the liquid crystal (LC) formation mechanism, which requires consideration of multiple driving forces mentioned above. It is a state of matter that has properties between those of a conventional liquid and those of a solid crystal, for it may flow like a liquid, but its molecules may be oriented in a crystal-like way. For example, the nematic phase, one of the most common LC phases, has fluidity similar to that of ordinary (isotropic) liquids but they can be easily aligned by an external magnetic or electric field; aligned nematic phase LCs have the optical properties of uniaxial crystals, which can be taken advantage of in the important application of liquid crystal displays (LCD). Moreover, lyotropic liquid crystals rely on a subtle balance of intermolecular interactions; thus, it is more difficult to analyze their structures and properties than those of thermotropic liquid crystals. Two mechanisms are created based on when the ordered phase is generated. Liquid crystal templating (LCT) forms a liquid crystal structure in later phase transitions and requires strongly acidic or basic conditions to enhance interactions stated above; however, in true liquid crystal templating (TLCT), the surfactant forms a lyotropic liquid crystal phase of well-defined geometry and dimensions at the start of the synthesis.

Templating method for porous silica formation is intriguing because diverse

structures can be created from different amounts and different types of surfactants. Some of the structures follow the traditional surfactant micelle structure, such as spherical and rod shapes, but some are different from the micelle structure, such as the layer-by-layer vesicular structure.[1.35] As this cannot be explained by the conventional liquid-crystal templating mechanism, an alternative mechanism needs to be proposed.

Two different mechanisms for the synthesis of mesoporous silica in the presence of surfactants have been suggested before.[1.36] The first one assumes that a preformed water/surfactant liquid-crystal phase exists prior to the addition of the precursor (true liquid-crystal templating mechanism), so the structure is defined by the organization of the surfactant molecules into micellar liquid crystals that serve as pore templates. In this approach, the concentration of the templating surfactant should be high. The liquid crystal structures that form in surfactant solutions are sensitive to solution conditions: ionic strength, counterion polarizability, surfactant concentration, counterion charge, temperature, and the addition of co-surfactants or additives like alcohols or hydrocarbons. Also, it proposes that silicate condensation is not the dominant factor in the formation of the structure, but rather just works as a glue.[1.37] The second mechanism proposes that the surfactant mesophase is only formed after the addition of the silica source (cooperative self-assembly templating mechanism). The initial surfactant concentration could be lower here, and interactions between template and silica species are supposed to work cooperatively to form a liquid crystal phase. This means that polymerization and formation of a lyotropic phase occurs simultaneously.

Inspired by the above mechanisms, two mechanisms can be proposed (Figure 1.7) for evaporation-induced self-assembly. The initial solution has TEOS (blue dots) and CTAB

(black, with a hydrophilic head and a hydrophobic tail) molecules in it. There is no self-assembly in the initial solution because of the low concentration. The first hypothesis originates from the above true liquid-crystal templating mechanism: driven by the electrostatic attraction force, two types of units, silica nanoclusters and self-assembled surfactant micelles, proceed to grow heterogeneously in the system as concentration increases due to the evaporation. Another is analogous to the cooperative self-assembly templating mechanism: primary silica nanoclusters is formed in the surfactant template due to the initial hydrophobic property of TEOS, coated by amphipathic surfactants; as these units collide, surfactants restructure themselves to form pore templates on the particle, and it is homogeneous growth compared to the first mechanism. Because homogeneous and heterogeneous processes have different influencing factors, the kinetics and thermodynamics will be different for these two mechanisms.

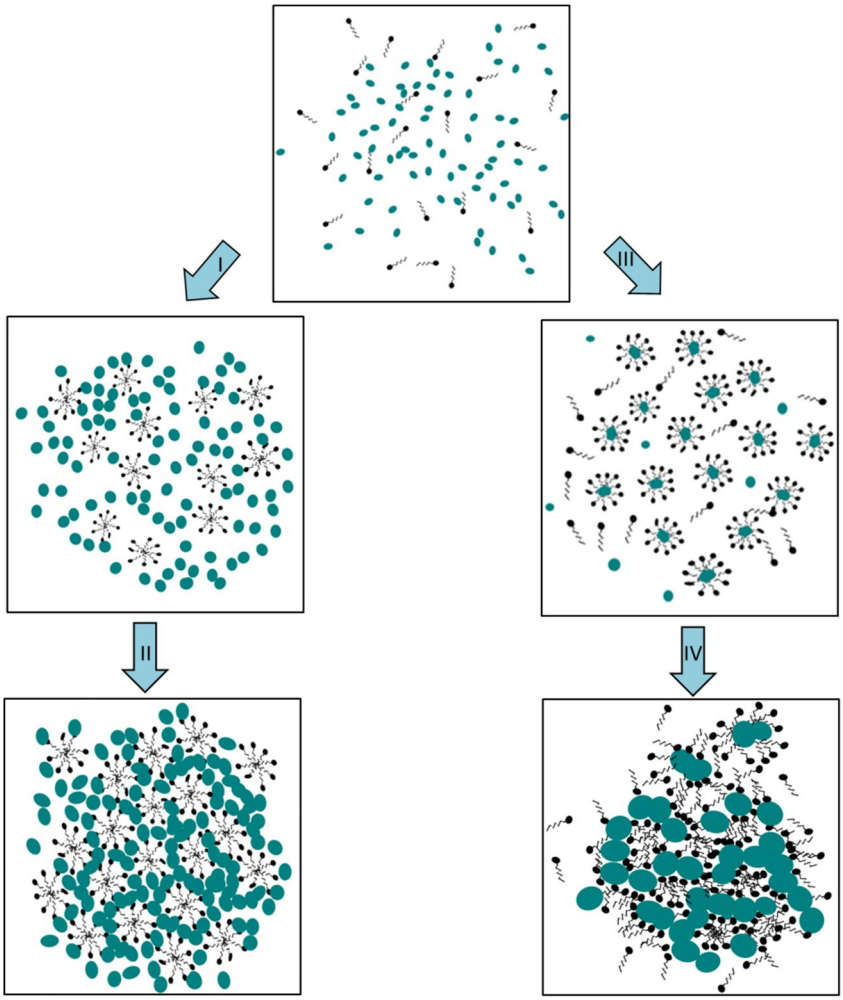


Figure 1.7. Ⅰ Ⅱ are for heterogeneous growth models and Ⅲ Ⅳ are for homogeneous models.
Ⅰ: Micelles and silica primary clusters form simultaneously;
Ⅱ: Micelles self-organize as crystal, and silica primary clusters function as glue due to their covalent condensation;
Ⅲ: TEOS is not water soluble in the beginning; therefore, the precursor droplets tend to form primary clusters in micelles;
Ⅳ: As hydrolysis and condensation proceed, silica clusters tend to get out of the micelle because it is more water soluble. Collisions of surfactant-wrapped particles facilitate growth of secondary particles and restructuration of surfactant templates.

Realistically, it is possible that the actual mechanism is the middle ground between these two mechanisms. Another possibility is that because some conditions change as time passes, the process turns from one mechanism to another. But, we may control the reaction occurrence under a particular mechanism by adjusting the parameters, and thus the particle structure.

#### 1.1.3.3 Instrumental Analysis for Mechanism Study

Some structural characterizations, such as pore order, wall thickness, and elemental distribution if phase separation occurs in a multi-composite particle, should be conducted in the mechanism research. For the spray pyrolysis system, some other factors can affect the core-shell structure of the composite aerosol particles, such as solubility of precursor chemicals, mass transport of composites, melting point of intermediate products, and effect of additives to the above properties. For example, if the solvent evaporation is much faster than the mass transport, reaching the solubility first on the shell will create a hollow particle. However, if the mass transport is fast enough or the melting point of the precursor is lower than the boiling point of the solute, no hollow structure can be formed.

Some important characterization methods include DLS (dynamic light scattering) and SEM (scanning electron microscopy) to measure the size of particles, TEM (transmission electron microscopy) and SAXS (Small-angle X-ray scattering) to characterize the pore structure. BET (nitrogen sorption Brunauer-Emmett-Teller methodology) and tandem DMA-APM (differential mobility analyzer-aerosol particle mass analyzer) methods can be used to study the pore infrastructure in detail. XPS (X-ray photoelectron spectroscopy), FTIR (Fourier transform infrared spectroscopy) and UV-Vis (Ultraviolet–visible spectroscopy) are needed to characterize the functionalized particles.[1.38]

## 1.2 Structure-Manipulated Particles

### 1.2.1 Size and Shape Control of Nanoparticles

Nanocrystals of various sizes and shapes have been successfully synthesized over the past years. Because the properties of nanosized materials are strongly influenced by sizes and shape (nano- dots, rods, spindles and tetrapods), it is very important to explore the growth mechanisms that lead to a particular nanocrystal shape to systematically produce the desired material. For a given monomer concentration, there is a critical nanoparticle size formed. As mentioned above, when the nanocrystals present in the solution are slightly larger than the critical size, smaller nanocrystals in the distribution grow more rapidly than the larger ones: narrowing or focusing of the size distribution occurs first. The next stage can be defocusing (Ostwald ripening): when the monomer concentration is depleted due to particle growth, smaller nanocrystals are shrinking and will eventually disappear, whereas the larger ones keep growing. The distribution can be refocused by injection of additional monomers, which compensates for the depletion due to the growth and shifts the critical size back to a smaller value.[1.39] In this step of nanocrystal growth, the focusing time as well as the focused size changes with the different initial concentration of the monomer, as the time for depleting the monomer concentration varies. Two distinct kinetic regimes in the actual example of CdSe synthesis are: during the first 22 min growth period, the average size increases relatively rapidly from the diameter of 2.1 nm to 3.3 nm, and the size distribution focuses from 20% to 7.7% polydispersity.[1.40] Subsequently, the nanocrystals grow more slowly to the diameter of 3.9 nm, and the nanocrystal size distribution broadens to 10.6%. A second injection of molecular precursors increases the growth rate and refocuses the size distribution to 8.7%. Because the time for depleting the monomer concentration changes, the focusing time as well as the focused size can be changed by varying the initial concentration of the

monomer. In the above case of CdSe synthesis, just decreasing the volume of the first injection by about 15% and keeping all the other conditions the same, the focusing time was shortened from 22 to 11 min, and the focused size decreased from 3.3 to 2.7 nm with a tighter size distribution. In addition, a higher ratio of Cd to Se can lead to a longer size distribution focusing period before defocusing occurs.[1.40]

The nucleation stage for the growth of anisotropic shapes plays a key role in determining the size/shape of the resulting nanocrystals. In the extremely small size range, the relative chemical potential is highly size- and configuration-dependent of the nuclei. Thermodynamically, all of the nanocrystals will grow toward the shape having the lowest energy at equilibrium, which is governed by the classic theory. Before the reaction reaches the equilibrium stage, any metastable nanocrystal shapes can be arrested by tuning the reaction conditions, shown in Figure 1.8. As is experimentally observed and demonstrated in Figure 1.9, the diffusion-controlled shape evolution of a nanorod experiences 1D-growth (highly-concentrated solution monomers grow more on tips), 3D-growth (monomers of median concentration grow evenly on the outer layer), and 1D-to-2D intraparticle ripening. (chemical potential minimization driven, without net monomer exchange between the nanocrystals and the solution).[1.4, 1.41]

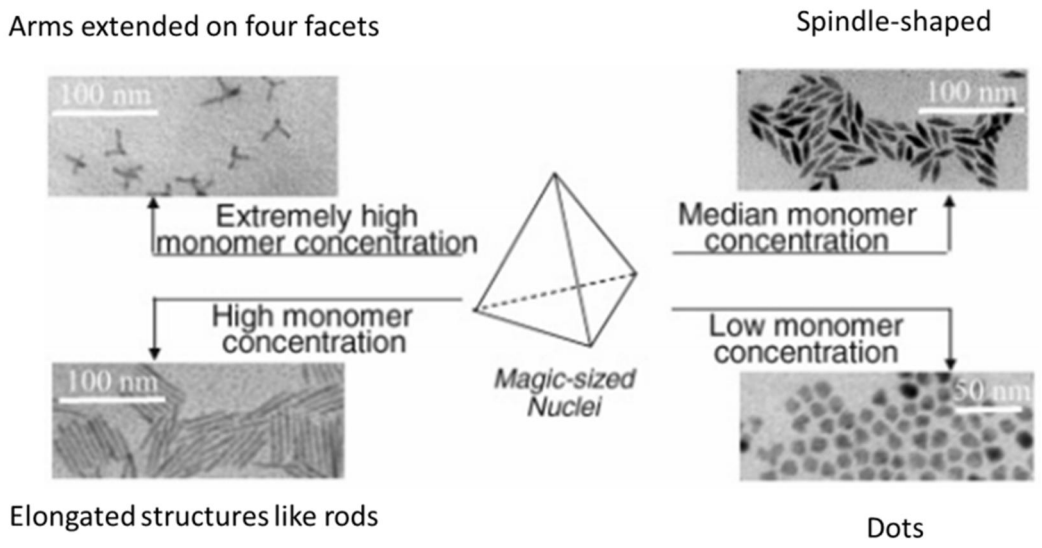


Figure 1.8. Illustration of the growth conditions and products from tetrahedral magic-sized nuclei.[1.42]

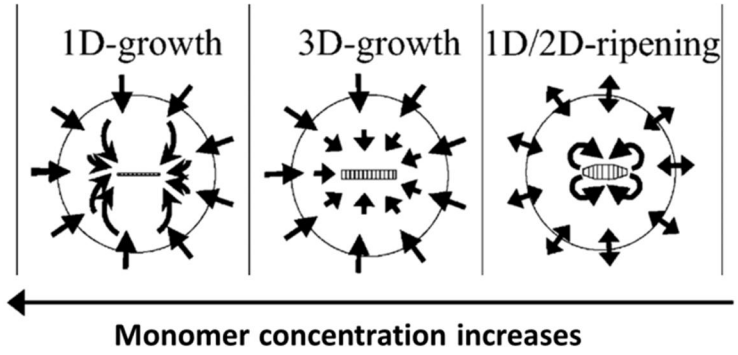


Figure 1.9. Diffusion controlled shape evolution of a nanorod.[1.42]

(i)

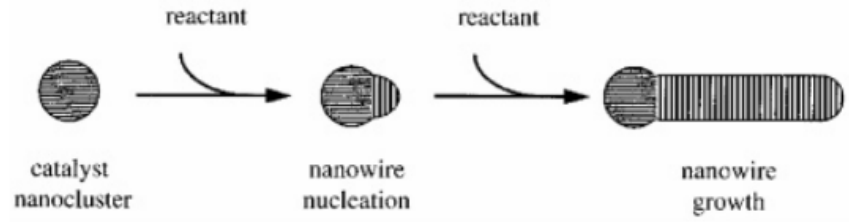


(ii)

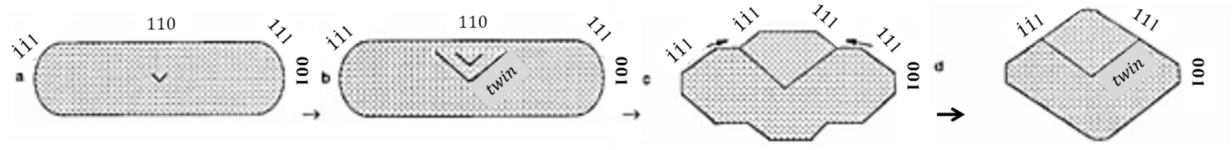


Figure 1.10. (i) Vapor deposition and (ii) light-induced nanostructure evolution.[1.42]

There also exists catalyst employed nanostructure manipulation, by CVD/PVD or pulsed laser light. Mechanisms are shown in figure 10. Vapor-liquid-solid growth for the nanowire (Figure 1.10i) processes vapor phase condenses on the catalyst and forms a co-alloy in liquid phase, and the target solid wire grows after nucleation from this liquid phase resulting from the continuing condensation of the vapor phase. The liquid catalyst alloy cluster serves as a preferential site for absorption of reactant, comparing to a solid surface, and when supersaturated, acts as the nucleation site for crystallization. Preferential one-dimensional growth occurs in the presence of the reactant as long as the catalyst remains as a liquid. Usually, the catalyst defines the diameter of the structure and localizes the reactant at the end of the growing nanowire, and thus the specific composition to form a liquid alloy and the synthesis temperature are key components to the growth of well-controlled nanowires.

Figure 1.10 (ii) illustrates a proposed mechanism of the rod-to-sphere shape transformation of light-induced process. While being illuminated by pulsed laser light, point defects are first created in the body of the nanorods, which served as the nuclei for the formation of twins and stacking faults. The melting first takes place at the defect sites in order to form a twinned crystal, followed by surface diffusion that enhances the growth of the twinned crystal, which is driven by reduction of the surface energy through the decrease of unstable {110} surface and increase of the more stable {111} surface, eventually transforming the Au nanorods into spherical nanoparticles.

### 1.2.2 Template Route

A surfactant template is broadly used in making structure-manipulated silica material. Electrostatic attraction is usually the self-assembly driving force for ionic building blocks.

The isoelectric point (IEP), is the pH at which a particular molecule or surface carries no net electrical charge. Adjusting the pH of the system, the charge of the building blocks can be tuned, which importantly affects the physicochemical properties of the system. For example, a system with pH higher than the IEP of silica nanocluster (negative charged) is usually used to build cationic surfactant templates (positive charged) into silica porous structures, because two types of units should attract each other to build the structure.[1.43]

On the other hand, nonionic surfactants like poly- or oligoethyleneoxide may bind with the surface due to the free electron pairs of oxygen via the H-bridge.[1.44] By this method, the pluronic type or polyethyleneoxide-b-polybutadiene could form pores of controllable sizes with variable lengths. Ordered self-assembled structures are tunable by the concentrations, in the form of cubic, hexagonal columnar or lamellar phase. The fine structure is adjustable even within the same phases: the layer distances increase with the solvent volume in lamellar phases. For the post-treatment of template route synthesis, solvent removal and calcinations are preceded for the gel formation, material solidification and pore generation.

#### 1.2.2.1 Hard-Template Route

Templating against hard colloids, such as polymer and metal, is a commonly used approach.[1.45] Subsequent removal of the template by calcination or selective etching generates porous or capsule-shaped particles whose inner diameters are determined by the size of templates.

Colloid-templated layer-by-layer electrostatic assembly is versatile with the help of some medium, followed by direct chemical deposition or adsorption. For example, CTAB (Cetyltrimethylammonium bromide) protected particles could form porous silica on the

outer layer,[1.46] but this method is usually arduous, and precise control of its pore and particle sizes is still an unsolved challenge (Figure 1.11).

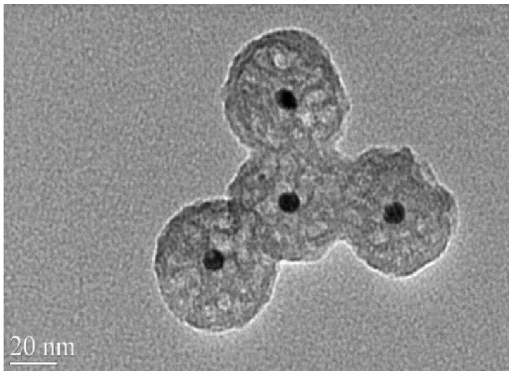


Figure 1.11. Porous silica coated gold nanoparticle.

### 1.2.2.2 Soft-Template Route

Soft templates could show some advantages at times, as removing hard templates inevitably degrades structural robustness and integrity of target products. These systems like micelles, reverse micelles, vesicles, polyelectrolyte capsules or gaseous templates can be organized through a self-assembly process.

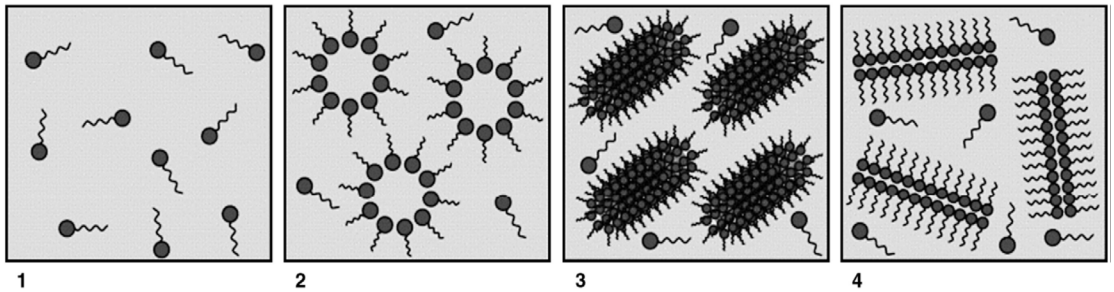


Figure 1.12. Different concentration of surfactant in water/oil phase.[1.47]

Surfactants can self-assemble to a rich variety of organized structures, which has been mentioned in the micelles synthesis method in section 1.1.2.3.[1.47] (Figure 1.12) Therefore, surfactant molecular structure, surfactant/precursor ratio and surfactant concentration are very important factors for manipulating the pore structure. A good example is in the

evaporation-induced self-assembly (EISA) method, where ordered porous silica particles are shown like a crystal lattice (P63n/ P6m).[1.48] EISA precedes liquid crystal templating and the phase transition process. As previously stated, not only the loading volume of pores, but also toxicity properties in vivo may differ distinctively, though the reason is not yet clear.

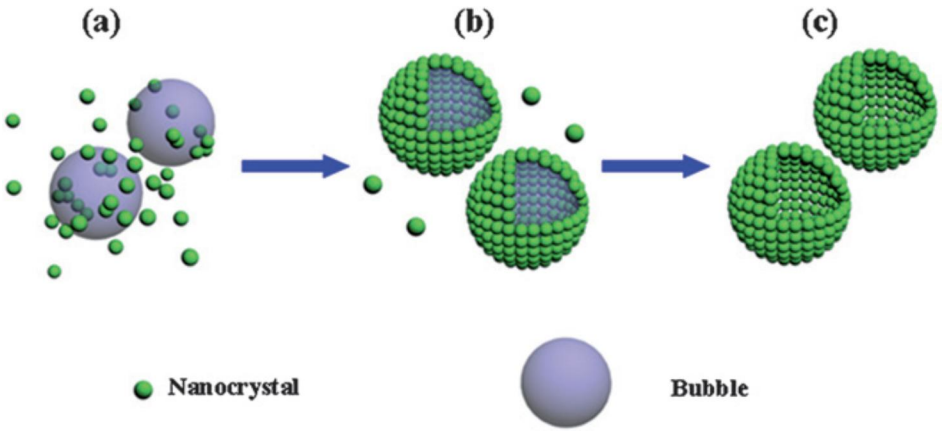


Figure 1.13. Bubble-template route formation process.[1.49]

The bubble-template route could be looked on as an interfacial reaction, which is shown in Figure 1.13. As monomers nucleate into nanoclusters, they tend to aggregate to reduce the high surface energy, and bubbles produced during the reaction provide a simultaneous aggregation center. Gas/liquid bubbles could make hollow capsules directly[1.50], or mini-emulsion "bubbles" could also store phase transition chemicals inside for energy storage.[1.51] Different from traditional emulsion to form particles inside the micelle templates, pickering emulsion facilitates solid particles assembly on the interface between two phases, and thus capsule formation by radiation catalysis. The gamma-ray can induce the polymerization of styrene by initiating radiolysis of water. Because the radicals (•H and •OH) and styrene monomers are from different phases, polymerization occurs on the interface. (Figure 1.14) In this system, the content of water, Span 80,

styrene, magnetic nanoparticles and dose rate can affect the morphology of the capsules.[1.52]

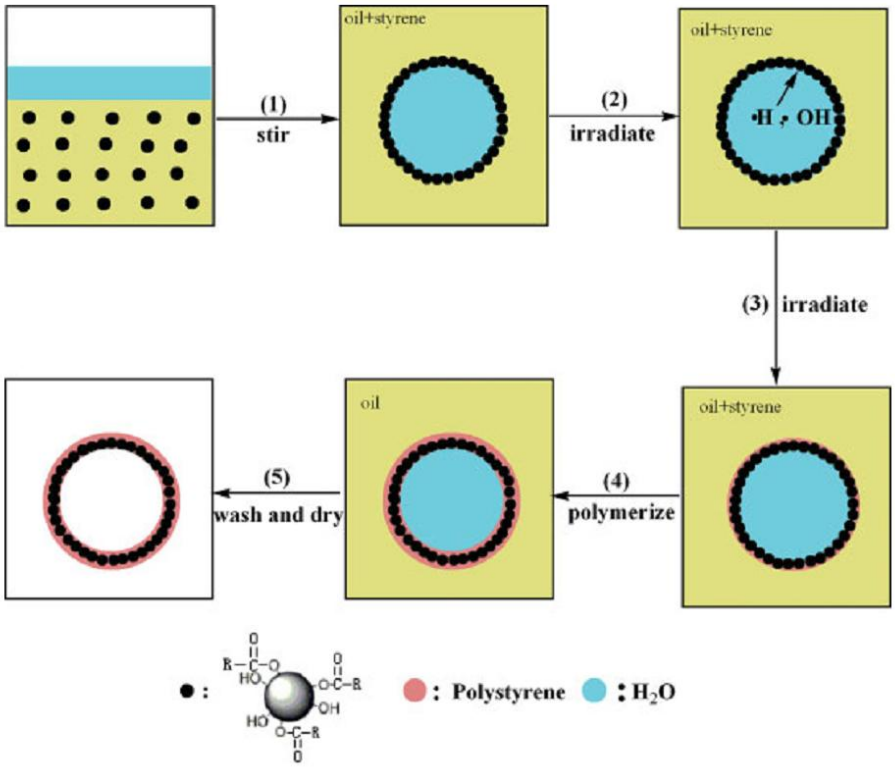


Figure 1.14. Interfacial reaction catalyzed by gamma-ray.[1.52]

### 1.2.2.3 Sacrificial Template Route

The sacrificial template route no only acts as the simple shape-defining mold but also as a porogen. Similar to the hard template route, the shape of the product particle is determined by the template shape (Figure 1.15). However, its advantage over the hard template route is that, because the template is consumed partially or completely during the shell-forming process as one of the reagents, high-temperature calcination, and base or acid etching could be omitted. In the reaction process, since the diffusion rate of inner reagent should be larger than the coming reagent to form the hollow structure, critical size of template particle is required.[1.49]

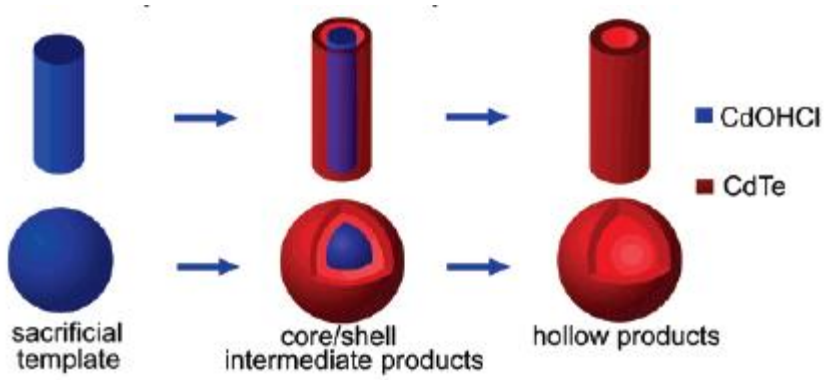

Figure 1.15. Sacrificed template shape determines the final product shape.[1.53]

### 1.2.3 Template-Free Route

As templating synthesis is widely used, template-free routes could avoid high cost and post-treatment processes.

The Ostwald ripening process could make template-free hollow particles,[1.54] consisting of three steps: 1) under the driving force of minimizing surface energy, metastable nanoclusters aggregate to reduce supersaturation of the solution; 2) when crystal materials grow in solution, the concentration of growth units reduce in the mother solution; and 3) voids gradually generate and grow in the cores, and the shell thickness increases owing to outward diffusion of solutes through the permeable shell.

Co-condensation is an alternative to make ordered pore structure in silica systems.[1.55] It is based on sodium hydroxide catalyzed reactions of TEOS with various organoalkoxysilanes in the absence or presence of a low concentration of surfactant, such as CTAB. By varying the type and the amount of organoalkoxysilanes used, a series of nanoparticles were obtained in the form of spheres, rods, and hexagonal tubes, and functionalized at the same time. The non-alkoxy group on silanes contributes to the formation of pores, as it cannot continue the condensation. The organoalkoxysilanes

successfully used in this method and mechanism in the presence of a surfactant are illustrated in Figure 1.16.

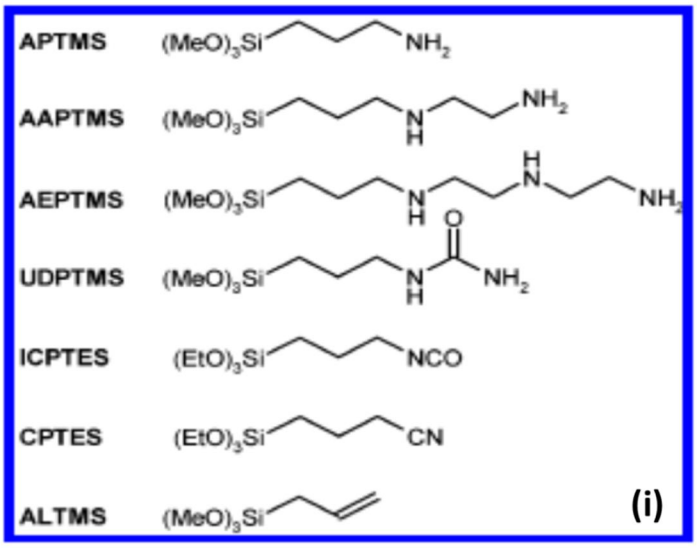


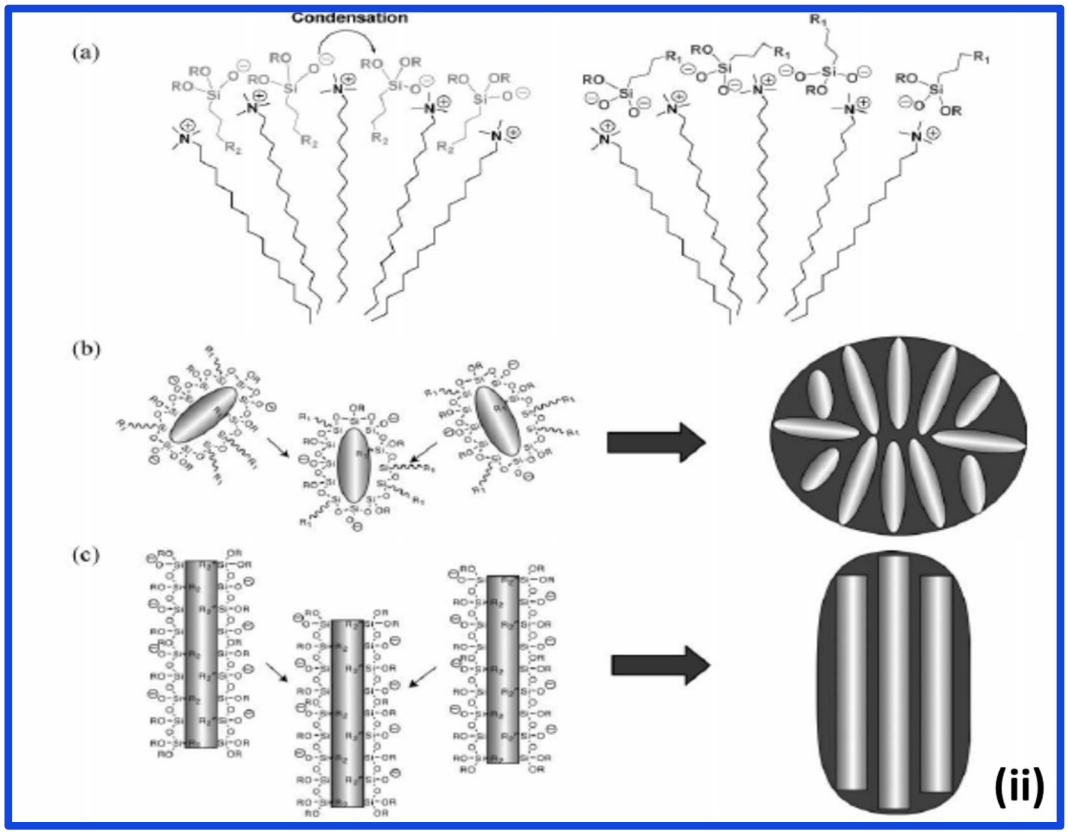


Figure 1.16.(i)Types of organoalkoxysilanes used in co-condensation and (ii) mechanism.[1.55]

### 1.2.4 Other Structure Manipulation

Combining the above technologies, many interesting structures and surface functionalization could be created (Figure 1.17), for advanced application needs. For example, silica coating on colloidal systems such as nanoscale metals, semiconductors, magnetic nanoparticles, and quantum confinement, brings silica magnetic and optical properties. Also, the coating can highly improve cores' stability in water, chemical inertness and dispensability due to the steric and electrostatic protection.

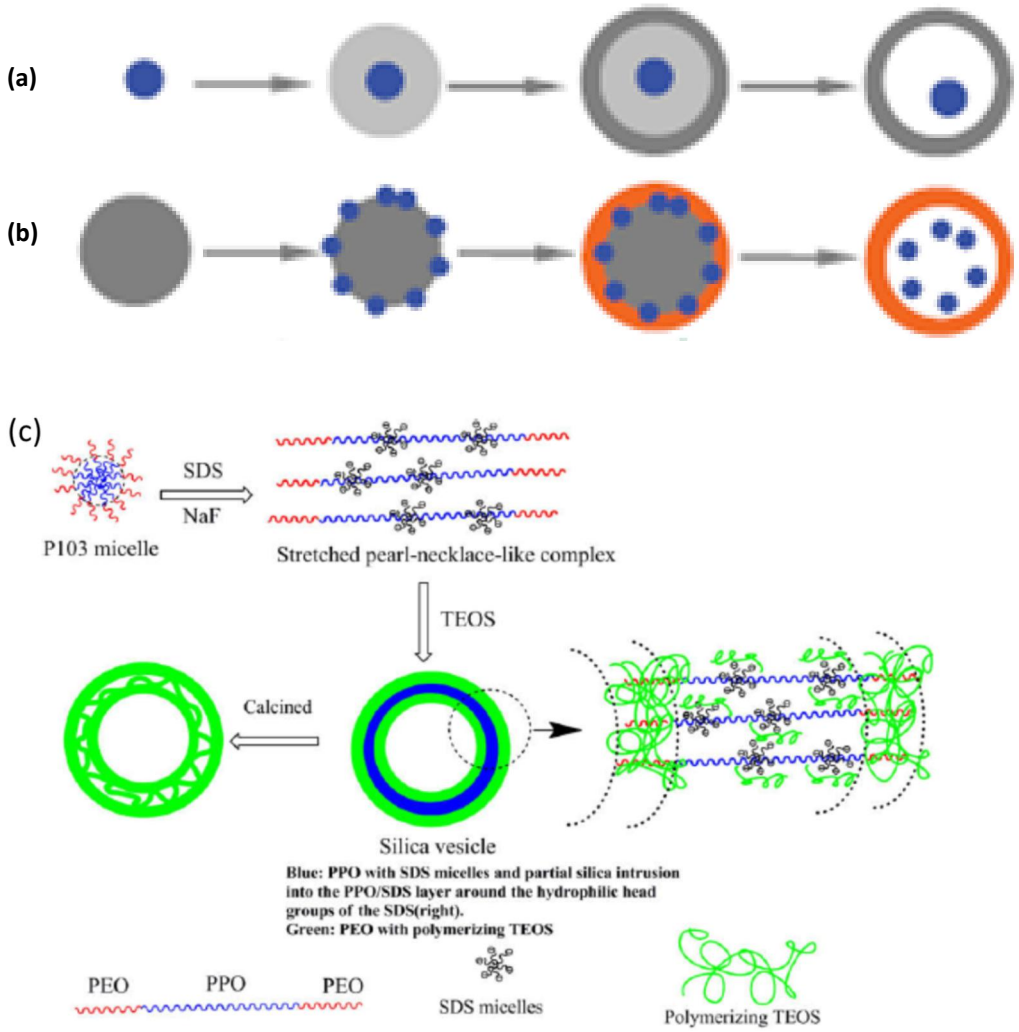


Figure 1.17(a)(b) Layer by layer synthesis of rattle-type particles and (c) scheme of dual surfactant role in vesicular structure.[1.56]

## 1.3 Set-Up System

### 1.3.1 Conventional System

The conventional nanoparticle synthesis system in this thesis is defined as the set-up where the reaction occurs in the bulk liquid phase, such as sol, sol-gel, micelle (two-phase systems such as emulsion or microemulsion), chemical precipitation, and hydrothermal process in the section of synthesis methods. In the conventional system, the precursor and the solvent are both liquid, and self-assembly occurs in a non-evaporation system.

In such systems, reaction precursors of particles are from a fixed bulk reservoir; reaction temperature cannot be higher than the evaporation temperature of solvent under the reaction pressure; the time of particle formation ranges from minutes to days; and reaction conditions should be considered for the interaction between building blocks.

### 1.3.2 CVD/ALD/Physical Deposition

Chemical vapor deposition, atomic layer deposition and physical deposition include one gas precursor in the particle formation.[1.57] Compared to a conventional set-up, the deposition amount and rate of a vapor source is more flexible: as the technology develops, thickness of the deposited layer can be controlled and various materials can be created. What is the same as the bulk liquid colloidal system is that, particles grow from the inside out.

### 1.3.3 Spray Synthesis

Aerosol synthesis of nanoparticles is also very interesting, where the hollow or templated structure forms in one step. The spray system in this section does not process

vaporization of the solute as for CVD process. The set-up for evaporation-induced self-assembly (EISA) is shown in Figure 1.18, which includes an atomizer (to produce aerosol droplets), a diffusion drier (to remove solvent), a high-temperature furnace (to proceed structure manipulation or chemical reaction) and a filter (to collect product). The primary distinction to the conventional colloidal system is that one aerosol droplet itself is a reactor, evaporation of solvent drives the packing to form a particle, and attractive force among building blocks is not important or even should be prevented to keep the precursor solution stable. The precursor concentrations increase during the evaporation of the solvent, compared to the concentration decrease in the bulk reactor during the reaction. The heating section can be rapidly raised to a very high temperature and heating residence time is short, from several seconds to several minutes. All these factors bring many advantages of this method in creating special structured particles, which will be focused on more in later chapters.

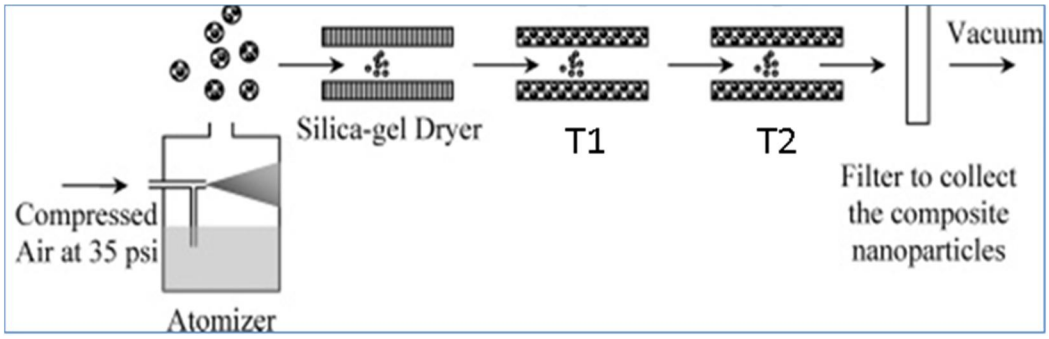


Figure 1.18. Aerosol spray pyrolysis set-up.

Spray-freeze-drying is another spray method to generate powders. It is broadly used in the manufacture of pharmaceuticals and in the food industry. The process includes: 1) atomization of liquid solutions or suspensions using ultrasound, one- or two-fluid nozzles or vibrating orifice droplet generators; 2) freezing the droplets in a cryogenic liquid or cryogenic vapor; and 3) ice sublimation at a low temperature and pressure or alternatively

atmospheric freeze-drying using a cold desiccant gas stream. The benefits of this process include rapid cooling rates ($10^3$ K/s) that support the formation of glassy water before the protein undergoes aggregation and denaturation in the freeze-concentrated solution[1.58]; and that it has a high process yield (>95%) and better control of final particle size compared to spray-drying. However, complicated scalability is a common limitation as for the spray-drying methods.

Besides mimicking micro sol-gel phase reaction, chemical vapor deposition is also possible on spray methods.[1.59] Because this method involves gas flow and a high reaction temperature, CVD-like deposition (vapor deposits on aerosols) can occur online or during the particle formation. So, the adjustable parameters for this set-up system are atomized droplet size, heating/freezing zone temperature(s) and residence time, gas flow, evaporation rate/ selection of solvent(s) and selection of precursors.

## 1.4 Characterization

Besides commonly used chemical characterization (UV-Vis, FTIR, NMR, fluorescent spectroscopy, Raman spectroscopy, TEM, SEM, TGA, XPS and so on), there are more characterization methods for special properties (VSM, photoelectrochemical characterization, electrochemistry characterization). Here, we will concentrate on the characterization methods for aerosol nanoparticles (DMA, APM, PAS, CRD are all online methods).

### 1.4.1 Differential Mobility Analyzer (DMA)

Various kinds of aerosol classification devices have been developed so far. The basic principle for classification employed in most of these devices involves the balancing of

the drag force exerted by the surrounding air on the particles with some constant external force. Figure 1.19 is an example of forces acting on a particle in an electrical field; gravity is ignored because the electrostatic force can be thousands of times greater than the force of gravity.

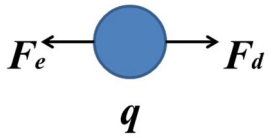


Figure 1.19. Forces to be balanced in DMA theory.

Examples of such external forces include: the electrostatic force for the electrical aerosol analyzer[1.60] and the differential mobility analyzer;[1.61] gravity for the horizontal elutriator[1.62] and the sedimentation cell;[1.63] involvement of the centrifugal force for the cyclone,[1.64] the conifuge,[1.65] the cylindrical aerosol spectrometer,[1.66] the Goetz aerosol spectrometer,[1.67] and the Stober centrifuge.[1.68] The particle properties utilized for this purpose include the electrical mobility, the mechanical mobility, the relaxation time, and the diffusion coefficient. These properties are important in that they directly govern the particle motion resulting from the relevant external forces. Since the drag force, which may be described by the Stokes formula modified by the slip correction factor, is determined by the particle diameter, the properties according to which particles are classified with these devices are functions of the particle diameter. Due to the particle interaction with the surrounding air, properties of flow need to be considered in the model calculation. Besides, when the particles are not spherical, the classification properties depend on the particle orientation relative to their movement, so the interpretation and use of these properties often become somewhat complicated.

Differential mobility analyzer (DMA) is also called an electrostatic classifier, which is used to measure article size distribution in the size range from about 0.01 μm to 0.5 μm. The classifier is operated at atmospheric pressure to select narrow size ranges from a polydisperse aerosol. The concentration in each size range is usually measured with a condensation particle counter (CPC), which will be discussed in a later section. In this way, the particle size distribution can be determined, and the profile conveyed from the software is a curve of number concentration per unit volume versus a particle diameter.

As shown in Figure 1.20, particle classification takes place in the annular region between a stainless steel outer cylinder and a coaxial stainless steel center rod. The advantages of a cylindrical geometry is that distortion of the electric field between the electrodes is minimal due to the absence of corners and edges, and it can offer advantages in flow stability at high flow rates, which in turn help minimize diffusion losses of nanometer-sized particles.[1.61]

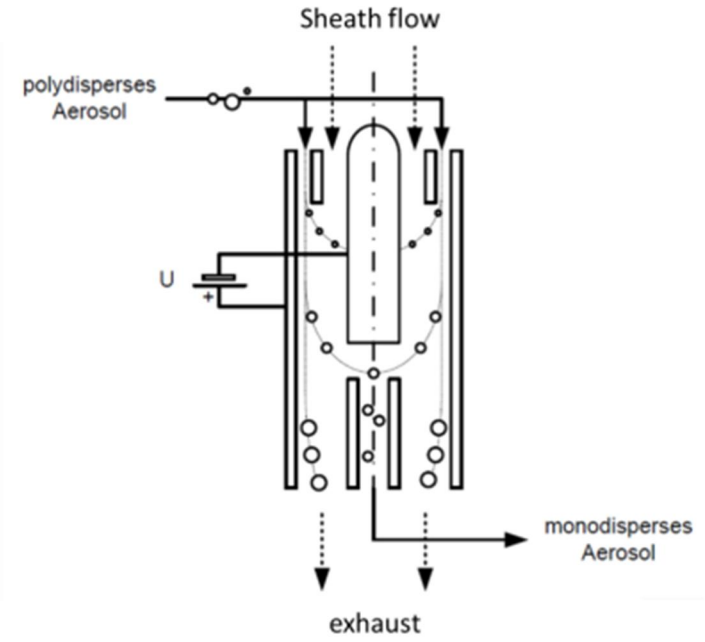


Figure 1.20. Particle selection scheme of DMA.
( from http://commons.wikimedia.org/wiki/File:DEMC_DMA.PNG, accessed on Aug 10, 2012)

Before entering the analyzers of electrostatic force, not only for DMA, the polydisperse aerosol is passed over a radioactive source that generates bipolar gas ions that attach to the particles to produce a bipolar charged aerosol. Not all of the particles become charged nor do the charged particles obtain a single charge; the distribution of the aerosol particle charges at Boltzmann equilibrium is shown in table 1.

Table 1. Charge distribution of aerosol particles at Boltzmann equilibrium.[1.69]

| $d_p$ | Average | % of particles carrying the indicated number of charges | | | | | | | | |
|---|---|---|---|---|---|---|---|---|---|---|
| (μm) | Charges | < -3 | -3 | - 2 | -1 | 0 | +1 | + 2 | + 3 | > +3 |
| 0.01 | 0.007 | | | | 0.3 | 99.3 | 0.3 | | | |
| 0.02 | 0.104 | | | | 5.2 | 89.6 | 5.2 | | | |
| 0.05 | 0.411 | | | 0.6 | 19.3 | 60.2 | 19.3 | 0.6 | | |
| 0.1 | 0.672 | | 0.3 | 4.4 | 24.1 | 42.6 | 24.1 | 4.4 | 0.3 | |
| 0.2 | 1.00 | 0.3 | 2.3 | 9.6 | 22.6 | 30.1 | 22.6 | 9.6 | 2.3 | 0.3 |
| 0.5 | 1.64 | 4.6 | 6.8 | 12.1 | 17.0 | 19.0 | 17.0 | 12.1 | 6.8 | 4.6 |
| 1.0 | 2.34 | 11.8 | 8.1 | 10.7 | 12.7 | 13.5 | 12.7 | 10.7 | 8.1 | 11.8 |
| 2.0 | 3.33 | 20.1 | 7.4 | 8.5 | 9.3 | 9.5 | 9.3 | 8.5 | 7.4 | 20.1 |
| 5.0 | 5.28 | 29.8 | 5.4 | 5.8 | 6.0 | 6.0 | 6.0 | 5.8 | 5.4 | 29.8 |
| 10.0 | 7.47 | 35.4 | 4.0 | 4.2 | 4.2 | 4.3 | 4.2 | 4.2 | 4.0 | 35.4 |

The DMA operates by selecting particles based on a balance of electrical ($F_E$) and drag forces ($F_D$).[1.70]

$$F_D = F_E \Rightarrow \frac{3\pi\mu d_p v}{C_c} = neE \qquad (1.4)$$

$$Z = \frac{v}{E} = \frac{eC_c}{3\pi\mu d_p} \qquad (1.5)$$

,where $n$ is the number of charges, $e$ is the unit of charge, $E$ is electrical field strength, $\mu$ is the gas viscosity, $Cc$ is the velocity slip correction factor, needed for particle in the free molecule flow, $d_p$ is the particle mobility diameter and $v$ is particle velocity.

Equation 1.4 is a unique relationship existing among the particle mobility diameter, the measured velocity, and the applied electric field. At a fixed electrostatic field, only

one mobility size will exit the instrument, which can either be counted (DMA works as an analyzer) or sent to another instrument for further characterization (DMA works as a sampler).

The electrical mobility, *Z*, is defines as the coefficient of proportionality between the migration velocity and the field intensity, illustrating the ability of charged particles to move through a medium in response to an electric field that is pulling them. The selected mobility is often identified with the diameter of a singly charged spherical particle (equation 1.5); thus, the "electrical-mobility diameter" becomes a characteristic of the particle, regardless of whether it is actually spherical. Electrical mobility is the basis for electrostatic precipitation, which is used to remove particles from exhaust gases on an industrial scale.

### 1.4.2 Aerosol Particle Mass Analyzer (APM)

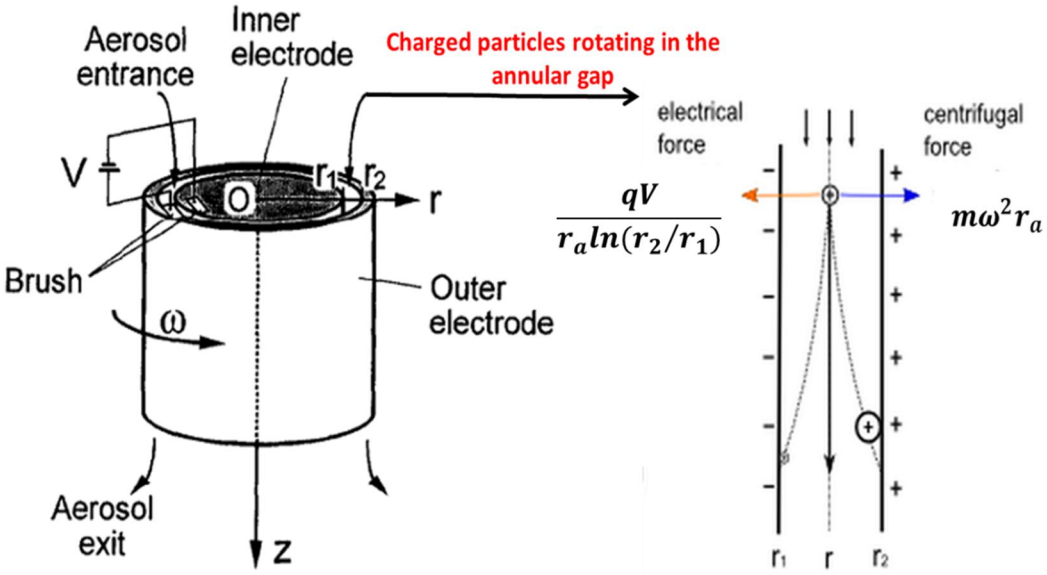


Figure 1.21. Schematic drawing of rotating coaxial cylindrical electrodes of APM.[1.71]

Aerosol Particle Mass Analyzer (APM) classifies aerosol particles according to their mass-to-charge ratio.[1.72] As shown in Figure 1.21, the essential part of APM is the

rotating coaxial cylindrical electrodes. The inner and outer electrodes rotate at the same angular velocity $\omega$. The narrow annular space, the operating space, between the electrodes constitutes the space where classification occurs. The aerosol introduced into the operating space rotates at the same angular velocity $\omega$ as electrodes. It operates by balancing electrostatic and centrifugal forces (The drag force plays only a secondary role, and particle inertia, Brownian motion, the interaction between aerosol particles, and the image potential are neglected.), such that at a fixed applied electric field and rotation speed, particles of only one mass will pass through the instrument.

$$m\omega^2 r_a = \frac{qV}{r_a \ln(r_2/r_1)} \Rightarrow \frac{m}{q} = \frac{V}{\ln(r_2/r_1) r_a{}^2 \omega^2} \qquad (1.6)$$

Where $m$ is the particle mass, $\omega$ is the APM angular speed, $V$ is the applied voltage between the electrodes, $q$ is the particle charge, $r_1$, $r_2$ and $r_a$ are inner, outer and rotating radii at the equilibrium, respectively.

This instrument provides a direct relationship between applied voltage, rotation speed and the particle mass, and effectively operates as a mass spectrometer. By selecting a voltage and rotation speed or scan one of these, it can also be used to generate mass-to-charge monodisperse particles or to measure the mass-to-charge distribution by counting the classified particles, just like DMA.

### 1.4.3 Photoacoustic Spectroscopy (PAS)

Photoacoustic spectroscopy (PAS) is an indirect technique in that an effect of absorption is measured rather than the absorption itself, wherein comes the name of photoacoustic: light absorption is detected through its accompanying acoustic effect. In laser photoacoustic spectroscopy, the nonradiative relaxation that generates heat is of

primary importance, because it is much faster than radiative decay. The spectral dependence of absorption makes it possible to determine the nature of the trace components.

PAS relies on the photoacoustic effect for the detection of absorbing analytes (simplified mechanism is shown in Figure 1.22). The sample gas is in a confined chamber, where modulated radiation enters and is locally absorbed by the molecular species. The temperature of the gas thereby increases, leading to a periodic expansion and contraction of the gas volume synchronous with the modulation frequency of the radiation. This generates a pressure wave that can be acoustically detected by a suitable sensor, such as a microphone.

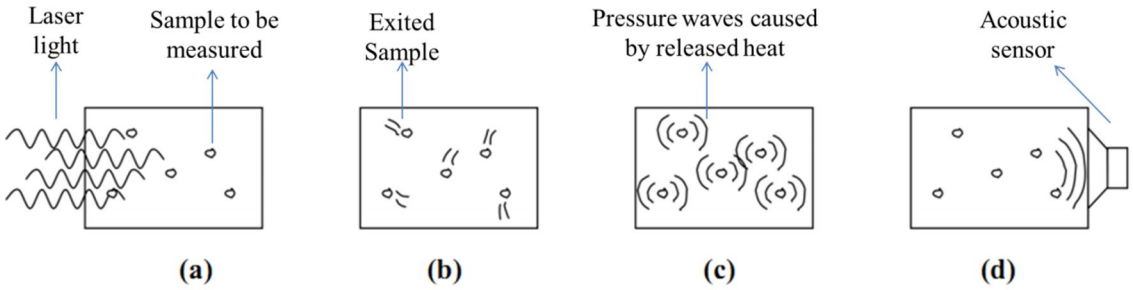


Figure 1.22. Visualization of the mechanism of photoacoustic effect: (a) pulsed light that is incident on a sample is absorbed; (b) the constituent aerosol (molecules) become thermally excited; (c) periodic heat flow from the sample to the surrounding gas causes pressure waves; (d) the pressure waves are in turn detected by an acoustic sensor. The pressure waves are characteristic of the sample and are used to determine composition, concentration, and other thermophysical properties.
(from http://uw.physics.wisc.edu/~timbie/P325/Spike_photoacoustic_effect.pdf, accessed Aug 10, 2012)

The advantages of the photoacoustic method are high sensitivity (absorption of light is measured on a zero background) and small sample volume or measured online; besides, it makes optical detection unnecessary. It is in contrast with direct absorption techniques, where a decrease of the source light intensity has to be observed, which makes the sensitivity lower. The main sensitivity drawback is from the acoustic noise; thus, a well-maintained working station is required for PAS. Also, because of the confounding

absorber- and matrix-specific processes involved in converting absorbed light into sound, absent independent knowledge of the cell constant, a photoacoustic spectrometer requires calibration in order to yield quantitative information. As PAS is increasingly applied to the study of gases and aerosols, I conducted research on aerosol optical standard and calculated particles' refractive indexes, which will be discussed in a later chapter.

### 1.4.4 Cavity Ring-Down Spectroscopy (CRDS)

Cavity ring-down spectroscopy (CRDS) is a highly sensitive optical spectroscopic technique that enables measurement of absolute optical extinction, including scattering and absorption. A typical CRDS setup consists of a laser that is used to illuminate a high-finesse optical cavity, and the laser is so constructed with resonance matching a cavity mode, that intensity builds up in the cavity due to interference. The laser is then turned off in order to allow the measurement of the exponentially decaying light intensity leaking from the cavity. The cavity consists of two highly reflective mirrors, so during this decay, light is reflected back and forth thousands of times between the mirrors giving an effective path length for the extinction on the order of a few kilometers. A CRDS setup measures how long it takes for the light to decay to 1/e of its initial intensity, and this "ring-down time" can be used to calculate the extinction of the gas mixture in the cavity.

Cavity ring down spectroscopy is a direct laser extinction spectrometry, special for a longer light path. The intensity of its trapped laser pulse will decrease by a fixed percentage during each round trip within the cell due to both absorption and scattering by the medium within the cell and reflectivity losses (though reflectivity is higher than 99.9%). The principle of operation is based on the measurement of a decay rate rather

than an absolute decrease of the light intensity, so its increased sensitivity is far beyond traditional light spectroscopy. As is shown in equation 1.7, the intensity of light within the cavity is determined as an exponential function of time.

$$I(t) = I_0 \exp(-t/\tau) \qquad (1.7)$$

The decay constant, $\tau$, is called the ring-down time, dependent on the loss within the cavity, shows the characteristic of the material in the cavity. For an empty cavity, the decay constant $\tau_0$ is related to mirror loss and miscellaneous optical losses.

Except for high sensitivity mentioned above (within 1%),[1.73] another advantage of CRDS is that the ring-down time is not affected by fluctuations in the laser intensity. However, the main limitations are the availability of tunable laser light at the appropriate wavelength and also the availability of high reflectance mirrors at those wavelengths for the analytes.

### 1.4.5 Condensation Particle Counter (CPC)

Most of the particle analyzers measure properties averaged over large numbers of particles; though the nature of particle counting is based upon single particle counting, by light scattering, light obscuration, or direct imaging. A condensation particle counter (CPC) is a particle counter that detects and counts small particles (in the size range from a few nanometers to 1 μm) in the way of enlarging them by using the particles to create droplets in a supersaturated gas. The aerosol is introduced into the instrument where it is saturated with a vapor such as water or an alcohol. As a supersaturated state is produced, the vapor condenses on the particles to form droplets in the size range from 5 to 15 μm,

to be detected. The systems differ according to (a) the condensable vapor, (b) the method of producing supersaturation and (c) the detection scheme.

Importantly, CPC is always used in the end of aerosol characterization set-up, to either create a distribution or assist with optical properties research. The CPC (model 3776, TSI) used in our set-ups is an alcohol-based CPC, and an aerosol sample is drawn continuously through a heated saturator in which alcohol is vaporized and diffused into the sample stream. Together, the aerosol sample and alcohol vapor pass into a cooled condenser where the alcohol vapor becomes supersaturated and ready to condense. Particles present in the sample stream serve as condensation nuclei. Once condensation begins, particles that are larger than a threshold diameter grow quickly into larger droplets and pass through an optical detector where they are counted easily.

## 1.5 Application and Impact

As nanotechnology is considered a key technology for the future, most of the nanoscale world still remains mysterious. Consequently, billions of dollars have been invested in its future.

A number of physical properties like mechanical, electrical, optical, thermal and catalytical properties draw distinctions from the macroscopic system. When brought into a bulk material, nanoparticles can strongly influence the mechanical properties of the material, such as stiffness and elasticity. For example, traditional polymers can be reinforced by nanoparticles resulting in novel materials that can be used as lightweight replacements for metals. Such nanotechnologically enhanced materials will enable a weight reduction accompanied by an increase in stability and improved functionality. Because the confinement of the electronic motion to a length scale is comparable to or

smaller than the length scales of the electronic motion, quantum dots are semiconductors whose electronic characteristics are closely related to the size and shape of the individual crystal. Generally, the smaller the size of the crystal, the larger the band gap, and the greater the difference in energy between the highest valence band and the lowest conduction band becomes; therefore more energy is needed to excite the dot, and concurrently, more energy is released when the crystal returns to its resting state. Optical and thermal properties, *e.g.*, fluorescence and melting point, become a function of the particle diameter when the feature sizes are shrunk. Chemical catalysis benefits especially from nanoparticles, due to the extremely large surface-to-volume ratio, ranging from fuel cell to catalytic converters and photocatalytic devices.

Nanomaterials and devices already have a vast range of applications in medicine, electronics, biomaterials, environmental engineering and energy production.[1.74] They are effective carriers for drugs, memory storage, tissue engineering, absorbents and catalysts. Nanotechnology uses size-induced properties to generate new material qualities, which can provide pioneering solutions to many technological problems. As is developed, it helps manipulate (with precision) matter on previously impossible scales, presenting possibilities that many could never have imagined-it therefore seems unsurprising that few areas of human technology are exempt from the benefits that nanotechnology could potentially bring. However, on the other hand, nanotechnology is also faced with the problem of any kind of new technology, especially with concerns about toxicity and environmental impact.[1.75] To balance the risk of "nanopollution" and the benefits of this technology will be a hot spot on the world level.

## 1.6 Scope of the Dissertation

This dissertation is focused on functionalized nanoparticle synthesis and the formation mechanisms, factors that affect the structures, properties and applications. To support the mechanism research, a new density measure method is developed, for aerosol samples. Since no generic approach exists to produce materials that can resolve all the problems, the high-fluorescent drug delivery ends up by emulsion synthesis, superior to spray aerosol synthesis.

The work for this dissertation will be discussed in three parts. Chapter 2 to chapter 5 are more for spray pyrolysis of nanoparticles of various morphologies and magnetic properties (chapter 2), nanoparticles for the application of optical standard (chapter 3), carbon dispersed metal oxide manoparticle as anode material (chapter 4), and structure control of multi-composite nanoparticles (chapter 5). The second part is chapter 6, which emphasizes the initiation of an aerosol density measurement method and its importance in mechanism research. The last part chapter 7, discusses that while spray-pyrolysis requires high temperature to form firm porous structure as drug delivery in short residence time, dye would mostly decompose in this process, so an alternative synthesis route was developed, which is outstanding for its simplicity and durable fixation of dyes.

## Reference


1.1. Hancock, Y., The 2010 Nobel Prize in physics-ground-breaking experiments on graphene. *Journal of Physics D-Applied Physics* **2011,** *44* (47).

1.2. Mullin, J. M., *Crystallization*. 4th ed.; 2001.

1.3. Peng, Z. A.; Peng, X. G., Formation of high-quality CdTe, CdSe, and CdS nanocrystals using CdO as precursor. *Journal of the American Chemical Society* **2001,**

*123* (1), 183-184; Qu, L. H.; Peng, Z. A.; Peng, X. G., Alternative routes toward high quality CdSe nanocrystals. *Nano Letters* **2001,** *1* (6), 333-337.

1.4. Peng, Z. A.; Peng, X. G., Nearly monodisperse and shape-controlled CdSe nanocrystals via alternative routes: Nucleation and growth. *Journal of the American Chemical Society* **2002,** *124* (13), 3343-3353.

1.5. Wright, J. D.; Sommerdijk, N. A. J. M., *Sol-Gel Materials: Chemistry and applications*. 2000.

1.6. Callegari, A.; Tonti, D.; Chergui, M., Photochemically grown silver nanoparticles with wavelength-controlled size and shape. *Nano Letters* **2003,** *3* (11), 1565-1568; Maillard, M.; Giorgio, S.; Pileni, M. P., Silver nanodisks. *Advanced Materials* **2002,** *14* (15), 1084-; Hao, E.; Bailey, R. C.; Schatz, G. C.; Hupp, J. T.; Li, S. Y., Synthesis and optical properties of "branched" gold nanocrystals. *Nano Letters* **2004,** *4* (2), 327-330; Yu, Y. Y.; Chang, S. S.; Lee, C. L.; Wang, C. R. C., Gold nanorods: Electrochemical synthesis and optical properties. *Journal of Physical Chemistry B* **1997,** *101* (34), 6661-6664; Link, S.; Burda, C.; Mohamed, M. B.; Nikoobakht, B.; El-Sayed, M. A., Laser photothermal melting and fragmentation of gold nanorods: Energy and laser pulse-width dependence. *Journal of Physical Chemistry A* **1999,** *103* (9), 1165-1170; Jana, N. R.; Gearheart, L.; Murphy, C. J., Wet chemical synthesis of high aspect ratio cylindrical gold nanorods. *Journal of Physical Chemistry B* **2001,** *105* (19), 4065-4067; Lisiecki, I.; Billoudet, F.; Pileni, M. P., Control of the shape and the size of copper metallic particles. *Journal of Physical Chemistry* **1996,** *100* (10), 4160-4166.

1.7. Uskokovic, V.; Drofenik, M., Synthesis of materials within reverse micelles. *Surface Review and Letters* **2005,** *12* (2), 239-277.

1.8. Taleb, A.; Petit, C.; Pileni, M. P., Synthesis of highly monodisperse silver nanoparticles from AOT reverse micelles: A way to 2D and 3D self-organization. *Chemistry of Materials* **1997,** *9* (4), 950-959; Barnickel, P.; Wokaun, A., Synthesis of metal colloids in inverse microemultions. *Molecular Physics* **1990,** *69* (1), 1-9; Chen, Z. J.; Ou, X. M.; Tang, F. Q.; Jiang, L., Effect of nanometer particles on the adsorbability and enzymatic activity of glucose oxidase. *Colloids and Surfaces B-Biointerfaces* **1996,** *7* (3-4), 173-179; Lisiecki, I.; Pileni, M. P., Synthesis of copper metallic clusters using reverse micelles as microreactors. *Journal of the American Chemical Society* **1993,** *115* (10), 3887-3896.

1.9. Kawai, T.; Fujino, A.; KonNo, K., Synthesis of monodisperse $ZrO_2$ particles in polyoxyethylated nonionic reversed micelles. *Colloids and Surfaces a-Physicochemical and Engineering Aspects* **1996,** *109*, 245-253; Chang, S. Y.; Liu, L.; Asher, S. A., Preparation and properties of tailored morphology, monodisperse colloidal silica cadmium-sulfide nanocomposites. *Journal of the American Chemical Society* **1994,** *116* (15), 6739-6744; Joselevich, E.; Willner, I., Phtosensitization of quantum-size $TiO_2$ particles in water-in-oil microemulsions. *Journal of Physical Chemistry* **1994,** *98* (31), 7628-7635; Chhabra, V.; Pillai, V.; Mishra, B. K.; Morrone, A.; Shah, D. O., Synthesis, characterization, and properties of microemulsion-mediated nanophase $TiO_2$ particles. *Langmuir* **1995,** *11* (9), 3307-3311; Osseoasare, K.; Arriagada, F. J., Preparation of $SiO_2$ nanoparticles in a nonionic reverse micellar system. *Colloids and Surfaces* **1990,** *50*, 321-339.

1.10. Qi, L. M.; Ma, J. M.; Cheng, H. M.; Zhao, Z. G., Reverse micelle based formation of $BaCO_3$ nanowires. *Journal of Physical Chemistry B* **1997,** *101* (18), 3460-3463.

1.11. Kandori, K.; Konno, K.; Kitahara, A., Formation of ionic water oil microemulsions and their application in the preparation of $CaCO_3$ particles. *Journal of Colloid and Interface Science* **1988,** *122* (1), 78-82; Kandori, K.; Konno, K.; Kitahara, A., Preparation of BaCO3 particles in ionic W/O microemulsions. *Journal of Dispersion Science and Technology* **1988,** *9* (1), 61-73.

1.12. Dvolaitzky, M.; Ober, R.; Taupin, C.; Anthore, R.; Auvray, X.; Petipas, C.; Williams, C., Silver-chloride micro-crystals suspensions in microemulsion media. *Journal of Dispersion Science and Technology* **1983,** *4* (1), 29-45; Chew, C. H.; Gan, L. M.; Shah, D. O., The effect of alkanes on the formation of ultrafine silver bromide particles in ionic W/O microemulsions. *Journal of Dispersion Science and Technology* **1990,** *11* (6), 593-609; Monnoyer, P.; Fonseca, A.; Nagy, J. B., Preparation of colloidal AgBr particles from microemlsions. *Colloids and Surfaces a-Physicochemical and Engineering Aspects* **1995,** *100*, 233-243; Bagwe, R. P.; Khilar, K. C., Effects of the intermicellar exchange rate and cations on the size of silver chloride nanoparticles formed in reverse micelles of AOT. *Langmuir* **1997,** *13* (24), 6432-6438.

1.13. Hopwood, J. D.; Mann, S., Synthesis of barium sulfate nanoparticles and nanofilaments in reverse micelles and microemulsions. *Chemistry of Materials* **1997,** *9* (8), 1819-1828.

1.14. Hirai, T.; Shiojiri, S.; Komasawa, I., Preparation of metal sulfide composite ultrafine particles in reverse micellar systems and their photocatalytic property. *Journal of Chemical Engineering of Japan* **1994,** *27* (5), 590-597.

1.15. Matijevic, E., Preparation and properties of uniform size colloids. *Chemistry of Materials* **1993,** *5* (4), 412-426.

1.16. Huang, Y. X.; Guo, C. J., Synthesis of nanosized zirconia particles via urea hydrolysis. *Powder Technology* **1992,** *72* (2), 101-104; Potdar, H. S.; Deshpande, S. B.; Date, S. K., Chemical coprecipitation of mixed (Ba+Ti) oxalates precursor leading to BaTiO3 powders. *Materials Chemistry and Physics* **1999,** *58* (2), 121-127; Sheen, S. R.; Hsu, Y. J.; Chen, D. H.; Ho, J. S.; Shei, C. Y.; Chang, C. T., Synthesis and characterization of high-Tc Y-Ba-Cu-O superconducting oxides by coprecipitation from triethylamine-oxalate media. *Materials Letters* **1991,** *10* (11-12), 489-493; Spanhel, L.; Haase, M.; Weller, H.; Henglein, A., Photochemistry of colloidal semiconductors. 20. Surface modification and stability of strong luminescing CdS particles. *Journal of the American Chemical Society* **1987,** *109* (19), 5649-5655; Rogach, A. L.; Kornowski, A.; Gao, M. Y.; Eychmuller, A.; Weller, H., Synthesis and characterization of a size series of extremely small thiol-stabilized CdSe nanocrystals. *Journal of Physical Chemistry B* **1999,** *103* (16), 3065-3069; Gao, M. Y.; Kirstein, S.; Mohwald, H.; Rogach, A. L.; Kornowski, A.; Eychmuller, A.; Weller, H., Strongly photoluminescent CdTe nanocrystals by proper surface modification. *Journal of Physical Chemistry B* **1998,** *102* (43), 8360-8363; Mews, A.; Eychmuller, A.; Giersig, M.; Schooss, D.; Weller, H., Preparation, characterization, and photophysics of the quantum-dot quantum-well system CdS/HgS/CdS. *Journal of Physical Chemistry* **1994,** *98* (3), 934-941.

1.17. Dhara, S., Formation, dynamics, and characterization of nanostructures by ion beam irradiation. *Critical Reviews in Solid State and Materials Sciences* **2007,** *32* (1-2), 1-50.
1.18. Demianets, L. N.; Lobachev, A. N., Hydrothermal synthesis of crystals. *Kristall Und Technik-Crystal Research and Technology* **1979,** *14* (5), 509-525.
1.19. O'Donoghu，Michael, *A guide to man-made gemstones*. Van Nostrand Reinhold Company: Great Britain, 1983.
1.20. *50 years progress in crystal growth*. Elsevier: Stanford, CA, 2004.
1.21. Tan, L.; Wang, L.; Wang, Y., Hydrothermal synthesis of $SnO_2$ nanostructures with different morphologies and their optical properties. *Journal of Nanomaterials* **2011**.
1.22. *Aqueous systems at elevated temperatures and pressures*. Elsevier Ltd: 2004.
1.23. Hiruma, K.; Katsuyama, T.; Ogawa, K.; Koguchi, M.; Kakibayashi, H.; Morgan, G. P., Quantum size microcrystals grown using organometallic vapor-phase epitaxy. *Applied Physics Letters* **1991,** *59* (4), 431-433; Hiruma, K.; Yazawa, M.; Katsuyama, T.; Ogawa, K.; Haraguchi, K.; Koguchi, M.; Kakibayashi, H., Growth and optical-properties of nanometer-scale GaAs and InAs whiskers. *Journal of Applied Physics* **1995,** *77* (2), 447-462; Yazawa, M.; Koguchi, M.; Hiruma, K., Heteroepitaxial ultrafine wire-like growth of InAs on GaAs substrates. *Applied Physics Letters* **1991,** *58* (10), 1080-1082; Yazawa, M.; Koguchi, M.; Muto, A.; Ozawa, M.; Hiruma, K., Effect of one monolayer of surface gold atoms on the epitaxial-growth of InAs nanowhiskers. *Applied Physics Letters* **1992,** *61* (17), 2051-2053; Bai, Z. G.; Yu, D. P.; Wang, J. J.; Zou, Y. H.; Qian, W.; Fu, J. S.; Feng, S. Q.; Xu, J.; You, L. P., Synthesis and photoluminescence properties of semiconductor nanowires. *Materials Science and Engineering B-Solid State Materials for Advanced Technology* **2000,** *72* (2-3), 117-120; Dai, H. J.; Wong, E. W.; Lu, Y. Z.; Fan, S. S.; Lieber, C. M., Synthsis and characterization of carbide nanorods. *Nature* **1995,** *375* (6534), 769-772; Han, W. Q.; Fan, S. S.; Li, Q. Q.; Liang, W. J.; Gu, B. L.; Yu, D. P., Continuous synthesis and characterization of silicon carbide nanorods. *Chemical Physics Letters* **1997,** *265* (3-5), 374-378; Han, W. Q.; Fan, S. S.; Li, Q. Q.; Gu, B. L.; Zhang, X. B.; Yu, D. P., Synthesis of silicon nitride nanorods using carbon nanotube as a template. *Applied Physics Letters* **1997,** *71* (16), 2271-2273; Wu, Y.; Cui, Y.; Huynh, L.; Barrelet, C. J.; Bell, D. C.; Lieber, C. M., Controlled growth and structures of molecular-scale silicon nanowires. *Nano Letters* **2004,** *4* (3), 433-436; Zhong, Z. H.; Qian, F.; Wang, D. L.; Lieber, C. M., Synthesis of p-type gallium nitride nanowires for electronic and photonic nanodevices. *Nano Letters* **2003,** *3* (3), 343-346.
1.24. Jung, D. S.; Bin Park, S.; Kang, Y. C., Design of particles by spray pyrolysis and recent progress in its application. *Korean Journal of Chemical Engineering* **2010,** *27* (6), 1621-1645.
1.25. Herlin-Boime, N.; Mayne-L'Hermite, M.; Reynaud, C., Advances in the laser pyrolysis synthesis of nanoparticles. *Annales De Chimie-Science Des Materiaux* **2006,** *31* (3), 295-315.
1.26. Kim, J. H.; Yi, J. H.; Ko, Y. N.; Kang, Y. C., Electrochemical properties of nano-sized $LiNi_{1/3}Co_{1/3}Mn_{1/3}O_2$ powders in the range from 56 to 101 nm prepared by flame spray pyrolysis. *Materials Chemistry and Physics* **2012,** *134* (1), 254-259.

1.27. Meyers, R. A., *Encyclopedia of physical science and technology*. 3rd ed.; Academic Press, Inc.: San Diego, 2001.
1.28. Gopi, K. R.; Nagarajan, R., Advances in nanoalumina ceramic particle fabrication using sonofragmentation. *IEEE Transactions on Nanotechnology* **2008,** *7* (5), 532-537.
1.29. Chen, D.; Liu, H.-y.; Xia, S.-r., One-step decomposition of basic carbonates into single-phase crystalline metallic oxides nanoparticle by ultrasonic wave-assisted ball milling technology. *Ceramics International* **2012,** *38* (1), 821-825; Shu, C.; Zhang, J.; Ge, J.; Sim, J. H.; Burke, B. G.; Williams, K. A.; Rylander, W. M.; Campbell, T.; Puretzky, A.; Rouleau, C.; Geohegan, D. B.; More, K.; Esker, A. R.; Gibson, H. W.; Dorn, H. C., A facile high-speed vibration milling method to water-disperse single-walled carbon nanohorns. *Chemistry of Materials* **2010,** *22* (2), 347-351; Hedayati, A.; Golestan, Z.; Ranjbar, K.; Borhani, G. H., Effect of ball milling on formation of $ZnAl_2O_4$ by reduction reaction of ZnO and Al powder mixture. *Powder Metallurgy and Metal Ceramics* **2011,** *50* (5-6), 268-274.
1.30. Mansoori, G. A., *Principles of nanotechnology*. World Scientific: Singapore, 2005.
1.31. Anguelouch, A.; Leheny, R. L.; Reich, D. H., Application of ferromagnetic nanowires to interfacial microrheology. *Applied Physics Letters* **2006,** *89* (11); Fung, A. O.; Kapadia, V.; Pierstorff, E.; Ho, D.; Chen, Y., Induction of cell death by magnetic actuation of nickel nanowires internalized by fibroblasts. *Journal of Physical Chemistry C* **2008,** *112* (39), 15085-15088; Tanase, M.; Bauer, L. A.; Hultgren, A.; Silevitch, D. M.; Sun, L.; Reich, D. H.; Searson, P. C.; Meyer, G. J., Magnetic alignment of fluorescent nanowires. *Nano Letters* **2001,** *1* (3), 155-158; Gao, J. H.; Zhang, B.; Zhang, X. X.; Xu, B., Magnetic-dipolar-interaction-induced self-assembly affords wires of hollow nanocrystals of cobalt selenide. *Angewandte Chemie-International Edition* **2006,** *45* (8), 1220-1223.
1.32. Yan, M.; Fresnais, J.; Berret, J. F., Growth mechanism of nanostructured superparamagnetic rods obtained by electrostatic co-assembly. *Soft Matter* **2010,** *6* (9), 1997-2005.
1.33. Kralchevsky, P. A.; Paunov, V. N.; Denkov, N. D.; Ivanov, I. B.; Nagayama, K., Energetical and force approaches to the capillary interactions between particles and force approaches to the capillary interactions between particles attached to a liquid fluid interface. *Journal of Colloid and Interface Science* **1993,** *155* (2), 420-437; Paunov, V. N.; Kralchevsky, P. A.; Denkov, N. D.; Nagayama, K., Lateral capillary forces between floating submillimeter particles. *Journal of Colloid and Interface Science* **1993,** *157* (1), 100-112.
1.34. Green, D. L.; Lin, J. S.; Lam, Y. F.; Hu, M. Z. C.; Schaefer, D. W.; Harris, M. T., Size, volume fraction, and nucleation of Stober silica nanoparticles. *Journal of Colloid and Interface Science* **2003,** *266* (2), 346-358.
1.35. Okuyama, K.; Abdullah, M.; Lenggoro, I. W.; Iskandar, F., Preparation of functional nanostructured particles by spray drying. *Advanced Powder Technology* **2006,** *17* (6), 587-611.

1.36. Schiller, R.; Weiss, C. K.; Geserick, J.; Husing, N.; Landfester, K., Synthesis of mesoporous silica particles and capsules by miniemulsion technique. *Chemistry of Materials* **2009,** *21* (21), 5088-5098.
1.37. Beck, J. S.; Vartuli, J. C.; Roth, W. J.; Leonowicz, M. E.; Kresge, C. T.; Schmitt, K. D.; Chu, C. T. W.; Olson, D. H.; Sheppard, E. W.; McCullen, S. B.; Higgins, J. B.; Schlenker, J. L., A new family of mesoporous molecular-sieves prepared with liquid-crystal templates. *Journal of the American Chemical Society* **1992,** *114* (27), 10834-10843.
1.38. Riviere, J. C.; Myhra, S., *Handbook of surface and interface analysis: methods for problem-solving*. 2nd ed.; Taylor&Francis Group: 2009.
1.39. Clark, M. D.; Kumar, S. K.; Owen, J. S.; Chan, E. M., Focusing nanocrystal size distributions via production control. *Nano Letters* **2011,** *11* (5), 1976-1980.
1.40. Peng, X. G.; Wickham, J.; Alivisatos, A. P., Kinetics of II-VI and III-V colloidal semiconductor nanocrystal growth: "Focusing" of size distributions. *Journal of the American Chemical Society* **1998,** *120* (21), 5343-5344.
1.41. Peng, Z. A.; Peng, X. G., Mechanisms of the shape evolution of CdSe nanocrystals. *Journal of the American Chemical Society* **2001,** *123* (7), 1389-1395.
1.42. Burda, C.; Chen, X. B.; Narayanan, R.; El-Sayed, M. A., Chemistry and properties of nanocrystals of different shapes. *Chemical Reviews* **2005,** *105* (4), 1025-1102.
1.43. Nan, Z. D.; Wang, M. Y.; Yang, B. Q., In situ investigation on the formation mechanism of MCM-41 mesoporous silica by microcalorimetry. *Journal of Chemical and Engineering Data* **2009,** *54* (1), 83-89.
1.44. Decher, G., Fuzzy nanoassemblies: Toward layered polymeric multicomposites. *Science* **1997,** *277* (5330), 1232-1237.
1.45. Guerrero-Martinez, A.; Perez-Juste, J.; Liz-Marzan, L. M., Recent progress on silica coating of nanoparticles and related nanomaterials. *Advanced Materials* **2010,** *22* (11), 1182-1195.
1.46. Gorelikov, I.; Matsuura, N., Single-step coating of mesoporous silica on cetyltrimethyl ammonium bromide-capped nanoparticles. *Nano Letters* **2008,** *8* (1), 369-373.
1.47. Capek, I., On inverse miniemulsion polymerization of conventional water-soluble monomers. *Advances in Colloid and Interface Science* **2010,** *156* (1-2), 35-61.
1.48. Wan, Y.; Shi, Y. F.; Zhao, D. Y., Designed synthesis of mesoporous solids via nonionic-surfactant-templating approach. *Chemical Communications* **2007,** (9), 897-926.
1.49. Liu, J.; Liu, F.; Gao, K.; Wu, J. S.; Xue, D. F., Recent developments in the chemical synthesis of inorganic porous capsules. *Journal of Materials Chemistry* **2009,** *19* (34), 6073-6084.
1.50. Arakawa, T.; Yamamoto, T.; Shoji, S., Micro-bubble formation with organic membrane in a multiphase microfluidic system. *Sensors and Actuators a-Physical* **2008,** *143* (1), 58-63.
1.51. Zhang, G. H.; Bon, S. A. F.; Zhao, C. Y., Synthesis, characterization and thermal properties of novel nanoencapsulated phase change materials for thermal energy storage. *Solar Energy* **2012,** *86* (5), 1149-1154.

1.52. Yang, S.; Liu, H. R.; Zhang, Z. C., A facile route to hollow superparamagnetic magnetite/polystyrene nanocomposite microspheres via inverse miniemulsion polymerization. *Journal of Polymer Science Part a-Polymer Chemistry* **2008,** *46* (12), 3900-3910.
1.53. Miao, J.-J.; Jiang, L.-P.; Liu, C.; Zhu, J.-M.; Zhu, J.-J., General sacrificial template method for the synthesis of cadmium chalcogenide hollow structures. *Inorganic Chemistry* **2007,** *46* (14).
1.54. Li, H. X.; Bian, Z. F.; Zhu, J.; Zhang, D. Q.; Li, G. S.; Huo, Y. N.; Li, H.; Lu, Y. F., Mesoporous titania spheres with tunable chamber stucture and enhanced photocatalytic activity. *Journal of the American Chemical Society* **2007,** *129* (27), 8406-.
1.55. Huh, S.; Wiench, J. W.; Yoo, J. C.; Pruski, M.; Lin, V. S. Y., Organic functionalization and morphology control of mesoporous silicas via a co-condensation synthesis method. *Chemistry of Materials* **2003,** *15* (22), 4247-4256.
1.56. Yang, B.; Edler, K.; Guo, C.; Liu, H. Z., Assembly of nonionic-anionic co-surfactants to template mesoporous silica vesicles with hierarchical structures. *Microporous and Mesoporous Materials* **2010,** *131* (1-3), 21-27.
1.57. Lou, X. W.; Archer, L. A.; Yang, Z. C., Hollow micro-/nanostructures: Synthesis and applications. *Advanced Materials* **2008,** *20* (21), 3987-4019.
1.58. Yu, Z. S.; Johnston, K. P.; Williams, R. O., Spray freezing into liquid versus spray-freeze drying: Influence of atomization on protein aggregation and biological activity. *European Journal of Pharmaceutical Sciences* **2006,** *27* (1), 9-18; Heller, M. C.; Carpenter, J. F.; Randolph, T. W., Protein formulation and lyophilization cycle design: Prevention of damage due to freeze-concentration induced phase separation. *Biotechnology and Bioengineering* **1999,** *63* (2), 166-174.
1.59. Han, Z. H.; Yang, B.; Kim, S. H.; Zachariah, M. R., Application of hybrid sphere/carbon nanotube particles in nanofluids. *Nanotechnology* **2007,** *18* (10).
1.60. Yeh, H. C.; Cheng, Y. S., Electrical aerosol analyzer-an alternate method for use at high-altitude or reduced pressure. *Atmospheric Environment* **1982,** *16* (5), 1269-1270.
1.61. Intra, P.; Tippayawong, N., An overview of differential mobility analyzers for size classification of nanometer-sized aerosol particles. *Songklanakarin Journal of Science and Technology* **2008,** *30* (2), 243-256.
1.62. Kulkarni, P.; Baron, P. A.; Willek, K., *Aerosol Measurement: Principles, techniques, and applications*. Wiley: 2011.
1.63. Richardson, J. F.; Wooding, E. R., The use of a sedimentation cell in the sampling of aerosols. *Chemical Engineering Science* **1955,** *4* (1), 26-28.
1.64. Gong, G. C.; Yang, Z. Z.; Zhu, S. L., Numerical investigation of the effect of helix angle and leaf margin on the flow pattern and the performance of the axial flow cyclone separator. *Applied Mathematical Modelling* **2012,** *36* (8), 3916-3930.
1.65. Sawyer, K. F.; Walton, W. H., The confuge-a size-separating sampling device fro airborne particles. *Journal of Scientific Instruments* **1950,** *27* (10), 272-276.
1.66. Zhang, S. H.; Akutsu, Y.; Russell, L. M.; Flagan, R. C.; Seinfeld, J. H., Radial differential mobility analyzer. *Aerosol Science and Technology* **1995,** *23* (3), 357-372.

1.67. Gerber, H. E., Performance of goetz aerosol spectrometer. *Atmospheric Environment* **1971,** *5* (12), 1009-.
1.68. Oeseburg, F.; Roos, R., Properties of the srober contrifugal aerosol spectrometer at a high sampling flow: Calibration, resolving power and correction factors for particle losses. *Journal of Aerosol Science* **1979,** *10* (6), 539-.
1.69. Kim, S. H.; Woo, K. S.; Liu, B. Y. H.; Zachariah, M. R., Method of measuring charge distribution of nanosized aerosols. *Journal of Colloid and Interface Science* **2005,** *282* (1), 46-57.
1.70. Hinds, W. C., *Aerosol technology: Properties, behavior, and measurement of airborne particles*. Wiley: 1999.
1.71. Olfert, J. S.; Collings, N., New method for particle mass classification - the couette centrifugal particle mass analyzer. *Journal of Aerosol Science* **2005,** *36* (11), 1338-1352.
1.72. Ehara, K.; Hagwood, C.; Coakley, K. J., Novel method to classify aerosol particles according to their mass-to-charge ratio - Aerosol particle mass analyser. *Journal of Aerosol Science* **1996,** *27* (2), 217-234.
1.73. Havey, D. K.; Bueno, P. A.; Gillis, K. A.; Hodges, J. T.; Mulholland, G. W.; van Zee, R. D.; Zachariah, M. R., Photoacoustic Spectrometer with a Calculable Cell Constant for Measurements of Gases and Aerosols. *Analytical Chemistry* **2010,** *82* (19), 7935-7942.
1.74. Makhijani, K., *Nanotechnology: Fundamentals and applications*. I. K. International: New Delhi, 2008.
1.75. Sahu, S. C.; Casciano, D. A., *Nanotoxicity: From in vivo and in vitro models to health risks*. John Wiley&Sons Ltd: Chichester, 2009.

# Chapter 2. Synthesis of Porous Iron Oxide Nanoparticles with Various Morphologies and Magnetic Properties

## 2.1 Background of Magnetic Properties and Their Applications

### 2.1.1 Magnetic Behavior

Magnetic nanoparticles cover a broad spectrum of magnetic recording media and biomedical applications.[2.1] Each potential application of magnetic nanoparticles requires diverse properties. For example, a stable, switchable magnetic state, unaffected by temperature fluctuation is ideal for generating signals and for storing data. For biomedical uses, the application of particles that demonstrate superparamagnetic behavior at room temperature is preferred because the on-off nature of magnetization modulated by external magnetic fields can realize transportation control. Furthermore, applications in biological therapy and medical diagnoses require that magnetic particles be stable in a physiological aqueous neutral environment. Especially for *in vivo* applications, first of all, the materials must be non-toxic and non-immunogenic. Secondly, magnetic nanoparticles must be encapsulated within biocompatible polymers to prevent structural changes, aggregation, and biodegradation when exposed to the biological system. Additionally, they also have to work as a binding of drugs by entrapment on the particles, adsorption, or covalent attachment.[2.2]

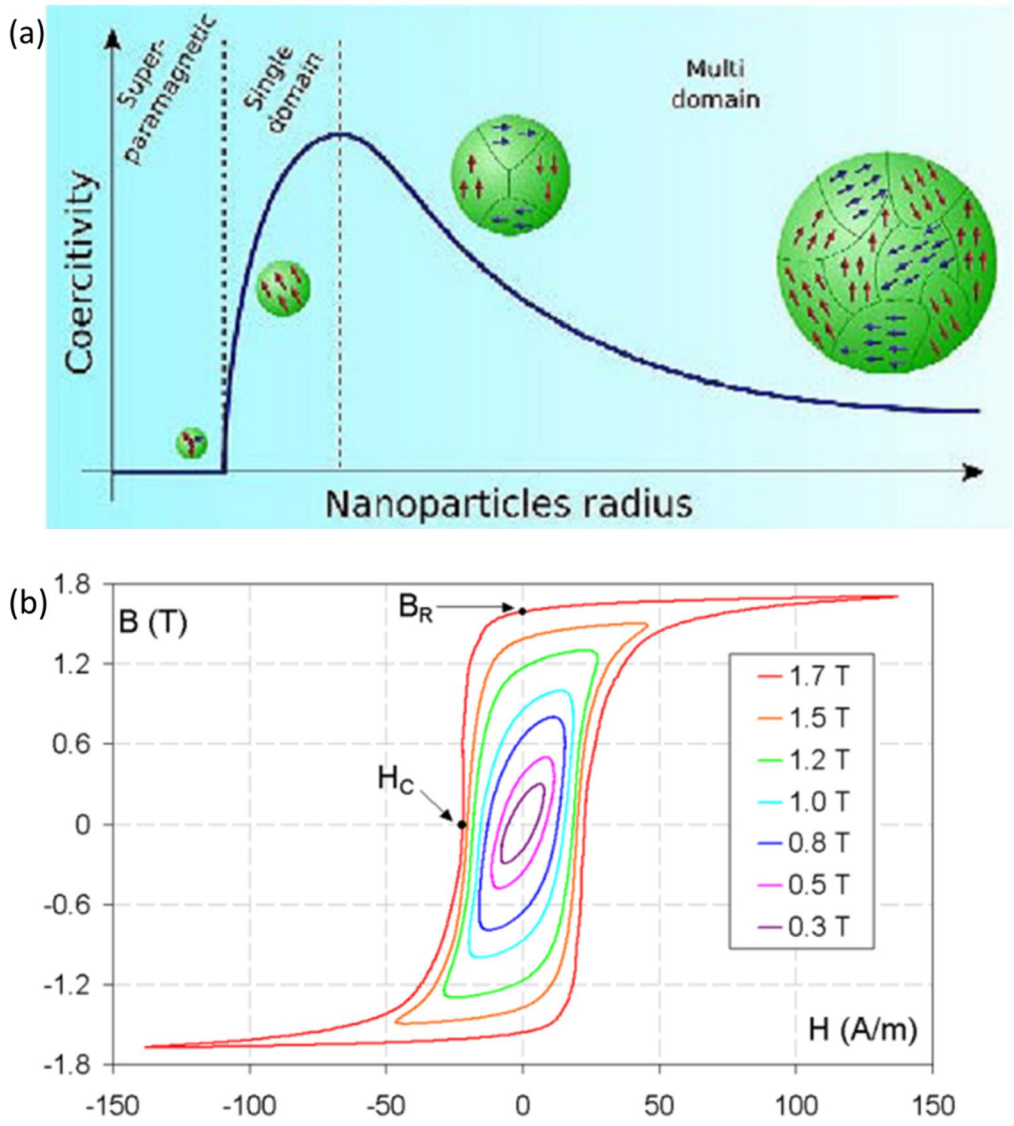


Figure 2.1. (a) Schematic illustration of the coercivity-size relations of small particles (from http://www.nanoscalereslett.com/content/7/1/144/figure/F1, accessed Aug 10, 2012); (b) a family of AC hysteresis loops of different external magnetic fields applied on grain-oriented electrical steel; BR and HC denotes remanence and coercivity, respectively. (from http://en.wikipedia.org/wiki/File:B-H_loop.png, accessed Aug 10, 2012)

Magnetic effects are caused by movements of particles that have both mass and electric charges. These particles can be electrons, holes, protons, and cations/anions. A magnetic domain refers to a volume of ferromagnetic material in which all magnetrons (a spinning electric-charged particle that creates a magnetic dipole) are aligned in the same direction by the exchange forces. When the size of a ferromagnetic material is reduced

below a critical value, it itself becomes a single domain (Figure 2.1a), which causes size effects of fine particle magnetism. It is assumed that the state of lowest free energy of ferromagnetic particles has uniform magnetization for particles smaller than a certain critical size, which is referred to as superparamagnetic, compared to nonuniform magnetization for larger particles. In superparamagnetic particles, thermal fluctuations are strong enough to spontaneously demagnetize a previously saturated assembly; therefore, these particles have zero coercivity (defined in Figure 2.1b) and have no hysteresis. Nanoparticles become magnetic (active) in the presence of an external magnetic field, but are reverted to a nonmagnetic (inactive) state when the external magnetic field is removed; this unique advantage makes the material controllable in biological environments.

Except for the size effect that cause special response to an externally applied magnetic field, orientations of the magnetic moments in a material identifies five different forms of magnetism observed in nature: diamagnetism, paramagnetism, ferromagnetism, antiferromagnetism and ferrimagnetism. Generally, in the presence of an externally applied magnetic field, the atomic current loops created by the orbital motion of electrons respond to oppose the applied field. In terms of the electronic configuration of the materials, diamagnetism is observed in materials with filled electronic subshells where the magnetic moments are paired and overall cancel each other out; thus, they appear to be very weak. It only displays this type of weak repulsion to a magnetic field, with a negative susceptibility (a dimensionless proportionality constant that indicates the degree of magnetization of a material in response to an applied magnetic field, $\chi<0$). In contrast, any other form of magnetic behavior that a material may possess usually

overpowers the effects of the current loops, whether the material displays a net magnetic moment or has a long-range ordering of its magnetic moments.[2.3, 2.4] All other types of magnetic behaviors are observed in materials that are at least partially attributed to unpaired electrons in their atomic valence shells, often in the 3d or 4f shells of the atoms. Materials whose atomic magnetic moments are uncoupled, *i.e.*, without long-range order, display paramagnetism; thus, its positive magnetic susceptibility is very small ($\chi \approx 0$).[2.5] Materials that possess ferromagnetism have aligned atomic magnetic moments of equal magnitude, and their crystalline structures allow for direct coupling interactions between the moments. Furthermore, the aligned moments in ferromagnetic materials can confer a spontaneous magnetization in the absence of an applied magnetic field; certain materials that retain permanent magnetization in the absence of an applied field are known as hard magnets. Materials having atomic magnetic moments of equal magnitude that are arranged in an antiparallel fashion display antiferromagnetism, thus leaving a zero net magnetization.[2.6] Antiferromagnetism is a strong temperature-dependent phenomenon. While above the Néel temperature, thermal energy is sufficient to cause the equal and oppositely aligned atomic moments to randomly fluctuate, leading to a disappearance of the long-range order, in which the materials become paramagnetic. Analogous to temperature-dependent property of antiferromagnetism, a ferrimagnetic material is one in which the magnetic moments of the atoms on different sublattices are ordered and opposed below the Curie temperature; however, its opposing moments are unequal and a spontaneous magnetization remains. The macroscopic behavior is similar to ferromagnetism, and the materials turn to paramagnetic above the Curie temperature.

Different magnetisms will show different characteristics in hysteresis loops, including remanence, coercivity, susceptibility and saturation flux density.

### 2.1.2 Applications of Magnetic Materials

Magnetism is highly used in industrial and biomedical fields, especially for the following applicable properties:

1. Recording: Magnetic storage uses different patterns of magnetization in a magnetizable material to store data by electromagnetic transduction. When recording, the writing head magnetizes the tape with current proportional to the signal. A magnetization distribution is achieved along the magnetic tape. In reverse, the distribution of the magnetization can be read out, reproducing the original signal. Magnetic storage media, primarily hard disks, are widely used to store computer data and other audio/video signals.

2. Hyperthermia principle: Placing superparamagnetic iron oxide in altering current (AC) magnetic fields randomly flips the magnetization direction between the parallel and antiparallel orientations, allowing the transfer of magnetic energy to the particles in the form of heat. This property can be used *in vivo* to increase the temperature of tumor tissues to destroy the pathological cells by hyperthermia.

3. Magnetorelaxometry: The relaxation of the net magnetic moment of a system of magnetic nanoparticles after removal of a magnetic field is measured to quantify specific bindings of biomolecules. The fact that magnetorelaxometry can be correlated to the core size, the hydrodynamic size, and the anisotropy allows this technique to distinguish between the free and bound conjugates by their different magnetic behavior and therefore can be used as an analytical tool for the evaluation of immunoassays.

4. Imaging: The principle is that when a radiofrequency pulse can induce atomic spinning and relaxing, the material that emits energy can be detected by the scanner and is mathematically converted into an image. A sensitive and simple technique for *in situ* monitoring of the NPs in living cells is desirable; it is reported that superparamagnetic contrast agents have an advantage of producing an enhanced proton relaxation in magnetic resonance imaging (MRI) in comparison with paramagnetic ones.

5. Targeting: Magnetic nanoparticles in combination with an external magnetic field and magnetizable implants allow the delivery of particles to the targeted area and fix them at the local site while the medication is released.[2.7] Surfaces of these particles are modified to be biocompatible, and transportation of drugs to a specific site can be expected to eliminate side effects and also reduce the dosage required.

### 2.1.3 Current Status of Iron Oxide Magnetic Nanoparticles Development

Iron oxide nanoparticles are invariably applied in magnetic fluids, catalysis, biomedication, resonance imaging and data storage. Depending on the particular application, the nature of the desired magnetic property may be different. For example, ferromagnetic carrier colloids are utilized in wastewater treatment.[2.8] Paramagnetic particles are extremely efficient vehicles for the capture and concentration of infectious retroviral vectors.[2.9] Superparamagnetic materials are increasingly of interest in biomedical and chemotherapy applications.[2.10] Different crystalline structures of iron oxide can be applied in different fields. Besides hemite ($\alpha$-$Fe_2O_3$), maghemite ($\gamma$-$Fe_2O_3$) and magnetite ($Fe_3O_4$) are of interest in medical application for hyperthermic therapy.[2.11] Considerable emphasis has been focused on synthesizing nano magnetic particles with controllable magnetic properties, crystalline phases and also morphology.

An added dimension to composition, size and shape is porosity. No work is reported on combining the properties of magnetic and porous materials, although numerous methods have been developed to synthesize magnetic nanoparticles, as below.

Coprecipitation of iron oxides from aqueous $Fe^{2+}/Fe^{3+}$ solution by the addition of a base under inert atmosphere at room temperature is a well-established protocol, where the solid particles are not very stable.[2.12] Thermal[2.3] or sonochemical[2.13] decomposition of organometallic compounds can produce size and shape controlled magnetic oxide nanocrystals; however, hydrophobic property of the particles and toxic precursors confer limitation for these methods. Microemulsion synthesis[2.14] has the advantage of preparing core-shell particles in one step, compared to sol-gel synthesis,[2.15] hydrothermal reaction,[2.16] electrospray synthesis,[2.17] and laser pyrolysis,[2.18] all of which can only produce non-porous iron oxide particles without post-treatment. Recently, the hydrothermal treatment,[2.19] surfactant-assisted solvothermal method[2.20] or the template method[2.21] have been developed to create hollow iron oxide particles to improve catalytic properties and drug-loading capability. The hollow structures offer the opportunity to create a porous shell by either processing phase changes that result in stress induced micro-cracks, or acid etching.[2.22]

## 2.2 Experimental Approach

In this work the synthesis of porous iron oxide nanoparticles by a single-step, aerosol spray-pyrolysis is demonstrated. Experimental set-up can be found in the introduction section. Briefly, a precursor solution is sprayed using a collision-type nebulizer. The initial droplet diameter is about 1μm, which is dried by passing through a silica gel diffusion dryer. The aerosol is then passed through a tube furnace to create the porous

iron oxide with a residence time of about 1s. Particles exiting the aerosol reactor are then collected on a 0.4 μm DTTP Millipore filter. Different solutions were prepared and a range of temperatures were employed to manipulate particle properties (magnetism and phase), summarized in Table 2.1.

## 2.3 Result and Discussion

Table 2.1 lists examples of three precursor starting solutions. A is a solution of iron nitrate in water, which yields directly to iron oxide when sprayed and dried. In solutions B and C, a surfactant (F127 or CTAB) was added as a pore forming agent, as well as urea as a gas generator. Though the particle structures are the same with or without urea when surfactant F127 was added, the porous structure could not exist without urea when surfactant CTAB was added. (Figure 2.2g) This proves the role of urea in assistance of generating ordered pores.

Table 1.1. Synthesis Conditions and Properties.

| Synthesis Precursor | Furnace Temperature(°C) | Crystalline Structure | Magnetic Category (Room Temperature) |
|---|---|---|---|
| A. 0.2M iron (III) nitrate nonahydrate aqueous solution | 400 | Mostly γ-$Fe_2O_3$ | N/A |
| | 500 | Mostly γ-$Fe_2O_3$ | Paramagnetic |
| | 600 | Mostly γ-$Fe_2O_3$ | Weak ferromagnetic |
| | 900 | α-$Fe_2O_3$ | Ferromagnetic |
| B. 1.616g $Fe(NO_3)_3 \cdot 9H_2O$, 0.198g F127, 1.44g urea in 20ml distilled water | 600 | γ-$Fe_2O_3$ | Superparamagnetic |
| C. 1.616g $Fe(NO_3)_3 \cdot 9H_2O$, 0.1456g CTAB, 1.44g urea in 20ml distilled water | 600 | [23]γ-$Fe_2O_3$ | Superparamagnetic |

Comparing the results at 600 °C, it is found that BET surface area results for the iron nitrate only precursor solution is 5.0 $m^2/g$, compared with 15.8 and 12.0 $m^2/g$ for

solutions B and C, respectively. This increase in surface area is attributed to the surfactant since the addition of urea alone, resulted in particles that were indistinguishable from the neat nitrate case properties. After passing through the tube furnace of 600°C, the surfactant should partially decompose, which is confirmed by TGA (Thermogravimetric Analysis) analysis in Figure 2.3(a). By calculation, CTAB-$Fe_2O_3$ should have 68.7% mass left (after a complete burn) if urea is fully decomposed, and all the CTAB remains in the particle. A decrease in mass is observed to just 77.0% implying that some of the template is being burned out in the aerosol phase. To further remove the pore template surfactant, plasma etching or washing with water was conducted, as demonstrated in Figures 2.3(b), (c) and (d). An important parameter in the resulting morphology is the reactor temperature. For the $Fe(NO_3)_3$-only precursor cases, as the furnace temperature increases, pore size becomes larger (Figures 2.2a, b and c). For the surfactant template porous $Fe_2O_3$ nanoparticle, 600°C furnace temperature was used because at a low temperature (like 400°C), the crystallinity is not quite good, and at high temperatures (like 900°C), surfactant decomposed, instead of primarily templating pore orders. But surfactants really help control crystalline grain size, from the comparison of Figure 2.2(h)(i) and Figure 2.2(d), as well as the much broader XRD (X-ray powder diffraction) peaks of surfactant-templated material in Figure 2.4. Though BET results show the trend of pore diameter consistent with the TEM images, a more accurate porosity should be determined from the DMA-APM method, which demonstrates that higher furnace temperature can make larger pores, higher particle density and lower porosity.[2.23] Apparently, the key to forming a porous structure rather than core-shell is to start from a relatively small droplet size, so the mass transport inwards for smaller

particles is fast enough relative to the solvent evaporation rate. It is approved by a more possible shell formation for larger particles in Figure 2.2(h), and also similar experiments with 10 times larger droplets, resulting in hollow particles, have been reported.[2.24] Furthermore, in that work they found crystallinity to initiate at 740 °C, while our XRD results show crystallinity down to 400 °C (Figure 2.4). Thus, besides the nature of the structure formation, the mass transfer constraints when using larger droplets also impact the crystallization process. In these studies, two templating agents, F127 and CTAB, are employed; and consistent with other studies on silica,[2.25] our iron oxide materials have larger pores with F127 surfactant.

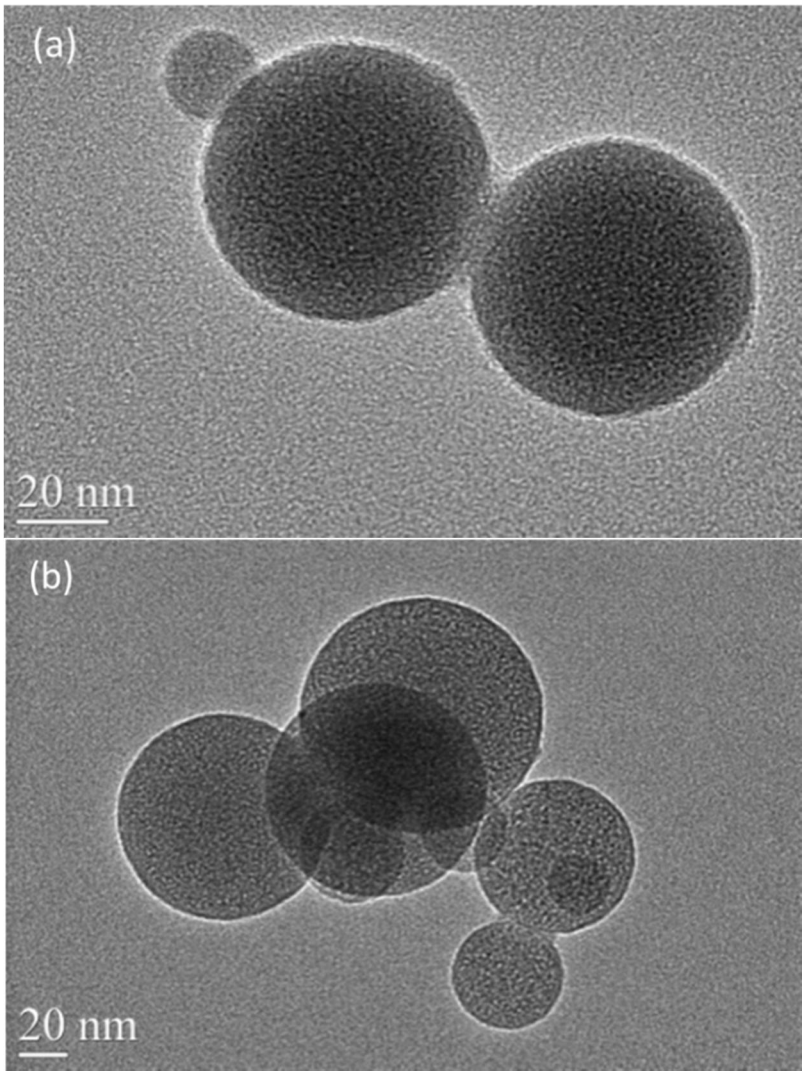

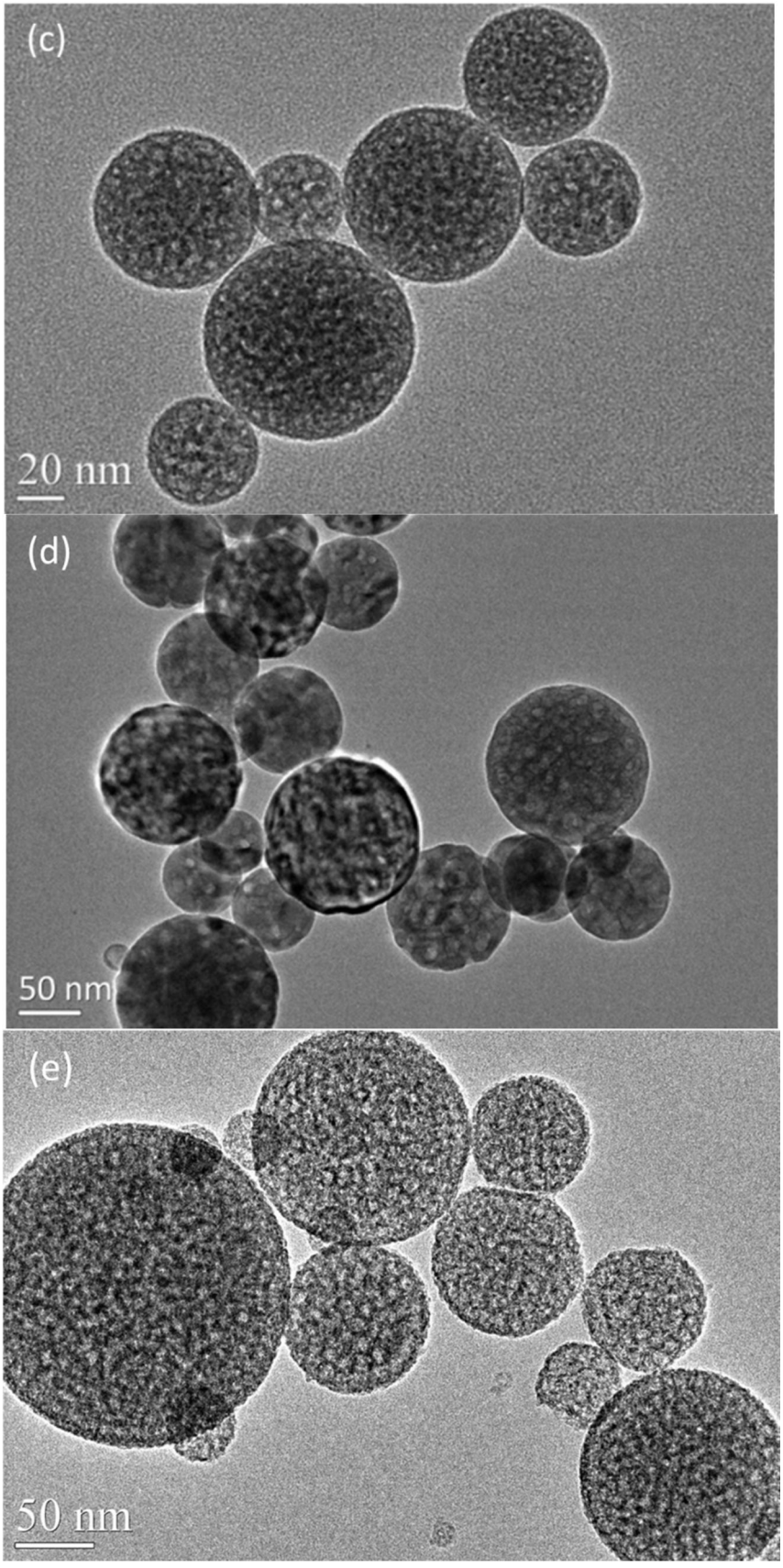
(c)
20 nm
(d)
50 nm
(e)
50 nm

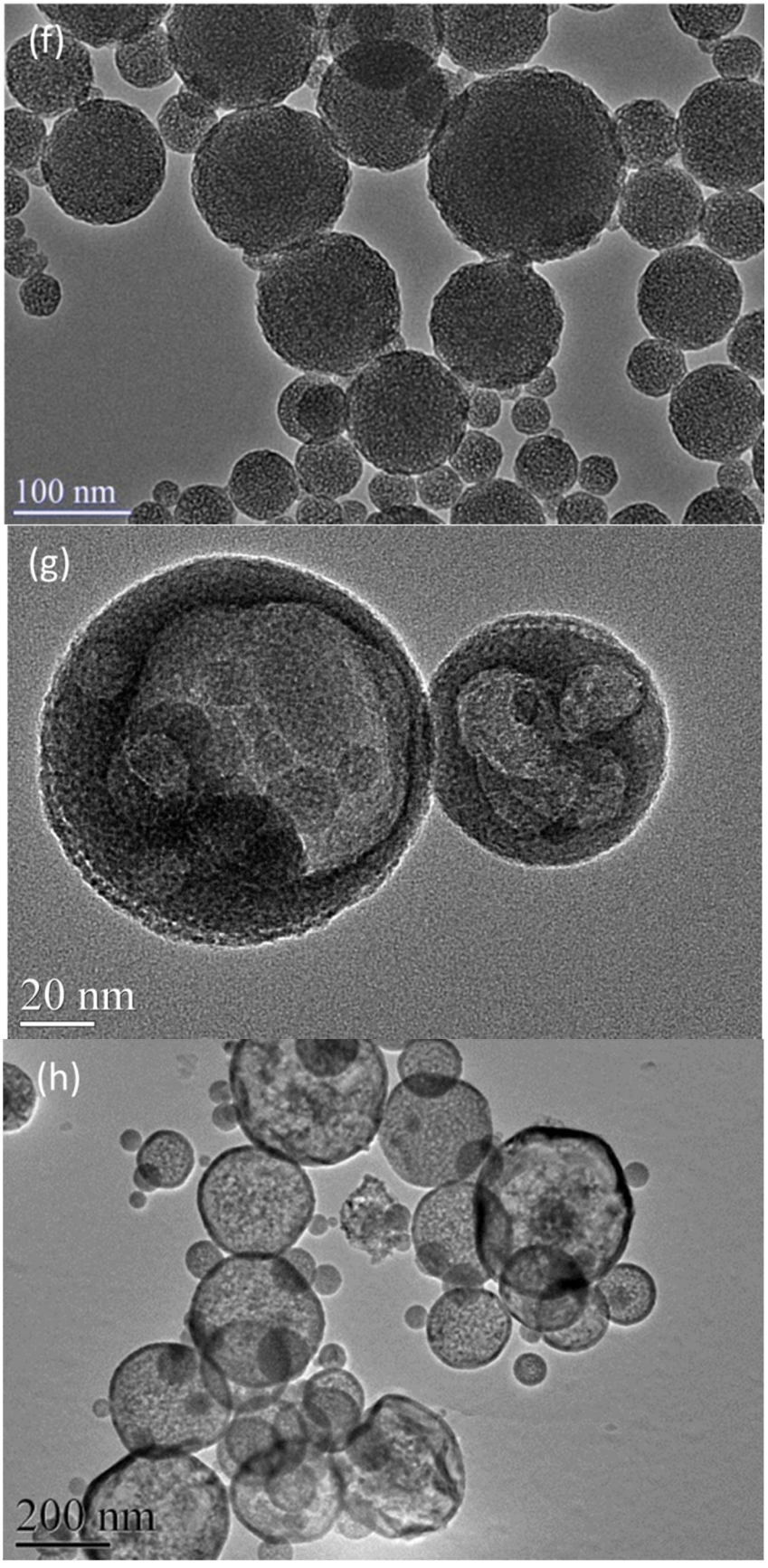
(f)
100 nm
(g)
20 nm
(h)
200 nm

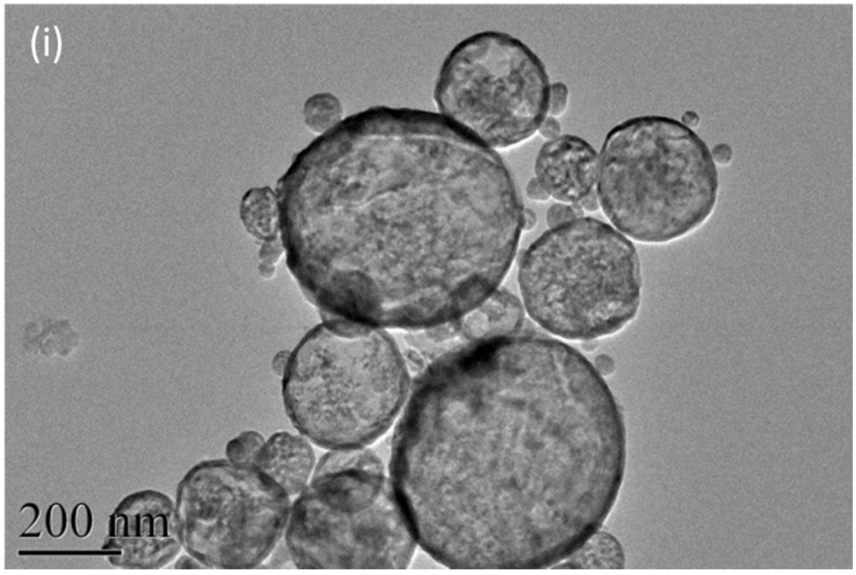


Figure 2.2. TEM (Transmission Electron Microscopy) images of iron oxide particles generated from precursor solution A at (a) 400 ℃, (b) 500 ℃, (c) 600 ℃, (d) 900 ℃; particles generated from (e) precursor solution B and (f) precursor solution C; (g) particle synthesized by the same procedure in Table 1C, except for without urea addition; (h) particle synthesized from precursor solution B, furnace temperature 900 °C; (i) particle synthesized from precursor solution C, furnace temperature 900 °C.

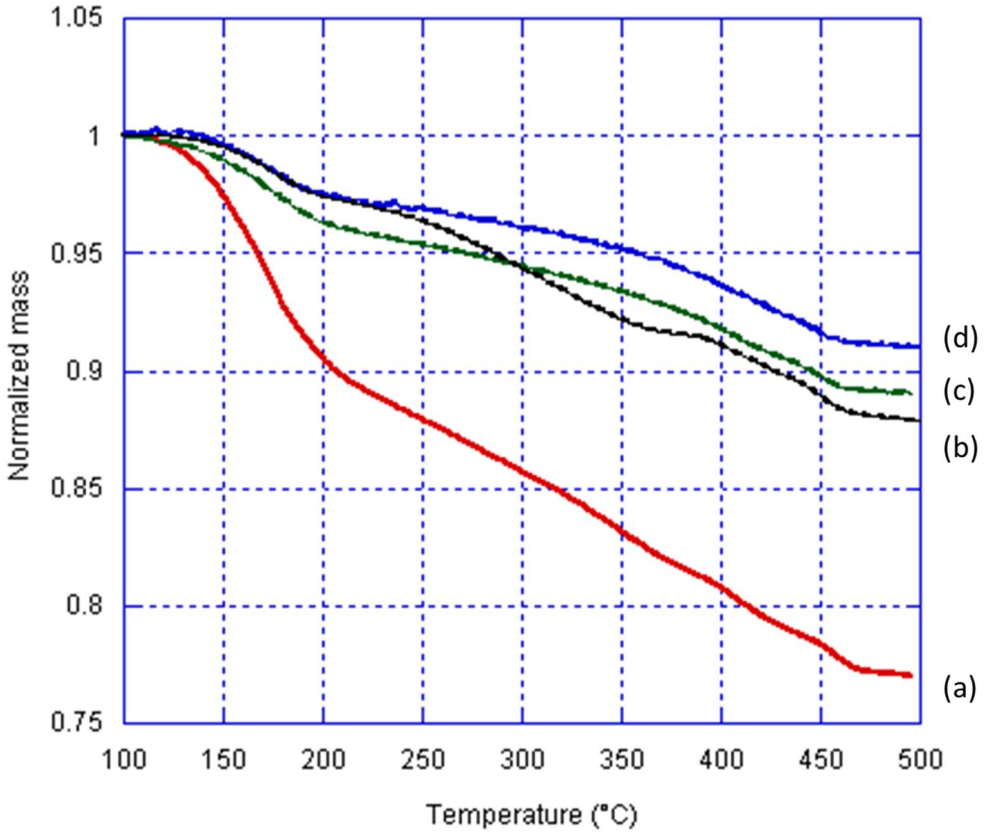


Figure 2.3. Mass change of sample (a) CTAB-$Fe_2O_3$ without treatment, (b) CTAB-$Fe_2O_3$ cleaned with water, (c) F127-$Fe_2O_3$ after plasma etching, and (d) CTAB-$Fe_2O_3$ after plasma etching.

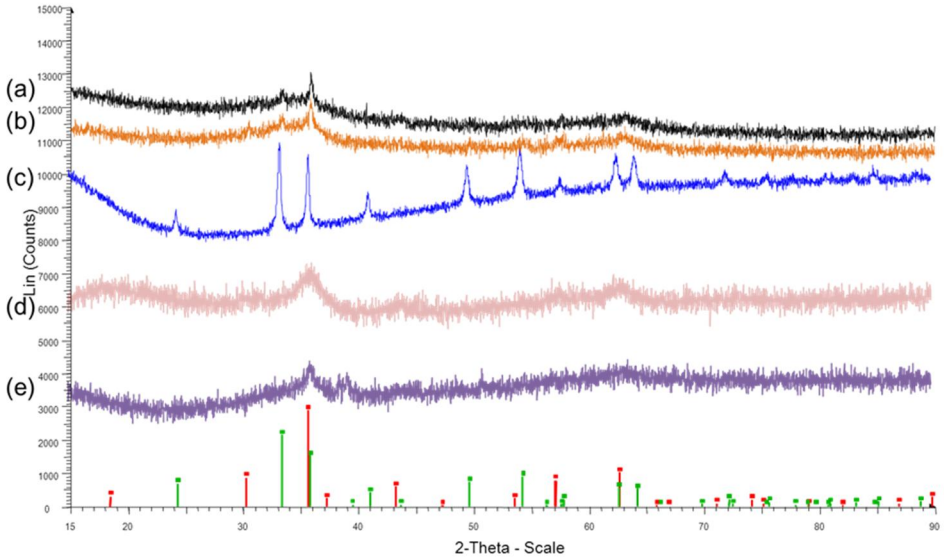


Figure 2.4. XRD profiles of precursor solution sample A synthesized at (a) 400 °C, (b) 600 °C and (c) 900 °C, precursor solution sample B(d) and precursor solution sample C(e); theoretical peak values of maghemite and hematite are labeled in red and green on the x-axis, respectively.

VSM (Vibrating Sample Magnetometer) results were presented in Figure 2.5. It indicates that, magnetic properties vary significantly as a result of processing conditions, in addition to significant morphological changes.

For the iron nitrate-only precursor solution samples, particles synthesized below 600 °C show paramagnetic properties (linear dependency in Figure 2.5a), where only a small fraction of the spins will be oriented by the field and the fraction is proportional to the field strength; those synthesized at 600 °C show weak ferromagnetic hysteresis loops (Figure 2.5c), due to a higher extent of crystalline grain sintering. At 900 °C strong ferromagnetism is seen (Figure 2.5b). Addition of surfactants results in superparamagnetic behavior (Figures 2.5d and e). Presumably, the templating agent generates the pore structure, prevents significant grain growth and also serves the same purpose of maintaining a separation of the magnetic domains.

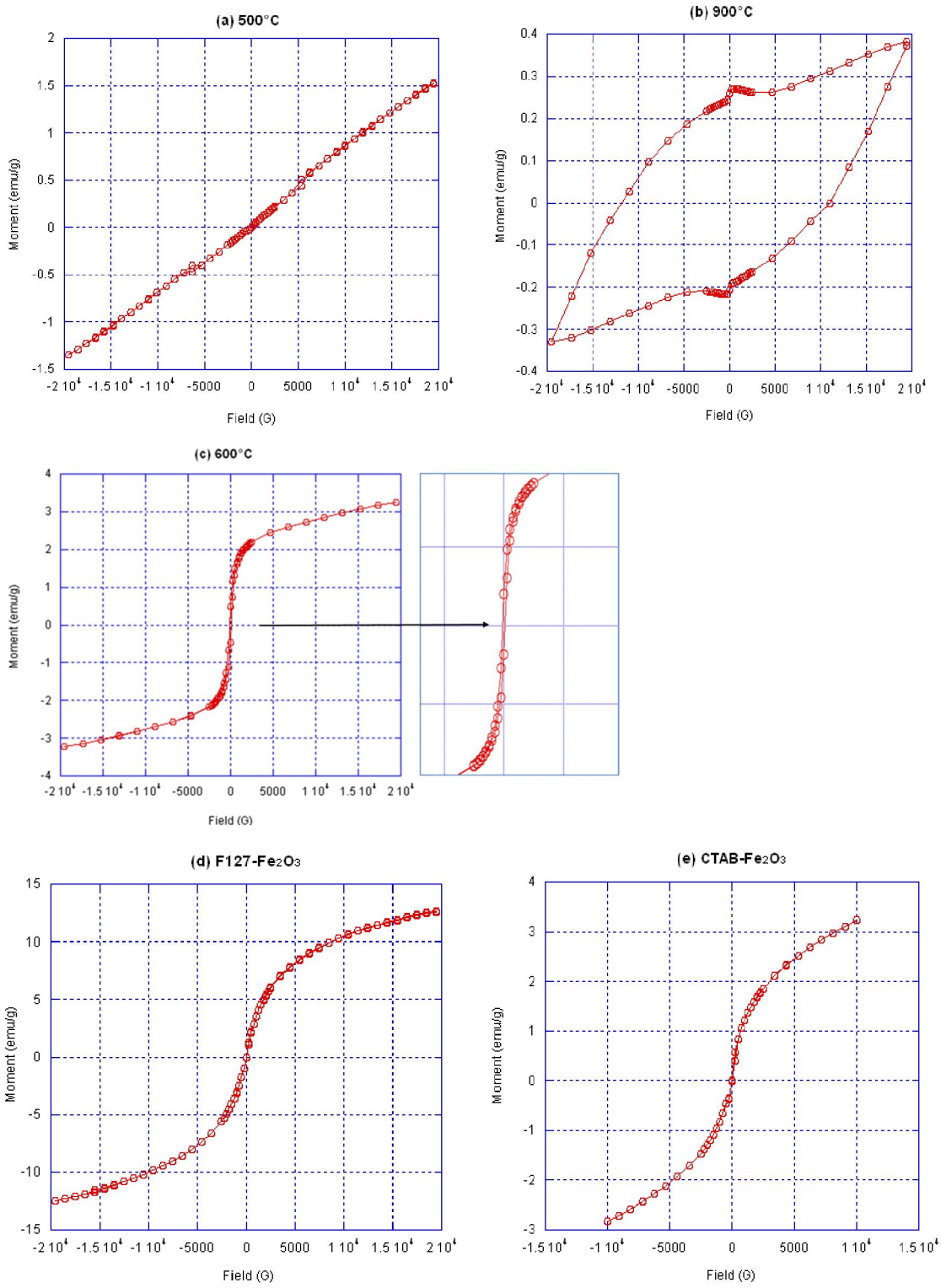


Figure 2.5. VSM (Vibrating Sample Magnetometer) characterization of pure iron oxide particles synthesized at (a) 500°C, (b) 900°C, (c) 600°C; and (d) F127-$Fe_2O_3$, (e) CTAB-$Fe_2O_3$.

## 2.4 Conclusion

In conclusion, a series of porous iron oxide nanoparticles can be generated by spray-pyrolysis which enables the creation of particles with magnetic properties in addition to the pore structures. This general method can be extended to other metal oxide systems and other surfactants. An added benefit to the surfactant-templated materials is that they enhance the dispersion of the particles in water. These findings open up the opportunity for future studies on coating modification of these specialized porous magnetic nanoparticles and applications of these special properties.

## Reference


2.1. Akbarzadeh, A.; Samiei, M.; Davaran, S., Magnetic nanoparticles: preparation, physical properties, and applications in biomedicine. *Nanoscale Research Letters* **2012,** *7*, 1-13.

2.2. Sosnovik, D. E.; Nahrendorf, M.; Weissleder, R., Molecular magnetic resonance imaging in cardiovascular medicine. *Circulation* **2007,** *115* (15), 2076-2086; Moghimi, S. M.; Hunter, A. C.; Murray, J. C., Long-circulating and target-specific nanoparticles: Theory to practice. *Pharmacological Reviews* **2001,** *53* (2), 283-318; Muldoon, L. L.; Sandor, M.; Pinkston, K. E.; Neuwelt, E. A., Imaging, distribution, and toxicity of superparamagnetic iron oxide magnetic resonance nanoparticles in the rat brain and intracerebral tumor. *Neurosurgery* **2005,** *57* (4), 785-796.

2.3. Jana, N. R.; Chen, Y. F.; Peng, X. G., Size- and shape-controlled magnetic (Cr, Mn, Fe, Co, Ni) oxide nanocrystals via a simple and general approach. *Chemistry of Materials* **2004,** *16* (20), 3931-3935.

2.4. Park, J.; An, K. J.; Hwang, Y. S.; Park, J. G.; Noh, H. J.; Kim, J. Y.; Park, J. H.; Hwang, N. M.; Hyeon, T., Ultra-large-scale syntheses of monodisperse nanocrystals. *Nature Materials* **2004,** *3* (12), 891-895; Hyeon, T.; Lee, S. S.; Park, J.; Chung, Y.; Bin Na, H., Synthesis of highly crystalline and monodisperse maghemite nanocrystallites without a size-selection process. *Journal of the American Chemical Society* **2001,** *123* (51), 12798-12801.

2.5. Sun, S. H.; Zeng, H.; Robinson, D. B.; Raoux, S.; Rice, P. M.; Wang, S. X.; Li, G. X., Monodisperse MFe2O4 (M = Fe, Co, Mn) nanoparticles. *Journal of the American Chemical Society* **2004,** *126* (1), 273-279; Chen, M.; Liu, J. P.; Sun, S. H., One-step synthesis of FePt nanoparticles with tunable size. *Journal of the American Chemical*

*Society* **2004,** *126* (27), 8394-8395; Sun, S. H.; Murray, C. B.; Weller, D.; Folks, L.; Moser, A., Monodisperse FePt nanoparticles and ferromagnetic FePt nanocrystal superlattices. *Science* **2000,** *287* (5460), 1989-1992.

2.6. Weissleder, R.; Mahmood, U., Molecular imaging. *Radiology* **2001,** *219* (2), 316-333.

2.7. Kwon, S. G.; Piao, Y.; Park, J.; Angappane, S.; Jo, Y.; Hwang, N. M.; Park, J. G.; Hyeon, T., Kinetics of monodisperse iron oxide nanocrystal formation by "heating-up" process. *Journal of the American Chemical Society* **2007,** *129* (41), 12571-12584.

2.8. Hildebrand, H.; Mackenzie, K.; Kopinke, F. D., Novel nano-catalysts for wastewater treatment. *Global Nest Journal* **2008,** *10* (1), 47-53.

2.9. Chan, L.; Nesbeth, D.; MacKey, T.; Galea-Lauri, J.; Gaken, J.; Martin, F.; Collins, M.; Mufti, G.; Farzaneh, F.; Darling, D., Conjugation of lentivirus to paramagnetic particles via nonviral proteins allows efficient concentration and infection of primary acute myeloid leukemia cells. *Journal of Virology* **2005,** *79* (20), 13190-13194.

2.10. Hao, R.; Xing, R. J.; Xu, Z. C.; Hou, Y. L.; Gao, S.; Sun, S. H., Synthesis, Functionalization, and Biomedical Applications of multifunctional magnetic nanoparticles. *Advanced Materials* **2010,** *22* (25), 2729-2742.

2.11. Sreeja, V.; Joy, P. A., Microwave-hydrothermal synthesis of gamma-$Fe_2O_3$ nanoparticles and their magnetic properties. *Materials Research Bulletin* **2007,** *42* (8), 1570-1576.

2.12. Massart, R., Preparation of aqueous magnetic liquids in alkaline and acidic media. *IEEE Transactions on Magnetics* **1981,** *17* (2), 1247-1248.

2.13. Abu Mukh-Qasem, R.; Gedanken, A., Sonochemical synthesis of stable hydrosol of $Fe_3O_4$ nanoparticles. *Journal of Colloid and Interface Science* **2005,** *284* (2), 489-494.

2.14. Deng, Y.; Wang, L.; Yang, W.; Fu, S.; Elaissari, A., Preparation of magnetic polymeric particles via inverse microemulsion polymerization process. *Journal of Magnetism and Magnetic Materials* **2003,** *257* (1), 69-78.

2.15. Dacoata, G. M.; Degrave, E.; Debakker, P. M. A.; Vandenberghe, R. E., Synthesis and characterization of some iron-oxides by sol-gel method. *Journal of Solid State Chemistry* **1994,** *113* (2), 405-412.

2.16. Chen, D.; Xu, R., Hydrothermal synthesis and characterization of nanocrystalline $Fe_3O_4$ powders. *Materials Research Bulletin* **1998,** *33* (7), 1015-1021.

2.17. Basak, S.; Chen, D. R.; Biswas, P., Electrospray of ionic precursor solutions to synthesize iron oxide nanoparticles: Modified scaling law. *Chemical Engineering Science* **2007,** *62* (4), 1263-1268.

2.18. Veintemillas-Verdaguer, S.; Morales, M. P.; Serna, C. J., Continuous production of gamma-$Fe_2O_3$ ultrafine powders by laser pyrolysis. *Materials Letters* **1998,** *35* (3-4), 227-231.

2.19. Mao, B. D.; Kang, Z. H.; Wang, E. B.; Tian, C. G.; Zhang, Z. M.; Wang, C. L.; Song, Y. L.; Li, M. Y., Template free fabrication of hollow hematite spheres via a one-pot polyoxometalate-assisted hydrolysis process. *Journal of Solid State Chemistry* **2007,** *180* (2), 489-495.

2.20. Chen, D. H.; Chen, D. R.; Jiao, X. L.; Zhao, Y. T., Hollow-structured hematite particles derived from layered iron (hydro)oxyhydroxide-surfactant composites. *Journal of Materials Chemistry* **2003,** *13* (9), 2266-2270.

2.21. Shiho, H.; Kawahashi, N., Iron compounds as coatings on polystyrene latex and as hollow spheres. *Journal of Colloid and Interface Science* **2000,** *226* (1), 91-97.
2.22. Cheng, K.; Peng, S.; Xu, C. J.; Sun, S. H., Porous hollow $Fe_3O_4$ nanoparticles for targeted delivery and controlled release of cisplatin. *Journal of the American Chemical Society* **2009,** *131* (30), 10637-10644.
2.23. Liu, Q.; Ma, X.; Zachariah, M. R., Combined on-line differential mobility and particle mass analysis for determination of size resolved particle density and microstructure evolution. *Microporous and Mesoporous Materials* **2012,** *153*, 210-216.
2.24. Gadalla, A. M.; Yu, H. F., Thermal-decomposition of Fe (III) nitrate and its aerosol. *Journal of Materials Research* **1990,** *5* (6), 1233-1236.
2.25. Hu, Q. Y.; Hampsey, J. E.; Jiang, N.; Li, C. J.; Lu, Y. F., Surfactant-templated organic functionalized mesoporous silica with phosphino ligands. *Chemistry of Materials* **2005,** *17* (6), 1561-1569.

# Chapter 3. Spray-drying Nanoparticles as an Optical Standard and the Determination of Their Refractive Index

## 3.1 Background

The aerosol spray pyrolysis method was shown in the previous chapter as a convenient way to synthesize nanoparticles with various properties. The target of this project is to synthesize a specific type of spherical carbon nanoparticles that can work as an optical standard, which could absorb and scatter light over a broad spectral range. Most carbon sources, such as commercial carbon black, are carbon aggregates, preventing them from being dispersed well in solution. Other carbon sources require catalysts to break down the carbohydrates to active carbon (*e.g.*, sugars),[3.1] however, it is challenging to control the homogeneous distribution of multicomponent particles. In this project, a soluble carbon source, $C_{60}(OH)_{24}$, a derivative of fullerene, could be packed into nanoparticles at as low as room temperature or generate "blacker" nanoparticles (stronger absorption) at a higher temperature, forming nonporous structures ideal for optical standards. Advantages, methods and property analysis will be discussed in this chapter.

### 3.1.1 Aerosol Optics

Light can be scattered or absorbed by aerosol particles suspended in the air. Within the visible range, light scattering is the dominant process over absorption.

For many applications, including atmospheric scattering measurement and optical instrument design, the parameters of most interest are the intensity function and related quantities, defined as below: the total energy scattered in all directions by the particle can

be converted to the energy of the incident beam falling on the area $C_{sca}$, which is the scattering cross section, with the dimension of area yet generally not being equal to the particle cross-sectional area. Scattering efficiency can be described as: $Q_{sca}=C_{sca}/S_g$, where $S_g$ is the geometric cross section. Absorption ($Q_{abs}$) and extinction efficiencies ($Q_{ext}$) are defined in the same way, and their correlation is defined as:

$$Q_{ext} \equiv Q_{abs} + Q_{sca} \qquad (3.1)$$

So when any two of the three variables are identified, the third one can be deduced. Both scattering and absorption can be taken into account by expressing the refractive index as the sum of a real and an imaginary component:

$$m=a+bi \qquad (3.2)$$

Together with the size parameter $x=2\pi r/\lambda$, where $r$ is the radius of particles and $\lambda$ is the light wavelength, efficiency factors can be determined by different theories.

Rayleigh scattering can be used to describe small spherical absorbing particles ($x \ll 1$); the scattering and absorption efficiencies are given by

$$Q_{sca} = \frac{8}{3}x^4 Re\{\frac{m^2-1}{m^2+2}\}^2 \qquad (3.3)$$

$$Q_{abs} = -4xIm\{\frac{m^2-1}{m^2+2}\} \qquad (3.4)$$

where *Re* and *Im* indicate the real and imaginary part of the expression, respectively.

For very small particles of absorbing materials, the particle extinction coefficient, defining the strength that a substance absorbs light at a given wavelength, varies only with the first power of $x$ and absorption should be proportional to the particle volume.

On the other hand, geometrical optics is used to describe large particles ($x \gg 1$). Extinction law provides useful limiting relationships for the efficiency factor, $Q_{ext} \rightarrow 2$, which is independent of shape, internal structure and refractive index of the material.

The fact that the extinction cross section is twice the geometrical cross-section of the particle can be explained by taking into account not only rays incident on the particle, but also on those in the close vicinity of the scatter influenced by a particle due to the diffraction phenomenon.[3.2]

Very small and very large particles can be treated using simple models. The range $x \sim 1$ is more complex, yet frequently important. For example, atmospheric visibility is limited by articles whose size is of the same order as the wavelength of light in the optical range, from 0.1 to 1μm in diameter.[3.2] In this range, neither the theory of Rayleigh nor the large particle extinction law is applicable because the field is not uniform over the entire particle volume. As a result, the much more complicated Mie theory is used to treat the general problem of scattering and absorption of a plane wave by a homogeneous sphere in this range. Expressions for the scattering and extinction are obtained by solving Maxwell's equation for the regions inside and outside the sphere with suitable boundary conditions, and efficiency factors are only functions of size parameter and refractive index. The computer program of this theory is available online and in some references.[3.3]

### 3.1.2 Refractive Index of Aerosol Particles

Aerosol is ubiquitous in the earth's atmosphere. Aerosol light interactions (absorption and scattering) play an important role in many atmospheric processes. Through direct and semi-direct radiative forcing, aerosol can influences relative humidity, atmospheric circulation and thereby cloud formation and lifetime. Both aerosol light absorption and scattering are determined by the spatial complex refractive index distribution that forms the particle. In general, the refractive index increases with its density, *e.g.* glass.[3.4] Also, it is reported that the refractive index can be a function particle size.[3.5] However, an

overall relation between the refractive index and the density has not been discovered yet. The Debye series allows a detailed view of scattering by decomposing it into various orders; in this way, the physical cause of various features of the Mie scattering curve and their dependence on the particle properties can be explained.[3.6]

A significant number of aerosol instruments have been developed. However, the response of some aerosol instruments depends on particle properties including density, complex refractive index and shape. More information on such properties is required to improve the understanding of measurement accuracy.[3.7] Therefore, the measurement methods of those properties are demanded.

Refractometer is the instrument used to measure the refractive index. Although it is best known for measuring liquids, some are also designed to measure gases and solids, such as glass and gemstones.[3.8] To our knowledge, no refractometry for nanoparticles has been reported yet, which is an issue waiting to be resolved to retrieve the refractive indexes of aerosol particles.

### 3.1.3 Limitations and Calibration of the Spectrometers

The principles of the spectrometers used in this research, the photoacoustic spectrometer (PAS) and the cavity ring-down spectrometer (CRD), have already been discussed in the nanoparticle characterization section in chapter one. Herein, we will only pay attention to the limitation of the spectrometers and discuss how to improve the accuracy and standardize the instrumentation.

For PAS, the main drawback regarding sensitivity is from background acoustic noises; also, because of the confounding absorber- and matrix-specific processes involved in converting absorbed light into sound, absent independent knowledge of the cell constant,

a photoacoustic spectrometer requires calibration in order to yield quantitative information.[3.9] An analyte-free background signal is taken before measurement, which comprises all gases in the analyte flow as well as flow noise. The governing equation for PAS measurement is as follows:

$$\alpha = \frac{R}{W_L K_N} \tag{3.5}$$

Here, $\alpha$ is the absorption coefficient along the acoustic cell, $R$ is the measured signal with analyte, $W_L$ is the beam power of the laser (660 nm for our system) at the center of the PAS cell, and $K_N$ is the frequency-dependent photo-acoustic system constant, which is related to cell geometry, microphone sensitivity, relaxation response, and must be evaluated at the modulation frequency. For aerosols and soots, independent measurements of the particle number density are required for PAS determination of particle cross section, so $N$ is particle number concentration measured by the condensed particle counter (CPC). Soot or aerosol particle cross section ($\sigma$) is defined by:

$$\sigma = \frac{\alpha}{N} \tag{3.6}$$

The photo-acoustic system constant is calibrated based on measurements of a gaseous species having known concentration and absorption, for example, $O_3$,[3.10] $O_2$ *A*-band[3.11] and $NO_2$[3.12] in the air. In an aerosol study, Petzold and Niessner used diesel soot as a sample of a known absorption coefficient.[3.13]

Using gas or soot particles for calibration has limitations. Gas cannot have absorption over the entire spectrum range, so different calibration gases are needed for different wavelengths. For example, oxygen presents two spectrophotometric absorption bands peaking at the wavelengths 687 and 760 nm, and $O_3$ or $NO_2$ are used for ultraviolet and visible band. To use soot for calibration, the fact should be accounted for that soot

particles can vary in size, shape, mixing state, and chemical composition depending on how they are generated, which directly affect the optical properties.

The main limitations of CRD are the availability of precise laser light at the appropriate wavelength and also the availability of high-reflectance mirrors at those wavelengths for the analytes. Due to an easier process that occurs in the vacuum cell, calibration is easier: the system provides an inherent self-calibration of the CRDS technique; absolute wavelength calibration was also provided by measuring the spectrum of a known molecular iodine source, where the wavelengths are known to high precision.[3.14]

Therefore, the new optical standard to be designed should have some advantages superior to the ones that are in use: 1) the standard should be not expensive or difficult to produce or maintain; 2) one sample should be able to calibrate the equipment for a broad spectral range; and 3) a controllable morphology is preferred as a standard. In addition, refractive index of an aerosol nanoparticle should be taken as a standard optical factor, and be retrieved. So, when one standard is selected for the calibration, its refractive index and the laser wavelength are the only information needed to standardize all the parameters of the instrumentation.

## 3.2 Introduction to This Research

A list of environmental issues is caused by atmospheric pollution, and then the climate change will bring even more problems. So it is essential to monitor the air quality and restrain the environmental deterioration. For example, the greenhouse effect is the process by which absorption and emission of infrared radiation by gases (carbon dioxide, methane, tropospheric ozone, chlorofluorocarbon and nitrous oxide) in the atmosphere

warm a planet's lower atmosphere and surface, thus further influencing many physical and biological systems.[3.15] Future warming is projected to have a range of impacts, including sea level rise, increased frequencies and severities of some extreme weather events, loss of biodiversity, and regional changes in agricultural productivity.[3.15] Besides, ozone depletion is caused by the destruction of stratospheric ozone by chlorofluorocarbons, and global dimming is a gradual reduction in the amount of global direct irradiance at the Earth's surface by an increase in particulates such as sulfate aerosols.

In climate science, black carbon, formed through the incomplete combustion of fossil fuels, biofuel, and biomass, is emitted in both anthropogenic and naturally occurring soot. It warms the earth, second only to $CO_2$, by absorbing heat in the atmosphere and by reducing albedo (the ability to reflect sunlight) when deposited on snow and ice; also by absorbing solar radiation, it dims the surface of the ocean and transports to other areas such as Himalayas where glacial melting may occur. Detection of greenhouse gases typically involves spectroscopic methods, such as non-dispersive infrared and tunable diode laser absorption spectroscopy. Exact analysis of particulate, especially black carbon, is of importance because particles of scattering and absorbing properties may influence differently in cooling and warming; thus, advanced spectroscopic methods were developed, such as cavity ring-down spectroscopy (CRDS) or similar cavity-enhanced methods for extinction, nephelometry for scattering and photoacoustic spectroscopy (PAS) for absorption.

Measurement of optical properties of atmospheric aerosol has been significantly applied in atmospheric visibility and climate change studies, atmospheric remote sensing

and particulate matter monitoring from space. These applications are investigated at many research centers worldwide; the primary interest lies in the determination of the vertical aerosol optical thickness, the single scattering albedo, the absorption and extinction coefficient, the phase function, the phase matrix and the refractive indexes.[3.16]

In this research, a new fullerene-based aerosol particle is designed, which can be used as a candidate for online optical standard to calibrate optical instruments, superior to the gas and soot standards currently in use. To further study its optical characteristics, a methodology to calculate the refractive index of these standardized nanoparticles is proposed, by measuring absorption from photoacoustic spectroscopy (PAS) and extinction from cavity ring-down spectroscopy (CRDS). Finally, a correlation of optical property with synthesis temperature and particle size is revealed.

## 3.3 Experiment

### 3.3.1 Sample Preparation

A carbon sphere (CS) was synthesized using a spray pyrolysis method. The solution, 1g/L $C_{60}(OH)_{24}$ (MER Corp.) water solution, was atomized in air flow by a collision-type nebulizer (TSI). The aerosol was subsequently dried by passing through the silica gel diffusion dryer, before entering a tubular furnace which can be set at different temperatures. Under the experimental condition, the residence time for aerosol particle in the furnace is ~1 s. The final product, CS, was collected on a slide for the UV-Vis absorption characterization (LAMBDA 1050 spectrophotometer-USA-PerkinElmer) or was directly sampled for online aerosol size, mass and optical properties characterization.

### 3.3.2 Equipment Set-up

Figure 3.1 shows the schematic of the experimental set-up, in which the atomizing-drying-heating is for generating the particles, followed by various aerosol analyses. Figure 3.1(a) shows the set-up for particle size distribution measurement, from which we can know the particle peak size and determine the size range to focus on. Figure 3.1(b) is set-up for particle density measurement using DMA-APM,[3.17] which will build a map of particles' densities in terms of their sizes and synthesis temperatures. As is shown in Figure 3.1(c), atomized droplets are dried first, and then DMA, as a screen machine, selects particles of a certain size to go through the heating furnace and finally create a mass distribution. Thus, mass change of particles of a certain size through different heating processes can be monitored. Figure 3.1(d) is the absorption measurement of size-selected CS; and the last one is the extinction measurement. Therefore, the experiments will provide complete information about particle size, density, mass, extinction, absorption and scattering. For all the set-ups, particles are counted downstream by a condensation particle counter (CPC). The particle counter is used to generate size and mass distributions (for set-ups in Figures 3.1a, b and c), and to determine the number of particles entering the optical instruments for calculating absorption and extinction cross section per particle (for set-ups in Figures 3.1d and e).

In this work, we use the laser at the wavelength of 660 nm, so all the optical property measurements, by PAS and CRD, were conducted at this wavelength.

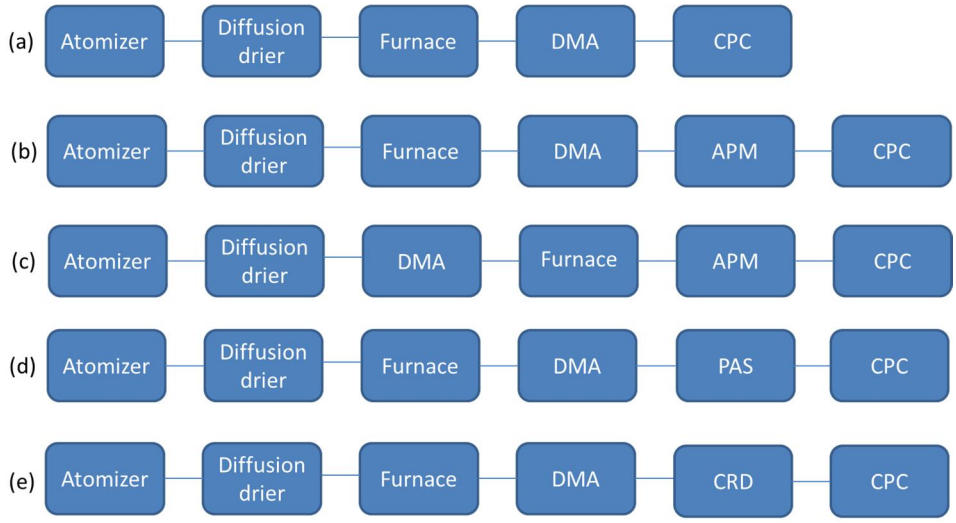


Figure 3.1. Online aerosol characterizations of (a) size distribution, (b) density measurement, (c) mass characterization of particles of a certain size; (d) absorption and (e) extinction of size selected particles.

## 3.4 Result and Analysis

### 3.4.1 TEM

As can be seen in Figure 3.2, the CS particles packed at both room temperature and 400 °C are solid, non-aggregated and spherically-shaped. It is the case and preferable that both without and with chemical change, particles remain a well-packed shape, and comparatively constant density, because hollow or porous structure is more difficult to control the porosity as optical standard.

Aerosol size distribution is measured by using the set-up in Figure 3.1(a). At room temperature, the size distribution peaks around 110 nm, which was then selected for the optical property measurement, together with 200 nm and 300 nm particles.

### 3.4.2 UV-Vis Absorption Spectra of Particles/Molecules Collected on Slides

Figure 3.3 shows UV-Vis absorption spectra of particles/molecules on slides, within the wavelength range from 190 nm to 850 nm. For the molecular sample, the absorption of the molecular sample was determined by measuring a solid thin film drop-casted on a

glass slide prepared from the $C_{60}(OH)_{24}$ solution for atomization. For the nanoparticle sample, aerosol was collected electrostatically onto a slide using an aerosol sampler. With the furnace set at 300 °C, this sample was collected for half an hour, to make sure the film is still translucent but also thick enough to obtain absorption signal. It is obvious that absorption of both samples sharply increased at the wavelength of about 300 nm, with five bumps around 370 nm, 408 nm, 468 nm, 565 nm and 720 nm, which illustrates heating at 300 °C for 1 s might not change the chemical composition and optical character distinctively. It also demonstrated that CS is a broadband absorber; beyond the wavelength of 300 nm, optical properties are available to be studied, *e.g.*, 660 nm for this work.

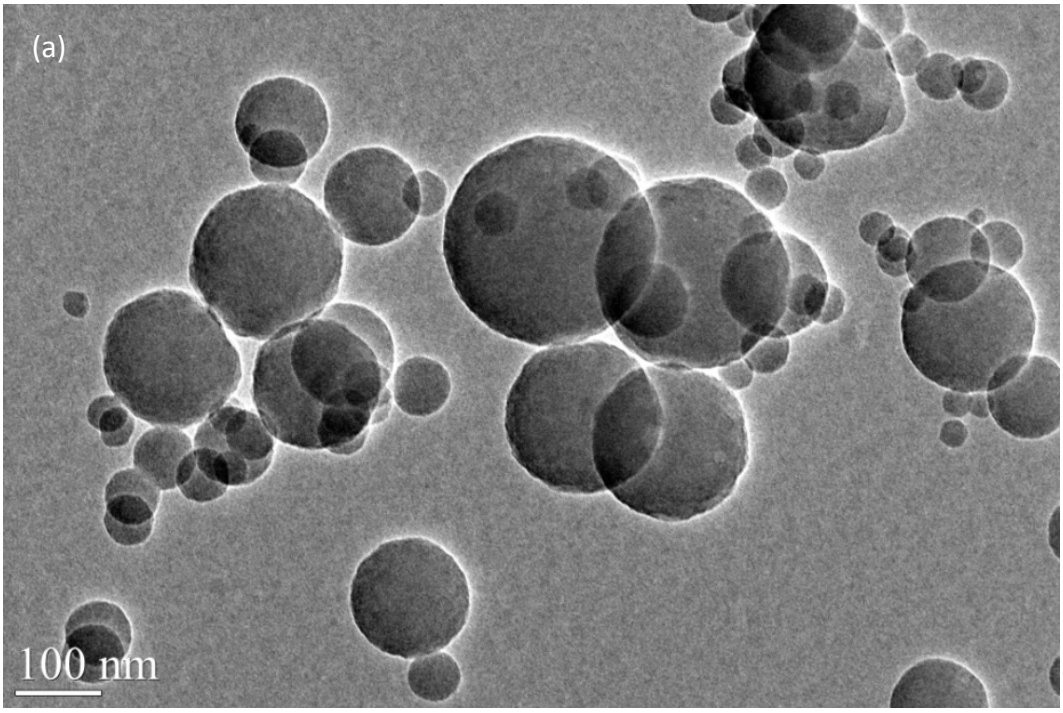

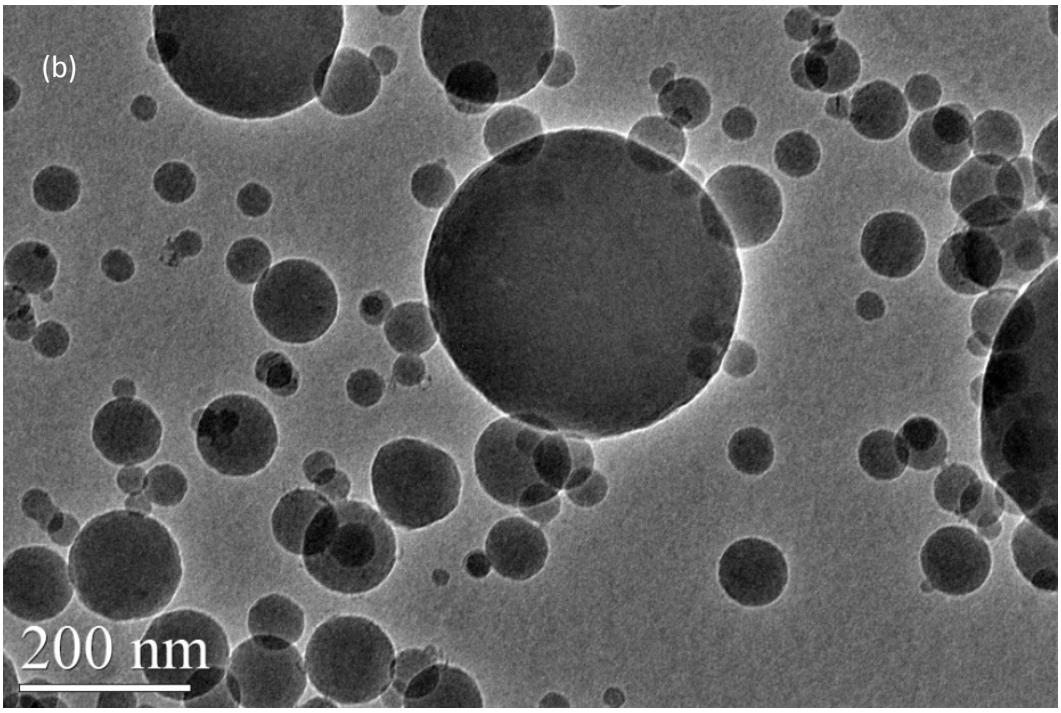


Figure 3.2. TEM images of CS particles produced at (a) room temperature and (b) 400°C.

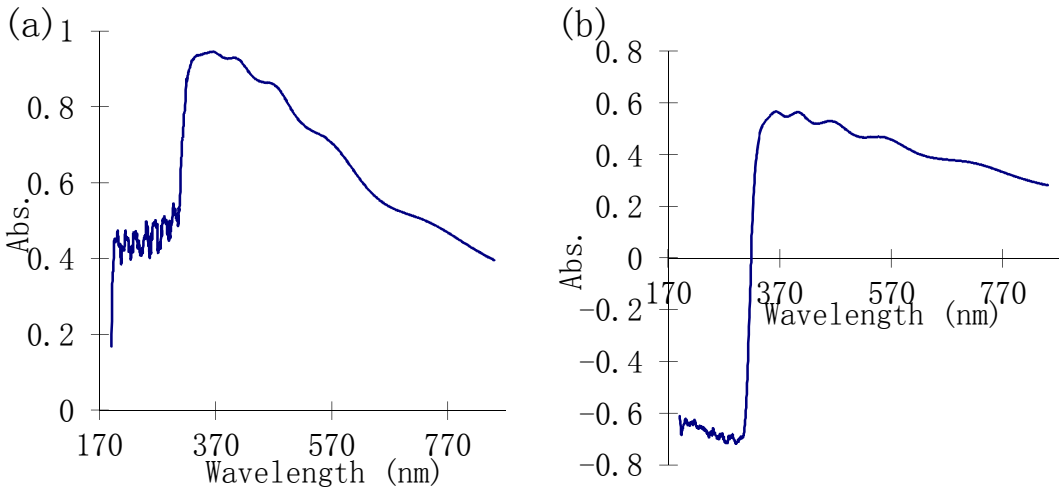


Figure 3.3. Absorption measured on slide of (a) $C_{60}(OH)_{24}$ solution after water evaporated; (b) CS particles synthesized at 300 °C.

### 3.4.3 Density/Mass Measurement

The results of particle density as a function of particle synthesis temperature and sizes are presented in Table 3.1. The density was determined by DMA-APM method. It can be concluded from Table 3.1 that for the same synthesis temperature, larger particles have

lower densities, which is probably caused by packing effect; for the same particle size, particles pyrolysed at a higher temperature have a higher density, which is caused by minor chemical composition change.

Table 3.1. Density of CS synthesized at different temperatures and of different diameters.

| Temperature (°C) | Density-110 nm ($g/cm^3$) | Density-200 nm ($g/cm^3$) | Density-300 nm ($g/cm^3$) |
|---|---|---|---|
| 150 | 1.54 | 1.44 | 1.39 |
| 200 | 1.44 | 1.43 | 1.43 |
| 250 | 1.46 | 1.43 | 1.43 |
| 300 | 1.46 | 1.43 | 1.43 |
| 350 | 1.48 | 1.45 | 1.44 |
| 400 | 1.49 | 1.46 | 1.45 |

Figure 3.4 shows how mass of a certain sized particle changes as a function of furnace temperature. This profile is conducted using the set-up as in Figure 3.3(c). Different from other assemblies, the DMA is equipped between diffusion drier and furnace. Setting the DMA voltage to select particles of 100 nm, particles of the same diameter were selected and pass through furnace and then are mass-measured. It is similar to a thermogravimetric analysis (TGA) process for nanoparticles, but what is more advantageous is that TGA can only analyze bulk material (polydisperse nanoparticles), this method can measure mass change as a function of heating temperature of monodisperse particles, or individual particle, to further study on size-resolved thermal decomposition process or kinetics. Particles (dia. 100 nm size-selected before entering furnace) start reducing mass significantly at about 250 °C. At 550 °C, mass is only 7.3% of that of the room temperature aerosol. Though the fullerol should be easily thermally decomposed beginning at about 50 °C, with production of water first, then $CO_2$ at higher temperatures,[3.18] the delay of mass decrease in Figure 3.4 indicates

same extent of decomposition requires a higher heating temperature due to aerosols' short residence time.

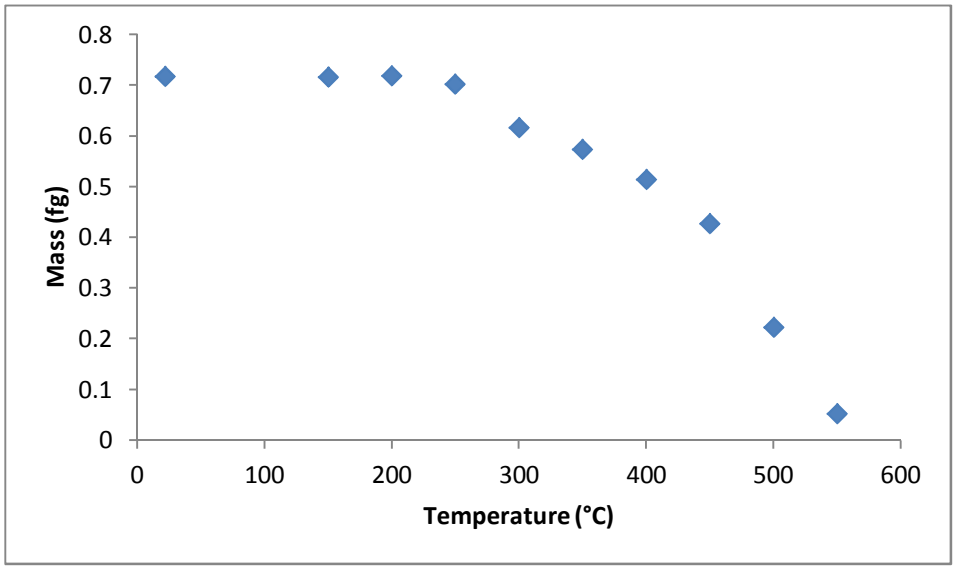


Figure 3.4. Particle mass (DMA size selected before entering furnace) as a function of furnace temperature.

### 3.4.4 Refractive Index

The result of the first run shows that refractive indexes, both the real and imaginary parts, decrease with the size, instead of invariant in size (Figure 3.5). Therefore, a modulation of this theory is needed.

Observed from qext1 and qsca1 versus particle size obtained from the first trial, the plot confers a nearly linear correlation, which becomes the assumption of the second trial. Under this linear-efficiency theory, inaccuracy (defined in Table 3.2), the deviation between qsca2 (qext2) of 200 nm particles and qsca1(qext1) of 300 nm particles, is still high, up to ~ 19%.

Perceived from the second run, the inaccuracy of the 400 °C sample is the lowest. When the linear assumption for 400 °C sample is accepted, a new modulation is needed to improve the accuracy. Based on the hypothesis that infinitesimal particles have

composition-independent infinitesimal qext and qsca, the plot is manipulated in terms of approaching points of 400 °C sample and power functions (see details in section 3.5). $R^2$s of all the functions are highly close to 1 in Figure 3.8, which demonstrates that the new correlation of efficiencies and particle sizes are valid. Put into the Matlab program, as is shown in Table 3.3, the result inaccuracy of this third run is controlled under 11%, within the theoretical uncertainty for PAS (～10%) and CRD (～2% caused by experimental error including CPC counting efficiency)[3.19] combined.

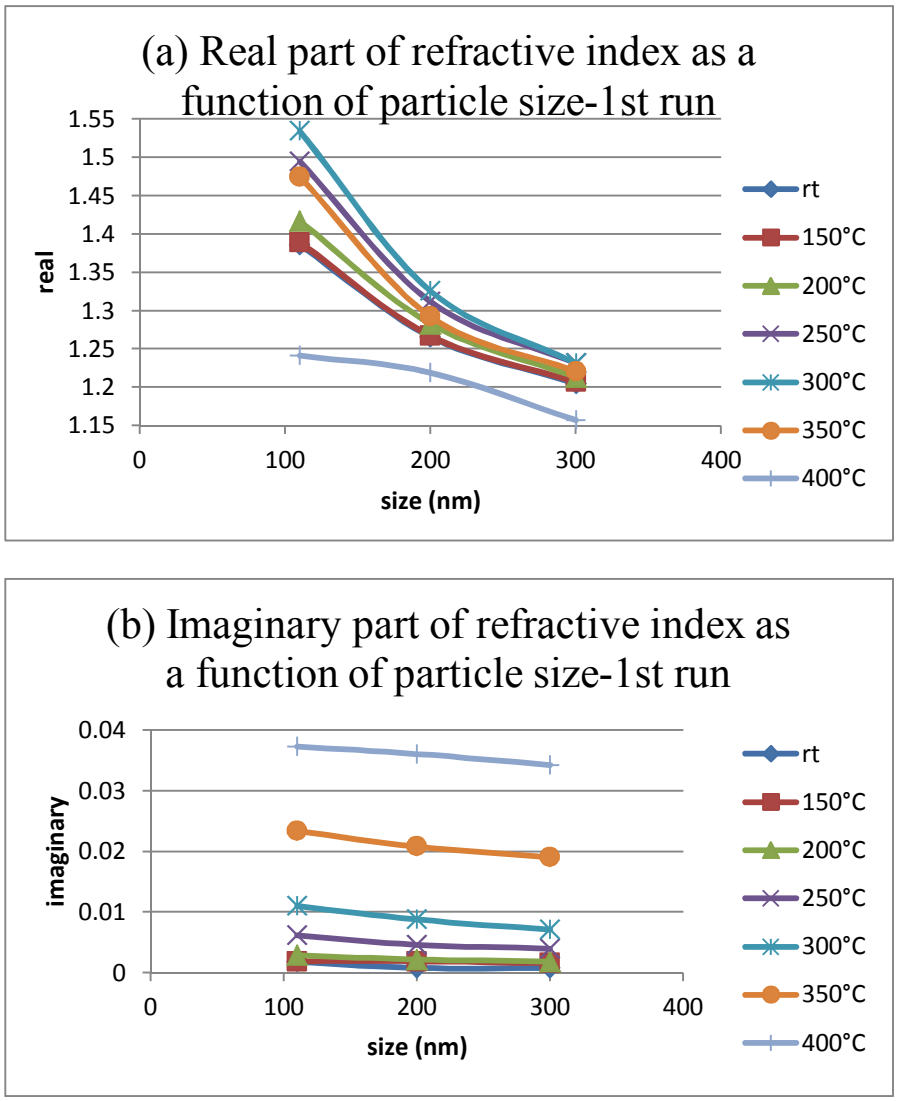


Figure 3.5. (a) Real and (b) imaginary value of refractive index *vs.* particle size of 1st run based on the assumption that refractive index is not a function of size. Obviously, the assumption is not supported by the result.

Table 3.2. A summary of data of the second run, assuming extinction and scattering efficiencies are linear to particle size.

| T (°C) | Size (nm) | [a]Real | [b]Imaginary | [c]qext1 | [d]qsca1 | [e]qext2 | [f]qsca2 | [g]qext | [h]qsca | [i]Inaccuracy of qext | [j]Inaccuracy of qsca |
|---|---|---|---|---|---|---|---|---|---|---|---|
| Room Temperature | 110 | 1.52 | 0.0020 | 0.0213 | 0.0189 | 0.0319 | 0.0284 | 0.0277 | 0.0246 | | |
| | 200 | 1.30 | 0.0008 | 0.0666 | 0.0645 | [i]0.100 | 0.0967 | 0.0769 | 0.0744 | [m]18% | 18% |
| | 300 | 1.22 | 0.0008 | [k]0.121 | 0.118 | 0.182 | 0.177 | 0.132 | 0.128 | | |
| 150 | 110 | 1.52 | 0.0021 | 0.0215 | 0.0190 | 0.0322 | 0.0285 | 0.0277 | 0.0245 | | |
| | 200 | 1.30 | 0.0019 | 0.0694 | 0.0643 | 0.104 | 0.0965 | 0.0795 | 0.0736 | 18% | 19% |
| | 300 | 1.22 | 0.0016 | 0.127 | 0.120 | 0.190 | 0.180 | 0.137 | 0.130 | | |
| 200 | 110 | 1.56 | 0.0033 | 0.0254 | 0.0216 | 0.0381 | 0.0323 | 0.0327 | 0.0278 | | |
| | 200 | 1.32 | 0.0022 | 0.0779 | 0.0720 | 0.117 | 0.108 | 0.0890 | 0.0823 | 15% | 17% |
| | 300 | 1.23 | 0.0019 | 0.138 | 0.130 | 0.207 | 0.195 | 0.152 | 0.143 | | |
| 250 | 110 | 1.67 | 0.0070 | 0.0371 | 0.0294 | 0.0556 | 0.0441 | 0.0474 | 0.0376 | | |
| | 200 | 1.35 | 0.0047 | 0.0992 | 0.0866 | 0.149 | 0.130 | 0.113 | 0.0983 | 11% | 14% |
| | 300 | 1.24 | 0.0040 | 0.167 | 0.150 | 0.251 | 0.225 | 0.182 | 0.163 | | |
| 300 | 110 | 1.73 | 0.0127 | 0.0471 | 0.0336 | 0.0706 | 0.0504 | 0.0598 | 0.0427 | | |
| | 200 | 1.36 | 0.0090 | 0.119 | 0.0944 | 0.178 | 0.142 | 0.135 | 0.107 | 2.4% | 6.4% |
| | 300 | 1.24 | 0.0072 | 0.182 | 0.151 | 0.273 | 0.227 | 0.200 | 0.166 | | |
| 350 | 110 | 1.64 | 0.0264 | 0.0564 | 0.0270 | 0.0845 | 0.0405 | 0.0718 | 0.0344 | | |
| | 200 | 1.32 | 0.0210 | 0.131 | 0.0754 | 0.197 | 0.113 | 0.149 | 0.0856 | 7.5% | 15% |
| | 300 | 1.23 | 0.0191 | 0.213 | 0.133 | 0.319 | 0.199 | 0.230 | 0.143 | | |
| 400 | 110 | 1.31 | 0.0389 | 0.0576 | 0.00740 | 0.0864 | 0.0111 | 0.0730 | 0.00940 | | |
| | 200 | 1.24 | 0.0363 | 0.137 | 0.0416 | 0.205 | 0.0623 | 0.154 | 0.0467 | 0.29% | 7.7% |
| | 300 | 1.16 | 0.0343 | 0.205 | 0.0675 | 0.307 | 0.101 | 0.224 | 0.0739 | | |

[a]retrieved real part (a value) and [b]imaginary part (b value) in complex refractive index m=a+bi; [cd]qext1 and qsca1 are the extinction and scattering efficiencies of the particles with the actual size DMA intends to select (singly charged); [ef]qext2 and qsca2 are the extinction and scattering efficiencies of doubly charged particles selected out by DMA; [gh]qext and qsca are the experimental efficiency data, also input parameters for matlab programing; [ij]inaccuracies are defined as the difference between qext2/qsca2 of 200nm and qext1/qsca1 of 300nm, over qext1/qsca1 of 300nm, *e.g.* [m]18%= ([k]0.121-[i]0.100)/ [k]0.121*100%, because ideally the hypothetical qext2/qsca2 of 200nm (doubly charged, actual 300nm) should be same as qext1/qsca1 of 300nm (singly charged, actual 300nm).

*Table 3.3. A summary of data of the third run, based on the hypothesis that both extinction and scattering efficiencies show power function dependencies on particle size.

| T (°C) | Size (nm) | Real | Imaginary | qext1 | qsca1 | qext2 | qsca2 | qext | qsca | Inaccuracy of qext | Inaccuracy of qsca |
|---|---|---|---|---|---|---|---|---|---|---|---|
| Room Temperature | 110 | 1.51 | 0.0020 | 0.0206 | 0.0183 | 0.0339 | 0.0303 | 0.0277 | 0.0246 | | |
| | 200 | 1.30 | 0.0009 | 0.0655 | 0.0631 | 0.108 | 0.105 | 0.0770 | 0.0743 | 10% | 10% |
| | 300 | 1.21 | 0.0008 | 0.120 | 0.117 | 0.197 | 0.193 | 0.132 | 0.128 | | |
| 150 | 110 | 1.51 | 0.0021 | 0.0208 | 0.0183 | 0.0347 | 0.0305 | 0.0278 | 0.0245 | | |
| | 200 | 1.30 | 0.0019 | 0.0681 | 0.0630 | 0.113 | 0.105 | 0.0795 | 0.0736 | 9.6% | 11% |
| | 300 | 1.22 | 0.0016 | 0.125 | 0.118 | 0.208 | 0.197 | 0.137 | 0.130 | | |
| 200 | 110 | 1.55 | 0.0032 | 0.0245 | 0.0208 | 0.0407 | 0.0349 | 0.0326 | 0.0278 | | |
| | 200 | 1.31 | 0.0023 | 0.0766 | 0.0704 | 0.127 | 0.118 | 0.0892 | 0.0821 | 7.8% | 9.1% |
| | 300 | 1.23 | 0.0019 | 0.138 | 0.130 | 0.207 | 0.195 | 0.152 | 0.143 | | |
| 250 | 110 | 1.66 | 0.0070 | 0.0360 | 0.0283 | 0.0597 | 0.0479 | 0.0475 | 0.0376 | | |
| | 200 | 1.34 | 0.0047 | 0.0974 | 0.0848 | 0.162 | 0.144 | 0.113 | 0.0983 | 2.3% | 3.1% |
| | 300 | 1.24 | 0.0040 | 0.165 | 0.148 | 0.274 | 0.251 | 0.182 | 0.163 | | |
| 300 | 110 | 1.72 | 0.0126 | 0.0460 | 0.0325 | 0.0742 | 0.0540 | 0.0598 | 0.0427 | | |
| | 200 | 1.36 | 0.0090 | 0.117 | 0.0928 | 0.189 | 0.154 | 0.135 | 0.108 | 4.5% | 3.2% |
| | 300 | 1.24 | 0.0073 | 0.181 | 0.149 | 0.291 | 0.247 | 0.200 | 0.166 | | |
| 350 | 110 | 1.63 | 0.0259 | 0.0552 | 0.0262 | 0.0884 | 0.0432 | 0.0717 | 0.0344 | | |
| | 200 | 1.32 | 0.0210 | 0.130 | 0.0739 | 0.208 | 0.122 | 0.149 | 0.0853 | 1.6% | 7.3% |
| | 300 | 1.23 | 0.0191 | 0.212 | 0.131 | 0.339 | 0.216 | 0.230 | 0.143 | | |
| 400 | 110 | 1.31 | 0.0389 | 0.0576 | 0.00740 | 0.0874 | 0.0112 | 0.073 | 0.00940 | | |
| | 200 | 1.24 | 0.0363 | 0.137 | 0.0417 | 0.207 | 0.0632 | 0.154 | 0.0468 | 1.4% | 6.4% |
| | 300 | 1.16 | 0.0343 | 0.205 | 0.0675 | 0.310 | 0.103 | 0.224 | 0.0739 | | |

*same definitions in this table as for Table 3.2

Results in the third run confers that both real and imaginary parts of refractive index decrease as particle size increases, which is most probably due to the packing effect of the aerosol particles. Molecular units in larger particles are not packed as tightly as those in smaller ones (also approved by the density measurement), so larger particles have more vacancies that weaker the scattering and absorption effects. (Due to the low porosity, we still defined them as “non-porous” structures.) Another indication is that imaginary parts of refractive index increase with synthesis temperature, which means that higher temperatures will create “blacker” particles. It is the chemical composition that

affects the refractive index at different synthesis temperatures. As the same trend as in Figure 3.4, that the mass loss emerges at 250 °C and becomes distinct at 300 °C, in Figure 3.6b, the imaginary part of the refractive index (denoting absorption) starts increasing at 250 °C and is distinctively lifted up at 300 °C, while real parts of refractive index increase from room temperature to 300 °C (Figure 3.6a), then decrease, corresponding to the proportion of scattering in extinction. In summary, for the real part, representing more for the scattering, size/packing effect overrides the chemical composition effect, confirmed by the discrete curves for different sizes in Figure 3.6a. However, for the imaginary part, more corresponding to absorption, the chemical composition effect is stronger than the size/packing effect, for the curves for 3 sizes in Figure 3.6b are almost overlapped but sharply rises with temperature.

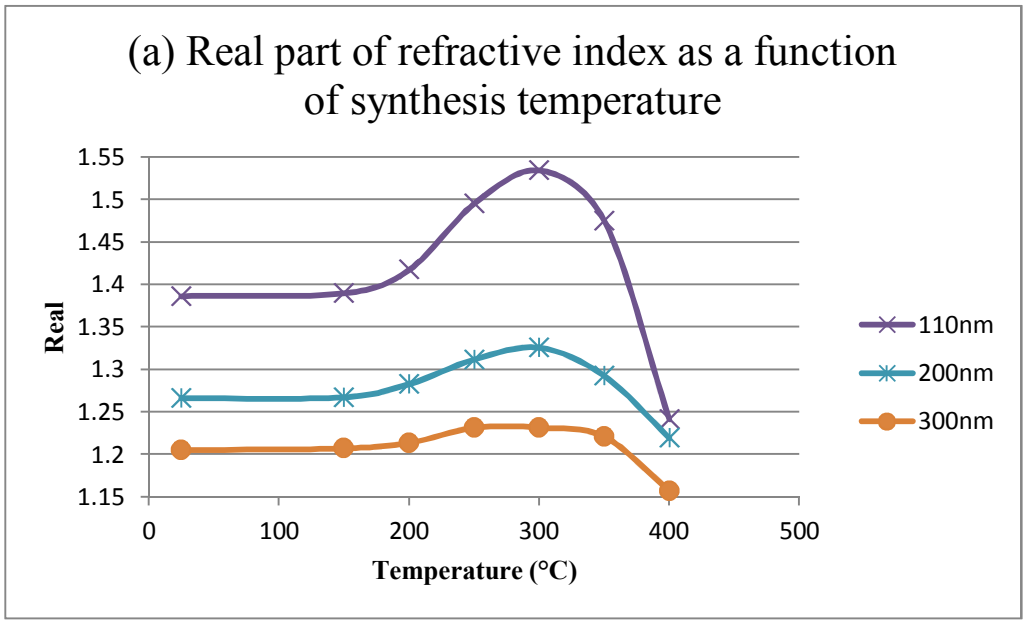

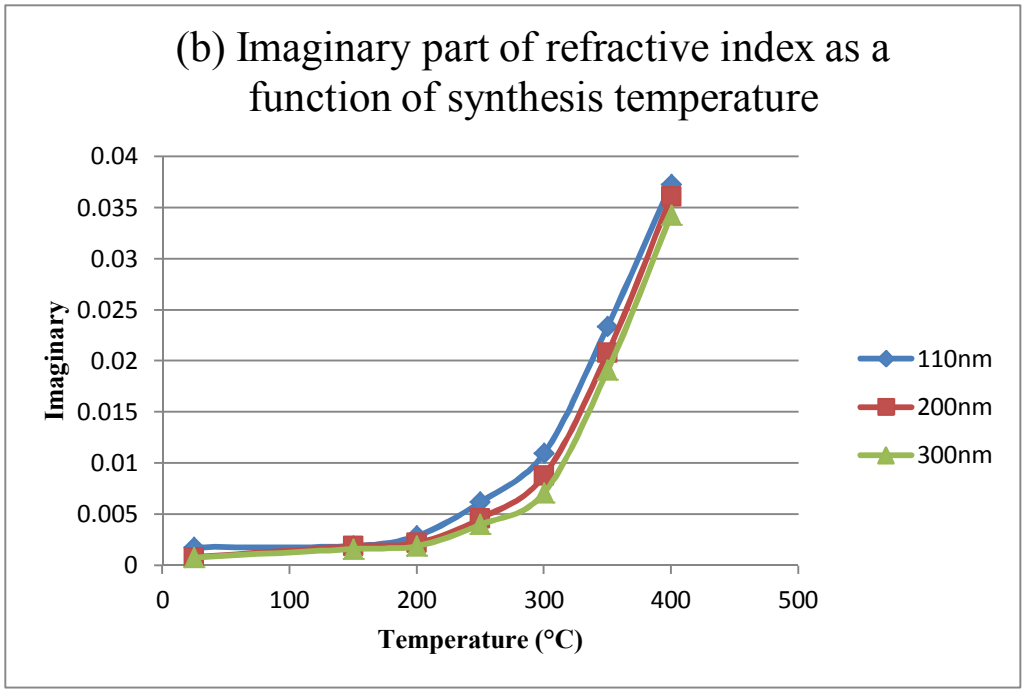


Figure 3.6. (a) Real and (b) Imaginary value of refractive index versus heating temperature of the third run.

3.5 Mathematical Methodology for Calculating Refractive Index

We begin the method by using commercial Mie theory software (MatLab; MathWorks, Natick, MA) as the main function. The original function requires the input of size parameter ($x=2\pi r/\lambda$), complex refractive index ($refrel=a+bi$) and number of angle for phase functions (nang), in a range from 1 to $\pi/2$. The output are phase functions (S1, S2), extinction efficiency (*Qext)*, scattering efficiency (*Qsca*), backscatter efficiency (*Qback*) and asymmetry parameter (*gsca*). What we gain experimentally are the extinction efficiency (directly from CRD) and scattering efficiency (*Qext* from CRD subtracted by *Qabs* from PAS), and what we tend to know from this calculation are the real and imaginary part of refractive indexes. This function can be solved reversely. Another consideration that should be taken into account is that the absorption and extinction cross section obtained by the set-up in Figures 3.2(d) and (e), are not from

particles of one size, because DMA could also select a fraction of doubly charged particles of diameter 1.5 times larger.[3.20] A charge correction was performed to remove the effect of doubly charged particles. Triple charged or higher ones are neglected due to their negligible small number fractions.

Then, the basic idea to loop this program is:

**Assuming**: real (a) and imaginary part (b) of the refractive index; extinction and scattering efficiencies of singly charged particles (*test_qext1, test_qsca1*); extinction and scattering efficiencies of doubly charged particles (*test_qext2, test_qsca2*)

**Known**: nang=1. Because its value does not affect the efficiencies, which are our concern, we simply pick a value in the reasonable range.

Size parameter $x$ ($=2\pi r/\lambda$) is identified after size and light wavelength are plugged in. Extinction and scattering efficiencies of DMA selected particles of the entire batch are qext and qsca, respectively, including the singly charged and doubly charged particles.

Cross section of geometric singly charged particles is $Sg1=\pi\times r_1^2$, and of doubly charged particles $Sg2=\pi\times r_2^2$. ($r_2=1.5\times r_1$)

Proportion of single and doubly charged particles are fraction1 and fraction2, respectively.

**Relations**:

$test\_qext\times Sg1=fraction1\times test\_qext1\times Sg1+fraction1\times test\_qext2\times Sg2$

$test\_qsca\times Sg1=fraction1\times test\_qsca1\times Sg1+fraction1\times test\_qsca2\times Sg2$

*test_qext* and *test_qsca* are calculated extinction and scattering efficiencies considering the singly and doubly charged particles; they are used to help loop the program by approaching these values to real experimental *qext* and *qsca* values.

**Loop**:

for a=1:0.0001:1.6; b=0.001:0.0001:0.04;

until a combination of a and b (in the interval from 1 to 1.6 and from 0.001 to 0.04, respectively, every 0.0001 unit) can have test_qext and test_qsca match the experimental data closest (sum of the absolute differences qext-test_qext and qsca-test_qsca should be the minimum.)

Of the basic concepts above, different assumptions are proposed to build relationship of *test_qext1/test_qsca1* and *test_qext2/test_qsca2*.

**First polstulate**: particles of different sizes (synthesized at same temperature) have the same refractive index.

**Second polstulate**: extinction/scattering efficiencies and particle size have linear correlation, which is: $\frac{test\_qext1}{test\_qext2} = \frac{r1}{r2}$; $\frac{test\_qsca1}{test\_qsca2} = \frac{r1}{r2}$

**Third polstulate**: When particles shrink to infinitesimal size, scattering and extinction efficiencies should approach the same values. Given that the 400 °C sample has a good linear relationship between the efficiency factors and size (observed from the second run), the approaching points are the interceptions of 400 °C-trendlines with *y* axes. (Functions are shown in Figure 3.7.) Origins of the coordinate axis are moved to the approaching points. Then, *Qext1* and *Qsca1* (from the first run in Figure 3.1) *vs.* $r_1$ are replotted in terms of power functions, where the value of power is variable for samples of different temperatures, which is shown in Figure 3.8. This is the third assumption to relate the efficiency factors and particle sizes.

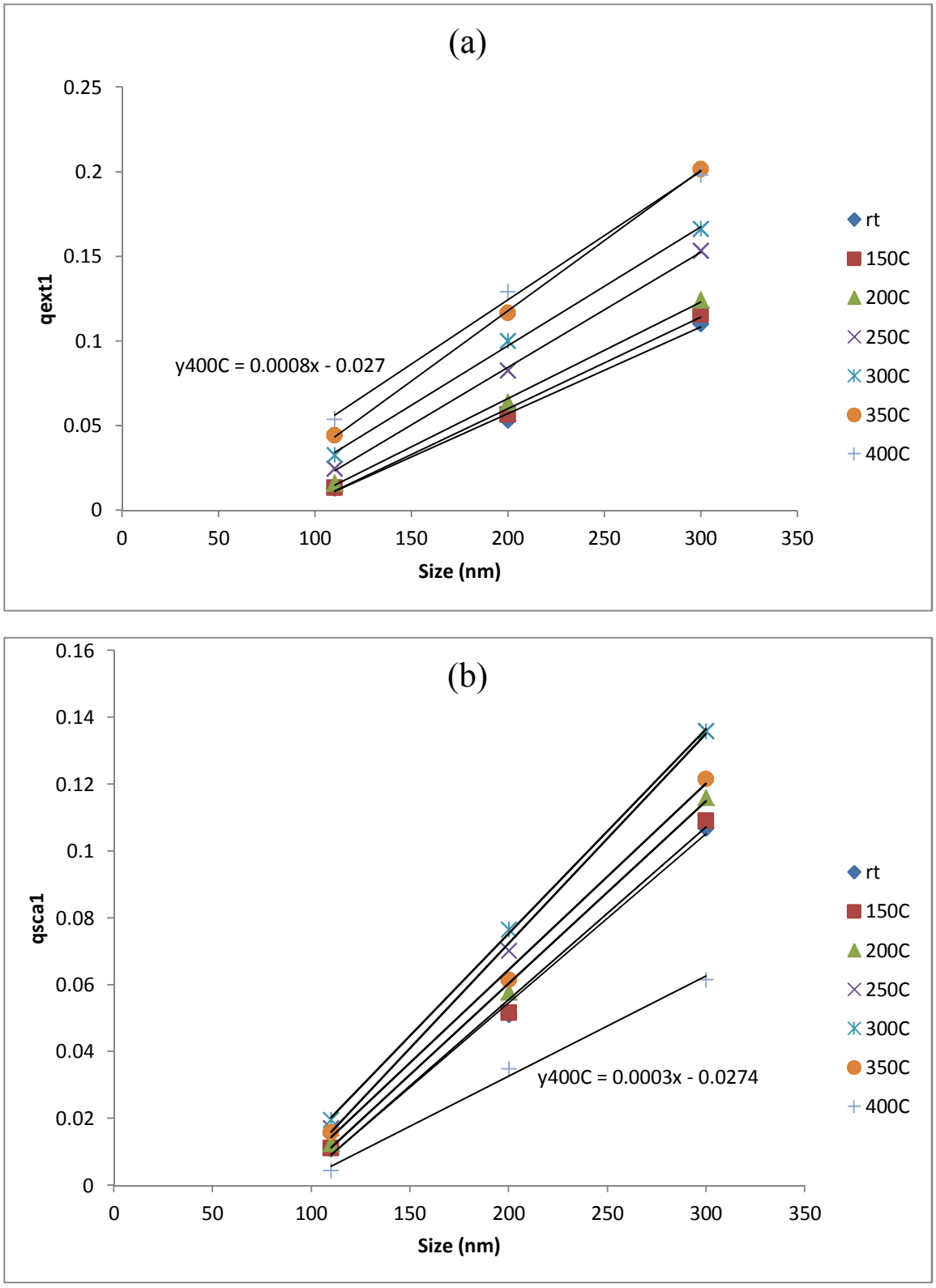


Figure 3.7. Plots of (a) qext1 and (b) qsca1 (from the second run) as a function of particle size, second assumption is proposed based on the good linear correlation and approaching point (qext1=-0.027 and qsca1=-0.0274 when size is approaching to 0) is gained for the third run.

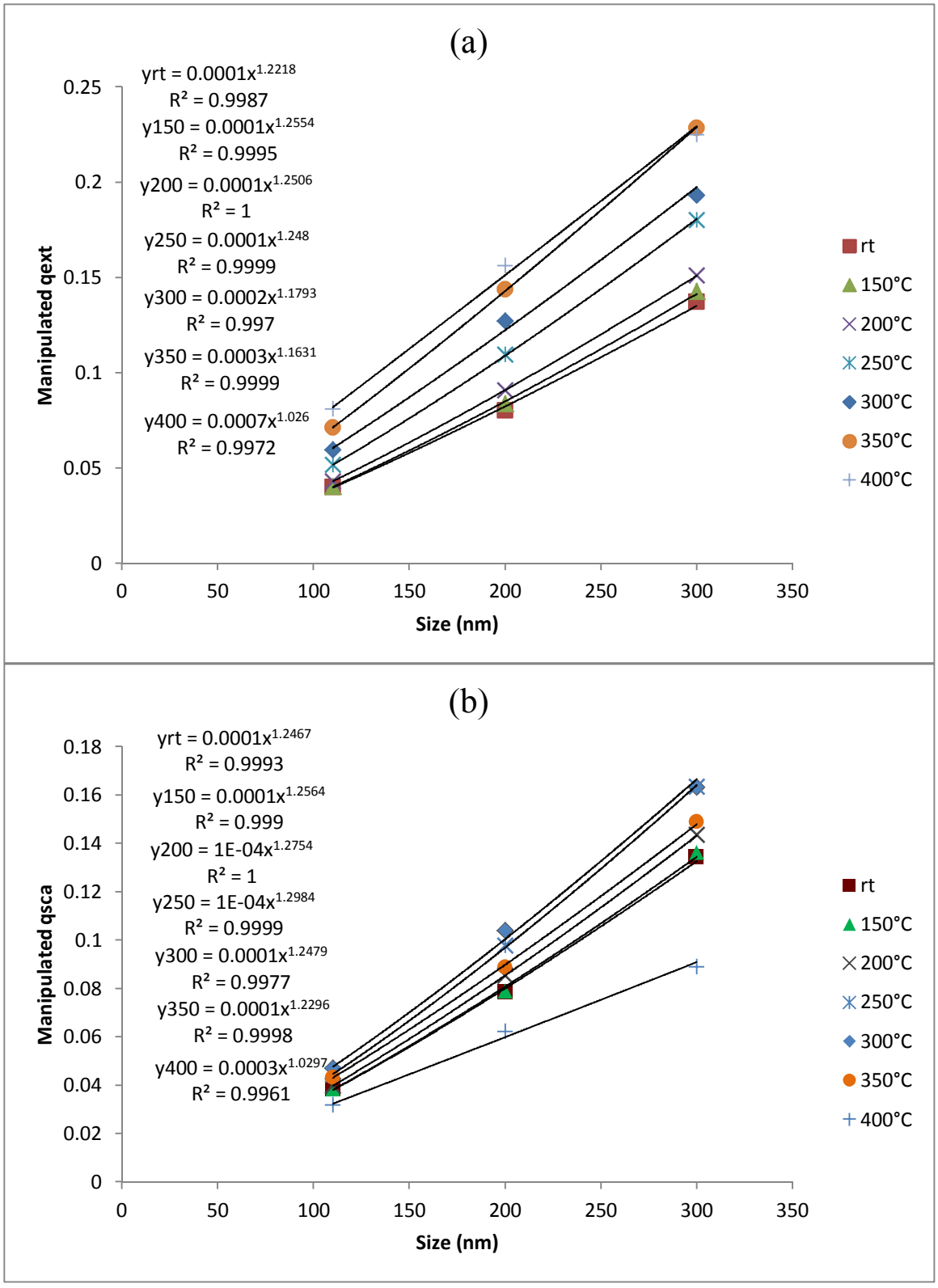


Figure 3.8. Coordinate axes of (a) extinction and (b) scattering efficiencies vs. size are moved down by 0.027 and 0.0274, respectively, before fitted into power function; 0.027 and 0.0274 are the y interception values (qext1 and qsca1) of linear function of 400 °C sample.

## 3.6 Conclusion

Optical characterizations of aerosol particles are practically important; for example, the measurement of particle light absorption can be used for the real-time characterization of black carbon mass concentrations and emission rates, from combustion processes such as biomass burning or internal combustion engines.[3.21] Extinction, as well as the relative extents of absorption and scattering, described by the single scattering albedo, govern a particle's contribution to the warming or cooling of the atmosphere.[3.22] It is known that the real and imaginary parts of the complex refractive index primarily reflect the scattering and absorption properties of a particle, respectively. However, there is no overall research conducted on refractive index of nanoparticle, and its correlation with particle size. This work is highlighted on this innovative material, which could be used as optical standard, and also its refractive index can be retrieved, from a series of data of absorption (by PAS) and extinction (by CRD). This optical standard is more promising than the ones in use, because it has a larger absorption range compared to molecular standard and a regular morphology relative to soot particles.

## References


3.1. Sunkara, B.; Zhan, J. J.; Kolesnichenko, I.; Wang, Y. Q.; He, J. B.; Holland, J. E.; McPherson, G. L.; John, V. T., Modifying Metal Nanoparticle Placement on Carbon Supports Using an Aerosol-Based Process, with Application to the Environmental Remediation of Chlorinated Hydrocarbons. *Langmuir* **2011,** *27* (12), 7854-7859.

3.2. Friedlander, S., *Smoke, Dust, and Haze*. 2nd ed.; Oxford University Press, Inc.: New York, USA, 2000.

3.3. Barber, P.; Hill, S., *Light scattering by particles: Computational methods*. 1990.

3.4. Spinner, S.; Waxler, R. M., Relation Between Refractive Index and Density of Glasses Resulting From Annealing Compared with Corresponding Relation Resulting from Compression. *Applied Optics* **1966,** *5* (12), 1887-.
3.5. Gopi, K. R.; Nagarajan, R., Advances in Nanoalumina Ceramic Particle Fabrication Using Sonofragmentation. *IEEE Transactions on Nanotechnology* **2008,** *7* (5), 532-537.
3.6. Pol, V. D.; Bremmer, The diffraction of electromagnetic waves from an electrical point source round a finitely conducting sphere. *Philosophical Magazine series 7* **1937,** *24*.
3.7. McMurry, P. H., A review of atmospheric aerosol measurements. *Atmospheric Environment* **2000,** *34* (12-14), 1959-1999.
3.8. Duan, D. W.; Rao, Y. J.; Zhu, T., High sensitivity gas refractometer based on all-fiber open-cavity Fabry-Perot interferometer formed by large lateral offset splicing. *Journal of the Optical Society of America B-Optical Physics* **2012,** *29* (5), 912-915; Gao, R. X.; Liu, W. J.; Wang, Y. Y.; Wang, Q.; Zhao, F.; Qu, S. L., Design and fabrication of SMS fiber refractometer for liquid. *Sensors and Actuators a-Physical* **2012,** *179*, 5-9.
3.9. Havey, D. K.; Bueno, P. A.; Gillis, K. A.; Hodges, J. T.; Mulholland, G. W.; van Zee, R. D.; Zachariah, M. R., Photoacoustic Spectrometer with a Calculable Cell Constant for Measurements of Gases and Aerosols. *Analytical Chemistry* **2010,** *82* (19), 7935-7942.
3.10. Orphal, J., A critical review of the absorption cross-sections of O-3 and NO2 in the ultraviolet and visible. *Journal of Photochemistry and Photobiology a-Chemistry* **2003,** *157* (2-3), 185-209.
3.11. Gillis, K. A.; Havey, D. K.; Hodges, J. T., Standard photoacoustic spectrometer: Model and validation using O-2 A-band spectra. *Review of Scientific Instruments* **2010,** *81* (6).
3.12. Arnott, W. P.; Moosmuller, H.; Walker, J. W., Nitrogen dioxide and kerosene-flame soot calibration of photoacoustic instruments for measurement of light absorption by aerosols. *Review of Scientific Instruments* **2000,** *71* (12), 4545-4552.
3.13. Petzold, A.; Niessner, R., Photoacoustic soot sensor for in-situ black carbon monitoring. *Applied Physics B-Lasers and Optics* **1996,** *63* (2), 191-197.
3.14. Moosmuller, H.; Varma, R.; Arnott, W. P., Cavity ring-down and cavity-enhanced detection techniques for the measurement of aerosol extinction. *Aerosol Science and Technology* **2005,** *39* (1), 30-39.
3.15. *IPCC Fourth Assessment Report: Climate Change 2007*; 2007.
3.16. Kokhanovsky, A., *Aerosol Optics*. Springer: Chichester, UK, 2008.
3.17. Liu, Q.; Ma, X.; Zachariah, M. R., Combined on-line differential mobility and particle mass analysis for determination of size resolved particle density and microstructure evolution. *Microporous and Mesoporous Materials* **2012,** *153*, 210-216.
3.18. Kleiman-Shwarsctein, A.; Jaramillo, T. F.; Baeck, S. H.; Sushchikh, M.; McFarland, E. W., Low-voltage electrodeposition of fullerol thin films from aqueous solutions. *Journal of the Electrochemical Society* **2006,** *153* (7), C483-C487.

3.19. Miles, R. E. H.; Rudic, S.; Orr-Ewing, A. J.; Reid, J. P., Sources of Error and Uncertainty in the Use of Cavity Ring Down Spectroscopy to Measure Aerosol Optical Properties. *Aerosol Science and Technology* **2011,** *45* (11), 1360-1375.
3.20. Kim, S. H.; Woo, K. S.; Liu, B. Y. H.; Zachariah, M. R., Method of measuring charge distribution of nanosized aerosols. *Journal of Colloid and Interface Science* **2005,** *282* (1), 46-57.
3.21. Schnaiter, M.; Gimmler, M.; Llamas, I.; Linke, C.; Jaeger, C.; Mutschke, H., Strong spectral dependence of light absorption by organic carbon particles formed by propane combustion. *Atmospheric Chemistry and Physics* **2006,** *6*, 2981-2990.
3.22. Seinfeld; Pandis, *Atmospheric Chemistry and Physics: From Air Pollution to Climate Change*. 1st edition ed.; J. Wiley: New York, 1998.

# Chapter 4: Carbon-Dispersed Metal Oxide Nanoparticle Synthesis by Spray-pyrolysis and its Application to Lithium-Ion Battery

## 4.1 Background

### 4.1.1 Lithium-Ion Battery

The lithium-ion battery (LIB) is one of the most popular types of rechargeable batteries for portable electronics, in which lithium ions move from the negative electrode to the positive electrode during discharge, and back when charging. It uses an intercalated lithium compound as the electrode material, with the advantage of high energy density, no memory effect and superior cycling stability. Therefore, a typical lithium-ion battery can store twice as much electrical energy of a nickel-metal hydride battery and about 6 times of a lead-acid battery; it does not need to be completely discharge before being recharging; and it can handle hundreds of charge/discharge cycles. For example, in a $LiCoO_2$-graphite lithium-ion battery, lithium ions are transported to and from the cathode or anode, through electrolytes, with the oxidation-reduction reaction of the transition metal, cobalt (Co). For the charging process:

The positive electrode half-reaction is:

$$LiCoO_2 \Leftrightarrow Li_{1-x}CoO_2 + nLi^+ + ne^-$$

The negative electrode half-reaction is:

$$C + nLi^+ + ne^- \Leftrightarrow Li_yC$$

Electrons flow through a closed external circuit as useful work. However, the overall reaction has its limits on temperature and extent of reaction. Overdischarge supersaturates lithium cobalt oxide, leading to the production of lithium oxide irreversibly:

$$LiCoO_2 + Li^+ + e^- \rightarrow Li_2O + CoO$$

Overcharge up to 5.2 Volts leads to the synthesis of cobalt (IV) oxide:

$$LiCoO_2 \rightarrow CoO_2 + Li^+ + e^-$$

Commercially used LIBs include lithium cobalt oxide (high energy density, but with safety concerns); Lithium iron phosphate, lithium manganese oxide and lithium nickel manganese cobalt oxide (lower energy density, but longer lives and inherent safety). Lithium nickel cobalt aluminum oxide, lithium titanate and some other new materials are specially being designed to improve the overall performance and aim at particular niche roles. Challenges that are waiting to be resolved in engineering science will be discussed later.

### 4.1.2 Motivation of Applying Spray Pyrolysis for LIB Material Synthesis

The motivation to use spray pyrolysis system to make battery nanomaterial is that 1) it is a commercially potential method to synthesis nanoparticles, and even smaller nanograins within the particle; 2) this system is good at generating porous structures; 3) the pore template can be substituted by carbon material which will is conductive and protective for real electrode material.

Roles of nanosize in lithium reactive nanomaterials are reflected on kinetic, mechanical and structural effects, in terms of decreasing the solid state diffusion path of $Li^+$, suppressing volume change thus cracking or pulverization, and lowering overpotential of the reactions.[4.1]

The morphology and surface area of particles within an electrode have a profound effect on the electrochemical properties of a material.[4.2] Porous structure, of larger specific surface area, leads to higher current density and the thin pore wall can further

reduce the lithium ion diffusion path. In addition, porous pathway facilitates the fast transport of electrolyte with lithium ion, and cavities can also act as a buffer layer to alleviate the volume expansion of the electrode materials during lithiation/delithiation.

The carbon filled in the pores of electrochemical material can 1) block the penetration of liquid electrolyte to the inside of $MnO_x$, thus reducing the SEI formation and lowering the irreversible capacity; 2) enhance the electronic and Li-ion conductivity and thus the rate capability; 3) prevent manganese grain agglomeration by the inter-dispersed carbon.

## 4.2. Introduction

To improve the current Li-ion battery technology, it is essential to use high-capacity materials such as silicon, tin, and transition metal oxides to replace the current carbon based anodes, to meet the demands from some fast emerging applications including plug-in electric vehicles and integrated grid systems.[4.3]

Transition metal oxides as anode materials were first proposed by Poizot *et al*. in 2000.[4.4] Among all the metal oxides that can be used as the anode for Li-ion batteries, manganese oxides was proven to be a superior choice due to its relatively lower electromotive force, *i.e.* lower thermodynamic equilibrium voltage *vs*. $Li/Li^+$,[4.5] its natural abundance, and its environmental benignity. The Li storage mechanism of manganese oxides is based on the reversible oxidation/reduction reaction between Li and manganese oxides as shown in the following reaction, assuming complete conversion of the metal oxides.

$$MnO_x + 2x\ Li \leftrightarrow Mn + x\ Li_2O$$

This reversible conversion mechanism is enabled by the formation of nano-sized (< 5 nm) Mn grains uniformly dispersed into a $Li_2O$ matrix during the manganese oxide

reduction reaction (forward reaction).[4.6] The nano-sized Mn grains create a large contact surface between metal and $Li_2O$ that makes the reverse reaction kinetically favorable. A variety of manganese oxide (MnO,[4.7-4.12] $Mn_2O_3$,[4.11, 4.12] $MnO_2$,[4.12-4.14] and $Mn_3O_4$[4.12, 4.15, 4.16]) anode materials have been investigated. The reversibility of conversion reaction depends on the $MnO_x$ phase structure, oxygen content x in $MnO_x$ and particle size. However, the realization of manganese oxide anodes is still hindered by several challenges including (1) poor cycling stability due to structural instability caused by gradual agglomeration of the metal grains, and the large volume change during phase transformation in the conversion reaction,[4.17] (2) inferior rate capability, *i.e.* capability to be charged and discharged rapidly while maintaining high capacity, due to low electronic conductivity of manganese oxides, (3) low coulombic efficiency, and (4) high potential hysteresis between lithiation and delithiation due to high accommodation energy associated with a large volume change.

Current techniques to overcome these challenges were to reduce the particle size of manganese oxides to nano-scale to accommodate the large volume change. Carbon nano-materials were also incorporated to enhance the electronic conductivity.[4.8-4.10, 4.13-4.19] Graphene[4.16], carbon nanotubes,[4.14, 4.18] and carbon nanofibers[4.19] have been used to fabricate manganese oxide-carbon nanocomposite anode materials. However, the high surface area of manganese oxide-carbon nanocomposites results in low coulombic efficiency due to the formation of large unstable solid electrolyte interphase (SEI) during lithiation/delithiation cycles. The agglomeration of manganese grains and phase transformation of crystalline manganese oxides during cycling also limit the cycling stability.[4.7, 4.8] Moreover, the large volume change during phase transformation of

crystalline manganese oxides decrease the conversion reaction rate, resulting in a low lithiation potential. It was reported that crystalline MnO particle composed of nano-sized (10-30 nm) MnO grains could be lithiated at a potential that was 0.4 V higher than the bulk MnO particle due to the enhanced conversion reaction kinetics.[4.8] Maier and coworkers also reported that amorphization of crystalline $RuO_2$ could enhance the lithiation potential owing to the enhanced Gibbs free energy compared with the crystalline bulk $RuO_2$.[4.20] These studies suggest that amorphous manganese oxide may be able to narrow the potential hysteresis and achieve faster conversion reaction rates.

Therefore, an ideal structure might comprise a porous amorphous manganese oxide particle filled with carbon in the pores. The inter-dispersed carbon would facilitate the transport of $Li^+$ ions and electrons without increasing the undesirable surface area between electrolyte and active materials. Another import function of the carbon is to prevent the agglomeration of the Mn grains during cycling as a barrier structure.

In this study, carbon filled manganese oxide-carbon nanocomposite particles were synthesized using aerosol spray pyrolysis as illustrated in Figure 4.1. The resulting nanoparticles had a unique structure of uniformly inter-dispersed amorphous manganese oxide ($MnO_x$) and carbon. These $MnO_x$-C composite nanoparticles demonstrated high Li storage capacity and superior cycling stability. Moreover, they also demonstrated impressive rate capacity and low charge/discharge voltage hysteresis. These amorphous $MnO_x$-C nanoparticles have demonstrated the best electrochemical performance of manganese oxide anode to date.

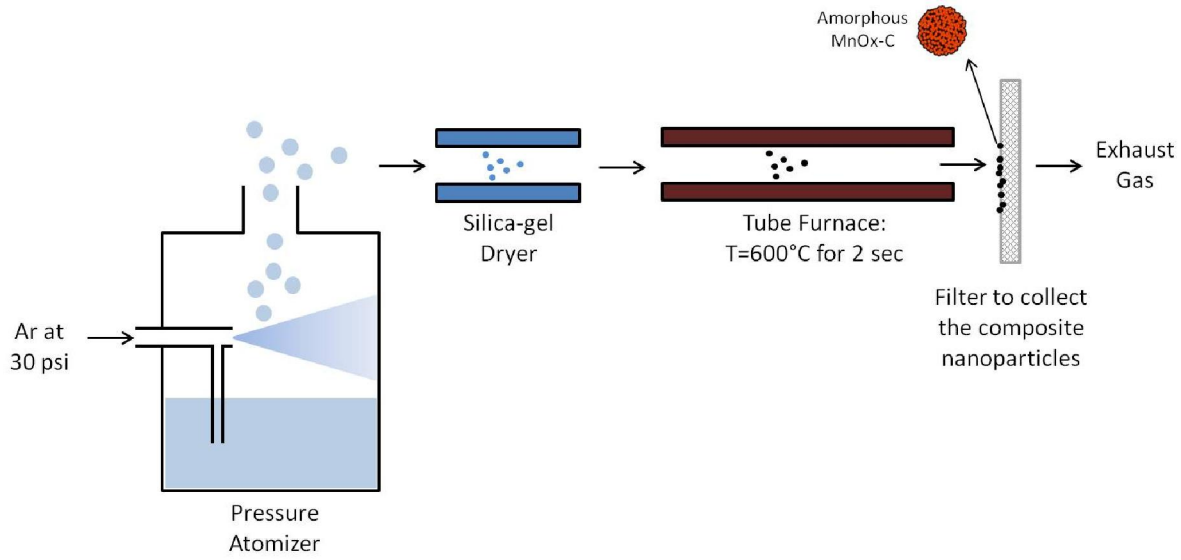

Figure 4.1. Diagram of the aerosol spray pyrolysis apparatus.

## 4.3. Results and Discussion

### 4.3.1. Nanostructure Characterization

The TEM image and the element mapping of the $MnO_x$-C composite nanoparticles are shown in Figure 4.2. The element mapping images in Figure 4.2b clearly demonstrated that the $MnO_x$-C nanoparticle had a homogeneous structure with uniform inter-dispersion of $MnO_x$ and carbon. The TEM image and the selected area electron diffraction (SAED) pattern shown in Figure 4.2a indicated the amorphous nature of the $MnO_x$-C nanoparticles, which was verified on the bulk sample from the XRD shown in Figure 4.3. On the other hand, the XRD pattern of the pure manganese oxide nanoparticle, synthesized using the same pyrolysis procedure but without sucrose, demonstrated a majority $Mn_3O_4$ (70 mol%) crystalline phase, with a small fraction of crystalline $Mn_2O_3$ (30 mol%). The pure manganese oxide nanoparticle clearly shows a porous structure, as shown in Figure 4.4**,** consisting of a compact aggregate of much smaller crystalline particles. Apparently the addition of sucrose played a critical role in the formation of the homogeneous amorphous $MnO_x$-C nanoparticles, and suppression of crystallization of

manganese oxide. It is likely that the nitrate decomposes first, but has insufficient time to create larger $MnO_x$ clusters, before the pyrolysis of sucrose leads to a carbon network blocking grain growth.

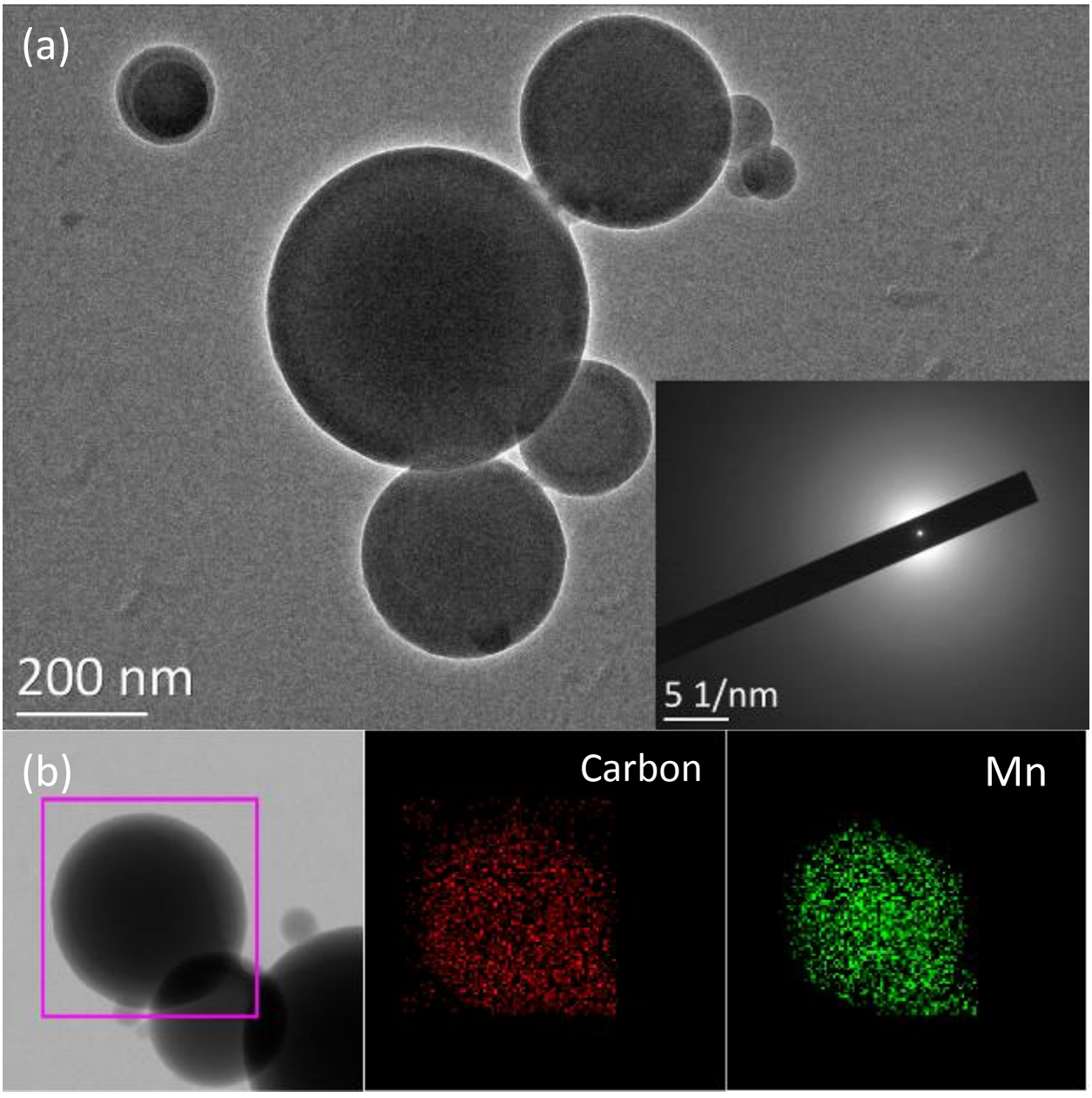


Figure 4.2. (a) TEM and SAED images of the amorphous $MnO_x$-C nanoparticles; (b) EDS mapping image of distribution of elemental carbon and Mn in the amorphous $MnO_x$-C nanoparticles.

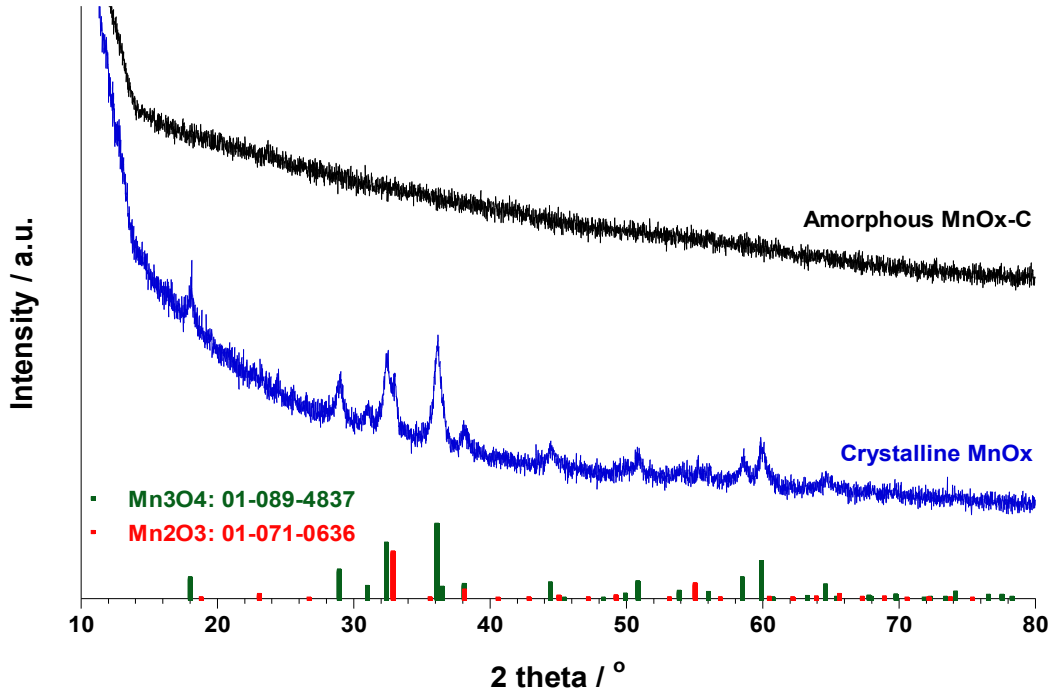


Figure 4.3. XRD patterns of the amorphous $MnO_x$-C nanoparticles and the crystalline $MnO_x$ nanoparticles.

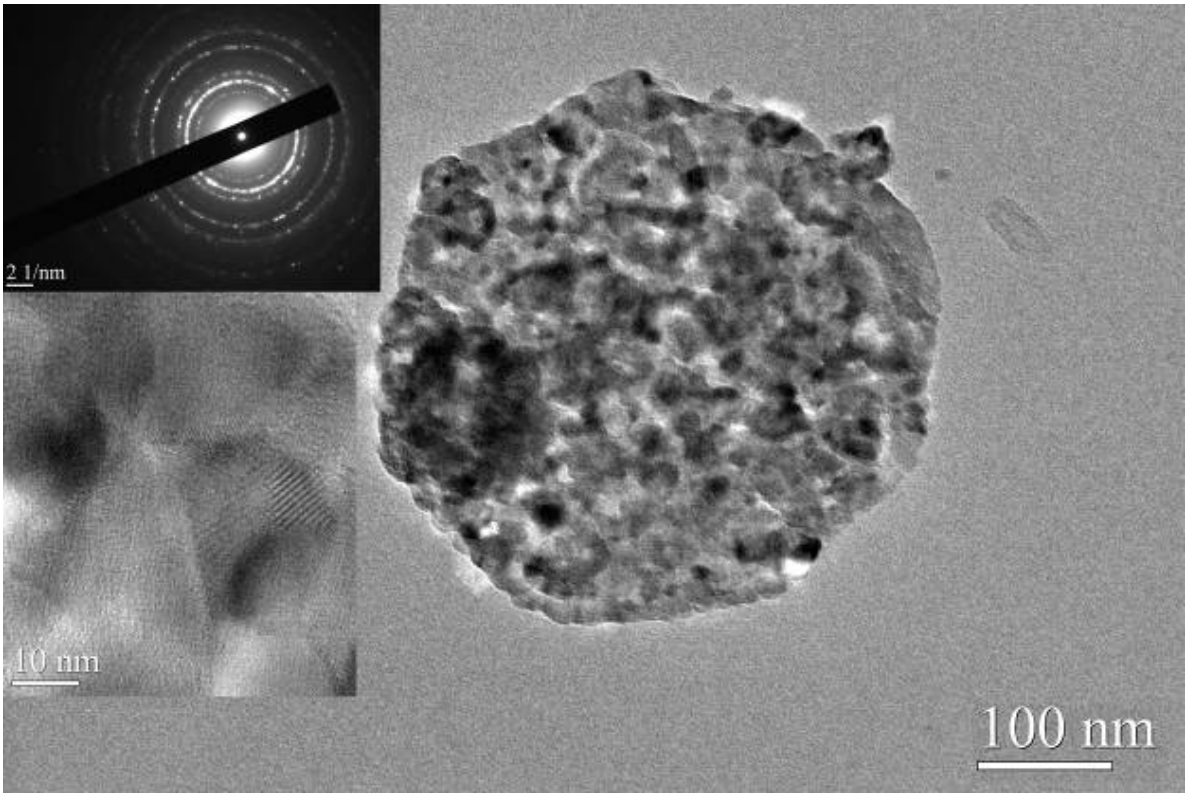


Figure 4.4. TEM, SAED, and high magnification TEM images of the crystalline $MnO_x$ nanoparticles.

The oxidation state x in the amorphous $MnO_x$ was determined using XPS. Since the mixed oxidation state of Mn is not easily determined using standard manganese oxide compounds as references, the crystalline $MnO_x$ particles prepared in this study was used as the reference. Figure 4.5 shows the Mn 2p spectra of the amorphous $MnO_x$-C and the crystalline $MnO_x$. The two peaks located at 640.8 eV and 652.7 eV can be attributed to Mn 2p3/2 and Mn 2p1/2, respectively, are identical in the two samples. Therefore, we conclude that the oxidation state of the amorphous $MnO_x$-C composite is the same as that of the crystalline pure $MnO_x$ and thus the nitrate decomposition and oxidation state is unaffected by the carbon reducing environment. From the XRD data, we determine the crystalline $MnO_x$ consisted of 70 mol% $Mn_3O_4$ and 30 mol% $Mn_2O_3$. Therefore, the oxidation state of amorphous $MnO_x$-C can be estimated as x = 1.37. From the oxidation state of the manganese, the theoretical capacity of both amorphous $MnO_x$ and crystalline $MnO_x$ can be calculated as 961 mAh/g based on assuming complete reaction between $MnO_x$ and Li.

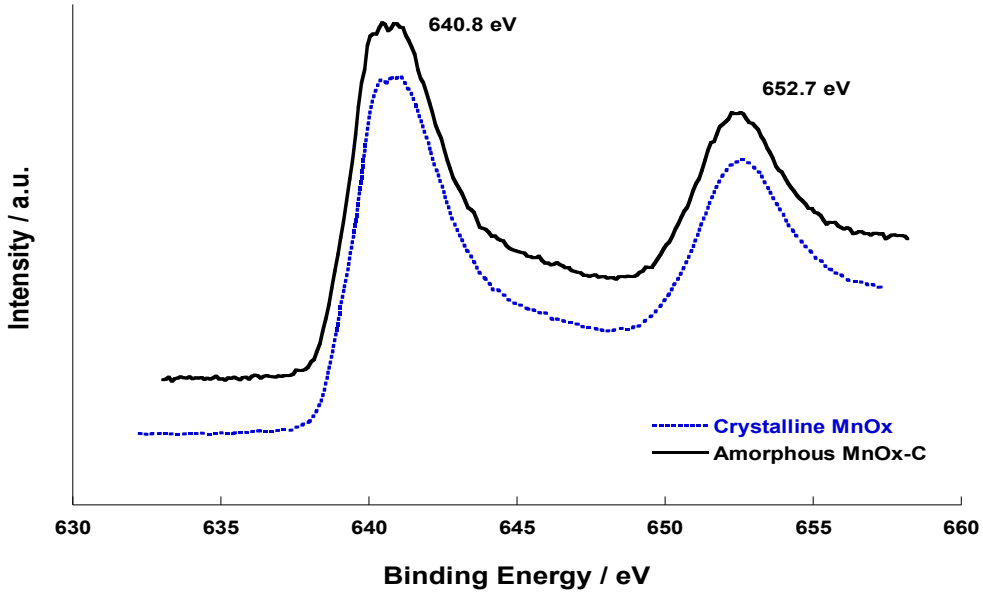


Figure 4.5. XPS spectra of amorphous $MnO_x$-C and crystalline $MnO_x$ nanoparticles.

The carbon content in the amorphous $MnO_x$-C particles was determined by TGA oxidation with air. As shown in Figure 4.6, complete carbon loss (oxidation) occurs by ~300°C. The final weight retention at 500°C was 38.4 wt.%. Assuming manganese oxide only exists in the most stable form, $Mn_3O_4$, at 500°C, we can based on the final weight retention of 38.4%, determine the carbon and $MnO_x$ content in the $MnO_x$-C nanoparticles as 61 wt.% and 39 wt.%, respectively.

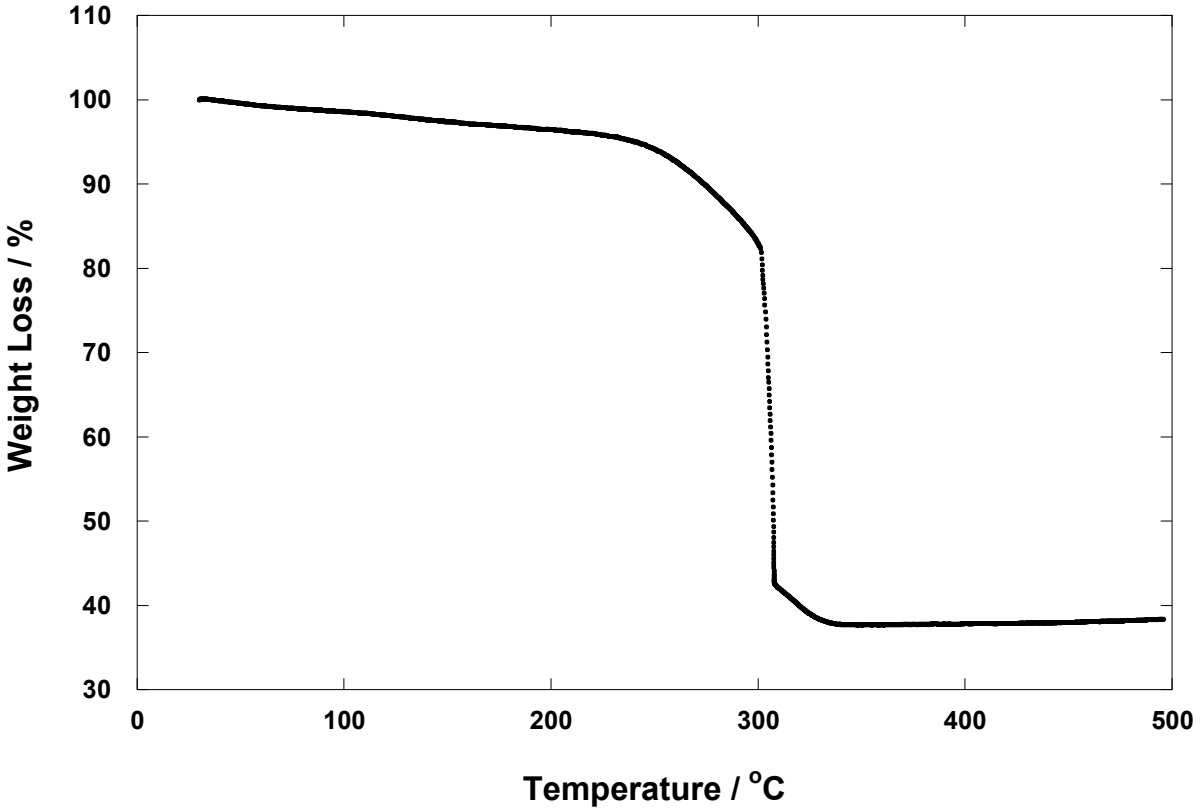


Figure 4.6. TGA curve of the amorphous $MnO_x$-C nanoparticles.

To demonstrate the internal distribution of carbon and $MnO_x$ phase in the amorphous $MnO_x$-C particles, the particles were heated in air at 310°C for 0.5 hr to remove the carbon. Since carbon was oxidized at 300°C, a slightly higher temperature of 310 °C and a short time of 0.5 hr were selected to minimize any $MnO_x$ phase growth. The TEM image of the amorphous $MnO_x$-C nanoparticle before and after the carbon removal is

shown in Figure 4.7a. It is clear that after the carbon removal the uniform $MnO_x$-C particle reveals an underlying porous $MnO_x$, consisting of aggregated $MnO_x$ primary particles (~5 nm), which is very similar in structure to the pure $MnO_x$ synthesized in the absence of sucrose (Figure 4.4). Figure 4.5a demonstrates that carbon is inter-dispersed in the $MnO_x$-C particles as represented schematically in Figure 4.7b. Moreover, $N_2$ adsorption surface area measurement (Figure 4.8) confirms the higher surface area and porosity of the particles after carbon removal. As the $N_2$ adsorption isotherms shown in Figure 4.8, the surface area after carbon removal is 1.7 times higher than before the carbon removal (40.4 $m^2/g$ and 24.4 $m^2/g$, respectively), which also indicates the inter-dispersed structure of $MnO_x$-C nanoparticles.

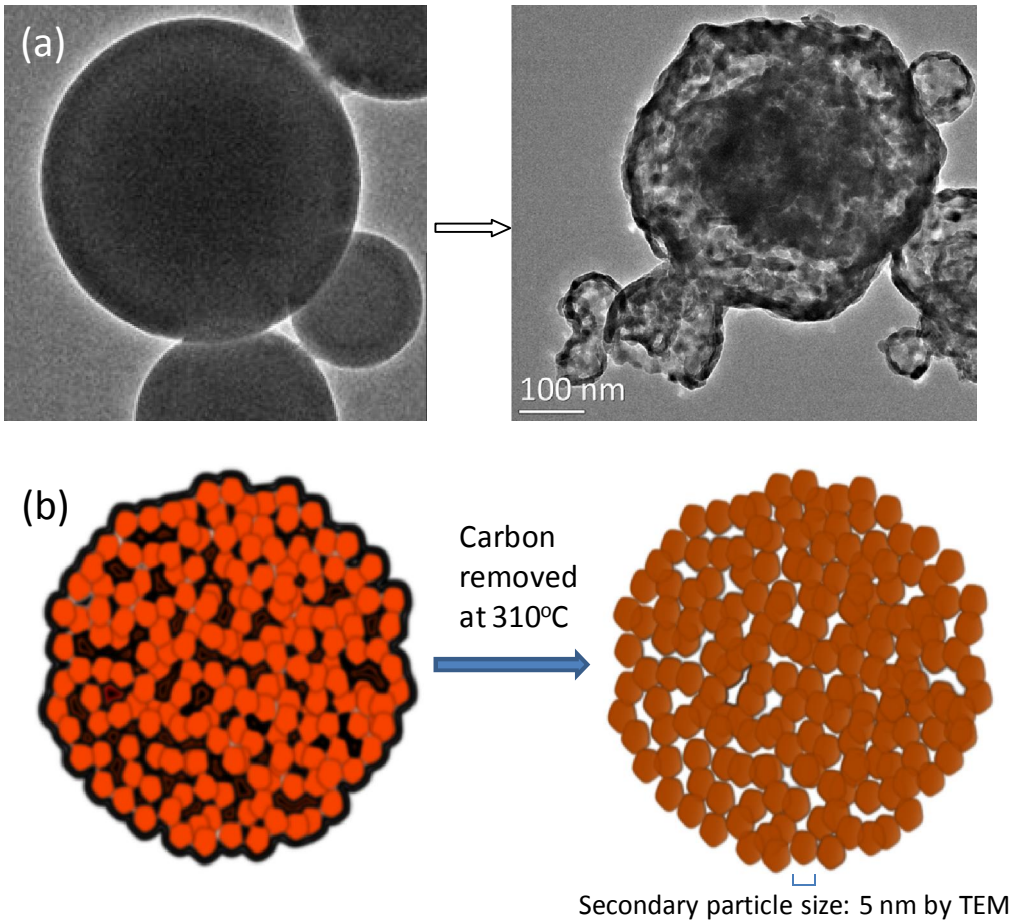


Figure 4.7. (a) TEM image of the amorphous $MnO_x$-C nanoparticles before and after carbon removal at 310 °C, (b) Schematic representation of $MnO_x$-C phase structure before and after carbon removal.

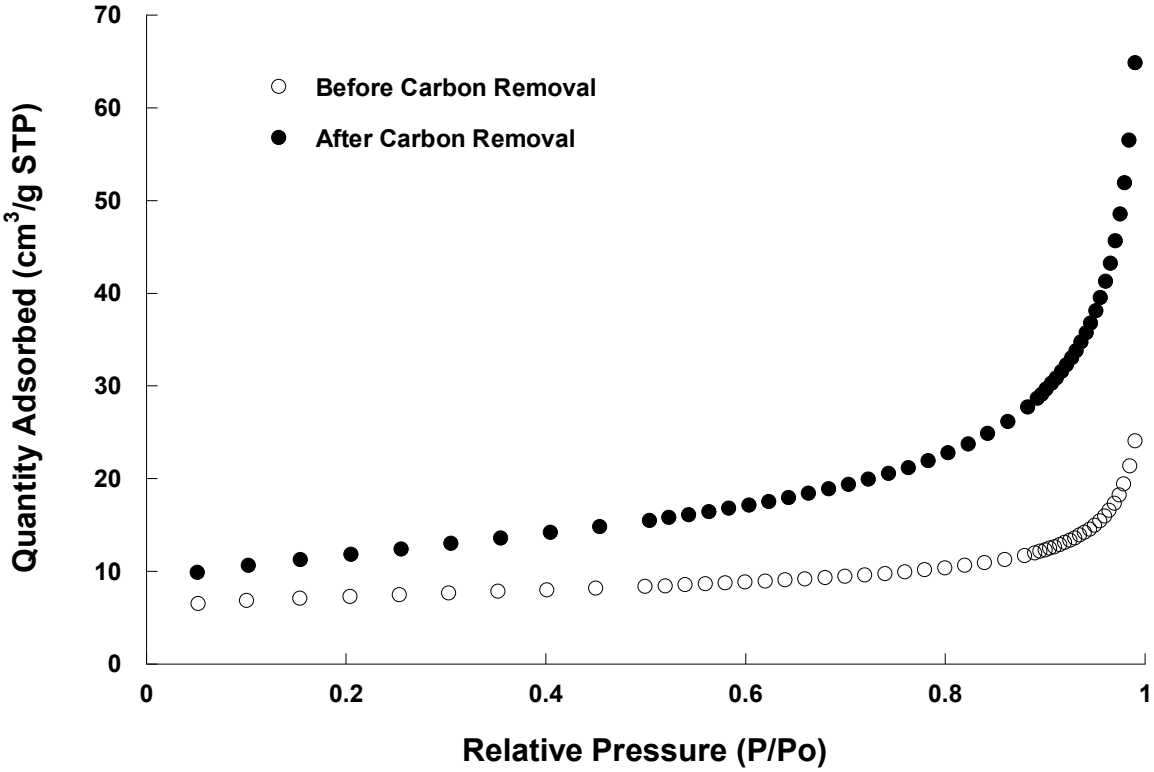


Figure 4.8. $N_2$ adsorption measurment of the $MnO_x$-C nanoparticles before and after carbon removal.

4.3.2. Electrochemical Performance

Owing to the unique structure, the amorphous $MnO_x$-C nanoparticles have demonstrated superior electrochemical performance as anode materials for Li-ion batteries. (Experiments and Figure-analyses in this section were conducted by Dr. Juchen Guo.) As shown in Figure 4.9a, the amorphous $MnO_x$-C nanoparticles showed a high reversible capacity of approximately 650 mAh/g under 200 mA/g charge/discharge current, which is two-fold of the graphite anode capacity. It also showed exceptional capacity retention of 93% after more than 130 cycles. By contrast, the crystalline $MnO_x$ nanoparticles showed very low reversible capacity (200 mAh/g) and poor cycling stability, which is consistent with reported results.[4.14, 4.16, 4.18] Based on the 39 wt.% $MnO_x$ (961 mAh/g theoretical capacity) content estimated previously, 375 mAh/g capacity could be attributed to $MnO_x$, and 275 mAh/g could be attributed to the carbon, consistent

with the previously reported capacity of disordered carbon from pyrolysis.[4.10] The irreversible capacity in the first cycle was 40% that could be mainly due to the partially irreversible $MnO_x$ conversion reaction with Li, and the formation of the SEI in the first few lithiation and delithiation cycles.[4.12] Since the amount of SEI is reduced by the carbon, the 40% irreversible capacity of the amorphous $MnO_x$-C is actually much lower than that of nano-$Mn_2O_3$ (72%) and nano-$Mn_3O_4$ (59%) with similar particle sizes.[4.12] The coulombic efficiency of the amorphous $MnO_x$-C in the subsequent cycles quickly rose to 100% and remained stable during the cycling. The 100% coulombic efficiency implies the absence of new SEI formation during cycling due to carbon blocking liquid electrolyte penetration into $MnO_x$-C particles, thus reducing the contact area between $MnO_x$ and electrolytes. The capacity retention and coulombic efficiency of the amorphous $MnO_x$-C particles are the highest among the reported $Mn_3O_4$ and $Mn_2O_3$ anode materials. Due to the high diffusivity of Li in carbon (~$10^{-9}$ $cm^2/s$),[4.21] the Li could easily diffuse into $MnO_x$ through carbon, resulting in a high rate performance. Figure 4.9b shows the superior rate capability of the amorphous $MnO_x$-C nanoparticles, which could maintain 500 mAh/g of capacity under 800 mA/g charge/discharge current. Moreover, the capacity under 200 mA/g charge/discharge rate was fully recovered when the current was reduced back to 200mA/g after 160 cycles.

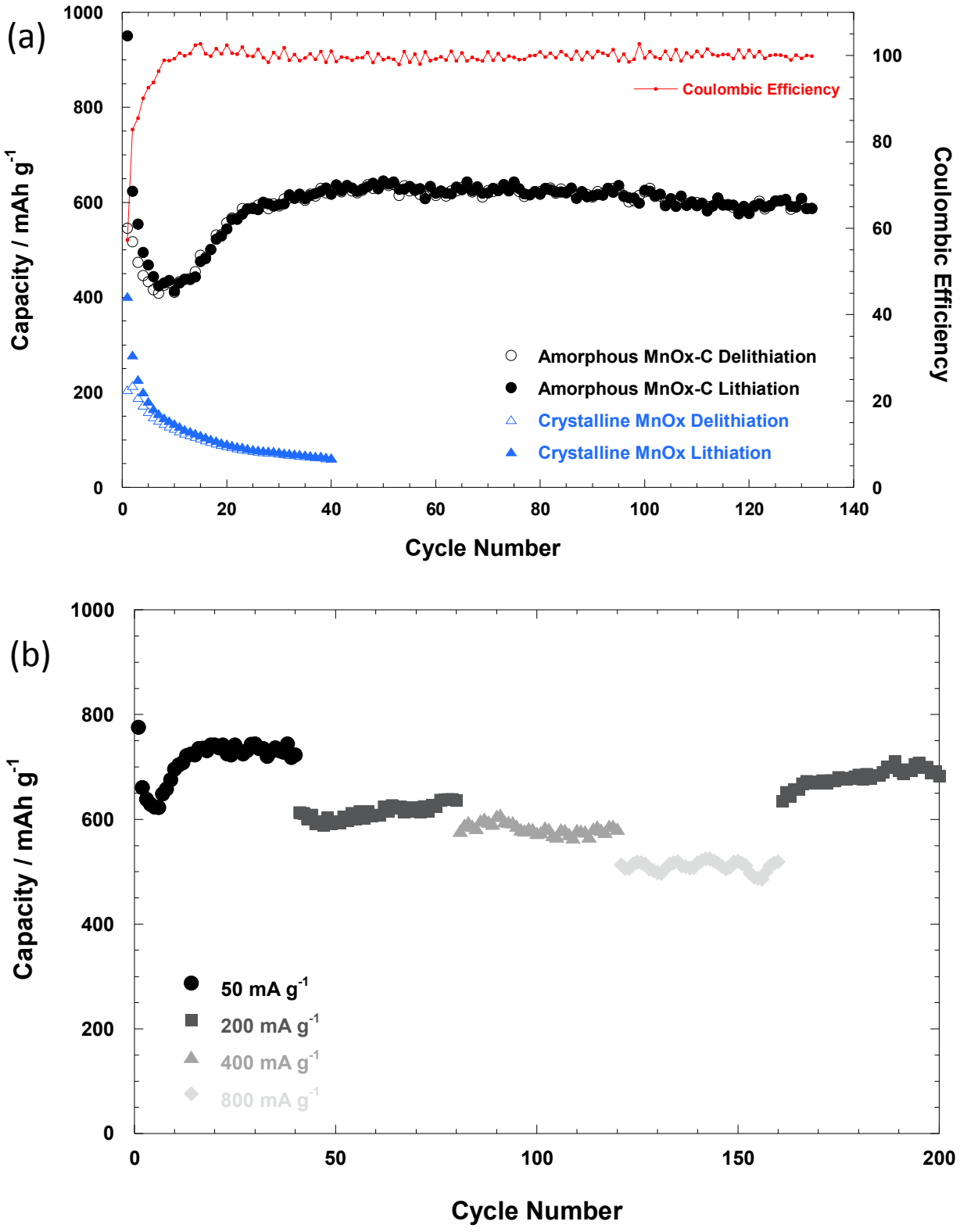


Figure 4.9. (a) Cyclability and (b) rate capacity of the amorphous $MnO_x$-C nanoparticles.

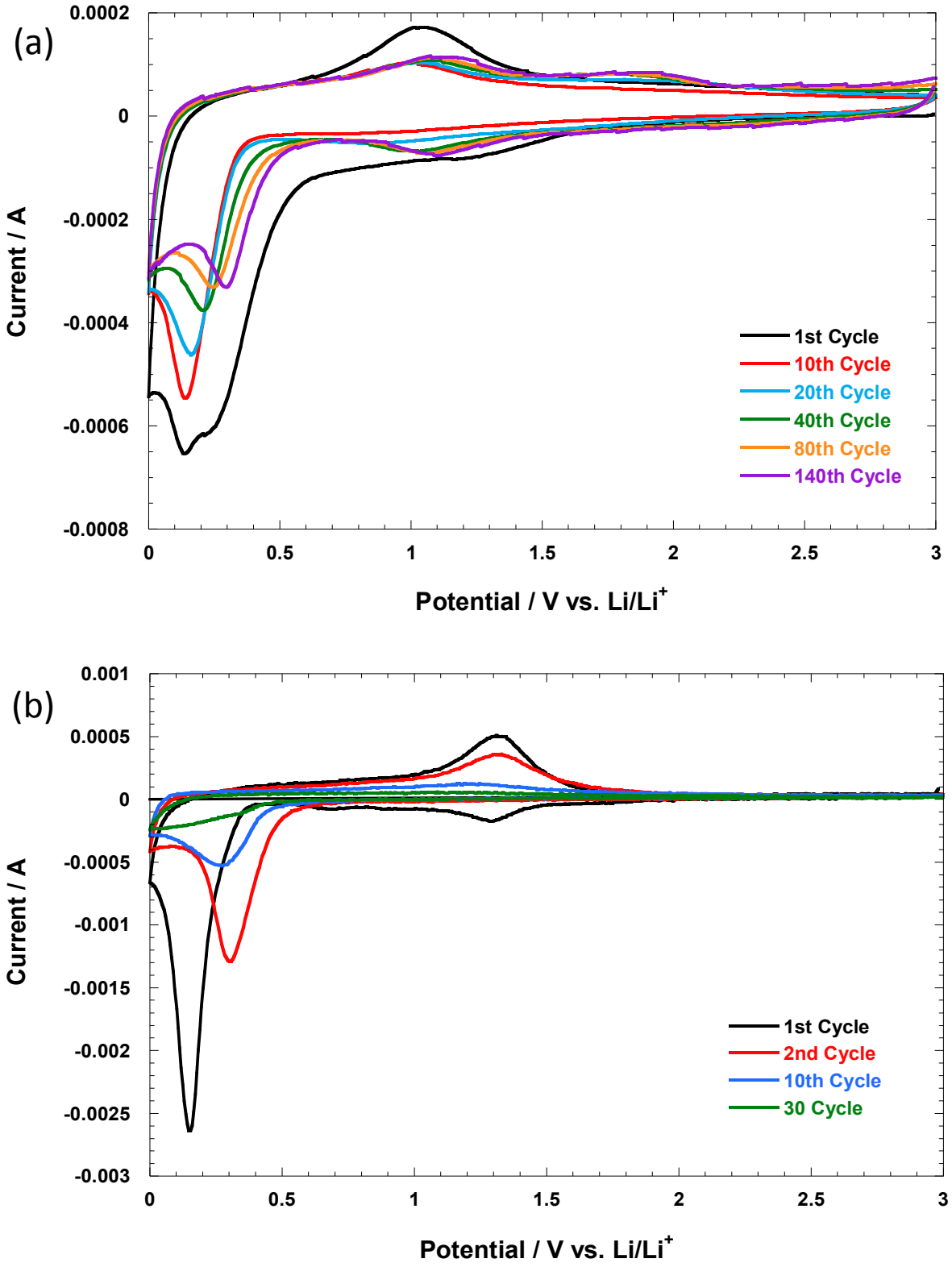


Figure 4.10. Representative cyclic voltammetry curves from continuous cycling of (a) amorphous $MnO_x$-C nanoparticles; and (b) crystalline $MnO_x$ nanoparticles.

The better capacity retention of amorphous $MnO_x$-C nanoparticles over the crystalline $MnO_x$ can be partially attributed to the low volume change of amorphous $MnO_x$ in the conversion reaction in the first lithiation compared with the crystalline $MnO_x$, which could enhance the structure stability of $MnO_x$-C. As shown in the continuous CV scans in Figure 4.10, the conversion reaction of the amorphous $MnO_x$ occurred in a broad potential range while the phase transformation of crystalline $MnO_x$ during conversion reaction occurred in a narrower potential range, indicating lower stress/strain for amorphous $MnO_x$ compared with crystalline $MnO_x$. The low stress/strain was evidenced by the similar lithiation potential in continuous CV cycles of the amorphous $MnO_x$-C shown in Figure 4.10a. In contrast, the lithiation potential of crystalline $MnO_x$ in the second cycle was 0.2 V higher than that in the first lithiation as shown in Figure 4.10b. The increased lithiation potential of crystalline $MnO_x$ after the first lithiation has been widely reported in the literature,[4.7, 4.8, 4.12] and is attributed to the high stress/strain caused by the large volume change of crystalline $MnO_x$ in the conversion reaction. The CV measurements in Figure 4.10 also revealed the different conversion reaction processes of these two electrodes. As demonstrated in the representative curves from the continuous CV scan of amorphous $MnO_x$-C nanoparticles, a broad shoulder gradually appeared at 1.2V and merged to the main reduction peak at 0.2 V in the first reduction process. The reaction current in the potential range between 0.8 V and 0.5 V was reduced in the subsequent cycles due to formation of a stable SEI in the first a few cycles. In addition, the intensity of the main reduction peak at 0.2 V was also reduced in the subsequent cycles. This broad shoulder, and the irreversible portion of the 0.2 V reduction peak could be attributed to the partially irreversible reduction of Mn ions from higher

oxidation state to lower oxidation state and the formation of SEI film. As shown in the CV curve of the first cycle, the Mn (averagely +2.74) in both amorphous and crystalline $MnO_x$ was reduced to Mn(II) at approximately 1.2 V for amorphous $MnO_x$-C and 1.3 V for crystalline $MnO_x$, and further reduced to Mn(0) at approximately 0.2 V in the first lithiation process. The Mn(0) could only be re-oxidized back to Mn(II) in the first delithiation at approximately 1.0 V for amorphous $MnO_x$-C and 1.3 V for crystalline $MnO_x$ particles. It is worth pointing out the pair of redox peaks for amorphous $MnO_x$-C at high potential which gradually appeared after approximately 20 lithiation/delithiation cycles. This redox pair, 1.1 V for lithiation and 1.8V for delithiation, is attributed to the reaction between Mn(II) and high oxidation state Mn. It can be speculated that after a number of cycles, the conversion reaction kinetics in amorphous $MnO_x$-C is improved by formation of defects during the cycling, resulting in a lower overpotential. Therefore, the Mn(II) in amorphous $MnO_x$-C could be re-oxidized back to a higher oxidation state, indicated by the emerging redox peak pair at 1.1 V and 1.8 V. In the contrast, the Mn(II) in crystalline $MnO_x$ could not be re-oxidized to a higher state as shown in Figure 4.10b. The irreversible conversion reaction of crystal $MnO_x$ due to the high phase transformation resistance of crystalline $MnO_x$ has been reported by Chen's group.[4.12] Therefore, it is clear that the conversion reaction of amorphous $MnO_x$-C is more reversible than that of crystalline $MnO_x$.

During the continuous CV cycling (Figure 4.10a), the shape of the two pairs of redox peaks for amorphous $MnO_x$-C gradually changed: the pair of redox peaks at low potential (0.2 V for reduction and 1.0 V for oxidation) became smaller and broader and an new redox pair appeared at high potential (1.1 V for reduction and 1.8 V for oxidation) with

increased number of cycles and the integrated peak area went through a decreasing-increasing-stabilizing process, accompanied with the peak shape change. This evolution might associate with accumulation of defects/strain/stress energy in amorphous $MnO_x$-C particles. Since the integrated peak area was equal to the capacity, the continuous CV cycling behavior of the amorphous $MnO_x$-C nanoparticles was consistent with the decreasing-increasing-stabilizing behavior of the capacity retention curve shown in Figure 4.9a (the "U" shape in the plot). The mechanism behind the "U" shaped capacity retention curve is not clear, but may be attributed to mixed effects of Mn cluster aggregation inside secondary $MnO_x$ particles and reversibility improvement of the conversion reaction in amorphous $MnO_x$ due to formation of defects and deformation. For comparison, the continuous CV cycling of the crystalline $MnO_x$ nanoparticles is shown in Figure 4.10b, which clearly shows an inferior performance: the redox peaks quickly diminished and no new redox pair occurred, and the CV curve became flat after only 30 cycles.

Based on the different structures and electrochemical performance of these two types of manganese oxide particles, it was clear that the high-capacity and superior capacity retention of the amorphous $MnO_x$-C nanoparticles should be attributed to its amorphous nature and unique inter-dispersed $MnO_x$-carbon structure. The conversion reaction of amorphous $MnO_x$ is more reversible, and faster than that of conventional crystalline $MnO_x$ materials. The uniformly inter-dispersed carbon in amorphous $MnO_x$ could function as barriers to prevent the aggregation of the Mn metal grains during the repeated conversion reaction. The carbon could also function as a mixed electron and Li ion conductive environment to improve the kinetics of the conversion reaction, thus resulting

in better rate performance. The high structural stability of amorphous $MnO_x$-C particles was confirmed by the TEM images and XRD analysis of post-cycling amorphous $MnO_x$-C. Figure 4.11a shows the TEM image of the $MnO_x$-C nanoparticle after over 100 cycles. The TEM image demonstrates that the $MnO_x$-C nanoparticles retained the original spherical shape after intensive cycling, while the EDS mapping shown in Figure 4.11b demonstrates that the inter-dispersion of $MnO_x$ and carbon is still uniform, which could be attributed to the role of carbon preventing agglomeration of $MnO_x$ clusters. XRD (Figure 4.12) showed that $MnO_x$-C nanoparticles still retained an amorphous structure after 100 cycles.

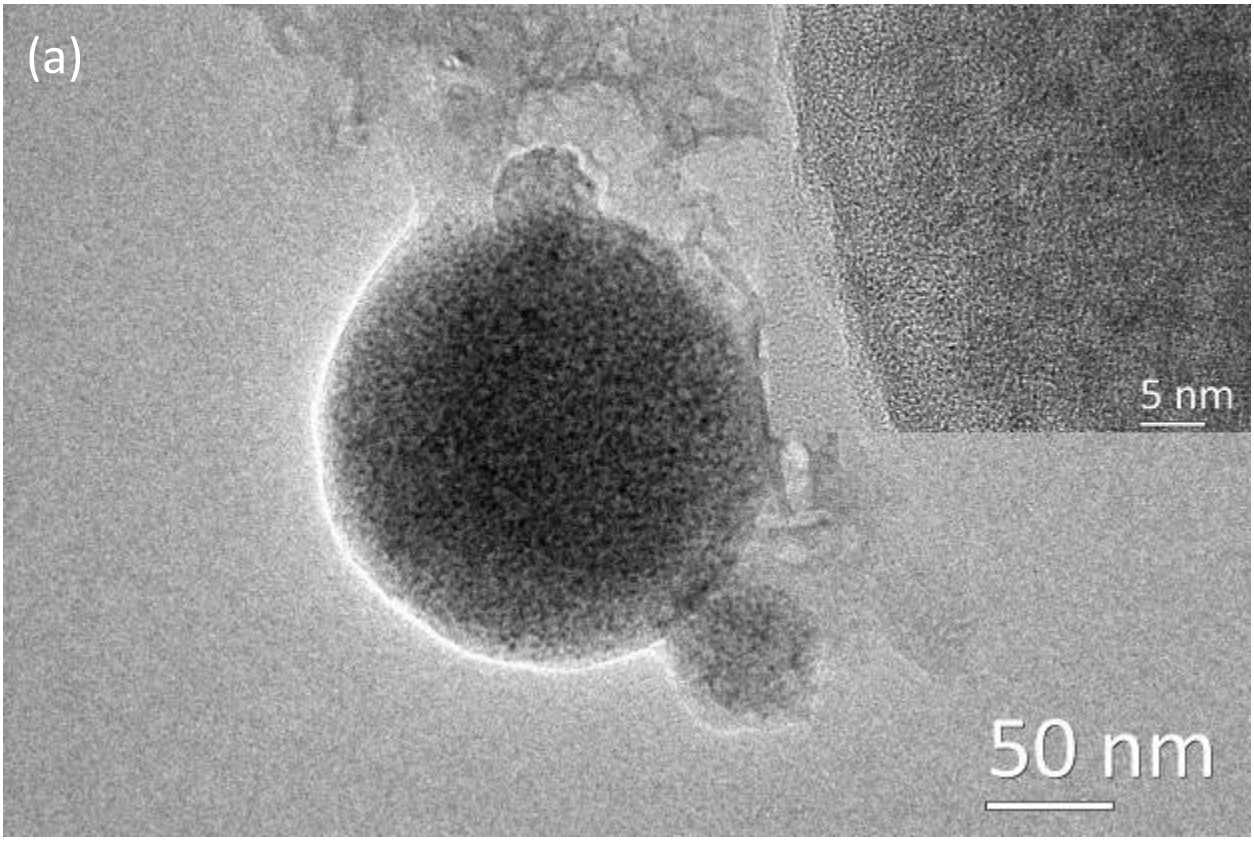

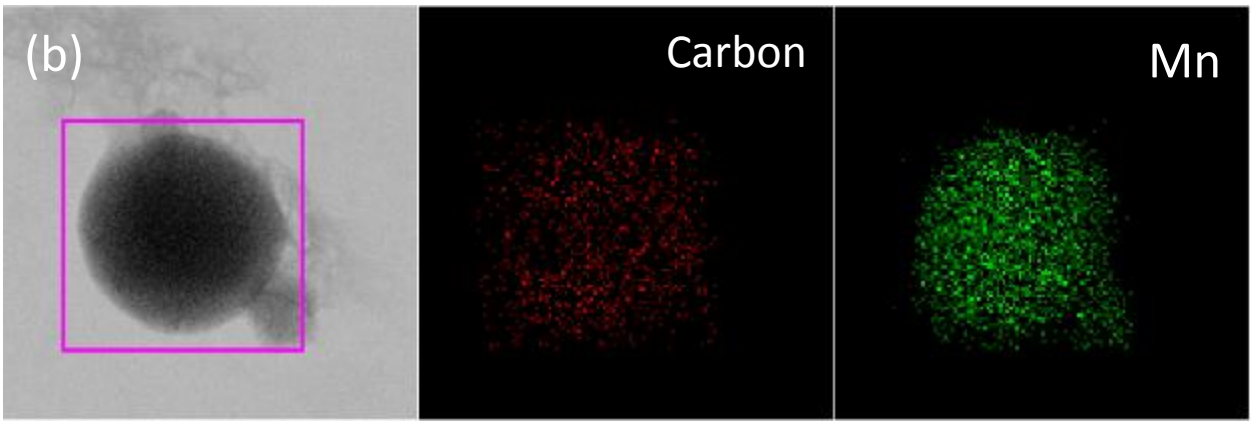


Figure 4.11. (a) TEM images and (b) EDS mapping image of distribution of elemental carbon and Mn of the post-cycling amorphous $MnO_x$-C nanoparticles.

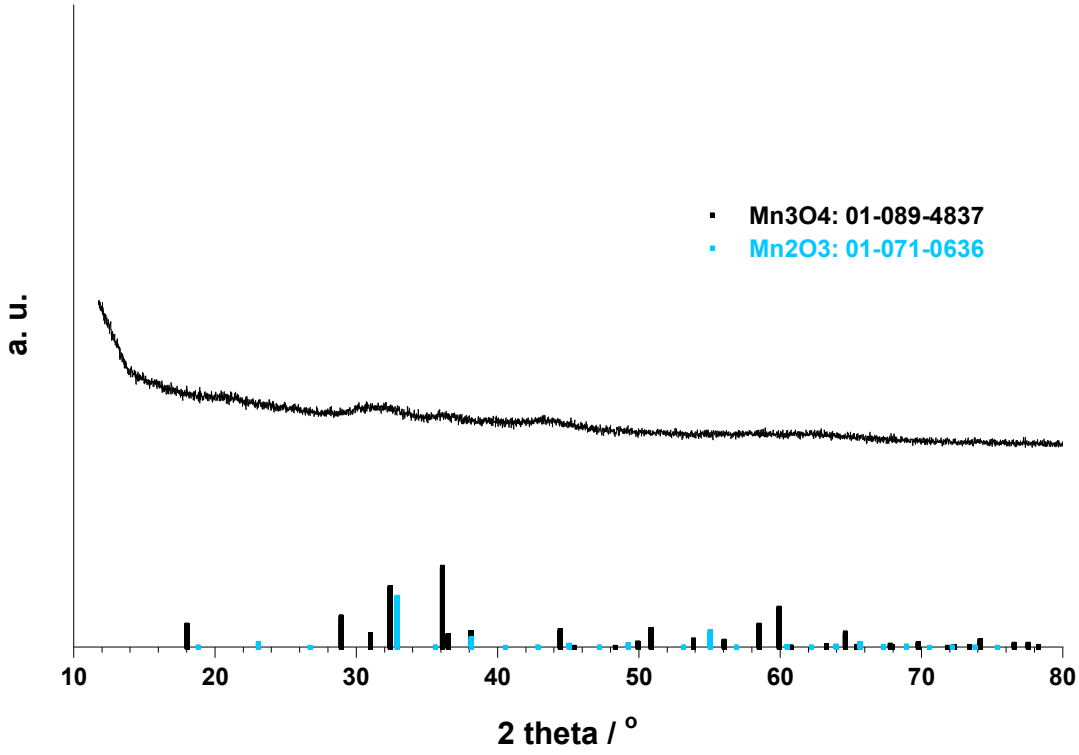


Figure 4.12. XRD pattern of the post-cycling amorphous $MnO_x$-C nanoparticles.

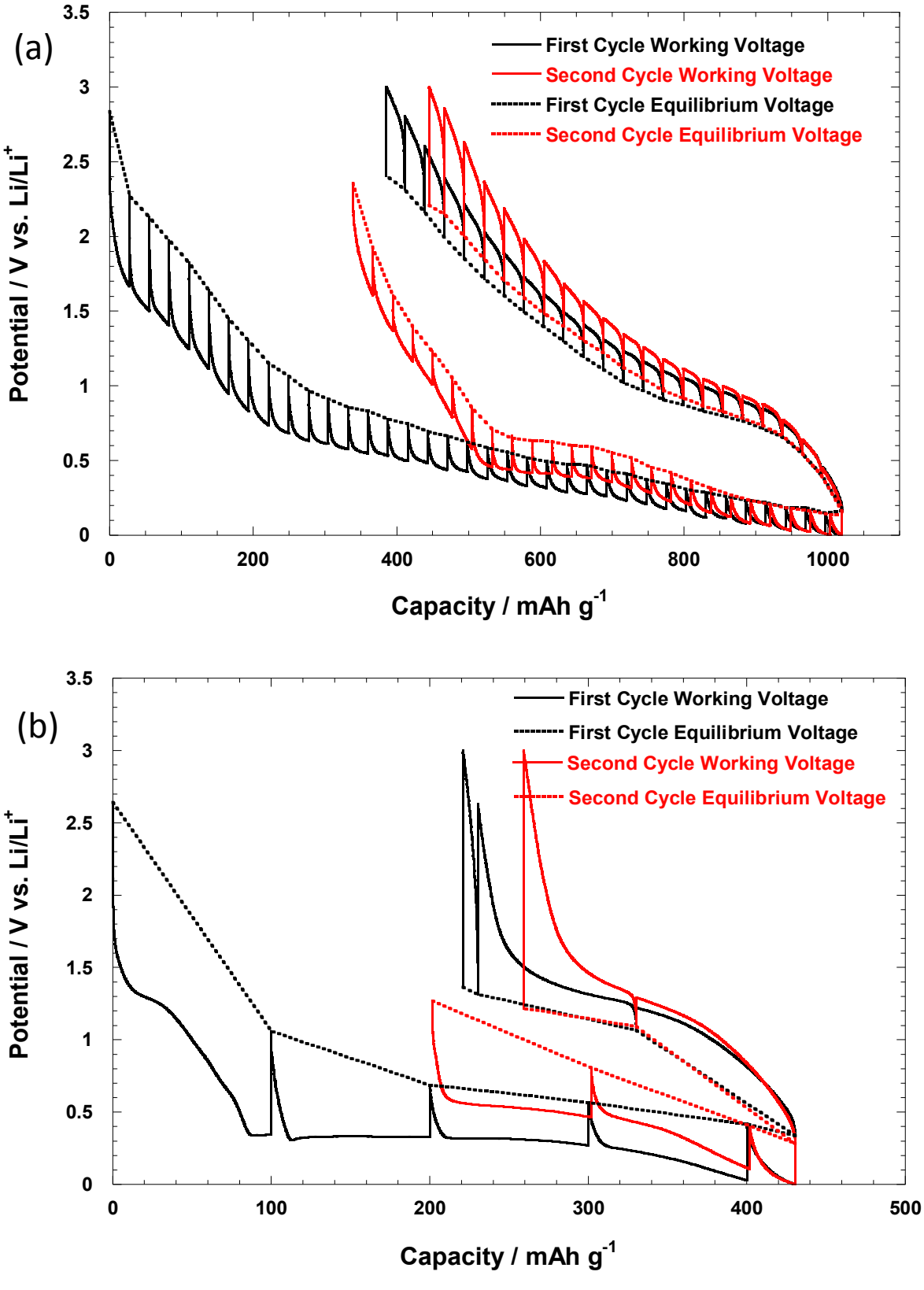


Figure 4.13. GITT curves of (a) amorphous $MnO_x$-C nanoparticles and (b) Crystalline $MnO_x$ nanoparticles.

Since the amorphous structure of $MnO_x$ lowers the resistance for the conversion reaction, and the inter-dispersed carbon in $MnO_x$ accelerates the electron/$Li^+$ conduction and charge-transfer reaction, it can be expected that the amorphous $MnO_x$-C nanoparticles should have faster reaction kinetics than that of crystalline $MnO_x$. The kinetics of the conversion reaction can be correlated to the overpotential, *i.e.* difference between equilibrium charge/discharge voltage and working voltage: inferior kinetics results in higher overpotential. The overpotentials of amorphous $MnO_x$-C and crystalline $MnO_x$ at different lithiation/delithiation levels were investigated using GITT as shown in Figures 4.13a and 4.13b, respectively. In addition to kinetics, GITT can also yield thermodynamic properties such as the equilibrium potential and potential hysteresis.[4.22] The overpotential of the amorphous $MnO_x$-C in the first lithiation gradually decreased with lithiation because (1) the defects and deformation generated from the volume change in initial lithiation decreased the resistance in subsequent lithiation processes, and (2) electronic conductivity of converted phase ($Li_2O$ + Mn) is higher than $MnO_x$. The defects and deformation energy introduced by the first lithiation also decreased the overpotential of amorphous $MnO_x$-C in the second lithiation. A significant result from Figure 4.13a is that the overpotential for both lithiation and delithiation was only approximately 0.2 V (difference between the working voltage and equilibrium voltage), and the previously reported lowest overpotential for manganese oxide was between 0.4 V and 0.5 V.[4.7] The low overpotential resulted in low charge/discharge hysteresis. In contrast, crystalline $MnO_x$ showed a 2X higher overpotential than that of the amorphous $MnO_x$-C nanocomposite, although the former had high contact area between $MnO_x$ and electrolyte, and the particle size of the two materials is nearly the same. Therefore, the amorphous

nature of the $MnO_x$ and the inter-dispersed carbon structure greatly accelerated the conversion reaction.

## 4.4. Conclusion

Amorphous $MnO_x$-carbon nanoparticles were synthesized by a spray pyrolysis as the anode material for Li-ion batteries. The particles have a unique structure with uniform inter-dispersed amorphous manganese oxide and carbon, which provides high capacity and conductivity, respectively. Such a structure effectively accelerates the conversion reaction, prevents the agglomeration of the Mn metal grains during the conversion reaction with Li, thus significantly improving the cyclability. The uniform distribution of carbon improves the electrochemical reaction kinetics, which results in superior rate capacity and lowers over-potentials. The unique structure of the amorphous $MnO_x$-C nanoparticles in this study demonstrates the best anode performance for manganese oxide to date, and introduces spray-pyrolysis as a very promising technique for electrode material production.

## 4.5. Experimental Section

$MnO_x$-C nanoparticles were prepared by a spray pyrolysis method as illustrated in Figure 4.1. Manganese(II) nitrate hydrate (0.716g, Sigma-Aldrich) and sucrose (1.37g, Sigma-Aldrich) was dissolved in 20 mL distilled water. The solution was atomized with argon in a collision-type nebulizer, and subsequently dried with a silica gel diffusion dryer, before entering a tubular furnace at 600°C. The nominal residence time in the heated region is ~ 2 sec. Thermal decomposition of manganese(II) nitrate yields amorphous manganese oxide, and sucrose carbonization. The final product, amorphous $MnO_x$-C nanoparticles were collected on a 0.4 μm (pore size) DTTP Millipore filter. As

comparison, pure crystalline manganese oxide nanoparticles were also synthesized through the same process with no sucrose added in the precursor solution.

Transmission electron microscopy (TEM) and energy-dispersive X-ray spectroscopy (EDS) were performed using a Field Emission Transmission Electron Microscope (JEOL JEM 2100F). X-ray diffraction (XRD) was performed on a Bruker Smart1000 using CuKα radiation. Thermogravimetric analysis (TGA) was carried out (TA instruments) with a heating rate of 10°C $min^{-1}$ in air. The porosity surface area of the $MnO_x$-C nanoparticles was analyzed by nitrogen adsorption measurement (TriStar II 3020). X-ray photoelectron spectroscopy (XPS) was conducted with a high sensitivity Kratos AXIS 165 spectrometer to analyze the oxidation state of the manganese oxide.

The electrode was prepared by mixing the $MnO_x$-C nanoparticles (80 wt.%) with carbon black (10 wt.%) and polyvinylidene fluoride (10 wt.%) in n-methyl-2-pyrrolidone. The obtained ink was coated on a nickel foil (99.5%, Alfa Aesar) current collector, followed by drying in a vacuum oven at 110°C for 24 hrs. Two-electrode coin cells with lithium foil as the counter electrode were assembled in argon-filled glove box. Electrolyte (Novolyte Technologies) consisting of 1M $LiPF_6$ in a mixture of ethylene carbonate/diethyl carbonate (1:1 by volume) was used with a micro-porous polymer membrane separator (Celgard 3501). The cells were charged and discharged between 0 V and 3 V (*vs.* $Li/Li^+$) using an Arbin battery test station. Galvanostatic intermittent titration technique (GITT) were performed by charging/discharging the cell using a current of 100mA/g for 1 hr, and a rest for 16 hrs until the cut-off voltage limits were reached. Prior to post-cycling characterization of the $MnO_x$-C nanoparticles, the cell was charged at 3 V for 48 hrs to ensure full extraction of Li. Cyclic voltammetry (CV) measurements were

carried out with a scan rate of 0.1 mV/s on Solartron 1287/1260 analyzer or Gamry Reference 3000 Potentiostat/Galvanostat/ZRA.

Reference


4.1. Lee, K. T.; Cho, J., Roles of nanosize in lithium reactive nanomaterials for lithium ion batteries. *Nano Today* **2011,** *6* (1), 28-41.

4.2. Li, H.; Shi, L. H.; Lu, W.; Huang, X. J.; Chen, L. Q., Studies on capacity loss and capacity fading of nanosized SnSb alloy anode for Li-ion batteries. *Journal of the Electrochemical Society* **2001,** *148* (8), A915-A922; Zhang, S. S.; Ding, M. S.; Xu, K.; Allen, J.; Jow, T. R., Understanding solid electrolyte interface film formation on graphite electrodes. *Electrochemical and Solid State Letters* **2001,** *4* (12), A206-A208; Li, H.; Shi, L. H.; Wang, Q.; Chen, L. Q.; Huang, X. J., Nano-alloy anode for lithium ion batteries. *Solid State Ionics* **2002,** *148* (3-4), 247-258; Doi, T.; Iriyama, Y.; Abe, T.; Ogumi, Z., Electrochemical insertion and extraction of lithium ion at uniform nanosized Li4/3Ti5/3O4 particles prepared by a spray pyrolysis method. *Chemistry of Materials* **2005,** *17* (6), 1580-1582.

4.3. Li, H.; Wang, Z. X.; Chen, L. Q.; Huang, X. J., Research on advanced materials for Li-ion batteries. *Advanced Materials* **2009,** *21* (45), 4593-4607.

4.4. Poizot, P.; Laruelle, S.; Grugeon, S.; Dupont, L.; Tarascon, J. M., Nano-sized transition-metaloxides as negative-electrode materials for lithium-ion batteries. *Nature* **2000,** *407* (6803), 496-499.

4.5. Li, H.; Balaya, P.; Maier, J., Li-storage via heterogeneous reaction in selected binary metal fluorides and oxides. *Journal of the Electrochemical Society* **2004,** *151* (11), A1878-A1885.

4.6. Li, H.; Richter, G.; Maier, J., Reversible formation and decomposition of LiF clusters using transition metal fluorides as precursors and their application in rechargeable Li batteries. *Advanced Materials* **2003,** *15* (9), 736-739; Debart, A.; Dupont, L.; Poizot, P.; Leriche, J. B.; Tarascon, J. M., A transmission electron microscopy study of the reactivity mechanism of tailor-made CuO particles toward lithium. *Journal of the Electrochemical Society* **2001,** *148* (11), A1266-A1274; Balaya, P.; Li, H.; Kienle, L.; Maier, J., Fully reversible homogeneous and heterogeneous Li storage in $RuO_2$ with high capacity. *Advanced Functional Materials* **2003,** *13* (8), 621-625.

4.7. Yu, X. Q.; He, Y.; Sun, J. P.; Tang, K.; Li, H.; Chen, L. Q.; Huang, X. J., Nanocrystalline MnO thin film anode for lithium ion batteries with low overpotential. *Electrochemistry Communications* **2009,** *11* (4), 791-794.

4.8. Zhong, K.; Xia, X.; Zhang, B.; Li, H.; Wang, Z.; Chen, L., MnO powder as anode active materials for lithium ion batteries. *Journal of Power Sources* **2010,** *195* (10), 3300-3308.

4.9. Liu, J.; Pan, Q., MnO/C Nanocomposites as high capacity anode materials for Li-ion batteries. *Electrochemical and Solid State Letters* **2010,** *13* (10), A139-A142.
4.10. Sun, B.; Chen, Z.; Kim, H.-S.; Ahn, H.; Wang, G., MnO/C core-shell nanorods as high capacity anode materials for lithium-ion batteries. *Journal of Power Sources* **2011,** *196* (6), 3346-3349.
4.11. Nayak, S.; Malik, S.; Indris, S.; Reedijk, J.; Powell, A. K., Pyrolysis of a three-dimensional Mn-II/Mn-III network to give a multifunctional porous manganese oxide material. *Chemistry-a European Journal* **2010,** *16* (4), 1158-1162.
4.12. Fang, X.; Lu, X.; Guo, X.; Mao, Y.; Hu, Y.-S.; Wang, J.; Wang, Z.; Wu, F.; Liu, H.; Chen, L., Electrode reactions of manganese oxides for secondary lithium batteries. *Electrochemistry Communications* **2010,** *12* (11), 1520-1523.
4.13. Toupin, M.; Brousse, T.; Belanger, D., Influence of microstucture on the charge storage properties of chemically synthesized manganese dioxide. *Chemistry of Materials* **2002,** *14* (9), 3946-3952; Wu, M. S.; Chiang, P. C. J.; Lee, J. T.; Lin, J. C., Synthesis of manganese oxide electrodes with interconnected nanowire structure as an anode material for rechargeable lithium ion batteries. *Journal of Physical Chemistry B* **2005,** *109* (49), 23279-23284; Wu, M. S.; Chiang, P. C. J., Electrochemically deposited nanowires of manganese oxide as an anode material for lithium-ion batteries. *Electrochemistry Communications* **2006,** *8* (3), 383-388; Li, B.; Rong, G.; Xie, Y.; Huang, L.; Feng, C., Low-temperature synthesis of alpha-$MnO_2$ hollow urchins and their application in rechargeable $Li^+$ batteries. *Inorganic Chemistry* **2006,** *45* (16), 6404-6410.
4.14. Xia, H.; Lai, M.; Lu, L., Nanoflaky $MnO_2$/carbon nanotube nanocomposites as anode materials for lithium-ion batteries. *Journal of Materials Chemistry* **2010,** *20* (33), 6896-6902.
4.15. Pasero, D.; Reeves, N.; West, A. R., Co-doped $Mn_3O_4$: a possible anode material for lithium batteries. *Journal of Power Sources* **2005,** *141* (1), 156-158; Fan, Q.; Whittingham, M. S., Electrospun manganese oxide nanofibers as anodes for lithium-ion batteries. *Electrochemical and Solid State Letters* **2007,** *10* (3), A48-A51.
4.16. Wang, H.; Cui, L.-F.; Yang, Y.; Casalongue, H. S.; Robinson, J. T.; Liang, Y.; Cui, Y.; Dai, H., $Mn_3O_4$-graphene hybrid as a high-capacity anode material for lithium ion batteries. *Journal of the American Chemical Society* **2010,** *132* (40), 13978-13980.
4.17. Fan, J.; Wang, T.; Yu, C. Z.; Tu, B.; Jiang, Z. Y.; Zhao, D. Y., Ordered, nanostructured tin-based oxides/carbon composite as the negative-electrode material for lithium-ion batteries. *Advanced Materials* **2004,** *16* (16), 1432-; Cheng, F.; Tao, Z.; Liang, J.; Chen, J., Template-directed materials for rechargeable lithium-ion batteries. *Chemistry of Materials* **2008,** *20* (3), 667-681.
4.18. Reddy, A. L. M.; Shaijumon, M. M.; Gowda, S. R.; Ajayan, P. M., Coaxial $MnO_2$/carbon nanotube array electrodes for high-performance lithium batteries. *Nano Letters* **2009,** *9* (3), 1002-1006.
4.19. Ji, L.; Zhang, X., Manganese oxide nanoparticle-loaded porous carbon nanofibers as anode materials for high-performance lithium-ion batteries. *Electrochemistry Communications* **2009,** *11* (4), 795-798.
4.20. Delmer, O.; Balaya, P.; Kienle, L.; Maier, J., Enhanced potential of amorphous electrode materials: Case study of RuO2. *Advanced Materials* **2008,** *20* (3), 501-+.

4.21. Guo, H. J.; Li, X. H.; Zhang, X. M.; Wang, H. Q.; Wang, Z. X.; Peng, W. J., Diffusion coefficient of lithium in artificial graphite, mesocarbon microbeads, and disordered carbon. *New Carbon Materials* **2007,** *22* (1), 7-11.
4.22. Zhu, Y.; Wang, C., Strain accommodation and potential hysteresis of $LiFePO_4$ cathodes during lithium ion insertion/extraction. *Journal of Power Sources* **2011,** *196* (3), 1442-1448.

# Chapter 5. One Step Synthesis of Metal-Encapsulated Carbon Spheres and Its Application to Lithium-Ion Battery

## 5.1 Background

The main challenge in the battery field is to meet the demands for commercial electric vehicles; a significant advance in energy storage density, power density and cycle life is required.[5.1] For this reason, carbon is used as the anode-active material in the current lithium ion rechargeable battery market. Graphite, crystalline state or almost amorphous state, has the advantage of resilience (easy insertion and deinsertion of lithium), relative high capacity (a theoretical capacity of 372 mA h/g to form $LiC_6$) and low cost. Because the graphite anodes' limited capacity is chiefly responsible for the relatively brief charge life of lithium-ion batteries, to improve the storage capacity, research has been expanded to many other types of anode materials.

Compared to cathode materials, which usually have lamellar and spinel crystalline structures ready for intercalation of lithium,[5.2] there are four groups of anode materials in Li-ion chemistry:[5.3]

(1) Carbonaceous materials:

$$Li^+ + e^- + C_6 \Leftrightarrow LiC_6$$

(charging voltage: 0.3 V)

(2) Sn/Si-based alloys and composites:

$$Si(Sn) + 4.4Li^+ + 4.4e^- \Leftrightarrow Li_{4.4}Si(Sn)$$

(charging voltage: 0.5 V for silicon and 0.7 V for tin)

(3) Metal oxide (MO): It is oxidation-reduction conversion in nano-composites, and reversible lithium storage was also observed in transition metal fluorides, sulfides, nitrides and phosphides.[5.4, 5.5]

$$MO + 2Li^+ + 2e^- \Leftrightarrow MO + Li_2O$$

(charging voltage: 0.7 V-1.7 V)

(4) Spinel structure:

*i.e.* $Li_4Ti_5O_{1\ 2} + xLi^+ + xe^- \Leftrightarrow Li_4 + xTi_5O_{1\ 2}$(where x is between 2 and 3)

(charging voltage: 1.6 V)

Comparing these anode materials, it is obvious that the second group is the most attractive anode candidate for lithium batteries because of its highest known theoretical charge capacity and low charging voltage. Though the density of silicon is lower than tin, resulting in a higher potential capacity, silicon synthesis demands very strict conditions,[5.5] so tin material is more feasible to produce by the spray pyrolysis set-up.

To continue the battery research of the last chapter, a tin nanoparticle dispersed carbon matrix is the new material to be created. Because water solution will hydrolyze the tin precursor to form SnO, the following irreversible reaction will decrease the capacity of the materials:

$$2Li + SnO \rightarrow Li_2O + Sn$$

As a result, non-hydrolytic and -oxidative conditions, as well as new carbon sources will be used.

## 5.2 Introduction

As is stated, tin anodes have attracted much attention because they can deliver a capacity up to three times higher than that of graphite.[5.6-5.10] Theoretically, one tin atom

can maximally react with 4.4 lithium atoms to form $Li_{4.4}Sn$ alloy, reaching a capacity of 993 mAh/g.[5.6] However, the large amount of lithium insertion/extraction into/from Sn causes a large volume change (about 300%), which results in pulverization of tin particles, and loss of contact with the current collector, resulting in poor cycling stability.[5.11]

Extensive efforts have been devoted to improve the cycling stability of Sn anodes. The most effective approaches include (1) reducing Sn particle size into the nano-scale (<10 nm) to efficiently mitigate the absolute strain caused by large volume change, and retard particle pulverization;[5.9, 5.12, 5.13] (2) using nano-Sn with a uniform particle size (narrow distribution) that will generate uniform stress/strain over the entire electrode, preventing local cracking;[5.12] (3) uniformly dispersing nano-Sn in a conductive matrix (such as carbon) to accommodate volume change and maintain the mechanical integrity of the composite electrode.[5.9, 5.10] Clearly, a Sn/C composite with uniform tin nano-particles (<10 nm) dispersed in a carbon matrix would be an ideal anode for Li-ion batteries. For example, Scrosati and co-works synthesized a nanostructured Sn/C composite by infiltrating a tin precursor into an organic gel, followed by calcination at a high temperature.[5.9] The nanostructured Sn/C composite can be charged/discharged for more than 100 cycles.[5.9] Very recently, we reported a sponge-like porous C/Sn composite synthesized by dispersing $SnO_2$ nanoparticles into a soft-template polymer matrix followed by carbonization, for which good electrochemical performance was demonstrated.[5.14] However, the low melting point of Sn promotes liquid coalescence, which makes it very difficult to control Sn particle size, to obtain a narrow size distribution, and to uniformly disperse the nano-Sn in the carbon matrix.

In this chapter, we introduce aerosol spray pyrolysis to realize the ideal structure with nano-grain Sn uniformly dispersed in a conductive carbon matrix. The primary success of this method is rooted in the rapid heating of micron size droplets containing the precursors to high temperature, allowing quick formation of Sn nano-grains and carbonization to generate the desired structure. The short residence time and rapid subsequent cooling enables one to freeze the structure to non-aggregated, uniformly sized nano-Sn grains in a carbon matrix. Even though the melting point of Sn is lower than carbonization temperature, Sn nucleation occurs rapidly and grain growth terminates at about 10 nm. In addition, the fast formation of the carbon network is another factor to further prevent Sn grain growth. By contrast, traditional synthesis cannot shorten the heating time to the second level, which inevitably sinters the Sn grains. The Sn/C composite spheres synthesized by aerosol spray pyrolysis, with 10 nm Sn uniformly dispersed in carbon spheres, show a reversible capacity of 710 mAh/g at a current density of 200 mA/g, and are able to maintain 330 mAh/g capacity even at a high current density of 3200 mA/g, and retain capacity of 645 mAh/g after 100 cycles. Such exceptional performance of the Sn/C composite can be attributed to its unique structure: 1) carbon matrix is able to accommodate the stress associated with the large volume change of nano-Sn, thus alleviating pulverization; 2) the carbon matrix prevents Sn nano-particle agglomeration upon prolonged cycling; and 3) carbon network provides high and continuous path for Li-ions and electrons inside the Sn/C composite spheres.

## 5.3 Experimental

### 5.3.1 Synthesis of Sn/C Composite Spheres

Sn/C composite spheres were synthesized by aerosol spray pyrolysis. 0.50 g $SnCl_2$ and 0.40 g Polyvinylpyrrolidone (PVP) were dissolved into 20 ml ethanol. The solution was atomized with argon/5% hydrogen flow by a collision-type nebulizer, and aerosol subsequently dried with a carbon black diffusion dryer (to absorb ethanol), consequently entering tubular furnace at 900 °C, for residence time of ~1 s. Thermal decomposition of tin source and carbonization of polymer yield Sn/C composite spheres, the final product, which was collected on a 0.4 μm (pore size) DTTP Millipore filter.

### 5.3.2 Material Characterization

Scanning electron microscopy (SEM) and transmission electron microscopy (TEM) images were taken by Hitachi SU-70 analytical ultra-high resolution SEM (Japan) and JEOL (Japan) 2100F field emission TEM, respectively. X-ray diffraction (XRD) pattern was recorded by Bruker Smart1000 (Bruker AXS Inc., USA) using CuKα radiation. Thermogravimetric analysis (TGA) was carried out using thermogravimetric analyzer (TA Instruments, USA) with a heating rate of 10°C/min in air. Density measurement of the product aerosol particle was conducted by on-line tandem differential mobility-particle mass analysis (DMA-APM).

### 5.3.3 Electrochemical Measurement

The Sn/C composite was mixed with carbon black and sodium carboxymethyl cellulose (CMC) binder to form a slurry at the weight ratio of 70:15:15. The electrode was prepared by casting the slurry onto copper foil with active material loading of ~1.0

mg/cm$^2$ using a doctor blade and dried in a vacuum oven at 100°C overnight. Coin cells were assembled with lithium foil as the counter electrode, 1M $LiPF_6$ in a mixture of ethylene carbonate/diethyl carbonate (EC/DEC, 1:1 by volume) as the electrolyte, and Celgard®3501 (Celgard, LLC Corp., USA) as the separator. Electrochemical performance was tested using Arbin battery test station (BT2000, Arbin Instruments, USA). Capacity was calculated on the basis of the total mass of the Sn/C composite. Cyclic voltammogram scanned at 0.1 mV/s between 0-3 V was recorded using Solatron 1260/1287 Electrochemical Interface (Solartron Metrology, UK).

## 5.4 Results and Discussion

### 5.4.1 Morphology and Phase Structure

Figure 5.1 shows SEM images of the Sn/C composite synthesized by aerosol spray pyrolysis. The Sn/C composite consists of two types of particles: large sized (>200nm) spheres and nano-sized (<100 nm) particles. Detailed structures of two types of Sn/C particles are shown in the TEM images in Figure 5.2. In the larger size Sn/C spherical particles (Figure 5.2a), uniform-sized nano-tin particles are homogeneously distributed in the carbon matrix. The lighter color in the spheres represents the carbon frame, and the darker color represents the metallic Sn particles. The high resolution TEM images (Figures 5.2b) revealed that the size of nano-Sn particles in the composite spheres is around 10 nm, and a thin layer (~ 10 nm) of carbon is coated on the surface of the Sn/C composite spheres. As for the smaller random-shape particles, a Sn/C core/shell structure can be clearly observed in Figure 5.2a. The different particle structures suggest two different formation processes during aerosol spray pyrolysis, which will be discussed later.

The crystal structure of the Sn/C composite was investigated using XRD (Figure 5.3). All the peaks in the XRD pattern can be well indexed to a tin crystal structure (JCPDS card No.: 862265). No $SnO_2$ is detected in the Sn/C composite because (1) the precursor solution uses ethanol as the solvent, so there is no hydrolysis, which is the primary reason for the formation of $SnO_2$; and (2) spray pyrolysis is conducted in the reduced atmosphere of $Ar/H_2$.

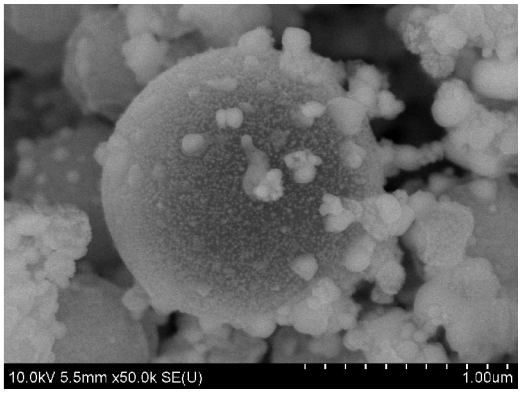

Figure 5.1. SEM image of the Sn/C composite.

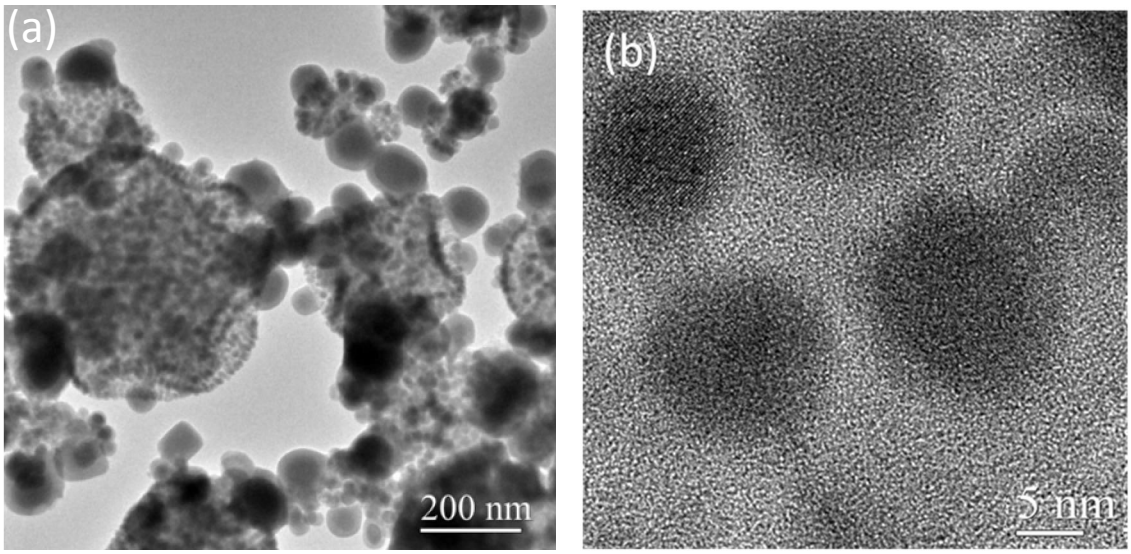

Figure 5.2. TEM images of Sn/C composite. (a) Overall scope view and (b) high resolution images.

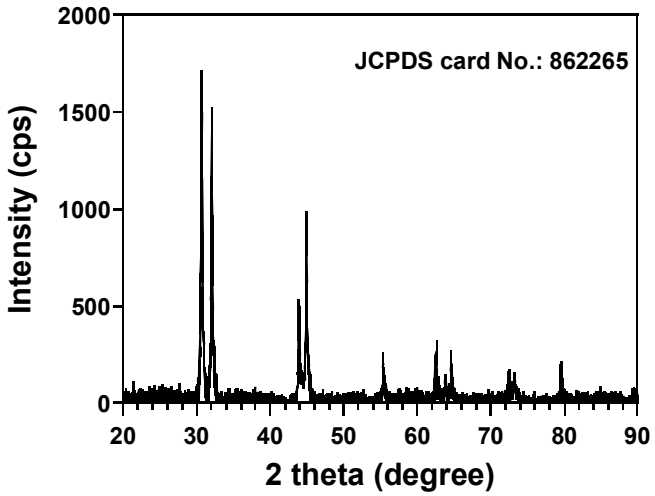


Figure 5.3. XRD diffraction pattern of Sn/C composite. It can be well indexed to crystal tin (JCPDS card No.: 862265).

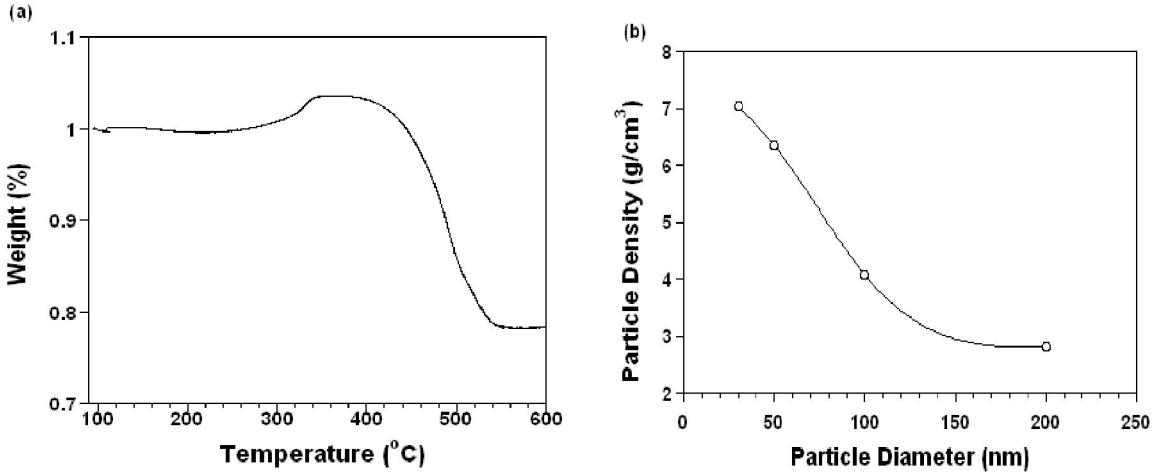


Figure 5.4. (a) Thermogravimetric analysis (TGA) in air and (b) particle density distribution at different particle diameter of the Sn/C composite.

The component of Sn/C composite was analyzed using TGA in air (Figure 5.4a). The results revealed that the component ratio is 62% tin and 38% carbon by weight, assuming that the TGA heating produces $SnO_2$. Since the density of Sn is 7400 kg/m$^3$, and carbon is about 2300 kg/m$^3$, the average density of the dense Sn/C composite should be around 5500 kg/m$^3$ according to the TGA results.

The real particle densities of Sn/C particles with sizes of 30 nm, 50 nm, 100 nm and 200 nm were measured using on-line tandem differential mobility-particle mass

analysis,[5.15, 5.16] are shown in Figure 5.4b. For the small composite particles (<150 nm), the particle density decreases as particle size increases: 7050 kg/m$^3$ for 30 nm, 6400 kg/m$^3$ for 50 nm, to 4050 kg/m$^3$ for 100 nm. While as the particle size is larger than 150 nm, a density of about 2900 kg/m$^3$ was observed. The high density in the small particles implies a high Sn component ratio, while the low density in large particles suggests either less Sn or probably the existence of small pores. Porosity of spray-pyrolysis synthesized particles cannot be easily observed under TEM, or measured by traditional BET methods because the closed pores will not allow $N_2$ access. In a prior work we demonstrated that the tandam DMA-APM method is a more robust measure of porosity since it determines porosity from density rather than permeation (*i.e.* BET).[5.15] The density difference between the larger and smaller particles is consistent with the two different structures shown in TEM images (Figure 5.2a). The smaller Sn/C particles in Figure 5.2a have a large Sn core, and thin carbon shell, resulting in a higher tin fraction, and thus high particle density. However, in the larger spherical Sn/C particles, tin nano-particles are dispersed in carbon matrix, which having a higher volume fraction of carbon results in lower density. Since the Sn/C composite on a mass basis consists primarily of larger size particles, the electrochemical performance of Sn/C composites would be dominant by the large particles.

### 5.4.2 Formation Mechanism of Two Types of Sn/C Composites

Two possible formation mechanisms are proposed to account for the two classes of material created here and summarized in Figure 5.5. It has been reported that metal or metal salt is required in the precursor solution to produce carbon materials by spray pyrolysis.[5.17] In this case, Sn grains function as a catalyst to promote the formation of

carbon. As the aerosol, which is a solid due to solvent evaporation, flows into the high temperature furnace at 900°C, $SnCl_2$ is reduced to Sn under the $Ar/H_2$ environment. The Sn nuclei grow through diffusion-coalescence processes since the Sn is molten at this point. Simultaneously, one expects the polymer pyrolysis and de-hydrogenations leads to carbon formation. The short residence time (~1 s) in the high-temperature furnace minimizes the time for the Sn nuclei to grow. The aerosol generator does not create monodisperse droplets. It appears that the larger droplets adopt a different morphology. Traditionally, it was thought that solvent evaporation in larger droplets would lead to an increase in solute concentration locally, resulting in local precipitation. And Sn nuclei do not sinter to a core, which is more likely in the smaller Sn/C particles, because (1) longer pathway (than that for the smaller Sn/C particles) combining with short residence time suppress the sintering, and (2) more catalytic sites accelerate the carbon frame formation which will further attenuate the diffusion of Sn. In this case this will results in, if the structure does not collapse, a less dense material with a higher carbon proportion.

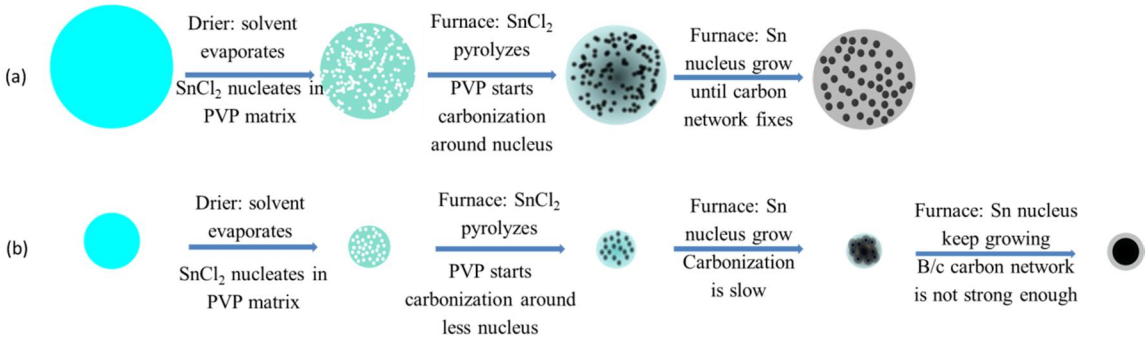


Figure 5.5. Schematic formation processes of (a) ultra-small nano-Sn dispersed carbon spheres and (b) Sn/C core-shell particles.

### 5.4.3 Electrochemical Performance

The electrochemical performance of the Sn/C composite electrodes was investigated in coin cells using lithium as the counter electrode; experiments and Figure analyses were

conducted by Dr. Yunhua Xu. Figure 5.6a shows cyclic voltammograms of the initial 5 cycles at a scan rate of 0.1 mV/s between 0 V and 3 V. Three small reduction peaks at 0.2 V, 0.37 V and 0.57 V, respectively, are assigned to the lithium insertion into tin to form a $Li_xSn$ alloy. Oxidation peaks at 0.53 V, 0.67 V and 0.8 V, respectively, corresponds to the delithiation reaction of $Li_xSn$ alloy. The broad anodic peak at 1.2 V represents lithium extraction from carbon.[5.8, 5.14] The difference in the cathodic scan between the first cycle and the consequent cycles is mainly attributed to the decomposition of the electrolyte to form solid-electrolyte interface (SEI) film. The unchanged peak current intensity except the first cycle implies good cycling stability of the Sn/C composite. The voltage profiles of Sn/C anodes in the initial three charge/discharge cycles between 0.02 and 3.0 V at the current density of 200 mA/g are shown in Figure 5.6b. The first lithiation delivers a capacity of 1029 mAh/g and 69% of the inserted Li can be reversible delithiated, providing charge capacity of 710 mAh/g. The first delithiation capacity is closed to the theoretical capacity of 756 mAh/g if we assume carbon delivers the capacity of 372 mAh/g. The capacity loss of 319 mAh/g in the first cycle is attributed to the formation of SEI (solid electrolyte interphase) film. The repeatable charge/discharge curves after the first cycle demonstrate a good cycling stability.

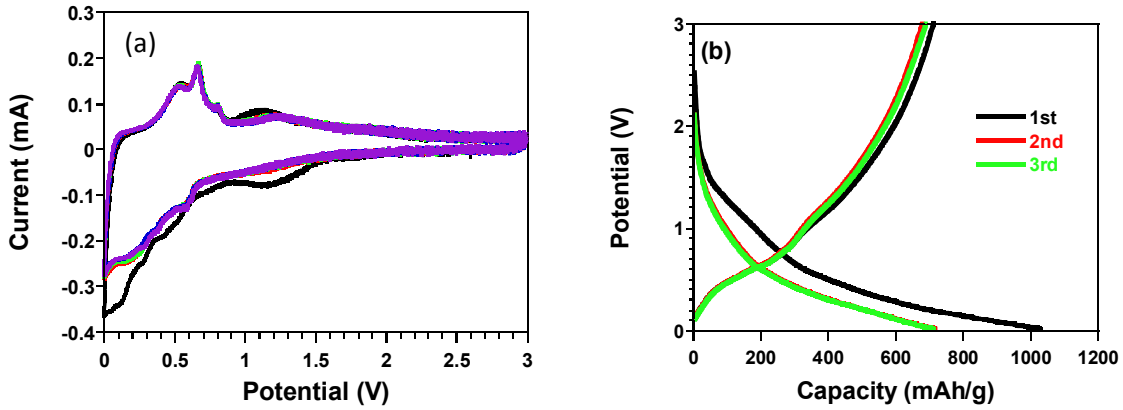

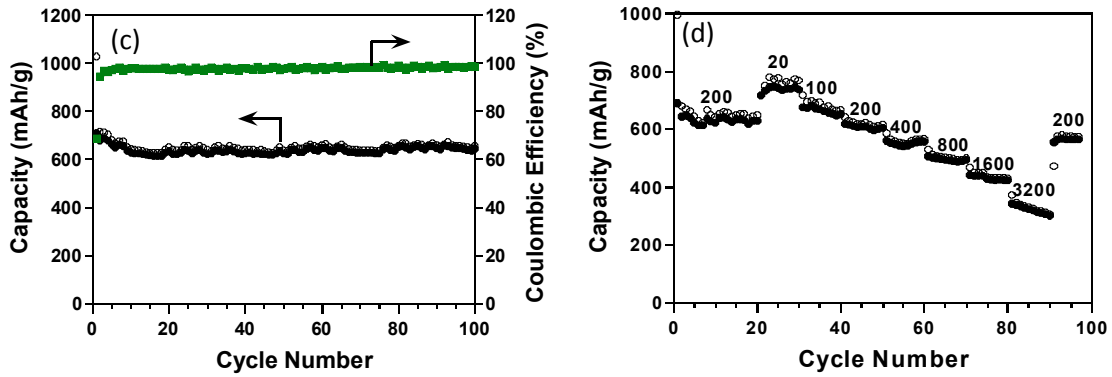


Figure 5.6. (a) Cyclic voltammograms of initial 5 cycles scanned between 0 – 3 V at a rate of 0.1 mV/s (black: 1st cycle), (b) charge/discharge profiles at the initial three cycles, (c) cycling performance at 0.02 – 3 V and 200 mA/g, and (d) rate capability at different current density of the Sn/C composite.

The long cycling stability of the Sn/C composite was investigated by charging/discharging the coin cell between 0.02 and 3.0 V at the current density of 200 mA/g. As shown in Figure 5.6c, after a slight decrease in the initial 10 cycles, the capacity stabilizes at ~ 640 mAh/g up to 100 cycles, corresponding to 91% of the first delithiation capacity. The columbic efficiency approaches 100% except the initial 10 cycles, showing excellent reversibility of the Sn/C composite. The rate capability of Sn/C composite anodes was also examined at different current densities and shown in Figure 5.6d. High capacity retention was observed with increasing current density. Even at a very high current density of 3200 mA/g, Sn/C composite anodes can still retain 330 mAh/g, which is comparable with the theoretical value of widely used graphite on market and superior to those previously reported Sn/C composite anodes.[5.18]

The morphology changes during charge/discharge cycles were investigated using TEM. Figure 5.7 shows the TEM images of the Sn/C composite anodes after 50 full charge/discharge cycles at 200 mA/g between 0.02 and 3.0 V. In comparison to the morphology before cycling shown in Figure 5.2, no obvious change was observed after charge/discharge cycles. The spherical shape of the C/Sn spheres was sustained as a

whole integration structure, suggesting that the carbon matrix can effectively accommodate the volume change and alleviate the strain during the insertion/deinsertion reactions. We also observe that the small tin nanoparticles still retain Sn/C composite morphology with a uniform distribution (Figure 5.7 left), indicating that the pulverization and aggregation commonly observed for tin-based anode materials were substantially reduced.

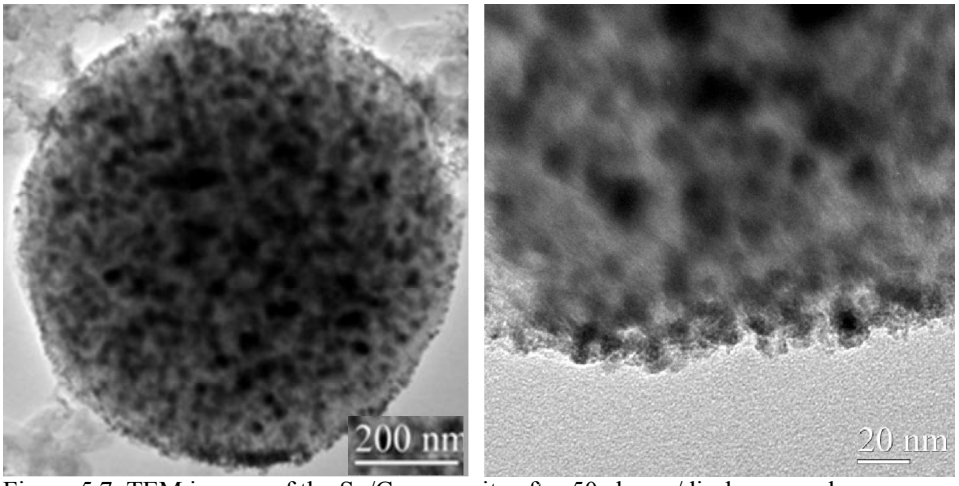

Figure 5.7. TEM images of the Sn/C composite after 50 charge/discharge cycles.

The superior cycling performance and rate capability are attributed to three unique features of the Sn/C composite spheres. The first is the ultra-small size of tin nano-particles. It has been shown that reduced particle size can significantly reduce the strain and improve electrochemical property of electrode materials. The second is the carbon frame combining with porous structure, which acts to release strain, accommodating large volume change, preventing metal aggregation and generating a balanced stress over the whole composite particles and electrode over repeated cycling. Finally, carbon network, which provides continuous path for both Li-ions and electrons with less resistance, makes the material more promising, in terms of rate capability.

## 5.5 Conclusion

Sn/C composites were synthesized using aerosol spray pyrolysis as anode material for lithium-ion batteries. Due to the fast carbonization of the carbon precursor under the catalytic effects of metallic Sn and very short carbonization time at high temperatures during the aerosol spray pyrolysis process, ultra-small Sn grains with a uniform size were homogenously dispersed in a carbon sphere matrix. The unique structure can effectively alleviate stress and accommodate large volume changes, as well as prevent the pulverization and agglomeration of Sn grains upon prolonged cycling. The Sn/C composite showed a reversible capacity of 710 mAh/g, and retained 91% of the initial capacity after 100 charge/discharge cycles at 200 mAh/g, which is superior to the Sn/C composite anodes reported in the literature using other techniques. Meanwhile, the synthesis of aerosol spray pyrolysis is a widely used technique for commercial nano-materials and easily scaled up, making the Sn/C composite much more promising and attractive as an anode material for lithium-ion batteries.

## Reference


5.1. Kasavajjula, U.; Wang, C. S.; Appleby, A. J., Nano- and bulk-silicon-based insertion anodes for lithium-ion secondary cells. *Journal of Power Sources* **2007,** *163* (2), 1003-1039.

5.2. Si, Y. C.; Zhao, L.; Yu, Z. B.; Wang, W. K.; Qiu, J. Y.; Yang, Y. S., A novel amorphous $Fe_2V_4O_{13}$ as cathode material for lithium secondary batteries. *Materials Letters* **2012,** *72*, 145-147.

5.3. Marom, R.; Amalraj, S. F.; Leifer, N.; Jacob, D.; Aurbach, D., A review of advanced and practical lithium battery materials. *Journal of Materials Chemistry* **2011,** *21* (27), 9938-9954.

5.4. Li, H.; Richter, G.; Maier, J., Reversible formation and decomposition of LiF clusters using transition metal fluorides as precursors and their application in

rechargeable Li batteries. *Advanced Materials* **2003,** *15* (9), 736-739; Badway, F.; Cosandey, F.; Pereira, N.; Amatucci, G. G., Carbon metal fluoride nanocomposites - High-capacity reversible metal fluoride conversion materials as rechargeable positive electrodes for Li batteries. *Journal of the Electrochemical Society* **2003,** *150* (10), A1318-A1327; Badway, F.; Pereira, N.; Cosandey, F.; Amatucci, G. G., Carbon-metal fluoride nanocomposites - Structure and electrochemistry of $FeF_3$ : C. *Journal of the Electrochemical Society* **2003,** *150* (9), A1209-A1218; Pereira, N.; Klein, L. C.; Amatucci, G. G., The electrochemistry of $Zn_3N_2$ and LiZnN - A lithium reaction mechanism for metal nitride electrodes. *Journal of the Electrochemical Society* **2002,** *149* (3), A262-A271; Silva, D. C. C.; Crosnier, O.; Ouvrard, G.; Greedan, J.; Safa-Sefat, A.; Nazar, L. F., Reversible lithium uptake by $FeP_2$. *Electrochemical and Solid State Letters* **2003,** *6* (8), A162-A165; Wang, Y.; Fu, Z. W.; Yue, X. L.; Qin, Q. Z., Electrochemical reactivity mechanism of $Ni_3N$ with lithium. *Journal of the Electrochemical Society* **2004,** *151* (4), E162-E167.

5.5. Okamoto, H.; Sugiyama, Y.; Nakano, H., Synthesis and modification of silicon nanosheets and other silicon nanomaterials. *Chemistry-a European Journal* **2011,** *17* (36), 9864-9887.

5.6. Winter, M.; Besenhard, J. O., Electrochemical lithiation of tin and tin-based intermetallics and composites. *Electrochimica Acta* **1999,** *45* (1-2), 31-50.

5.7. Lee, K. T.; Jung, Y. S.; Oh, S. M., Synthesis of tin-encapsulated spherical hollow carbon for anode material in lithium secondary batteries. *Journal of the American Chemical Society* **2003,** *125* (19), 5652-5653; Kim, I. S.; Blomgren, G. E.; Kumta, P. N., Sn/C composite anodes for Li-ion batteries. *Electrochemical and Solid State Letters* **2004,** *7* (3), A44-A48; Zhang, W. M.; Hu, J. S.; Guo, Y. G.; Zheng, S. F.; Zhong, L. S.; Song, W. G.; Wan, L. J., Tin-nanoparticles encapsulated in elastic hollow carbon spheres for high-performance anode material in lithium-ion batteries. *Advanced Materials* **2008,** *20* (6), 1160-; Kim, M. G.; Sim, S.; Cho, J., Novel core-shell Sn-Cu anodes for lithium rechargeable batteries prepared by a redox-transmetalation reaction. *Advanced Materials* **2010,** *22* (45), 5154-.

5.8. Jung, Y. S.; Lee, K. T.; Ryu, J. H.; Im, D.; Oh, S. M., Sn-carbon core-shell powder for anode in lithium secondary batteries. *Journal of the Electrochemical Society* **2005,** *152* (7), A1452-A1457.

5.9. Derrien, G.; Hassoun, J.; Panero, S.; Scrosati, B., Nanostructured Sn-C composite as an advanced anode material in high-performance lithium-ion batteries. *Advanced Materials* **2007,** *19* (17), 2336-+; Hassoun, J.; Derrien, G.; Panero, S.; Scrosati, B., A nanostructured Sn-C composite lithium battery electrode with unique stability and high electrochemical performance. *Advanced Materials* **2008,** *20* (16), 3169-3175.

5.10. Yu, Y.; Gu, L.; Zhu, C. B.; van Aken, P. A.; Maier, J., Tin nanoparticles encapsulated in porous multichannel carbon microtubes: Preparation by single-nozzle electrospinning and application as anode material for high-performance Li-based batteries. *Journal of the American Chemical Society* **2009,** *131* (44), 15984-+.

5.11. Mao, O.; Dunlap, R. A.; Dahn, J. R., Mechanically alloyed Sn-Fe(-C) powders as anode materials for Li-ion batteries - I. The $Sn_2Fe$-C system. *Journal of the Electrochemical Society* **1999,** *146* (2), 405-413; Li, H.; Shi, L. H.; Lu, W.; Huang, X. J.; Chen, L. Q., Studies on capacity loss and capacity fading of nanosized SnSb alloy

anode for Li-ion batteries. *Journal of the Electrochemical Society* **2001,** *148* (8), A915-A922; Courtney, I. A.; McKinnon, W. R.; Dahn, J. R., On the aggregation of tin in SnO composite glasses caused by the reversible reaction with lithium. *Journal of the Electrochemical Society* **1999,** *146* (1), 59-68.

5.12. Wang, Y.; Lee, J. Y.; Deivaraj, T. C., Tin nanoparticle loaded graphite anodes for Li-ion battery applications. *Journal of the Electrochemical Society* **2004,** *151* (11), A1804-A1809.

5.13. Li, H.; Shi, L. H.; Wang, Q.; Chen, L. Q.; Huang, X. J., Nano-alloy anode for lithium ion batteries. *Solid State Ionics* **2002,** *148* (3-4), 247-258.

5.14. Xu, Y. H.; Guo, J. C.; Wang, C. S., Sponge-like porous carbon/tin composite anode materials for lithium ion batteries. *Journal of Materials Chemistry* **2012,** *22* (19), 9562-9567.

5.15. Liu, Q.; Ma, X.; Zachariah, M. R., Combined on-line differential mobility and particle mass analysis for determination of size resolved particle density and microstructure evolution. *Microporous and Mesoporous Materials* **2012,** *153*, 210-216.

5.16. Ehara, K.; Hagwood, C.; Coakley, K. J., Novel method to classify aerosol particles according to their mass-to-charge ratio - Aerosol particle mass analyser. *Journal of Aerosol Science* **1996,** *27* (2), 217-234; Lall, A. A.; Ma, X. F.; Guha, S.; Mulholland, G. W.; Zachariah, M. R., Online nanoparticle nass neasurement by combined aerosol particle mass analyzer and differential mobility analyzer: Comparison of theory and measurements. *Aerosol Science and Technology* **2009,** *42* (11), 1075-1083.

5.17. Sunkara, B.; Zhan, J. J.; Kolesnichenko, I.; Wang, Y. Q.; He, J. B.; Holland, J. E.; McPherson, G. L.; John, V. T., Modifying metal nanoparticle placement on carbon supports using an aerosol-based process, with application to the environmental remediation of chlorinated hydrocarbons. *Langmuir* **2011,** *27* (12), 7854-7859.

5.18. Li, X. F.; Dhanabalan, A.; Gu, L.; Wang, C. L., Three-dimensional porous core-shell Sn@carbon composite anodes for high-performance lithium-ion battery applications. *Advanced Energy Materials* **2012,** *2* (2), 238-244.

# Chapter 6. Determination of Size-Resolved Particle Density and Microstructure Evolution

## 6.1 Introduction

Nanoparticles are being explored for a wide range of applications including their use in medicine, electronics, biomaterials and energy production. One important sub-class of nanomaterials is porous particles that usually possess very high surface/volume ratio, and can be applied to drug delivery, absorbants or catalysts.[6.1] For example, iron oxide is being considered as a vehicle for drug delivery because its magnetic properties enable heating, directed motion, as well as *in-vivo* monitoring.[6.2]

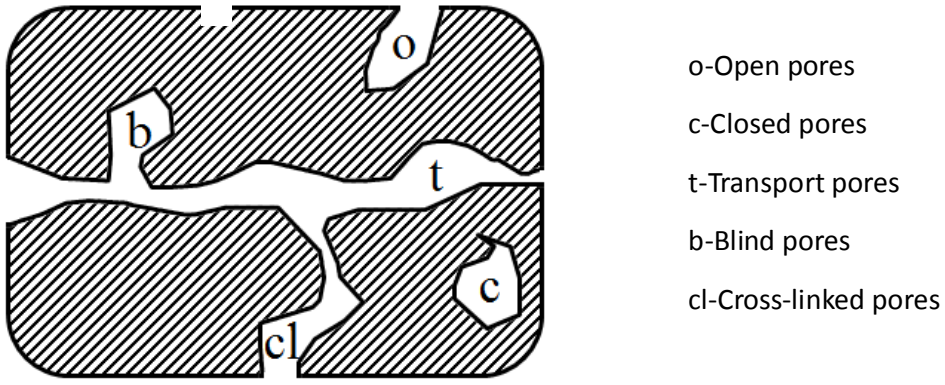


Figure 6.1. Cross-section of porous material.

Table 6.1. Definitions of porous structures.

| | |
|---|---|
| Open pore | cavity or channel with access to the surface |
| Blind pore (dead-end pore) | pore with a single connection to the surface |
| Closed pore | cavity not connected to the surface |
| Total porosity | ratio of volume of voids and pores(open and closed) to volume occupied by solid |
| Open porosity | ratio of volume of voids and open pores to volume occupied by solid |

Figure 6.1 and Table 6.1 give important definitions and characteristics of different types of porous materials. Characterization of porous solids and powders includes surface area, pore size and density measurement. Usually, pore size and surface area can be characterized by mercury porosimetry or by gas adsorption methods such as the Brunauer-Emmett-Teller (BET) approach. Mercury porosimetry can typically be applied over the range of 3.5 nm to 500 μm. However, it requires that the material be inert to mercury, and care must be taken to prevent creation of artificial pores due to powder packing. This leads to difficulties in characterizing fine spray-dried powders and small-pore containing samples.

The most common gas for adsorption measurements is nitrogen. However, it is sufficiently large so as to prevent penetration into the smallest pores of interest, and has been shown to be inaccurate for measuring low-surface-area materials.[6.3] Some other alternative gases such as water or other dipole molecules can enter very small pores, but the possibility of chemisorption makes the analysis more complicated.[6.4] Because the BET method requires an absorption model, the resulting extracted surface area and pore volume is highly dependent on the microscopic model employed and its validity for the specific system. As such the method itself suffers from significant errors in absolute accuracy but is comparatively sensitive to changes within a given material system. The hysteresis loop of adsorption isotherms is also used to determine the pore size, and as an indicator of pore connectivity. However, the isotherms are complex to analyze due to the mixture of pore types and a wide pore size distribution typically found in porous materials.

Though the porosity of a material can be estimated by adsorption methods, the disagreement with the calculated specific surface area can be very large.[6.5] The uncertainty again comes from the model assumptions for the BET method: That the Kelvin equation is applicable over the complete mesopore range; the meniscus curvature is controlled by the pore size and shape; the pores are rigid and of well-defined shape; the filling or emptying of each pore does not depend on its location within the network; the adsorption on the pore walls proceeds in exactly the same way as on the corresponding open surface. Finally, the universal limitation of all adsorption methods is that the closed pores are not accessible to the absorbants. Therefore, the porosity induced from these methods is the open porosity only, not the total porosity.

Another important property is density, which requires measurements of mass and volume. The challenge is that it is difficult to measure the volume directly from the geometry of the object if the sample has an irregular shape, or by fluid displacement if the sample is a fine powder. There are density measurement methods for the liquid sample, including pycnometery and hydrometery.[6.6] However, the measurement of density in nanoparticles is still an intriguing topic of research.

In this chapter, a material-independent method to measure the particle density by direct measurement of the mass and volume of particles is developed. The measurement employs two different electrostatic manipulations of particles in the series, which separately measures the size and mass. For porous particles of the type explored in this chapter, it also allows us to determine porosity of the sample with a

much higher accuracy than with that from BET methods and it can do so regardless the external accessibility of the pores. The method of this work has already been described in previous chapters.

## 6.2 Measurement Methodology

The two methods to be employed in series to determine porosity and pore volume both employ charged particles that are manipulated within a static electric field with either drag (DMA), or centrifugal (APM) as the balancing opposing force.

### A. Differential Mobility Analysis ( DMA)

The DMA operates by selecting particles based on a balance of electrical and drag forces.[6.7] Particles exit the DMA based on a balance of electrical ($F_E$) drag forces ($F_D$).

$$F_D = F_E \Rightarrow \frac{3\pi\mu d_p}{C_c}\upsilon = neE \qquad (6.1)$$

Where $n$ is the number of charges (n=1 in our analysis), $e$ is the unit of charge, $E$ is electrical field strength, $\mu$ is the gas viscosity, $Cc$ is the velocity slip correction factor, needed for particle in the free molecule flow, and $v$ is particle velocity.

Equation 6.1 shows a unique relationship exists between the particle mobility diameter, the measured velocity, and the applied electric field. At the fixed electrostatic field only one mobility size will exit the instrument which can either be counted or sent to another instrument for further characterization. More detailed discussion on DMA operation was previously reported by Kim et al.[6.8]

When employing ion-mobility methods, particles are first charged to a Boltzmann charge distribution by exposing the nanoparticle aerosol to a Po-210 radiation source.

This enables a known charge distribution on particles, and for fine particles such as those in this study we work with singly charged particles.[6.8]

B. Aerosol Particle Mass Analyzer (APM).

The second instrument employed is an Aerosol Particle Mass Analyzer (APM).[6.9] The APM operates by balancing electrostatic and centrifugal forces, such that at a fixed applied electric field and rotation speed particles of only one mass will pass through the instrument.

$$m\omega^2 r_a = \frac{qV}{r_a \ln(r_2 / r_1)} \Rightarrow \frac{m}{q} = \frac{V}{\ln(r_2 / r_1) r_a^2 \omega^2} \qquad (6.2)$$

Where $m$ is the particle mass, $\omega$ is the APM angular speed, $V$ is the applied voltage, $q$ is the particle charge, $r_1$, $r_2$ and $r_a$ are inner, outer and rotating radii at the equilibrium, respectively.

This instrument provides a direct relationship between applied voltage, rotation speed and the particle mass, and effectively operates as a mass spectrometer.

C. Combining the DMA and APM

As discussed above, the DMA directly measured mobility diameter, which for a sphere yields particle volume. The APM directly measures mass. The combination of volume and mass provides a density.

In prior work, we have measured the density of solid particles[6.10] to understand the mechanism of kinetics and mechanisms of metal nanoparticle oxidation.[6.10, 6.11] Recently, this method has also been extended to density measurement of non-solid particles, such as carbon nanotubes[6.12] and silica-aggregated particles.[6.13]

In prior work, we have estimated the uncertainties of the combined DMA-APM system. The theoretical uncertainty is estimated to be 5%, which is based on the transfer functions of the DMA, and APM.[6.10, 6.11] Our prior experimental work on density measurements of reference particles yields an uncertainty of 4%[6.12] and mass measurements on NIST SRM 60nm and 100nm PSL spheres using combined DMA-APM were within about 1.4% and 5.6%, respectively.[6.14]

A combined DMA-APM approach to measure the density of porous particles is implemented in this work, compare with BET results, and use the results to conjecture a mechanism of formation. We note that while the particles being characterized in a recreated aerosol phase, the methodology can be implemented on particles dispersed in liquid phase by electrospray generation.[6.15] One significant advantage of this method is that the measurement method does not depend on the composition of the material but only on its physical parameters (volume and mass).

## 6.3 Experimental Approach

The experiment system consists of two parts: 1) material preparation, and 2) size and mass measurement. In addition, transmission electron microscopy (TEM, JEM 2100 FEG), X-ray diffraction (XRD, Powder Diffractometers for Materials Characterization) and Brunauer-Emmett-Teller (BET, TriStar II 3020) analysis are used to confirm some of our findings and contrast results.

### 6.3.1 Preparations of Porous $Fe_2O_3$ Nanoparticles

To demonstrate the method, a reliable source of porous material is needed, which is adapted from my prior work in chapter 2 on synthesis of porous iron oxide by spray-pyrolysis methods. A 0.2 M aqueous solution of iron (III) nitrate nonahydrate is sprayed using a collision-type nebulizer. The initial mean droplet size is about 1 μm in diameter as in our previous work.[6.16] The droplets are dried by passing them through a silica gel diffusion dryer. The aerosol is then passed through a tube furnace with temperatures set from 100 °C to 600 °C to decompose the precursor and create the porous iron oxide. Particles exiting the aerosol reactor are then collected on a 0.4 μm DTTP Millipore filter for the XRD and TEM characterization, or are directly sampled by the tandem DMA-APM system for analysis.

### 6.3.2 Preparation of Hollow Copper Complex Nanoparticles

A 0.2M aqueous solution of Copper (II) nitrate is sprayed with the nebulizer, and the aerosol droplets pass through a diffusion drier and a 600 °C furnace. Particles are collected on the filter for the XRD and TEM characterization, or are directly sampled by the tandem DMA-APM system for analysis.

### 6.3.3 Tandem DMA-APM

Figure 6.2 shows the configuration used in this study, where the first three steps are to generate the particles, followed by DMA-APM density measurement. Essentially, the DMA is used to size select particles, which for a spherical particle defines its external volume. The size-selected particles are then passed to the APM,

which selects particles by mass. Particles are then counted by a condensation particle counter. The combination of particle volume and mass defines density, and if the theoretic density of the material is known, porosity can be extracted.

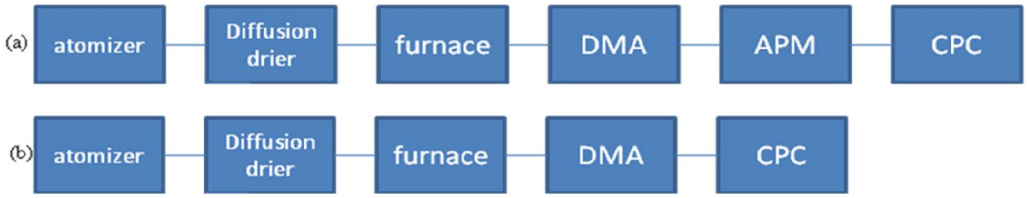


Figure 6.2. Experiment methodology (a) online density measurement; (b) size distribution measurement after furnace.

### 6.3.4 Density and Porosity Determination

At a fixed DMA voltage (fixed particle size), an APM mass distribution from scanning APM voltage (rotation speed was kept constant at 3000 rpm) was fit to a Gaussian distribution to give a peak mass for a DMA selected particle size. Using this approach the densities ρ of various size particles generated under different conditions can be determined.

$$\rho = \frac{m}{V} = \frac{6m}{\pi {d_p}^3} \tag{6.3}$$

Where $d_p$ is the particle diameter from the DMA; $m$ is the measured APM mass for that size particle.

The density measurement is independent of the material type; however, a porosity ($\varphi$) determination requires referencing to the theoretical solid density ($\rho_s$).

$$\varphi = \frac{\boldsymbol{V_p}}{\boldsymbol{V}} = \left(\frac{\boldsymbol{m}}{\rho} - \frac{\boldsymbol{m}}{\rho_s}\right) \Big/ \frac{\boldsymbol{m}}{\rho} = \mathbf{1} - \frac{\rho}{\rho_s} \tag{6.4}$$

The porosity measured here is of all the pore space in the particle independent of whether the pores are accessible of closed and thus is different from the measurement from BET.

## 6.4 Result and Discussion

### 6.4.1 Density Measurement of Porous Iron Oxide Particles

#### 6.4.1.1 Effective Density and Comparison with BET Measurement of Iron Oxide

Representative XRD analysis of the produced particles is shown in Figure 6.3 demonstrating that $Fe(NO_3)_3$ has been converted to $\gamma - Fe_2O_3$. The low crystallinity in the XRD patterns indicated that particle and crystalline grain sizes are small. Because the decomposition of the nitrate to $Fe_2O_3$ occurs around 150 ℃,[6.17] we can assume that particles generated at 400, 500 and 600 ℃ are iron oxide.

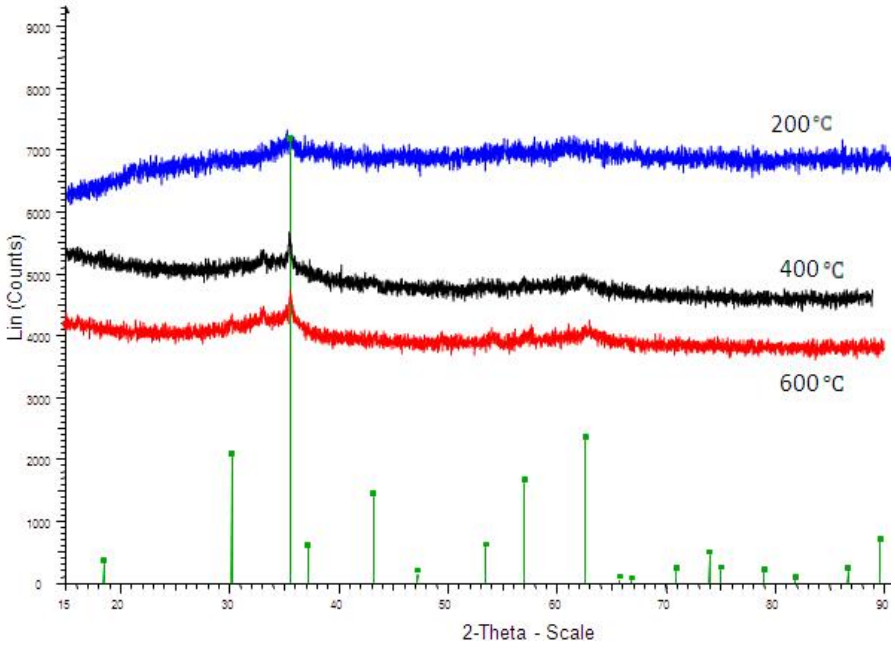


Figure 6.3. XRD analysis of iron oxide particles generated at 200, 400 and 600℃, respectively; the green lines on the x-axis are the theoretical maghemite peaks.

Figure 6.4 shows TEM images of the prepared particles as a function of furnace temperature. TEM images show that the particles are overall highly spherical with a porous internal structure. Furthermore, it is quite clear that the porous structures of the particles are very sensitive to the synthesis temperature: higher temperatures lead to larger pores.

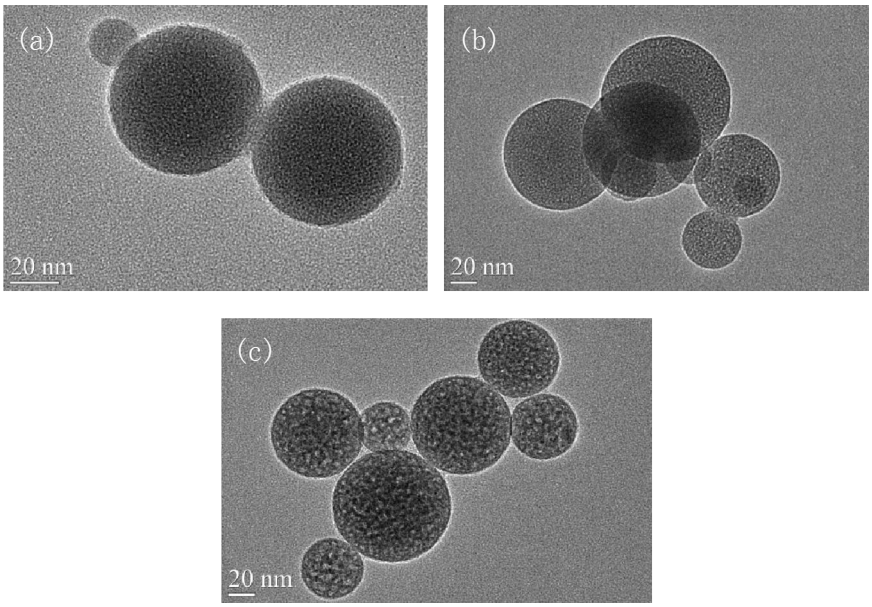


Figure 6.4. TEM images of iron oxide particles generated at (a) 400 °C, (b) 500 °C, and (c) 600 °C.

The solid density of γ-$Fe_2O_3$ is 4.9 g/$cm^3$, which will be used to calculate the porosity. Because samples made at low furnace temperatures may not be phase pure γ-$Fe_2O_3$, and possibly more hydrated, precise porosities cannot be obtained for these samples, although the density measurements are still valid.

The DMA-APM results are summarized in Table 6.2 and show that the density increases monotonically from about 2 g/cm3 at 100 ℃ to about 3.4 g/cm3 at 600 ℃. However, the resulting porosity measurements for the 400-600 ℃ measurements

show that even though the pore size increases as the furnace temperature increases, the porosity decreases.

Table 6.2. Results from tandem DMA-APM method.

| Sample No. | 1 | 2 | 3 | 4 | 5 | 6 |
|---|---|---|---|---|---|---|
| Furnace temperature(℃) | 100 | 200 | 300 | 400 | 500 | 600 |
| Average density(g/cm$^3$) | 2.09 | 2.11 | 2.46 | 3.12 | 3.22 | 3.44 |
| Porosity | - | - | - | 0.36 | 0.34 | 0.30 |
| Peak size ( nm) | 88.2 | 94.7 | 82.0 | 71.0 | 66.1 | 63.8 |

Porosity can be induced directly from the density of porous particles, or combining with the BET data—pore volume per unit mass, the BET porosity can be described as:

$$\varphi' = \frac{V_p}{V} = \frac{V_p' \times m}{m/\rho} = V_p' \times \rho \qquad (6.5)$$

Table 6.3. BET characterization results.

| Sample No. | 4 | 5 | 6 |
|---|---|---|---|
| External surface area( m²/g) | 14.2 | 9.30 | 6.60 |
| total surface area(m²/g) | 11.5 | 7.26 | 5.00 |
| Single point absorption of pores (Vp'-cm$^3$/g) | 0.020 | 0.015 | 0.018 |
| Porosity | 0.062 | 0.049 | 0.062 |
| Absorption average Pore diameter(Å) | 69.1 | 84.3 | 142.6 |

Table 6.3 shows the BET results and calculated porosity according to the BET data. The porosity calculated from BET is an order of magnitude lower than that determined from DMA-APM density data. Furthermore, a cursory inspection of the TEM images of Figure 6.4(c), would suggest that the void volume must be considerably larger than the 6% value determined from BET. In addition, the BET determined external surface area (surface area excluding micropore surface) is larger than BET total surface area in Table 6.3, so the difference between these two surface

areas, which is the surface area of the micropores is negative. Hence, there is an inherent incompatibility in the BET result.

BET methods are nominally the standard method to compute open porosity. Though the pore volume and surface area are clearly incompatible and likely both are inaccurate, possibly due to poor connectivity in pore structure, the trend observed in pore diameter seems to be consistent with the TEM images in Figure 6.4, probably from the accessible pore information.

On the other hand, given the demonstrated accuracy of the DMA-APM method as discussed previously, it is expected that the density measurement is highly reliable, and thus by inference the porosity should be more reliable than that determined from BET. However, because the DMA-APM method does not rely on any physics of the internal structure, it cannot be used to determine pore characteristics, and a reliance on BET is necessary.

#### 6.4.1.2 Density Distribution within a Particle Population for Iron Oxide

One of the significant advantages of the DMA-APM method is that it does not require macroscopic quantities to make a measurement. Furthermore, the inherent size fractionation of the material is integral to the measurement and thus amenable to density and porosity measurements as a function of particle size, which cannot be done by other methods. This is important because in any typical bulk synthesis process, one expects to produce a range of particle size that represents the overall size distribution. In the context of creating porous structures, one might also expect that there is a range of porosities that might be created that depend on particle size.

Figure 6.5 shows density measured as a function of DMA-selected particle size. The results show that at the highest temperatures of synthesis (600 ℃) the density is independent of particle size. However, at lower temperatures, the density starts out at a lower level and decreases monotonically as particle size increases. This suggests that the synthesis was not complete at lower temperatures. One should expect that if temperature or time were not sufficient, the largest particles would show the biggest effects. This is in fact clearly seen in Figure 6.6, where the full range of particle population is imaged. The largest particle at the lowest temperature has the lowest density, and shows a monotonic increase in density approaching the higher temperature cases as particle size is decreased. These results indicate that the DMA-APM method has the potential to understand the kinetics of the pore formation process.

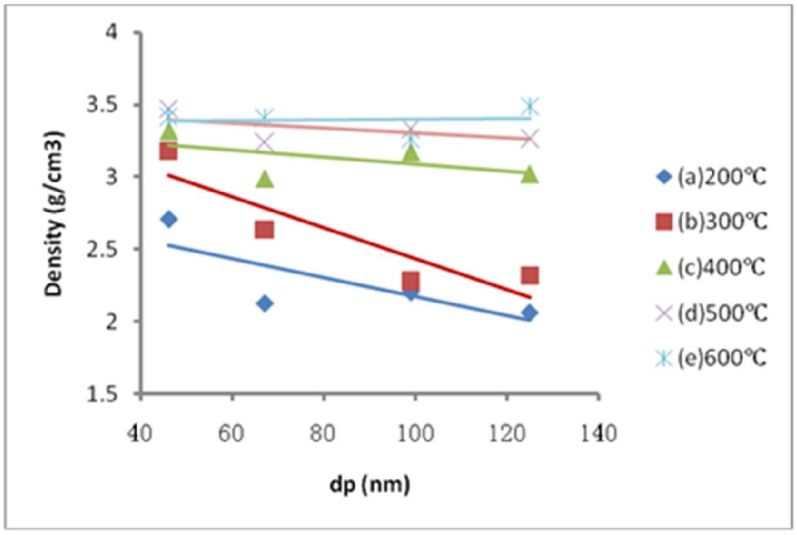


Figure 6.5. Particle density as a function of particle diameter, for different process temperature conditions.

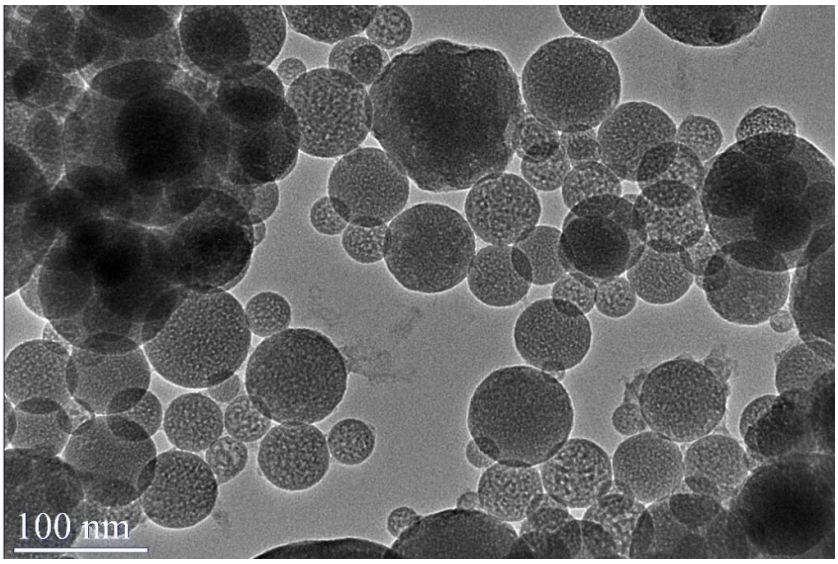


Figure 6.6. TEM image showing the range of particle porosity and size in sample 5.

#### 6.4.1.3 Pore Structure Creation

The results in Table 6.2 show that average particle density increases with reaction temperature, but that the overall particle size decreased. There are two likely factors that could cause such a trend in density: gas generation during synthesis and sintering. Since the decomposition temperature of the nitrate is low, it is expected that gas generation occurs first to make a porous structure. Higher temperatures should lower the viscosity of the melt allowing for the gas to escape easier, and thus creating a more dense structure before being frozen in. A lower viscosity melt will also induce more channeling effects, which will tend to merge gas zone and thus produce larger pores as observed in the TEM images.[6.18] While this is occurring grain growth is likely to increase the primary particle size and collapse of pores, which will lead to a higher average pore size and a lower total pore volume.

Up to 200 ℃ the peak particle size increases, consistent with gas generation puffing the particle out like a balloon. Because the gas generation starts below 200 ℃; it dominates the size trend according to the amount of gas emitted. Above 200 ℃ there is a steady decrease in the size distribution with increasing temperature. In this case, all the gas generation whose tendency is to increase particle size is apparently offset by the tendency to collapse the structure.

#### 6.4.1.4 Identifying the Particle Precursor

While our starting precursor is $Fe(NO_3)_3$ there is no particular reason to expect that after aerosolization and drying, the remnant precursor particle (before it enters the furnace) is still a nitrate. One possibility is that $Fe(NO_3)_3$ droplets hydrolyze to form solid phase $Fe(OH)_3$ particles before reaction furnace, which then dehydrates in the furnace to make porous $Fe_2O_3$ (hydrolization occurs first). The second possibility is that, $Fe(NO_3)_3$ aqueous droplets form pure nitrate particle, which decompose to $Fe_2O_3$ and oxynitride to make pores (nitrate decomposes directly).

In Table 6.4 the solid densities of iron hydroxide are listed, iron nitrate and iron oxide. Comparing the densities of iron nitrate and the hydroxide with the measured densities of the particle at lower heating temperatures (Table 6.2), it is seen that at the lowest temperature (100 ℃), which is below the thermal decomposition temperature of nitrate, the density measured is above that of pure nitrate, indicating that the precursor particle is not the nitrate, or at least a mixture of the nitrate and the hydroxide precursor. Below 100 ℃, solvent water is not fully evaporated yet, which implies that an intermediate of solid $Fe(NO_3)_3$ cannot exist in this fast evaporation

process and would seem to confirm the first hypothesis that $Fe(OH)_3$ forms before the solvent fully evaporates.

Table 6.4. Density of various Iron containing compounds

| Pure composition | iron hydroxide | $Fe(NO_3)_3 \cdot 9H_2O$ | $\gamma - Fe_2O_3$ |
|---|---|---|---|
| Density (g/cm3) | 3.4-3.9 | 1.7 | 4.9 |

### 6.4.2 Density Measurement of Hollow Copper Oxide Particles

In this second example, hollow CuO particles are generaged by spray pyrolysis. XRD analysis of the second sample is shown in the supplemental data Figure 6.7, and demonstrate that $Cu(NO_3)_2$ has only partially been converted to CuO when heated at 600 ˚C for a residence time of 1s. Compared to iron oxide, the primary particle (grain) size is significantly larger, which is confirmed in the TEM image of Figure 6.8. More important, the image clearly shows that particles have a hollow structure, which is very different from the porous iron oxide particle. Analysis of the XRD pattern indicates that copper oxide constitutes about 75% of the crystalline particle. The density of $Cu_2(OH)_3(NO_3)$ and CuO is 3.4 and 6.3 $g/cm^3$ respectively, so the mass average solid density used to calculate particle's porosity is $5.6 g/cm^3$. Compared to our measured particle density of ~1.2 $g/cm^3$, the calculated porosity is 0.79.

Table 6.5. Measured density of copper oxide as a function of particle size.

| Diameter(nm) | 46 | 67 | 84 | 99 | 112 | 125 | 137 |
|---|---|---|---|---|---|---|---|
| Density($g/cm^3$) | 1.6 | 1.2 | 1.2 | 1.2 | 1.1 | 1.1 | 1.2 |

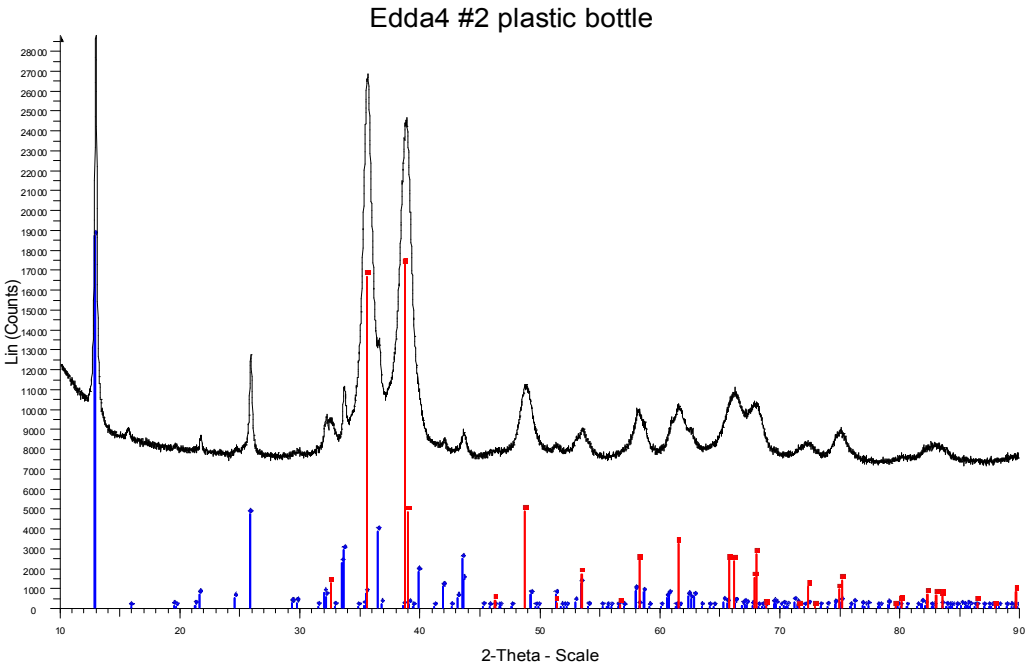


Figure 6.7. XRD analysis of the collected copper complex particles (black); CuO peaks (red) and $Cu_2(OH)_3(NO_3)$ peaks (blue).

As discussed previously, the BET method is best employed for a regular pore-structured material. Thus, a hollow particle is not amenable to a BET-type measurement, and illustrates some advantages in the uses of the DMA-APM approach.

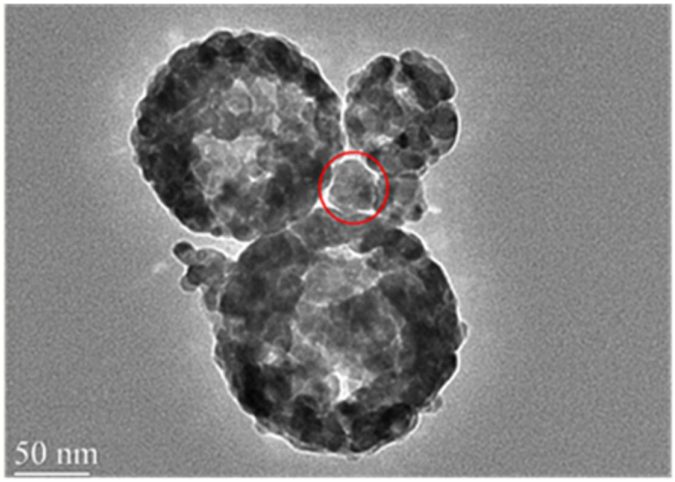


Figure 6.8. TEM analysis of hollow Copper complex particles. The red circle shows that some of the smaller particles may not be hollow.

### 6.4.3 Particle Formation Models and Verification

Table 6.5 shows that the density of copper complex particle is constant at 1.1-1.2 $g/cm^3$, across all particle sizes, unlike the iron oxide case. The highest density (1.6 $g/cm^3$) for the smallest particle sizes probably results from the fact that some of the smaller population sizes as seen from TEM are probably not hollow (see circle in Figure 6.8).

The formation of hollow particles in spray pyrolysis is well known.[6.19] The prevailing wisdom is that solvent evaporation from the droplet occurs faster than the internal solute diffusion, thus the concentration of the solute near the outer edge of the droplet reaches its solubility limit and precipitates to form a shell. This shell is then converted to the metal oxide in the pyrolysis step.

Figure 6.9 shows conceptual models for the formation of particles from spray pyrolysis for the two classes of materials observed. Table 6.6 shows that the melting point of iron nitrate is lower than the boiling point of the solvent water, so even if the concentration of salt exceeds the solubility on the shell in the evaporation process, it is still a fluid, and thus always behaves like a droplet; *i.e*. there should be no shell structure formation before chemical reaction and the porous structure is primarily driven by gas generation and sintering.

However, for the copper nitrate, the melting point is higher than the boiling point of water, so precipitation can occur before the solvent is fully evaporated. Evaporation of water from the droplet results in local increases in solute concentration near the

droplet edge leading to precipitation locally, and the formation of a crust. Subsequent decomposition/reaction freezes-in this hollow structure.

Table 6.6. Melting point and decompose temperature of nitrates.

| Stable state precursor | $Fe(NO_3)_3 \cdot 9H_2O$ | $Cu(NO_3)_2 \cdot 3H_2O$ |
|---|---|---|
| Melting point(℃) | 47 | 114 |
| Decompose temperature(℃) | 100-150 | 170 |

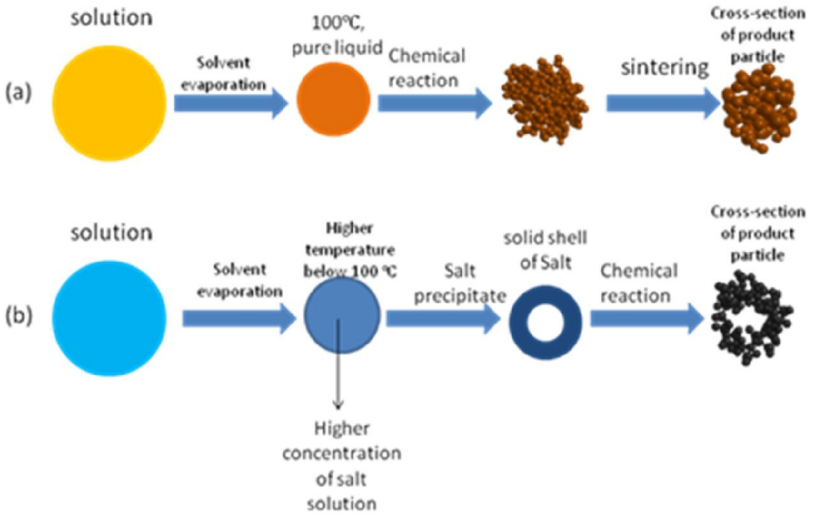


Figure 6.9. Particle formation mechanism from precursors of (a) iron nitrate and (b) copper nitrate.

## 6.5 Conclusion

In summary, an on-line method to measure size resolved density of porous particles is demonstrated. The method relies on combining a differential mobility analyzer (DMA) with a particle mass analyzer (APM) to make a simultaneous size resolved measurement of size and mass, from which density and porosity can be determined. The expected uncertainty of the density measurement is determined to be within 5%.

The method has several advantages over absorption methods such as BET in that no pore model is required, it is materials independent and will measure the density even in a particle with inaccessible pores.

As shown in this work the method can be used to monitor pore evolution and deduce likely mechanism of microstructure formation.

Reference


6.1. Vollath, D., *Nanomaterials: An introduction to synthesis, properties and application*. Wiley-VCH: 2008.

6.2. Schartl, W., Current directions in core-shell nanoparticle design. *Nanoscale* **2010,** *2* (6), 829-843.

6.3. deJonge, H.; MittelmeijerHazeleger, M. C., Adsorption of $CO_2$ and $N_2$ on soil organic matter: Nature of porosity, surface area, and diffusion mechanisms. *Environmental Science & Technology* **1996,** *30* (2), 408-413.

6.4. R. M. Cornell, U. S., *The iron oxides: Structure, properties, reactions, occurrences, and uses*. Wiley-VCH: 2003.

6.5. Galarneau, A.; Desplantier, D.; Dutartre, R.; Di Renzo, F., Micelle-templated silicates as a test bed for methods of mesopore size evaluation. *Microporous and Mesoporous Materials* **1999,** *27* (2-3), 297-308.

6.6. Eren, H., Density measurement. Wiley Encyclopedia of Electrical and Electronics Engineering. 1999.

6.7. Hinds, W. C., *Aerosol technology: Properties, behavior, and measurement of airborne particles*. Wiley: 1999.

6.8. Kim, S. H.; Woo, K. S.; Liu, B. Y. H.; Zachariah, M. R., Method of measuring charge distribution of nanosized aerosols. *Journal of Colloid and Interface Science* **2005,** *282* (1), 46-57.

6.9. Ehara, K.; Hagwood, C.; Coakley, K. J., Novel method to classify aerosol particles according to their mass-to-charge ratio - Aerosol particle mass analyser. *Journal of Aerosol Science* **1996,** *27* (2), 217-234.

6.10. Ma, X.; Zachariah, M. R., Size-resolved kinetics of Zn nanocrystal hydrolysis for hydrogen generation. *International Journal of Hydrogen Energy* **2010,** *35* (6), 2268.

6.11. Ma, X. F.; Zachariah, M. R., Oxidation anisotropy and size-dependent reaction kinetics of zinc nanocrystals. *Journal of Physical Chemistry C* **2009,** *113* (33), 14644-14650; Zhou, L.; Rai, A.; Piekiel, N.; Ma, X. F.; Zachariah, M. R., Ion-mobility spectrometry of nickel nanoparticle oxidation kinetics: Application to energetic materials. *Journal of Physical Chemistry C* **2008,** *112* (42), 16209-16218.
6.12. Kim, S. H.; Mulholland, G. W.; Zachariah, M. R., Density measurement of size selected multiwalled carbon nanotubes by mobility-mass characterization. *Carbon* **2009,** *47* (5), 1297-1302.
6.13. Park, K.; Kittelson, D. B.; Zachariah, M. R.; McMurry, P. H., Measurement of inherent material density of nanoparticle agglomerates. *Journal of Nanoparticle Research* **2004,** *6* (2-3), 267-272.
6.14. Lall, A. A.; Ma, X. F.; Guha, S.; Mulholland, G. W.; Zachariah, M. R., Online nanoparticle mass measurement by combined aerosol particle mass analyzer and differential mobility analyzer: Comparison of theory and measurements. *Aerosol Science and Technology* **2009,** *42* (11), 1075-1083.
6.15. Tsai, D. H.; DelRio, F. W.; Keene, A. M.; Tyner, K. M.; MacCuspie, R. I.; Cho, T. J.; Zachariah, M. R.; Hackley, V. A., Adsorption and conformation of serum albumin protein on gold nanoparticles investigated using dimensional measurements and in situ spectroscopic methods. *Langmuir* **2011,** *27* (6), 2464-2477.
6.16. Prakash, A.; McCormick, A. V.; Zachariah, M. R., Tuning the reactivity of energetic nanoparticles by creation of a core-shell nanostructure. *Nano Letters* **2005,** *5* (7), 1357-1360.
6.17. Gadalla, A. M.; Yu, H. F., Thermal-decomposition of Fe(III) nitrate and its aerosol. *Journal of Materials Research* **1990,** *5* (6), 1233-1236.
6.18. Ma, L. Q.; Song, Z. L., Cellular structure control of aluminium foams during foaming process of aluminium melt. *Scripta Materialia* **1998,** *39* (11), 1523-1528.
6.19. Yu, H. F.; Liao, W. H., Evaporation of solution droplets in spray pyrolysis. *International Journal of Heat and Mass Transfer* **1998,** *41* (8-9), 993-1001.

# Chapter 7. Synthesis of Fluorescent Porous Silica Nanoparticles for Drug Delivery Application

## 7.1 Introduction

Fluorescent nanoparticles have a variety of biomedical applications as diagnostics and traceable drug delivery agents. Silicas of various pore structures have been synthesized by the spray pyrolysis method. However, because most dyes decompose even below the temperature for silica synthesis from precursor, and the spray drying technique cannot stably fix dyes in the matrix, an alternative method developed will be discussed in this chapter.

Silica materials are used in a variety of biological applications because of its resistance to microbial attacks, stability in aqueous solutions, low toxicity, ability to be functionalized, and penetrability through biomembranes.[7.1, 7.2] Porous silica is particularly attractive due to the potential to transport drugs within the dead volume of the porous particles.[7.2] Common synthesis methods for the production of porous silica include templating[7.3] and co-condensation[7.4] with organoalkoxysilanes.

For many applications such as diagnostics and drug delivery, bright and stable luminescent labels are often required. Labeling methods include quantum dots, metal nanoparticles and doping dyes or chromophores.[7.5] Because of biodegradation and toxicity issues associated with quantum dots,[7.6] dye labeling of nanoparticles has been drawing recent attention. Research on the use of dye-functionalized nanoparticles has focuses on photostability of dyes, leakage of dyes from the matrix, and chemical stability of the matrix.

Several types of approaches to synthesizing the luminescent labeled silica nanoparticles have been reported. A typical approach to mitigating some of these problems is to encapsulate the dye within silica during particle formation and to employ electrostatic forces to assemble the cationic dye within the silica matrix.[7.7] However, due to the weakness of the electrostatic forces acting on the dye molecules in typical nanoparticle systems, an alternative method for preparing bright, stable nanoparticles is to modify the organic dye to make it more hydrophilic, and thus increase the dye affinity to the matrix.[7.8] To promote a stronger attachment, the dye is modified so as to be directly linked with organosilanes participating in the co-condensation process with the primary silica precursor, typically tetraethoxysilane (TEOS).[7.9] What is trying to be improved can be either the weak electrostatic assemblies or the complicated modification of the dye precursors. However, the complicated modification of the dye precursors and the weak electrostatic assemblies obstructs the widely application of the methods.

A second strategy for the preparation of fluorescent silica nanoparticles is to add the dye after the silica matrix has been created and allow the dye to become incorporated into the organic matrix by diffusion. Post-treatment can be accomplished either by wet impregnation, whereby the dye is physically absorbed onto the pre-synthesized porous silica material, or as a post-graft method, to chemically bond the dye to the matrix in a second step.[7.10] Beyond the added functionality that a fluorescent silica particle may offer, the silica matrix itself serves to isolate the dye from outside environment such as solvent, oxygen and free radicals caused by light exposure,[7.11] and protect dye molecules from photodecomposition. In addition, using a low concentration of bound dye in some cases has been shown to increase the relative quantum yield relative to a free dye, due to lower

self-quenching.[7.12] However, these methods suffer from dye leakage unless covalent modification is employed,[7.13] or an additional silica capping layer is applied to trap the dye in a core-shell structure.[7.14] The methods described above can be categorized as either one-step methods that may suffer from poor dye fixing ability, or multi-step methods that enjoy greater dye stability at the cost of synthetic complexity.

Another class of materials is to combine fluorescence with a porous structure. As in the solid particle cases, syntheses of fluorescent porous particles are typically multi-step processes.[7.15] Also, these methods cannot independently control pore structures, as a result of the employment of surfactant as pore template in the process of synthesis.

This work introduces a one-step method to label porous silica nanoparticles (PSN) with fluorescent dyes, using polystyrene (PS) as the extensive pore template, cetyltrimethylammoniumbromide (CTAB) as a micelle template,[7.16] and an embedding "lipid" dye. This approach also allows independent control of both pore and particle size. The use of a lipid dye enables the dye to function as a surrogate surfactant with the primary surfactant (CTAB) at the interface between the organic and inorganic phases. From BET analysis, by washing off the PS and micelle templates, particle surface area is increased for potential drug loading or subsequent modification, without eliminating the fluorescent effectiveness. Two different dyes were studied, both independently and in combination to demonstrate the reliability of the method.

## 7.2 Experimental

### 7.2.1 Materials

The materials used are: TEOS (98%, Aldrich) as the silica precursor; L-lysine (Aldrich) as the catalyst for silica size control;[7.17] styrene monomer (Aldrich) as the

template monomer, stabilizer removed before use; CTAB (Aldrich) as necessary template and surfactant; 2,2'-azobis (2-methylpropionamide) dihydrochloride (AIBA, Aldrich) as the initiator of styrene polymerization; octane (Aldrich, 98%) and distilled water to make oil/water reaction system; 1,2-dioleoyl-*sn*-glycero-3-phosphoethanolamine-N-(lissamine rhodamine B sulfonyl) ammonium salt (Liss Rhod PE, dye LR, Avanti Polar Lipids, in chloroform), 1,2-dioleoyl-*sn*-glycero-3-phosphoethanolamine-N-(5-dimethylamino-1-naphthalenesulfonyl) ammonium salt (Dansyl PE, dye D, Avanti Polar Lipids, in chloroform), Coumarin 440 (dye C, Exciton Chemical Company, Inc., Dayton, OH) and Rhodamine 590 (dye R, Exciton Chemical Company, Inc., Dayton, OH) as fluorescent sources.

### 7.2.2 Synthesis of Fluorescent Mesoporous Silica Nanoparticle

A typical synthesis of the fluorescent mesoporous silica nanoparticles is described as follows. First, about 0.3 mL dye solution (1mg/mL in chloroform) were added to a solution of 0.050 g CTAB in 15 mL of $H_2O$ heated to 60 °C in a three-necked flask reactor. Then, 0.15 g of styrene, 0.011 g of lysine, 0.50 g of TEOS, 5.1 g of octane and 0.013 g of AIBA were subsequently added to the system. The homogeneous reaction mixture was stirred under $N_2$ at 60 ˚C for 3 hours. After cooling, the resulting suspension was decanted from the fluorescent nanoparticles that had formed. The sample was subject to sonication in ethanol followed by centrifugation for 3 times to ensure that excess surfactant and unincorporated dye were removed. Finally, the polystyrene template was removed by sonication-centrifugation with tetrahydrofuran (THF) for 3 times.[7.18] Particles were collected by centrifugation and dried in the air.

Silica nanoparticles without polystyrene template (no-PS PSN) were prepared according to the same recipe except that styrene and AIBA addition was omitted. Synthesized according to the above procedure, PSN-LR, PSN-D, PSN-C and PSN-R are porous silica nanoparticle incorporated with Liss Rhod PE, Dansyl PE, Coumarin 440 and Rhodamine 590, respectively; PSN-LR&D is incorporated with Liss Rhod PE and Dansyl PE in combination.

### 7.2.3 Characterization

UV-vis absorption and fluorescent spectra of the solid product were obtained with a Lambda 850 UV-vis and Cary Eclipse fluorescent spectrophotometer, respectively. Transmission electron microscopy (TEM) was performed on a JEOL JEM 2100 FEG instrument. Pore size and porosity measurements were performed using the Brunauer-Emmett-Teller (BET) method on a Micrometrics TriStar II 3020 instrument.

## 7.3 Results and Discussion

A lipid-like dye is chosen for these experiments so as to enable the dye to serve also as a surrogate surfactant in conjunction with the primary surfactant CTAB to increase the fixing efficiency of the particle formation. Under either ambient or UV light, it was quite clear that the dye was successfully embedded in the particles. Furthermore, subsequent washing and centrifugation, showed little color in the supernatant indicating that this approach is quite efficient at incorporation of the dye into the matrix. To test for long-term stability of the fluorescent emission from the particles, the particles were kept in a water solution for a period of up to 6 months. No fluorescent degradation was detected, indicating that the particles were photostable with minimal dye leakage.

Two additional dyes were chosen for control experiments. Coumarin 440 is non-ionic dye, and Rhodamine 590 is an ionic dye; neither of which have a Liss Rhod PE's surrogate-surfactant structure. (Dye structures are shown in Figure 7.1.) Since PSN-C and PSN-R were not the subjects of this study, luminescent characterization was not conducted for the resulting nanoparticles.

Figures 7.2(a) and (b) show the fluorescence associated with the supernatant and the silica nanoparticles from the first washing, respectively. It is clear from these photos that all the four dyes can be incorporated into the particle, resulting all dye-PSNs with significant luminescence. However, dye incorporation efficiencies are different: as PSN-LR and PSN-D are washed, the supernatants are almost colorless, while as PSN-C and PSN-R are washed, dyes dissolve into the ethanol solution. Also, as PSN-C and PSN-R are washed more times, the supernatants show a more diminished color, as well as the particles, indicating that the organic Coumarin 440 and ionic Rhodamine 590 end up in the ethanol extracts rather than in the silica matrix.

(a) 18:1 Liss Rhod PE:

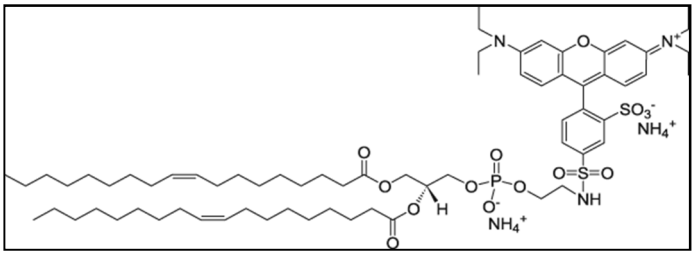

(b) 18:1 Dansyl PE:

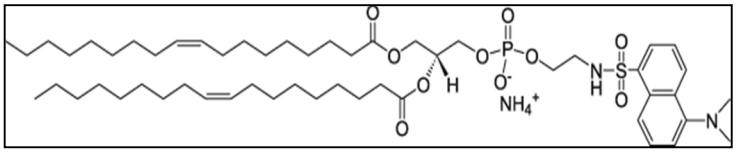

(c) Coumarin 440:

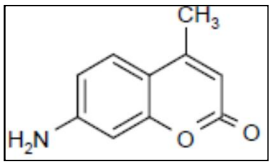

(d) Rhodamine 590:

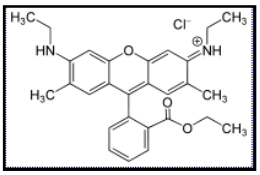

Figure 7.1. Molecular structure of (a) (b) lipid dyes, (c) small molecule nonionic dye and (d) small molecule ionic dye. ( Molecular structures are from http://www.avantilipids.com/ and http://www.exciton.com/)

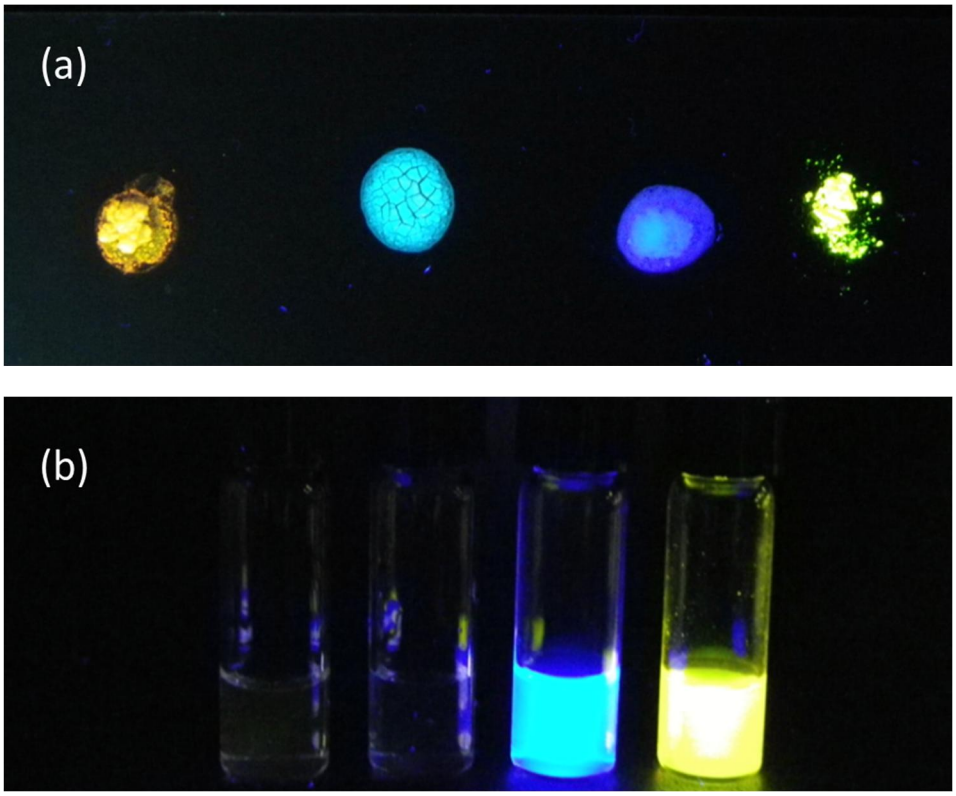

Figure 7.2. From left to right: (under UV light) (a)PSN-LR, D, C and R spots on a slide (b) supernatants of washing solvent of the same order after centrifugation

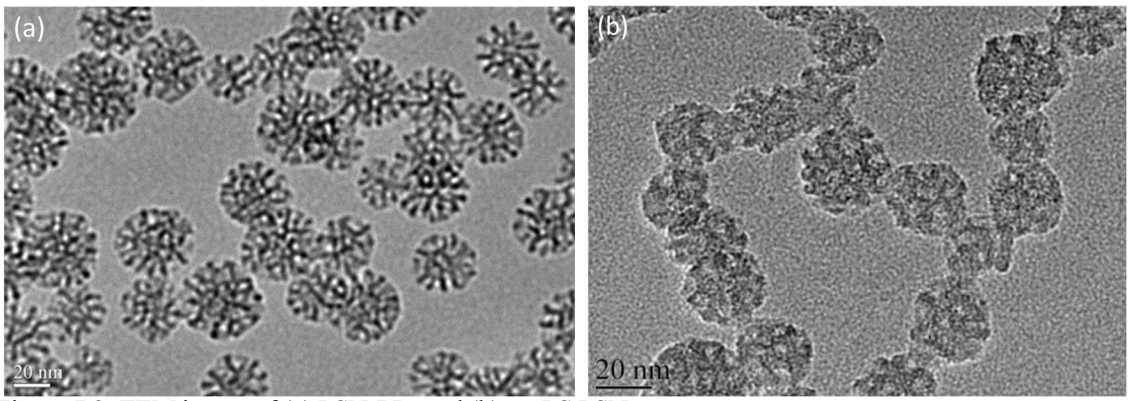

Figure 7.3. TEM image of (a) PSN-LR, and (b) no-PS PSN.

Figure 7.3 is a TEM image of the porous silica particles prepared by this method. While the particles are essentially monodispersed, we observe that the diameter of the nanoparticles prepared with the presence of polystyrene (PS) (~40 nm) is larger than that of particles prepared without PS (~30 nm). Also, the former particles have a more ordered pore structure, extending deeper to the center of the particle, though dye addition

or not, would make no structure difference. The porous structure was formed because of the addition of PS and CTAB, which also control the size distribution of the pores and the particles.[7.16] It has been reported that surfactant and polymer form hybrid threadlike micelles in aqueous solution.[7.19] In the case of when dye is added, styrene addition forms the dye-colored hybrid polymer-surfactant (P-S) template, and thus creates a more uniform and dense porous structure, which is also responsible for a larger porosity and larger diameter of particles. In the absence of PS, the morphology of the particles is different, comparing TEM images of Figure 7.3(a) and (b). Since the silica cluster is negative charged, and CTAB is a cationic surfactant, it is not unexpected that the P-S hybrid micelle or CTAB itself can be attracted to the silica matrix to make potential pore structure.

The proposed mechanism of dye incorporated porous silica particle formation is shown in Figure 7.4. The choice of a lipid dye is predicated on choosing something that has a surfactant like head-tail structure, so it can intercalate with CTAB to make dye-containning micelles. It is oberved experimentally that the lipid dye LR is insoluble in octane, but it dissolves when CTAB is added, which demonstrates that it can intercalate with CTAB. Initially, styrene and TEOS are oil soluble (inside micelle); lipid dye molecules transport into the micelle with the help of CTAB to form P-S pore template. Electrostatically, the cationic surfactant $CTA^+$ can also prevent the anionic dye $X^-$ from dimerizing,[7.20] and thus self-quenching. It is witnessed by comparing a increased ratio of dimer to monomer absorption in Figure 7.5b (the solid state), to the result in Figure 7.6 (dye fixed in PSN). The particle then grows due to electrostatic attraction of hybrid pore template and silica cluster until TEOS is completely consumed. For post-treatment,

traditional calcination to eliminate the template cannot be applied here because it would destroy the fluorescence of the dye. Instead, ethanol and THF are chosen to wash out the CTAB and pore template PS for two features: first, the long hydrophobic tail of the dye molecule can be trapped tightly in the structure, which prevents it from being washed out; second, removing the pore template by washing is more efficient for the pore structure closer to the surface, because it takes time for deeply trapped molecules to diffuse out of the matrix and escape the particle.

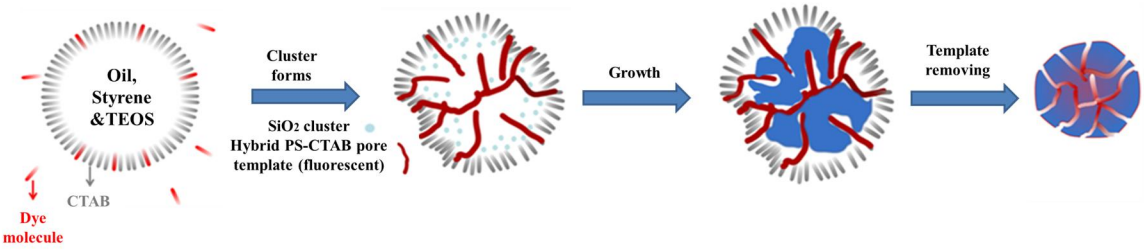


Figure 7.4: Proposed mechanism of dye incorporation and porous silica formation.

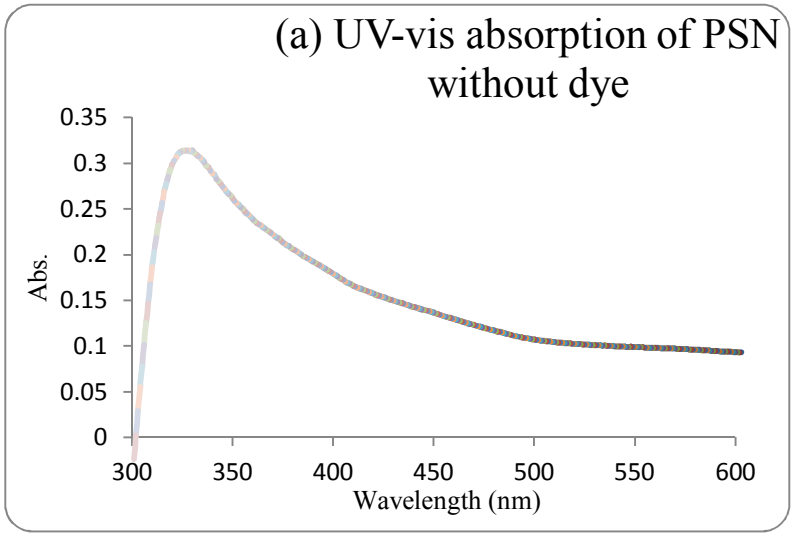

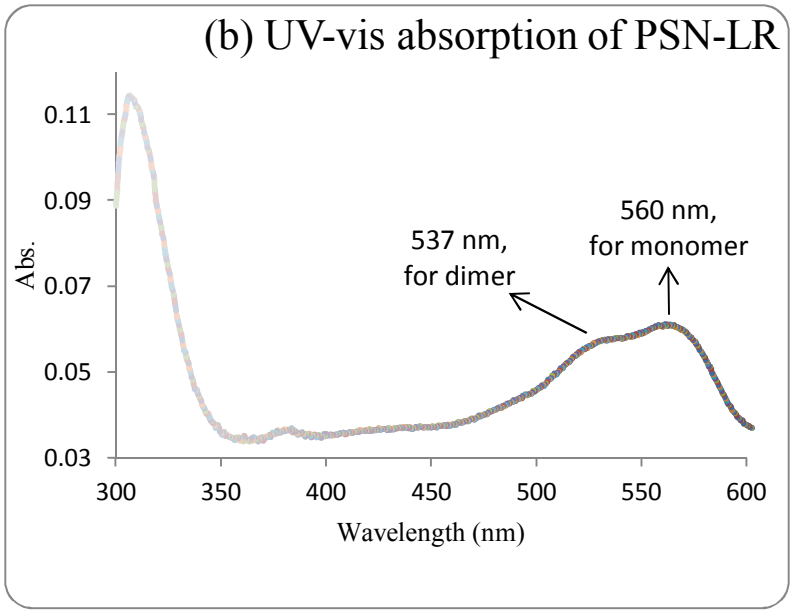
(b) UV-vis absorption of PSN-LR
0.11
0.09
0.07
0.05
0.03
Abs.
537 nm,
for dimer
560 nm,
for monomer
300
350
400
450
500
550
600
Wavelength (nm)

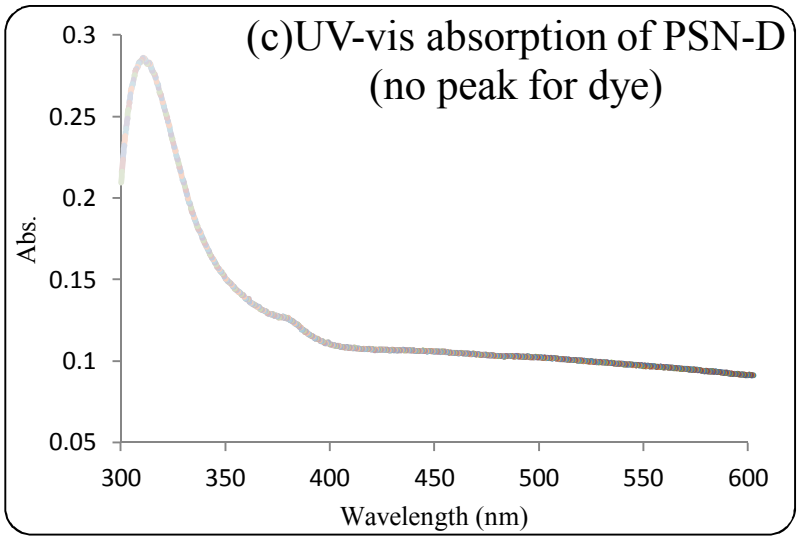
(c)UV-vis absorption of PSN-D
(no peak for dye)
0.3
0.25
0.2
0.15
0.1
0.05
Abs.
300
350
400
450
500
550
600
Wavelength (nm)

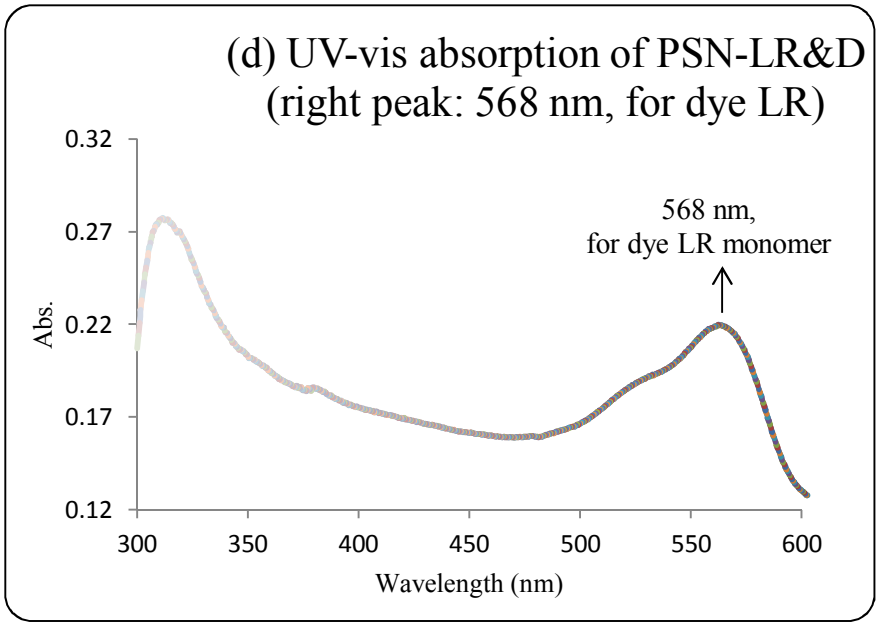


Figure 7.5. UV-vis absorption of (a) solid PSN without dye, (b)(c)(d) solid dye-PSNs. For PSN-LR in Figure 7.5(b), the major absorption peak at ca. 560 nm may be attributed to the absorbance of the monomers, while the small shoulder at ca. 537 nm is due to the formation of dimers.[21] In Figure 7.5(c) , no absorption was found for dye D, because the absorption profile of the silica (Figure 7.5a) is quite strong overlaps that of the dye D. Similarly, the absorption spectrum of PSN-LR&D (Figure 7.5d) shows only one peak for dye LR.

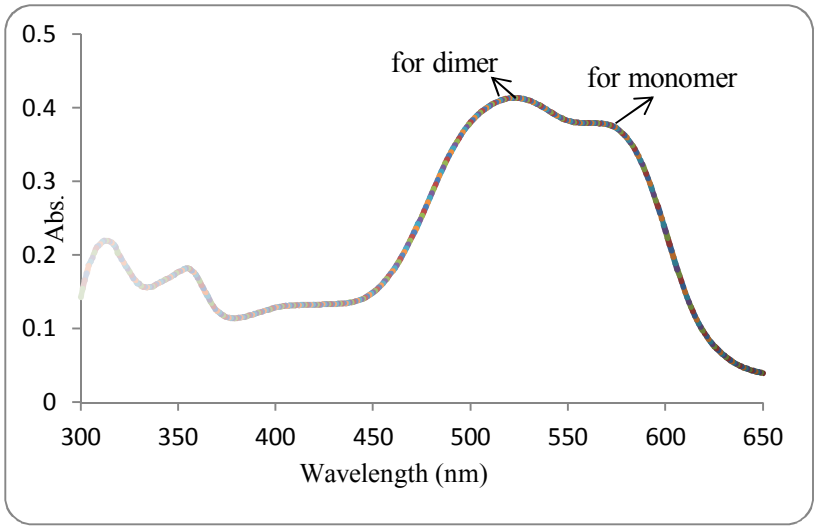


Figure 7.6. Absorption spectrum of solid dye LR.

The porous structure is also studied by BET specific surface area characterization. With the same particle generation procedure, except for the dye addition, particle

structures are the same under TEM; however, a calcination post-treatment could yield a surface area of about 600 $m^2/g$.[7.16], comparing to BET surface area of about 200 $m^2/g$ of the as-produced particles after removing the pore template by washing. Though not all the pores can be clean out by washing, this surface area is much larger than the theoretical surface area of 40 nm solid silica particle (12.8 $m^2/g$), which demonstrates the removal of pore template and is sufficient for the porous structure application.

Fluorescence spectra of dye-PSNs are shown in Figure 7.7. Because of inherent limit of fluorescence spectroscopy,[7.22] we talk about the fluorescence qualitatively, not quantitatively. PSN without dye has no fluorescence emission peak, which can be taken as the background for the fluorescence label (Figure 7.8). Because the only difference between these samples is whether there is incoporated dye(s), the fluorescence peaks must originate from the dyes. Figures 7.7(a), (b) and (c)(d) for emission spectra of PSN-LR, PSN-D and PSN-LR&D, exited by the optimized excitation wavelength to obtain strong emission. In spite of existence of both blue shift, comparing to the emission wavelength of fluorecent dyes, 587 nm at excitation of 557 nm[7.23] for dye LR and 510 nm at excitation of 340 nm[7.24] for dye D, high fluorescence at 564 nm and 476 nm for PSN-LR and PSN-D, respectively, confirms the efficient single dye incorporation into the PSN.

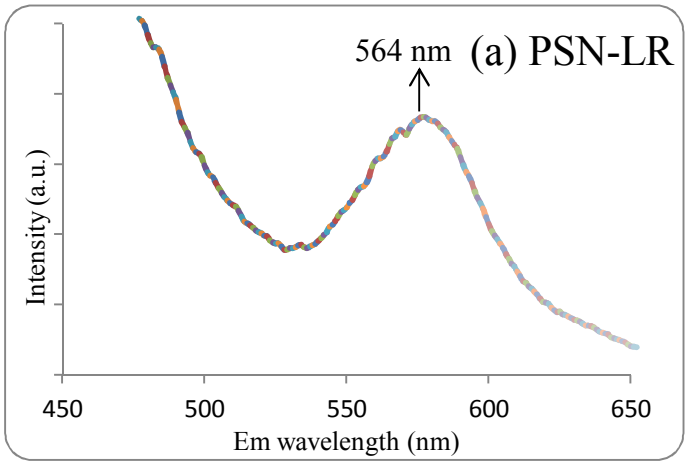

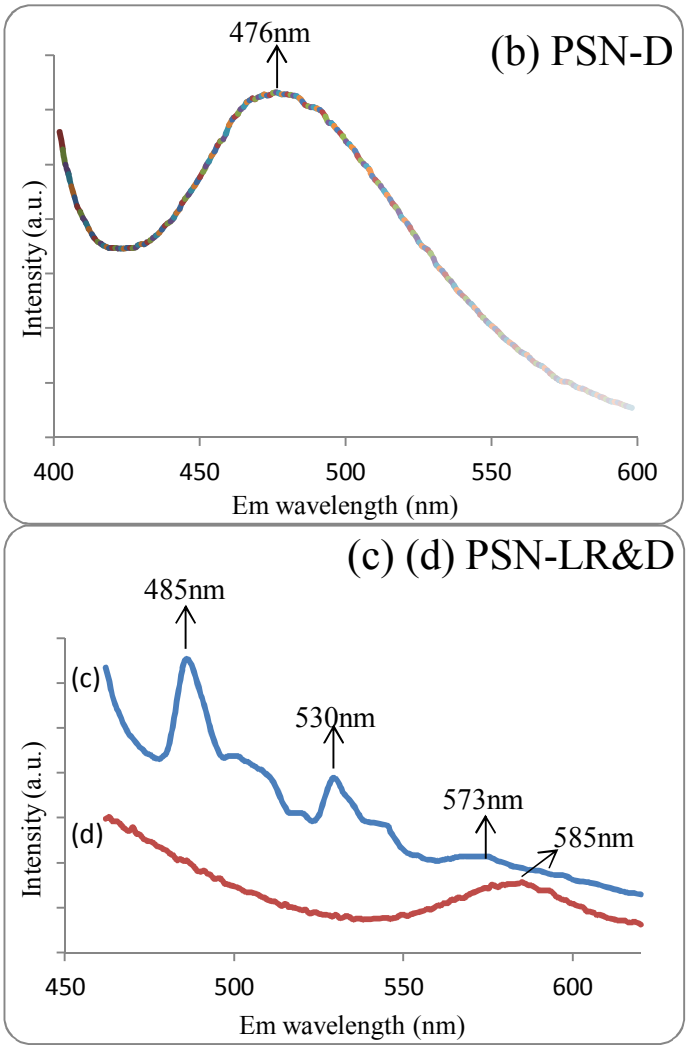


Figure 7.7. Fluorescence spectra of (a) PSN-LR at exitation of 350nm, (b) PSN-D at exitation of 340nm, (c) and (d) PSN-LR&D at exitation of 400nm and 350nm, respectively.

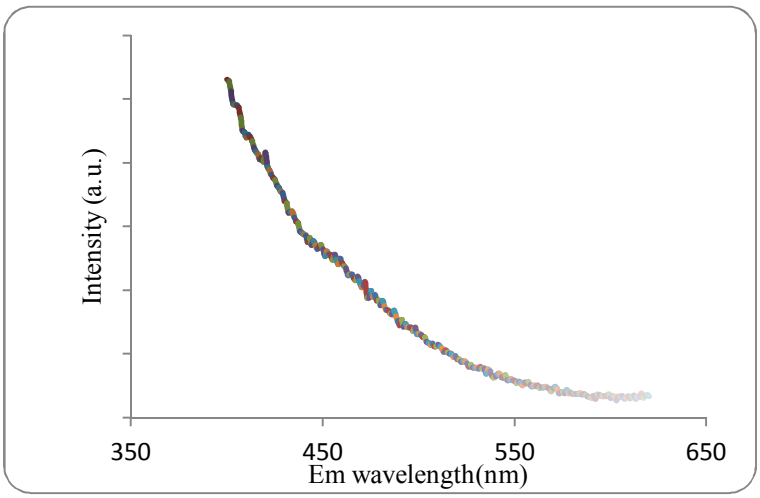


Figure 7.8. Fluorescence emission spectrum of PSN without dye.

The fluoresence spectrum of PSN-LR&D is more complicated, and is presented in Figures 7.7(c) and (d). Excitation at 350 nm results in one emission peak at 585 nm similar to what is seen for PSN-LR, but no peak consistent with the emission of PSN-D. However, excitation at 400 nm, gives three emission bands at 485, 530 and 573 nm. There are two possible reasons for this behavior. One is that LR absorbs strongly at 350 nm relative to D, or alternatively emission from dye D is reabsorbed by LR. In either case there appears to be significant quenching in emission as the quantum yeild is much lower when the two dyes are mixed. This latter result may be a generic problem in trying to mix more than one dye within a particle.

## 7.4 Conclusions

A single-step, efficient method to synthesize photo- and chemically-stable dye-doped porous silica nanoparticles have been developed. The resulting nanoparticles are highly fluorescent and this method is applicable to the production of virtually any "color" of nanoparticle for which the corresponding dye is available. Encapsulating dyes into nanoparticles, can stabilize dyes within the matrix, thus preventing aggregation and fluorescent quenching. For application of this material, pore template PS could be removed for potential drug loading; the particle and pore size are controllable by adjusting the o/w ratio, surfactant concentration, and the amount of styrene, according to previous research from Okuyama's group.[7.16] What is unique for this method is that, compared to the non-chemical bonded dye doping methods nominally used for cationic dyes,[7.7, 7.25] our fluorescent yield remained constant and dye leakage was negligible; compared to the strong bonded dye doping method, this method is synthetically easier. In addition, no toxic functional  is involved in the synthesis process.[7.26] Future study can

focus on fluorescence studies of PSN-LR, PSN-D and PSN-LR&D within body temperature range, and quantitative research to enhance the dyes' quantum yield.

References


7.1. Bharali, D. J.; Klejbor, I.; Stachowiak, E. K.; Dutta, P.; Roy, I.; Kaur, N.; Bergey, E. J.; Prasad, P. N.; Stachowiak, M. K., Organically modified silica nanoparticles: A nonviral vector for in vivo gene delivery and expression in the brain. *Proceedings of the National Academy of Sciences of the United States of America* **2005,** *102* (32), 11539-11544.

7.2. Wang, Y. J.; Price, A. D.; Caruso, F., Nanoporous colloids: Building blocks for a new generation of structured materials. *Journal of Materials Chemistry* **2009,** *19* (36), 6451-6464.

7.3. Capek, I., On inverse miniemulsion polymerization of conventional water-soluble monomers. *Advances in Colloid and Interface Science* **2010,** *156* (1-2), 35-61.

7.4. Huh, S.; Wiench, J. W.; Yoo, J. C.; Pruski, M.; Lin, V. S. Y., Organic functionalization and morphology control of mesoporous silicas via a co-condensation synthesis method. *Chemistry of Materials* **2003,** *15* (22), 4247-4256.

7.5. Yao, G.; Wang, L.; Wu, Y. R.; Smith, J.; Xu, J. S.; Zhao, W. J.; Lee, E. J.; Tan, W. H., FloDots: Luminescent nanoparticles. *Analytical and Bioanalytical Chemistry* **2006,** *385* (3), 518-524.

7.6. Michalet, X.; Pinaud, F. F.; Bentolila, L. A.; Tsay, J. M.; Doose, S.; Li, J. J.; Sundaresan, G.; Wu, A. M.; Gambhir, S. S.; Weiss, S., Quantum dots for live cells, in vivo imaging, and diagnostics. *Science* **2005,** *307* (5709), 538-544.

7.7. Shibata, S.; Taniguchi, T.; Yano, T.; Yamane, M., Formation of water-soluble dye-doped silica particles. *Journal of Sol-Gel Science and Technology* **1997,** *10* (3), 263-268.

7.8. Zhao, X. J.; Bagwe, R. P.; Tan, W. H., Development of organic-dye-doped silica nanoparticles in a reverse microemulsion. *Advanced Materials* **2004,** *16* (2), 173-+.

7.9. Vanblaaderen, A.; Vrij, A., Synthesis and characterization of colloidal dispersions of fluorescent, monodisperse silica spheres. *Langmuir* **1992,** *8* (12), 2921-2931.

7.10. Li, X. D.; Zhai, Q. Z.; Zou, M. Q., Optical properties of (nanometer MCM-41)-(malachite green) composite materials. *Applied Surface Science* **2010,** *257* (3), 1134-1140.

7.11. Xie, C. J.; Yin, D. G.; Li, J.; Zhang, L.; Liu, B. H.; Wu, M. H., Preparation of a novel type of fluorescein isothiocyanate doped fluorescent silica nanoparticles and its application as pH probe. *Chinese Journal of Analytical Chemistry* **2010,** *38* (4), 488-492.

7.12. Ma, D. L.; Kell, A. J.; Tan, S.; Jakubek, Z. J.; Simard, B., Photophysical properties of dye-doped silica nanoparticles bearing different types of dye-silica interactions. *Journal of Physical Chemistry C* **2009,** *113* (36), 15974-15981.
7.13. Gao, X. Q.; He, J.; Deng, L.; Cao, H. N., Synthesis and characterization of functionalized rhodamine B-doped silica nanoparticles. *Optical Materials* **2009,** *31* (11), 1715-1719.
7.14. Rocha, L. A.; Caiut, J. M. A.; Messaddeq, Y.; Ribeiro, S. J. L.; Martines, M. A. U.; Freiria, J. D.; Dexpert-Ghys, J.; Verelst, M., Non-leachable highly luminescent ordered mesoporous $SiO_2$ spherical particles. *Nanotechnology* **2010,** *21* (15).
7.15. Wang, Y.; Li, Z. H.; Zhong, W. Y.; Li, H.; Xu, D. K.; Chen, H. Y., Rhodamine B doped silica nanoparticle labels for protein microarray detection. *Science China-Chemistry* **2010,** *53* (4), 747-751; Stein, A.; Melde, B. J.; Schroden, R. C., Hybrid inorganic-organic mesoporous silicates - Nanoscopic reactors coming of age. *Advanced Materials* **2000,** *12* (19), 1403-1419; Tsyalkovsky, V.; Klep, V.; Ramaratnam, K.; Lupitskyy, R.; Minko, S.; Luzinov, I., Fluorescent reactive core-shell composite nanoparticles with a high surface concentration of epoxy functionalities. *Chemistry of Materials* **2008,** *20* (1), 317-325; Guli, M.; Chen, Y.; Li, X. T.; Zhu, G. S.; Qiu, S. L., Fluorescence of postgrafting Rhodamine B in the mesopores of rodlike SBA-15. *Journal of Luminescence* **2007,** *126* (2), 723-727.
7.16. Nandiyanto, A. B. D.; Kim, S. G.; Iskandar, F.; Okuyama, K., Synthesis of spherical mesoporous silica nanoparticles with nanometer-size controllable pores and outer diameters. *Microporous and Mesoporous Materials* **2009,** *120* (3), 447-453.
7.17. Thomassen, L. C. J.; Aerts, A.; Rabolli, V.; Lison, D.; Gonzalez, L.; Kirsch-Volders, M.; Napierska, D.; Hoet, P. H.; Kirschhock, C. E. A.; Martens, J. A., Synthesis and characterization of stable monodisperse silica nanoparticle sols for in vitro cytotoxicity testing. *Langmuir* **2010,** *26* (1), 328-335.
7.18. Lee, S. J.; Choi, M.-C.; Park, S. S.; Ha, C.-S., Synthesis and characterization of hybrid films of polyimide and silica hollow spheres. *Macromolecular Research* **2011,** *19* (6), 599-607.
7.19. Nakamura, K.; Yamanaka, K.; Shikata, T., Hybrid threadlike micelle formation between a surfactant and polymer in aqueous solution. *Langmuir* **2003,** *19* (21), 8654-8660.
7.20. He, Q.; Shi, J.; Cui, X.; Zhao, J.; Chen, Y.; Zhou, J., Rhodamine B-co-condensed spherical SBA-15 nanoparticles: Facile co-condensation synthesis and excellent fluorescence features. *Journal of Materials Chemistry* **2009,** *19* (21), 3395-3403.
7.21. Al-Shamiri, H. A. S.; Kana, M. T. H., Laser performance and photostability of Rhodamin B in solid host matrices. *Applied Physics B-Lasers and Optics* **2010,** *101* (1-2), 129-135.
7.22. Waters, J. C., Accuracy and precision in quantitative fluorescence microscopy. *Journal of Cell Biology* **2009,** *185* (7), 1135-1148.
7.23. Quemeneur, F.; Rinaudo, M.; Pepin-Donat, B., Influence of molecular weight and pH on adsorption of chitosan at the surface of large and giant vesicles. *Biomacromolecules* **2008,** *9* (1), 396-402.
7.24. Christensen, K.; Bose, H. S.; Harris, F. M.; Miller, W. L.; Bell, J. D., Binding of steroidogenic acute regulatory protein to synthetic membranes suggests an active molten globule. *Journal of Biological Chemistry* **2001,** *276* (20), 17044-17051.

7.25. Grasset, F.; Dorson, F.; Cordier, S.; Molard, Y.; Perrin, C.; Marie, A. M.; Sasaki, T.; Haneda, H.; Bando, Y.; Mortier, M., Water-in-oil microemulsion preparation and characterization of $Cs_2Mo_6X_{14}$ @$SiO_2$ phosphor nanoparticles based on transition metal clusters (X = Cl, Br, and I). *Advanced Materials* **2008,** *20* (1), 143-.
7.26. Nan, A. J.; Bai, X.; Son, S. J.; Lee, S. B.; Ghandehari, H., Cellular uptake and cytotoxicity of silica nanotubes. *Nano Letters* **2008,** *8* (8), 2150-2154.

# Chapter 8. Conclusion and Future Work

The work discussed in this dissertation resolves some challenges in nanoparticle synthesis and characterization. Mostly aerosol spray pyrolysis techniques were used, but when the limitations of this method were encountered, alternative routes were developed as needed.

Basically, the advantages of the spray pyrolysis system are: (i) the particles produced are spherical, as powders, ready to be used; (ii) the distribution of their diameters is controllable from micrometer to submicrometer, by types of atomizer and precursor concentration; (iii) fast heating and cooling enable some structures that will collapse during a long-time heating; (iv) multicomponent particles are easy to form, only by controlling the precursor solution constituents, and process of solvent evaporation and pyrolysis; (v) the purity of the product is high, due to the identical composition (by concentration) of the droplets; and (vi) low-cost, short running-time, high-output and continuous process ensure its potential to be industrialized. There also exist limitations of this method; thus, some other techniques or modification of the set-up are needed to overcome the deficiencies of the process. The significant problems to be addressed include: (i) polydisperse droplet size may cause size sensitive particles with different morphologies, and thus, with possibly different properties; (ii) efficiency of the equipment set-up is waiting to be improved (atomization, during flow and collection); (iii) some structures, such as high-crystalized lattice structure, are difficult to realize without post-treatment due to the short (heating) residence time. At the same time of amending the set-up and exploring factors to control the system (Chapter 2-5), conventional chemical syntheses, such as polymer-templated emulsion route, are also utilized to

resolve some problems (Chapter 7). To better understand mechanisms and properties of spray pyrolysis reaction pathways and kinetics, further development and improvement of the on-line aerosol/nanoparticle measurement techniques also deserve more dedication (Chapter 6). A more detailed discussion of the future extensive work is listed below.

1. Pursuing studies on effects of additives to the crystalline formation and photoelectric properties of copper compounds

In Chapter 2, iron oxides with a series of morphologies and properties were synthesized by adjusting spray pyrolysis conditions. This introductory study demonstrated that through choice of reactor temperature and templating compounds, the pore structure and magnetic properties can be varied. What is interesting is that though the particle structures are the same with or without urea, when surfactant F127 was added, the porous structure diminished without urea when the surfactant CTAB was added. This result suggests that the study the formation mechanism of the surfactant templated porous structure and the role of urea in generating porosity should be undertaken. Besides the materials of iron oxides, copper oxide is a photoelectric chemical, which can be used in solar cells.[8.1] By adjusting the crystalline structure and porous structure, its activity can be improved,[8.2] so similar study for copper oxide might be interesting. Part of my preliminary results are shown in Figures 8.1(XRD) and 8.2(TEM). Samples are prepared by spray-pyrolyzing at 400 °C, from aqueous solution of copper nitrate and CTAB (sample A) or F127 (sample B). The quantitative crystalline analyses were obtained by Rietveld method. Although both samples consisted of two crystalline phases of $Cu_2(OH)_3NO_3$ (phase 1: rouaite and phase 2: gerhardtite), sample A has a better crystalline structure, indicated by sharper peaks (Figure 8.1), with 76.1% of phase 1 and

23.9% of phase 2 (*cf.* 66.0% of phase 1 and 34.0% of phase 2 for sample B). But the reason beneath this phenomenon and its effect to the photoelectric properties will be the future focus.

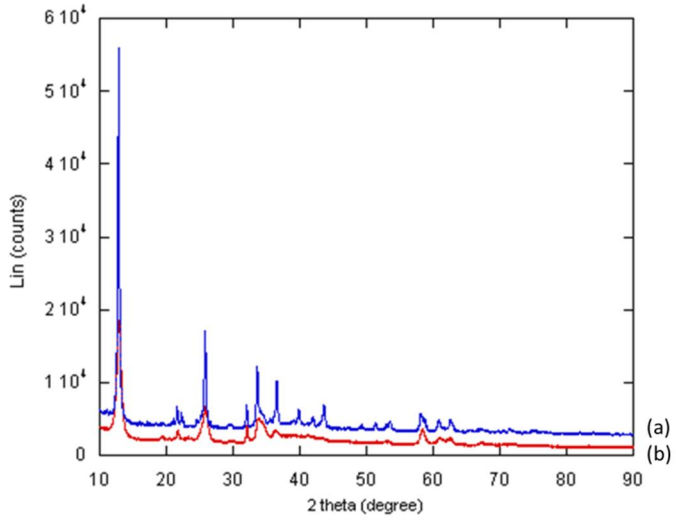


Figure 8.1. XRD analyses of (a) sample A and (b) sample B.

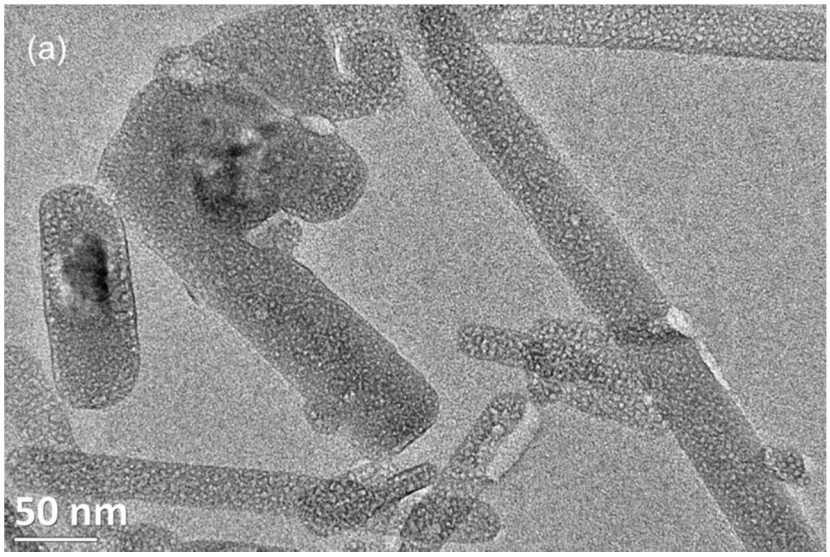

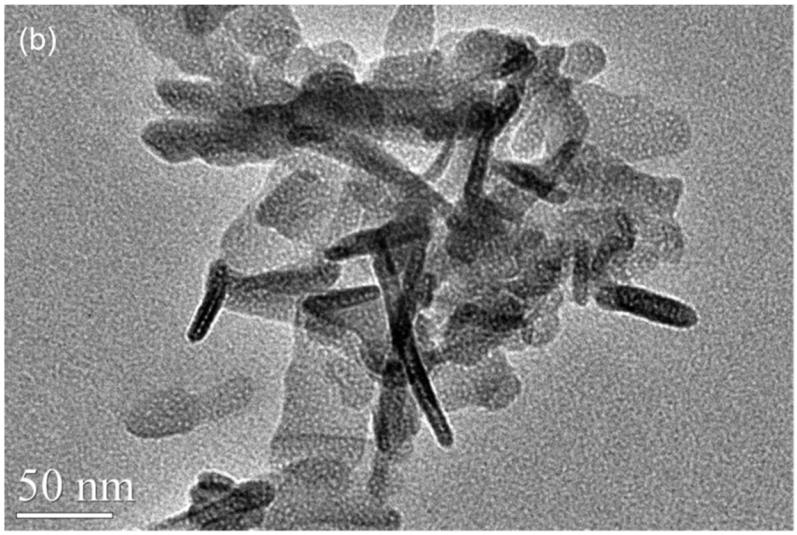

Figure 8.2. TEM images of (a) sample A and (b) sample B.

2. Conducting computer simulation to correlate the packing effect to the refractive index based on the Maxwell equation

In chapter 3, a synthesis route of new optical standards and a methodology to retrieve its refractive index have been designed. In this research, the results show that refractive index is a function of particle size, where the supportive theory should be strengthened for the data. Thereby, the theory will further complete the model of refractive index calculation for aerosol particles, with higher accuracy. Size-dependent refractive index of this sample may be caused by packing tightness; thus, the particle can be hypothesized as a two-component particle (void and carbon-like material), and then the Maxwell equation will be used to calculate the refractive index theoretically,[8.3] and end with a model to relate the porosity, particle size and refractive index.

3. Improving the electrochemical properties of cathode materials by spray pyrolysis

In chapters 4 and 5, spray pyrolysis synthesized nanoparticles are used as lithium ion battery anode materials. An ideational structure is the high charge-capacity nanoparticle dispersed in carbon frame, so that the carbon enables an electron and lithium-ion conductive path for its fast transportation. If this kind of material is realized, it will have

high charge-capacity, high rate capability and superior cycle life. This particular structure is conventionally difficult to attain because carbon will reduce the electro-active material, while the short- and high-temperature heating, followed by fast cooling to freeze the structure, enables the synthesis of this structure. We have already prepared some anode materials. In regard to the cathode design, the dilemma is that a well-crystalized lattice structure is needed for lithium ion intercalation, which, however, is less possible in short heating residence time. This will be the next research focus in this field.

4. Completing further research on structure-formation mechanism, regarding relative transportation of solute and solvent in the aerosol droplet

In chapter 6, a new density measurement method is designed; then, formation mechanisms of porous iron oxide and hollow copper oxide by spray pyrolysis are proposed. The mechanisms are based on the comparison of transportation of the solute and the solvent, confirmed by the density measurements. Transportation property is a comprehensive property that is affected by many factors, such as viscosity of the solution, solubility of the solute, melting point of solute, vapor pressure of the solvent in the flow system, influence of additives to the solution system, *etc.* Further research can be focused on contribution of each factor to the relative transportation of solute and solvent, and finalized in more complete mechanism models. By controlling the synthesis conditions, desired structures can be created by spray pyrolysis, such as hollow iron oxide and porous copper oxide.

5. Extending the drug delivery study to real biological system

In chapter 7, a one-step route to synthesize porous and stably fixed dye-silica nanoparticle is designed. This material is a potential drug delivery, within which pores

can load drug and fluorescence is responsible for tracking its metabolic pathway. The work is emphasizing the initiation of the synthetic idea, so the next step is to continue the quantitative analysis of the material's fluorescent intensity in a physiological environment for at least one period of its metabolic cycle. After drugs are loaded, research for its loading capacity and releasing profile will be engaged in. In addition, toxicity tests *in vitro* and eventually *in vivo* are essential to realize its application, with adequate modification if needed.

In conclusion, in spray pyrolysis, the salts are mixed at the molecular level in the precursor solution, so the multi-component particles can be formed as homogenous solid solutions or phase-separated materials, by properly controlling the conditions in terms of practical needs. A complete mechanism research of the entire process is required for the optimization of the synthetic conditions, with the assistance of the development of aerosol characterization techniques. Finally, by innovating this synthetic system or exploiting more promising alternatives, a leap in nanotechnology will be achieved.

Reference


8.1. Singh, D. P.; Ali, N., Synthesis of $TiO_2$ and CuO nanotubes and nanowires. *Science of Advanced Materials* 2010, *2* (3), 295-335.

8.2. Xiao, X. D.; Miao, L.; Xu, G.; Lu, L. M.; Su, Z. M.; Wang, N.; Tanemura, S., A facile process to prepare copper oxide thin films as solar selective absorbers. *Applied Surface Science* 2011, *257* (24), 10729-10736.

8.3. Pelinovsky, D.; Schneider, G., Justification of the coupled-mode approximation for a nonlinear elliptic problem with a periodic potential. *Applicable Analysis* 2007, *86* (8), 1017-1036.

# References


1.1. Hancock, Y., The 2010 Nobel Prize in physics-ground-breaking experiments on graphene. *Journal of Physics D-Applied Physics* **2011,** *44* (47).

1.2. Mullin, J. M., *Crystallization*. 4th ed.; 2001.

1.3. Peng, Z. A.; Peng, X. G., Formation of high-quality CdTe, CdSe, and CdS nanocrystals using CdO as precursor. *Journal of the American Chemical Society* **2001,** *123* (1), 183-184; Qu, L. H.; Peng, Z. A.; Peng, X. G., Alternative routes toward high quality CdSe nanocrystals. *Nano Letters* **2001,** *1* (6), 333-337.

1.4. Peng, Z. A.; Peng, X. G., Nearly monodisperse and shape-controlled CdSe nanocrystals via alternative routes: Nucleation and growth. *Journal of the American Chemical Society* **2002,** *124* (13), 3343-3353.

1.5. Wright, J. D.; Sommerdijk, N. A. J. M., *Sol-Gel Materials: Chemistry and applications*. 2000.

1.6. Callegari, A.; Tonti, D.; Chergui, M., Photochemically grown silver nanoparticles with wavelength-controlled size and shape. *Nano Letters* **2003,** *3* (11), 1565-1568; Maillard, M.; Giorgio, S.; Pileni, M. P., Silver nanodisks. *Advanced Materials* **2002,** *14* (15), 1084-; Hao, E.; Bailey, R. C.; Schatz, G. C.; Hupp, J. T.; Li, S. Y., Synthesis and optical properties of "branched" gold nanocrystals. *Nano Letters* **2004,** *4* (2), 327-330; Yu, Y. Y.; Chang, S. S.; Lee, C. L.; Wang, C. R. C., Gold nanorods: Electrochemical synthesis and optical properties. *Journal of Physical Chemistry B* **1997,** *101* (34), 6661-6664; Link, S.; Burda, C.; Mohamed, M. B.; Nikoobakht, B.; El-Sayed, M. A., Laser photothermal melting and fragmentation of gold nanorods: Energy and laser pulse-width dependence. *Journal of Physical Chemistry A* **1999,** *103* (9), 1165-1170; Jana, N. R.; Gearheart, L.; Murphy, C. J., Wet chemical synthesis of high aspect ratio cylindrical gold nanorods. *Journal of Physical Chemistry B* **2001,** *105* (19), 4065-4067; Lisiecki, I.; Billoudet, F.; Pileni, M. P., Control of the shape and the size of copper metallic particles. *Journal of Physical Chemistry* **1996,** *100* (10), 4160-4166.

1.7. Uskokovic, V.; Drofenik, M., Synthesis of materials within reverse micelles. *Surface Review and Letters* **2005,** *12* (2), 239-277.

1.8. Taleb, A.; Petit, C.; Pileni, M. P., Synthesis of highly monodisperse silver nanoparticles from AOT reverse micelles: A way to 2D and 3D self-organization. *Chemistry of Materials* **1997,** *9* (4), 950-959; Barnickel, P.; Wokaun, A., Synthesis of metal colloids in inverse microemultions. *Molecular Physics* **1990,** *69* (1), 1-9; Chen, Z. J.; Ou, X. M.; Tang, F. Q.; Jiang, L., Effect of nanometer particles on the adsorbability and enzymatic activity of glucose oxidase. *Colloids and Surfaces B-Biointerfaces* **1996,** *7* (3-4), 173-179; Lisiecki, I.; Pileni, M. P., Synthesis of copper metallic clusters using reverse micelles as microreactors. *Journal of the American Chemical Society* **1993,** *115* (10), 3887-3896.

1.9. Kawai, T.; Fujino, A.; KonNo, K., Synthesis of monodisperse $ZrO_2$ particles in polyoxyethylated nonionic reversed micelles. *Colloids and Surfaces a-Physicochemical and Engineering Aspects* **1996,** *109*, 245-253; Chang, S. Y.; Liu, L.; Asher, S. A., Preparation and properties of tailored morphology, monodisperse colloidal silica cadmium-sulfide nanocomposites. *Journal of the American Chemical Society* **1994,** *116* (15), 6739-6744; Joselevich, E.; Willner, I., Phtosensitization of

quantum-size $TiO_2$ particles in water-in-oil microemulsions. *Journal of Physical Chemistry* **1994,** *98* (31), 7628-7635; Chhabra, V.; Pillai, V.; Mishra, B. K.; Morrone, A.; Shah, D. O., Synthesis, characterization, and properties of microemulsion-mediated nanophase $TiO_2$ particles. *Langmuir* **1995,** *11* (9), 3307-3311; Osseoasare, K.; Arriagada, F. J., Preparation of $SiO_2$ nanoparticles in a nonionic reverse micellar system. *Colloids and Surfaces* **1990,** *50*, 321-339.

1.10. Qi, L. M.; Ma, J. M.; Cheng, H. M.; Zhao, Z. G., Reverse micelle based formation of $BaCO_3$ nanowires. *Journal of Physical Chemistry B* **1997,** *101* (18), 3460-3463.

1.11. Kandori, K.; Konno, K.; Kitahara, A., Formation of ionic water oil microemulsions and their application in the preparation of $CaCO_3$ particles. *Journal of Colloid and Interface Science* **1988,** *122* (1), 78-82; Kandori, K.; Konno, K.; Kitahara, A., Preparation of BaCO3 particles in ionic W/O microemulsions. *Journal of Dispersion Science and Technology* **1988,** *9* (1), 61-73.

1.12. Dvolaitzky, M.; Ober, R.; Taupin, C.; Anthore, R.; Auvray, X.; Petipas, C.; Williams, C., Silver-chloride micro-crystals suspensions in microemulsion media. *Journal of Dispersion Science and Technology* **1983,** *4* (1), 29-45; Chew, C. H.; Gan, L. M.; Shah, D. O., The effect of alkanes on the formation of ultrafine silver bromide particles in ionic W/O microemulsions. *Journal of Dispersion Science and Technology* **1990,** *11* (6), 593-609; Monnoyer, P.; Fonseca, A.; Nagy, J. B., Preparation of colloidal AgBr particles from microemlsions. *Colloids and Surfaces a-Physicochemical and Engineering Aspects* **1995,** *100*, 233-243; Bagwe, R. P.; Khilar, K. C., Effects of the intermicellar exchange rate and cations on the size of silver chloride nanoparticles formed in reverse micelles of AOT. *Langmuir* **1997,** *13* (24), 6432-6438.

1.13. Hopwood, J. D.; Mann, S., Synthesis of barium sulfate nanoparticles and nanofilaments in reverse micelles and microemulsions. *Chemistry of Materials* **1997,** *9* (8), 1819-1828.

1.14. Hirai, T.; Shiojiri, S.; Komasawa, I., Preparation of metal sulfide composite ultrafine particles in reverse micellar systems and their photocatalytic property. *Journal of Chemical Engineering of Japan* **1994,** *27* (5), 590-597.

1.15. Matijevic, E., Preparation and properties of uniform size colloids. *Chemistry of Materials* **1993,** *5* (4), 412-426.

1.16. Huang, Y. X.; Guo, C. J., Synthesis of nanosized zirconia particles via urea hydrolysis. *Powder Technology* **1992,** *72* (2), 101-104; Potdar, H. S.; Deshpande, S. B.; Date, S. K., Chemical coprecipitation of mixed (Ba+Ti) oxalates precursor leading to BaTiO3 powders. *Materials Chemistry and Physics* **1999,** *58* (2), 121-127; Sheen, S. R.; Hsu, Y. J.; Chen, D. H.; Ho, J. S.; Shei, C. Y.; Chang, C. T., Synthesis and characterization of high-Tc Y-Ba-Cu-O superconducting oxides by coprecipitation from triethylamine-oxalate media. *Materials Letters* **1991,** *10* (11-12), 489-493; Spanhel, L.; Haase, M.; Weller, H.; Henglein, A., Photochemistry of colloidal semiconductors. 20. Surface modification and stability of strong luminescing CdS particles. *Journal of the American Chemical Society* **1987,** *109* (19), 5649-5655; Rogach, A. L.; Kornowski, A.; Gao, M. Y.; Eychmuller, A.; Weller, H., Synthesis and characterization of a size series of extremely small thiol-stabilized CdSe nanocrystals. *Journal of Physical Chemistry B* **1999,** *103* (16), 3065-3069; Gao, M. Y.; Kirstein, S.; Mohwald, H.; Rogach, A. L.; Kornowski, A.; Eychmuller, A.; Weller,

H., Strongly photoluminescent CdTe nanocrystals by proper surface modification. *Journal of Physical Chemistry B* **1998,** *102* (43), 8360-8363; Mews, A.; Eychmuller, A.; Giersig, M.; Schooss, D.; Weller, H., Preparation, characterization, and photophysics of the quantum-dot quantum-well system CdS/HgS/CdS. *Journal of Physical Chemistry* **1994,** *98* (3), 934-941.

1.17. Dhara, S., Formation, dynamics, and characterization of nanostructures by ion beam irradiation. *Critical Reviews in Solid State and Materials Sciences* **2007,** *32* (1-2), 1-50.

1.18. Demianets, L. N.; Lobachev, A. N., Hydrothermal synthesis of crystals. *Kristall Und Technik-Crystal Research and Technology* **1979,** *14* (5), 509-525.

1.19. O'Donoghu，Michael, *A guide to man-made gemstones*. Van Nostrand Reinhold Company: Great Britain, 1983.

1.20. *50 years progress in crystal growth*. Elsevier: Stanford, CA, 2004.

1.21. Tan, L.; Wang, L.; Wang, Y., Hydrothermal synthesis of $SnO_2$ nanostructures with different morphologies and their optical properties. *Journal of Nanomaterials* **2011**.

1.22. *Aqueous systems at elevated temperatures and pressures*. Elsevier Ltd: 2004.

1.23. Hiruma, K.; Katsuyama, T.; Ogawa, K.; Koguchi, M.; Kakibayashi, H.; Morgan, G. P., Quantum size microcrystals grown using organometallic vapor-phase epitaxy. *Applied Physics Letters* **1991,** *59* (4), 431-433; Hiruma, K.; Yazawa, M.; Katsuyama, T.; Ogawa, K.; Haraguchi, K.; Koguchi, M.; Kakibayashi, H., Growth and optical-properties of nanometer-scale GaAs and InAs whiskers. *Journal of Applied Physics* **1995,** *77* (2), 447-462; Yazawa, M.; Koguchi, M.; Hiruma, K., Heteroepitaxial ultrafine wire-like growth of InAs on GaAs substrates. *Applied Physics Letters* **1991,** *58* (10), 1080-1082; Yazawa, M.; Koguchi, M.; Muto, A.; Ozawa, M.; Hiruma, K., Effect of one monolayer of surface gold atoms on the epitaxial-growth of InAs nanowhiskers. *Applied Physics Letters* **1992,** *61* (17), 2051-2053; Bai, Z. G.; Yu, D. P.; Wang, J. J.; Zou, Y. H.; Qian, W.; Fu, J. S.; Feng, S. Q.; Xu, J.; You, L. P., Synthesis and photoluminescence properties of semiconductor nanowires. *Materials Science and Engineering B-Solid State Materials for Advanced Technology* **2000,** *72* (2-3), 117-120; Dai, H. J.; Wong, E. W.; Lu, Y. Z.; Fan, S. S.; Lieber, C. M., Synthsis and characterization of carbide nanorods. *Nature* **1995,** *375* (6534), 769-772; Han, W. Q.; Fan, S. S.; Li, Q. Q.; Liang, W. J.; Gu, B. L.; Yu, D. P., Continuous synthesis and characterization of silicon carbide nanorods. *Chemical Physics Letters* **1997,** *265* (3-5), 374-378; Han, W. Q.; Fan, S. S.; Li, Q. Q.; Gu, B. L.; Zhang, X. B.; Yu, D. P., Synthesis of silicon nitride nanorods using carbon nanotube as a template. *Applied Physics Letters* **1997,** *71* (16), 2271-2273; Wu, Y.; Cui, Y.; Huynh, L.; Barrelet, C. J.; Bell, D. C.; Lieber, C. M., Controlled growth and structures of molecular-scale silicon nanowires. *Nano Letters* **2004,** *4* (3), 433-436; Zhong, Z. H.; Qian, F.; Wang, D. L.; Lieber, C. M., Synthesis of p-type gallium nitride nanowires for electronic and photonic nanodevices. *Nano Letters* **2003,** *3* (3), 343-346.

1.24. Jung, D. S.; Bin Park, S.; Kang, Y. C., Design of particles by spray pyrolysis and recent progress in its application. *Korean Journal of Chemical Engineering* **2010,** *27* (6), 1621-1645.

1.25. Herlin-Boime, N.; Mayne-L'Hermite, M.; Reynaud, C., Advances in the laser pyrolysis synthesis of nanoparticles. *Annales De Chimie-Science Des Materiaux* **2006,** *31* (3), 295-315.

1.26. Kim, J. H.; Yi, J. H.; Ko, Y. N.; Kang, Y. C., Electrochemical properties of nano-sized $LiNi_{1/3}Co_{1/3}Mn_{1/3}O_2$ powders in the range from 56 to 101 nm prepared by flame spray pyrolysis. *Materials Chemistry and Physics* **2012,** *134* (1), 254-259.
1.27. Meyers, R. A., *Encyclopedia of physical science and technology*. 3rd ed.; Academic Press, Inc.: San Diego, 2001.
1.28. Gopi, K. R.; Nagarajan, R., Advances in nanoalumina ceramic particle fabrication using sonofragmentation. *IEEE Transactions on Nanotechnology* **2008,** *7* (5), 532-537.
1.29. Chen, D.; Liu, H.-y.; Xia, S.-r., One-step decomposition of basic carbonates into single-phase crystalline metallic oxides nanoparticle by ultrasonic wave-assisted ball milling technology. *Ceramics International* **2012,** *38* (1), 821-825; Shu, C.; Zhang, J.; Ge, J.; Sim, J. H.; Burke, B. G.; Williams, K. A.; Rylander, W. M.; Campbell, T.; Puretzky, A.; Rouleau, C.; Geohegan, D. B.; More, K.; Esker, A. R.; Gibson, H. W.; Dorn, H. C., A facile high-speed vibration milling method to water-disperse single-walled carbon nanohorns. *Chemistry of Materials* **2010,** *22* (2), 347-351; Hedayati, A.; Golestan, Z.; Ranjbar, K.; Borhani, G. H., Effect of ball milling on formation of $ZnAl_2O_4$ by reduction reaction of ZnO and Al powder mixture. *Powder Metallurgy and Metal Ceramics* **2011,** *50* (5-6), 268-274.
1.30. Mansoori, G. A., *Principles of nanotechnology*. World Scientific: Singapore, 2005.
1.31. Anguelouch, A.; Leheny, R. L.; Reich, D. H., Application of ferromagnetic nanowires to interfacial microrheology. *Applied Physics Letters* **2006,** *89* (11); Fung, A. O.; Kapadia, V.; Pierstorff, E.; Ho, D.; Chen, Y., Induction of cell death by magnetic actuation of nickel nanowires internalized by fibroblasts. *Journal of Physical Chemistry C* **2008,** *112* (39), 15085-15088; Tanase, M.; Bauer, L. A.; Hultgren, A.; Silevitch, D. M.; Sun, L.; Reich, D. H.; Searson, P. C.; Meyer, G. J., Magnetic alignment of fluorescent nanowires. *Nano Letters* **2001,** *1* (3), 155-158; Gao, J. H.; Zhang, B.; Zhang, X. X.; Xu, B., Magnetic-dipolar-interaction-induced self-assembly affords wires of hollow nanocrystals of cobalt selenide. *Angewandte Chemie-International Edition* **2006,** *45* (8), 1220-1223.
1.32. Yan, M.; Fresnais, J.; Berret, J. F., Growth mechanism of nanostructured superparamagnetic rods obtained by electrostatic co-assembly. *Soft Matter* **2010,** *6* (9), 1997-2005.
1.33. Kralchevsky, P. A.; Paunov, V. N.; Denkov, N. D.; Ivanov, I. B.; Nagayama, K., Energetical and force approaches to the capillary interactions between particles and force approaches to the capillary interactions between particles attached to a liquid fluid interface. *Journal of Colloid and Interface Science* **1993,** *155* (2), 420-437; Paunov, V. N.; Kralchevsky, P. A.; Denkov, N. D.; Nagayama, K., Lateral capillary forces between floating submillimeter particles. *Journal of Colloid and Interface Science* **1993,** *157* (1), 100-112.
1.34. Green, D. L.; Lin, J. S.; Lam, Y. F.; Hu, M. Z. C.; Schaefer, D. W.; Harris, M. T., Size, volume fraction, and nucleation of Stober silica nanoparticles. *Journal of Colloid and Interface Science* **2003,** *266* (2), 346-358.
1.35. Okuyama, K.; Abdullah, M.; Lenggoro, I. W.; Iskandar, F., Preparation of functional nanostructured particles by spray drying. *Advanced Powder Technology* **2006,** *17* (6), 587-611.

1.36. Schiller, R.; Weiss, C. K.; Geserick, J.; Husing, N.; Landfester, K., Synthesis of mesoporous silica particles and capsules by miniemulsion technique. *Chemistry of Materials* **2009,** *21* (21), 5088-5098.
1.37. Beck, J. S.; Vartuli, J. C.; Roth, W. J.; Leonowicz, M. E.; Kresge, C. T.; Schmitt, K. D.; Chu, C. T. W.; Olson, D. H.; Sheppard, E. W.; McCullen, S. B.; Higgins, J. B.; Schlenker, J. L., A new family of mesoporous molecular-sieves prepared with liquid-crystal templates. *Journal of the American Chemical Society* **1992,** *114* (27), 10834-10843.
1.38. Riviere, J. C.; Myhra, S., *Handbook of surface and interface analysis: methods for problem-solving*. 2nd ed.; Taylor&Francis Group: 2009.
1.39. Clark, M. D.; Kumar, S. K.; Owen, J. S.; Chan, E. M., Focusing nanocrystal size distributions via production control. *Nano Letters* **2011,** *11* (5), 1976-1980.
1.40. Peng, X. G.; Wickham, J.; Alivisatos, A. P., Kinetics of II-VI and III-V colloidal semiconductor nanocrystal growth: "Focusing" of size distributions. *Journal of the American Chemical Society* **1998,** *120* (21), 5343-5344.
1.41. Peng, Z. A.; Peng, X. G., Mechanisms of the shape evolution of CdSe nanocrystals. *Journal of the American Chemical Society* **2001,** *123* (7), 1389-1395.
1.42. Burda, C.; Chen, X. B.; Narayanan, R.; El-Sayed, M. A., Chemistry and properties of nanocrystals of different shapes. *Chemical Reviews* **2005,** *105* (4), 1025-1102.
1.43. Nan, Z. D.; Wang, M. Y.; Yang, B. Q., In situ investigation on the formation mechanism of MCM-41 mesoporous silica by microcalorimetry. *Journal of Chemical and Engineering Data* **2009,** *54* (1), 83-89.
1.44. Decher, G., Fuzzy nanoassemblies: Toward layered polymeric multicomposites. *Science* **1997,** *277* (5330), 1232-1237.
1.45. Guerrero-Martinez, A.; Perez-Juste, J.; Liz-Marzan, L. M., Recent progress on silica coating of nanoparticles and related nanomaterials. *Advanced Materials* **2010,** *22* (11), 1182-1195.
1.46. Gorelikov, I.; Matsuura, N., Single-step coating of mesoporous silica on cetyltrimethyl ammonium bromide-capped nanoparticles. *Nano Letters* **2008,** *8* (1), 369-373.
1.47. Capek, I., On inverse miniemulsion polymerization of conventional water-soluble monomers. *Advances in Colloid and Interface Science* **2010,** *156* (1-2), 35-61.
1.48. Wan, Y.; Shi, Y. F.; Zhao, D. Y., Designed synthesis of mesoporous solids via nonionic-surfactant-templating approach. *Chemical Communications* **2007,** (9), 897-926.
1.49. Liu, J.; Liu, F.; Gao, K.; Wu, J. S.; Xue, D. F., Recent developments in the chemical synthesis of inorganic porous capsules. *Journal of Materials Chemistry* **2009,** *19* (34), 6073-6084.
1.50. Arakawa, T.; Yamamoto, T.; Shoji, S., Micro-bubble formation with organic membrane in a multiphase microfluidic system. *Sensors and Actuators a-Physical* **2008,** *143* (1), 58-63.
1.51. Zhang, G. H.; Bon, S. A. F.; Zhao, C. Y., Synthesis, characterization and thermal properties of novel nanoencapsulated phase change materials for thermal energy storage. *Solar Energy* **2012,** *86* (5), 1149-1154.
1.52. Yang, S.; Liu, H. R.; Zhang, Z. C., A facile route to hollow superparamagnetic magnetite/polystyrene nanocomposite microspheres via inverse miniemulsion

polymerization. *Journal of Polymer Science Part a-Polymer Chemistry* **2008,** *46* (12), 3900-3910.
1.53. Miao, J.-J.; Jiang, L.-P.; Liu, C.; Zhu, J.-M.; Zhu, J.-J., General sacrificial template method for the synthesis of cadmium chalcogenide hollow structures. *Inorganic Chemistry* **2007,** *46* (14).
1.54. Li, H. X.; Bian, Z. F.; Zhu, J.; Zhang, D. Q.; Li, G. S.; Huo, Y. N.; Li, H.; Lu, Y. F., Mesoporous titania spheres with tunable chamber stucture and enhanced photocatalytic activity. *Journal of the American Chemical Society* **2007,** *129* (27), 8406-.
1.55. Huh, S.; Wiench, J. W.; Yoo, J. C.; Pruski, M.; Lin, V. S. Y., Organic functionalization and morphology control of mesoporous silicas via a co-condensation synthesis method. *Chemistry of Materials* **2003,** *15* (22), 4247-4256.
1.56. Yang, B.; Edler, K.; Guo, C.; Liu, H. Z., Assembly of nonionic-anionic co-surfactants to template mesoporous silica vesicles with hierarchical structures. *Microporous and Mesoporous Materials* **2010,** *131* (1-3), 21-27.
1.57. Lou, X. W.; Archer, L. A.; Yang, Z. C., Hollow micro-/nanostructures: Synthesis and applications. *Advanced Materials* **2008,** *20* (21), 3987-4019.
1.58. Yu, Z. S.; Johnston, K. P.; Williams, R. O., Spray freezing into liquid versus spray-freeze drying: Influence of atomization on protein aggregation and biological activity. *European Journal of Pharmaceutical Sciences* **2006,** *27* (1), 9-18; Heller, M. C.; Carpenter, J. F.; Randolph, T. W., Protein formulation and lyophilization cycle design: Prevention of damage due to freeze-concentration induced phase separation. *Biotechnology and Bioengineering* **1999,** *63* (2), 166-174.
1.59. Han, Z. H.; Yang, B.; Kim, S. H.; Zachariah, M. R., Application of hybrid sphere/carbon nanotube particles in nanofluids. *Nanotechnology* **2007,** *18* (10).
1.60. Yeh, H. C.; Cheng, Y. S., Electrical aerosol analyzer-an alternate method for use at high-altitude or reduced pressure. *Atmospheric Environment* **1982,** *16* (5), 1269-1270.
1.61. Intra, P.; Tippayawong, N., An overview of differential mobility analyzers for size classification of nanometer-sized aerosol particles. *Songklanakarin Journal of Science and Technology* **2008,** *30* (2), 243-256.
1.62. Kulkarni, P.; Baron, P. A.; Willek, K., *Aerosol Measurement: Principles, techniques, and applications*. Wiley: 2011.
1.63. Richardson, J. F.; Wooding, E. R., The use of a sedimentation cell in the sampling of aerosols. *Chemical Engineering Science* **1955,** *4* (1), 26-28.
1.64. Gong, G. C.; Yang, Z. Z.; Zhu, S. L., Numerical investigation of the effect of helix angle and leaf margin on the flow pattern and the performance of the axial flow cyclone separator. *Applied Mathematical Modelling* **2012,** *36* (8), 3916-3930.
1.65. Sawyer, K. F.; Walton, W. H., The confuge-a size-separating sampling device fro airborne particles. *Journal of Scientific Instruments* **1950,** *27* (10), 272-276.
1.66. Zhang, S. H.; Akutsu, Y.; Russell, L. M.; Flagan, R. C.; Seinfeld, J. H., Radial differential mobility analyzer. *Aerosol Science and Technology* **1995,** *23* (3), 357-372.
1.67. Gerber, H. E., Performance of goetz aerosol spectrometer. *Atmospheric Environment* **1971,** *5* (12), 1009-.
1.68. Oeseburg, F.; Roos, R., Properties of the srober contrifugal aerosol spectrometer at a high sampling flow: Calibration, resolving power and correction factors for particle losses. *Journal of Aerosol Science* **1979,** *10* (6), 539-.

1.69. Kim, S. H.; Woo, K. S.; Liu, B. Y. H.; Zachariah, M. R., Method of measuring charge distribution of nanosized aerosols. *Journal of Colloid and Interface Science* **2005,** *282* (1), 46-57.
1.70. Hinds, W. C., *Aerosol technology: Properties, behavior, and measurement of airborne particles*. Wiley: 1999.
1.71. Olfert, J. S.; Collings, N., New method for particle mass classification - the couette centrifugal particle mass analyzer. *Journal of Aerosol Science* **2005,** *36* (11), 1338-1352.
1.72. Ehara, K.; Hagwood, C.; Coakley, K. J., Novel method to classify aerosol particles according to their mass-to-charge ratio - Aerosol particle mass analyser. *Journal of Aerosol Science* **1996,** *27* (2), 217-234.
1.73. Havey, D. K.; Bueno, P. A.; Gillis, K. A.; Hodges, J. T.; Mulholland, G. W.; van Zee, R. D.; Zachariah, M. R., Photoacoustic Spectrometer with a Calculable Cell Constant for Measurements of Gases and Aerosols. *Analytical Chemistry* **2010,** *82* (19), 7935-7942.
1.74. Makhijani, K., *Nanotechnology: Fundamentals and applications*. I. K. International: New Delhi, 2008.
1.75. Sahu, S. C.; Casciano, D. A., *Nanotoxicity: From in vivo and in vitro models to health risks*. John Wiley&Sons Ltd: Chichester, 2009.
2.1. Akbarzadeh, A.; Samiei, M.; Davaran, S., Magnetic nanoparticles: preparation, physical properties, and applications in biomedicine. *Nanoscale Research Letters* **2012,** *7*, 1-13.
2.2. Sosnovik, D. E.; Nahrendorf, M.; Weissleder, R., Molecular magnetic resonance imaging in cardiovascular medicine. *Circulation* **2007,** *115* (15), 2076-2086; Moghimi, S. M.; Hunter, A. C.; Murray, J. C., Long-circulating and target-specific nanoparticles: Theory to practice. *Pharmacological Reviews* **2001,** *53* (2), 283-318; Muldoon, L. L.; Sandor, M.; Pinkston, K. E.; Neuwelt, E. A., Imaging, distribution, and toxicity of superparamagnetic iron oxide magnetic resonance nanoparticles in the rat brain and intracerebral tumor. *Neurosurgery* **2005,** *57* (4), 785-796.
2.3. Jana, N. R.; Chen, Y. F.; Peng, X. G., Size- and shape-controlled magnetic (Cr, Mn, Fe, Co, Ni) oxide nanocrystals via a simple and general approach. *Chemistry of Materials* **2004,** *16* (20), 3931-3935.
2.4. Park, J.; An, K. J.; Hwang, Y. S.; Park, J. G.; Noh, H. J.; Kim, J. Y.; Park, J. H.; Hwang, N. M.; Hyeon, T., Ultra-large-scale syntheses of monodisperse nanocrystals. *Nature Materials* **2004,** *3* (12), 891-895; Hyeon, T.; Lee, S. S.; Park, J.; Chung, Y.; Bin Na, H., Synthesis of highly crystalline and monodisperse maghemite nanocrystallites without a size-selection process. *Journal of the American Chemical Society* **2001,** *123* (51), 12798-12801.
2.5. Sun, S. H.; Zeng, H.; Robinson, D. B.; Raoux, S.; Rice, P. M.; Wang, S. X.; Li, G. X., Monodisperse MFe2O4 (M = Fe, Co, Mn) nanoparticles. *Journal of the American Chemical Society* **2004,** *126* (1), 273-279; Chen, M.; Liu, J. P.; Sun, S. H., One-step synthesis of FePt nanoparticles with tunable size. *Journal of the American Chemical Society* **2004,** *126* (27), 8394-8395; Sun, S. H.; Murray, C. B.; Weller, D.; Folks, L.; Moser, A., Monodisperse FePt nanoparticles and ferromagnetic FePt nanocrystal superlattices. *Science* **2000,** *287* (5460), 1989-1992.

2.6. Weissleder, R.; Mahmood, U., Molecular imaging. *Radiology* **2001,** *219* (2), 316-333.
2.7. Kwon, S. G.; Piao, Y.; Park, J.; Angappane, S.; Jo, Y.; Hwang, N. M.; Park, J. G.; Hyeon, T., Kinetics of monodisperse iron oxide nanocrystal formation by "heating-up" process. *Journal of the American Chemical Society* **2007,** *129* (41), 12571-12584.
2.8. Hildebrand, H.; Mackenzie, K.; Kopinke, F. D., Novel nano-catalysts for wastewater treatment. *Global Nest Journal* **2008,** *10* (1), 47-53.
2.9. Chan, L.; Nesbeth, D.; MacKey, T.; Galea-Lauri, J.; Gaken, J.; Martin, F.; Collins, M.; Mufti, G.; Farzaneh, F.; Darling, D., Conjugation of lentivirus to paramagnetic particles via nonviral proteins allows efficient concentration and infection of primary acute myeloid leukemia cells. *Journal of Virology* **2005,** *79* (20), 13190-13194.
2.10. Hao, R.; Xing, R. J.; Xu, Z. C.; Hou, Y. L.; Gao, S.; Sun, S. H., Synthesis, Functionalization, and Biomedical Applications of multifunctional magnetic nanoparticles. *Advanced Materials* **2010,** *22* (25), 2729-2742.
2.11. Sreeja, V.; Joy, P. A., Microwave-hydrothermal synthesis of gamma-$Fe_2O_3$ nanoparticles and their magnetic properties. *Materials Research Bulletin* **2007,** *42* (8), 1570-1576.
2.12. Massart, R., Preparation of aqueous magnetic liquids in alkaline and acidic media. *IEEE Transactions on Magnetics* **1981,** *17* (2), 1247-1248.
2.13. Abu Mukh-Qasem, R.; Gedanken, A., Sonochemical synthesis of stable hydrosol of $Fe_3O_4$ nanoparticles. *Journal of Colloid and Interface Science* **2005,** *284* (2), 489-494.
2.14. Deng, Y.; Wang, L.; Yang, W.; Fu, S.; Elaissari, A., Preparation of magnetic polymeric particles via inverse microemulsion polymerization process. *Journal of Magnetism and Magnetic Materials* **2003,** *257* (1), 69-78.
2.15. Dacoata, G. M.; Degrave, E.; Debakker, P. M. A.; Vandenberghe, R. E., Synthesis and characterization of some iron-oxides by sol-gel method. *Journal of Solid State Chemistry* **1994,** *113* (2), 405-412.
2.16. Chen, D.; Xu, R., Hydrothermal synthesis and characterization of nanocrystalline $Fe_3O_4$ powders. *Materials Research Bulletin* **1998,** *33* (7), 1015-1021.
2.17. Basak, S.; Chen, D. R.; Biswas, P., Electrospray of ionic precursor solutions to synthesize iron oxide nanoparticles: Modified scaling law. *Chemical Engineering Science* **2007,** *62* (4), 1263-1268.
2.18. Veintemillas-Verdaguer, S.; Morales, M. P.; Serna, C. J., Continuous production of gamma-$Fe_2O_3$ ultrafine powders by laser pyrolysis. *Materials Letters* **1998,** *35* (3-4), 227-231.
2.19. Mao, B. D.; Kang, Z. H.; Wang, E. B.; Tian, C. G.; Zhang, Z. M.; Wang, C. L.; Song, Y. L.; Li, M. Y., Template free fabrication of hollow hematite spheres via a one-pot polyoxometalate-assisted hydrolysis process. *Journal of Solid State Chemistry* **2007,** *180* (2), 489-495.
2.20. Chen, D. H.; Chen, D. R.; Jiao, X. L.; Zhao, Y. T., Hollow-structured hematite particles derived from layered iron (hydro)oxyhydroxide-surfactant composites. *Journal of Materials Chemistry* **2003,** *13* (9), 2266-2270.
2.21. Shiho, H.; Kawahashi, N., Iron compounds as coatings on polystyrene latex and as hollow spheres. *Journal of Colloid and Interface Science* **2000,** *226* (1), 91-97.

2.22. Cheng, K.; Peng, S.; Xu, C. J.; Sun, S. H., Porous hollow $Fe_3O_4$ nanoparticles for targeted delivery and controlled release of cisplatin. *Journal of the American Chemical Society* **2009,** *131* (30), 10637-10644.
2.23. Liu, Q.; Ma, X.; Zachariah, M. R., Combined on-line differential mobility and particle mass analysis for determination of size resolved particle density and microstructure evolution. *Microporous and Mesoporous Materials* **2012,** *153*, 210-216.
2.24. Gadalla, A. M.; Yu, H. F., Thermal-decomposition of Fe (III) nitrate and its aerosol. *Journal of Materials Research* **1990,** *5* (6), 1233-1236.
2.25. Hu, Q. Y.; Hampsey, J. E.; Jiang, N.; Li, C. J.; Lu, Y. F., Surfactant-templated organic functionalized mesoporous silica with phosphino ligands. *Chemistry of Materials* **2005,** *17* (6), 1561-1569.
3.1. Sunkara, B.; Zhan, J. J.; Kolesnichenko, I.; Wang, Y. Q.; He, J. B.; Holland, J. E.; McPherson, G. L.; John, V. T., Modifying Metal Nanoparticle Placement on Carbon Supports Using an Aerosol-Based Process, with Application to the Environmental Remediation of Chlorinated Hydrocarbons. *Langmuir* **2011,** *27* (12), 7854-7859.
3.2. Friedlander, S., *Smoke, Dust, and Haze*. 2nd ed.; Oxford University Press, Inc.: New York, USA, 2000.
3.3. Barber, P.; Hill, S., *Light scattering by particles: Computational methods*. 1990.
3.4. Spinner, S.; Waxler, R. M., Relation Between Refractive Index and Density of Glasses Resulting From Annealing Compared with Corresponding Relation Resulting from Compression. *Applied Optics* **1966,** *5* (12), 1887-.
3.5. Gopi, K. R.; Nagarajan, R., Advances in Nanoalumina Ceramic Particle Fabrication Using Sonofragmentation. *IEEE Transactions on Nanotechnology* **2008,** *7* (5), 532-537.
3.6. Pol, V. D.; Bremmer, The diffraction of electromagnetic waves from an electrical point source round a finitely conducting sphere. *Philosophical Magazine series 7* **1937,** *24*.
3.7. McMurry, P. H., A review of atmospheric aerosol measurements. *Atmospheric Environment* **2000,** *34* (12-14), 1959-1999.
3.8. Duan, D. W.; Rao, Y. J.; Zhu, T., High sensitivity gas refractometer based on all-fiber open-cavity Fabry-Perot interferometer formed by large lateral offset splicing. *Journal of the Optical Society of America B-Optical Physics* **2012,** *29* (5), 912-915; Gao, R. X.; Liu, W. J.; Wang, Y. Y.; Wang, Q.; Zhao, F.; Qu, S. L., Design and fabrication of SMS fiber refractometer for liquid. *Sensors and Actuators a-Physical* **2012,** *179*, 5-9.
3.9. Havey, D. K.; Bueno, P. A.; Gillis, K. A.; Hodges, J. T.; Mulholland, G. W.; van Zee, R. D.; Zachariah, M. R., Photoacoustic Spectrometer with a Calculable Cell Constant for Measurements of Gases and Aerosols. *Analytical Chemistry* **2010,** *82* (19), 7935-7942.
3.10. Orphal, J., A critical review of the absorption cross-sections of O-3 and NO2 in the ultraviolet and visible. *Journal of Photochemistry and Photobiology a-Chemistry* **2003,** *157* (2-3), 185-209.
3.11. Gillis, K. A.; Havey, D. K.; Hodges, J. T., Standard photoacoustic spectrometer: Model and validation using O-2 A-band spectra. *Review of Scientific Instruments* **2010,** *81* (6).

3.12. Arnott, W. P.; Moosmuller, H.; Walker, J. W., Nitrogen dioxide and kerosene-flame soot calibration of photoacoustic instruments for measurement of light absorption by aerosols. *Review of Scientific Instruments* **2000,** *71* (12), 4545-4552.
3.13. Petzold, A.; Niessner, R., Photoacoustic soot sensor for in-situ black carbon monitoring. *Applied Physics B-Lasers and Optics* **1996,** *63* (2), 191-197.
3.14. Moosmuller, H.; Varma, R.; Arnott, W. P., Cavity ring-down and cavity-enhanced detection techniques for the measurement of aerosol extinction. *Aerosol Science and Technology* **2005,** *39* (1), 30-39.
3.15. *IPCC Fourth Assessment Report: Climate Change 2007*; 2007.
3.16. Kokhanovsky, A., *Aerosol Optics*. Springer: Chichester, UK, 2008.
3.17. Liu, Q.; Ma, X.; Zachariah, M. R., Combined on-line differential mobility and particle mass analysis for determination of size resolved particle density and microstructure evolution. *Microporous and Mesoporous Materials* **2012,** *153*, 210-216.
3.18. Kleiman-Shwarsctein, A.; Jaramillo, T. F.; Baeck, S. H.; Sushchikh, M.; McFarland, E. W., Low-voltage electrodeposition of fullerol thin films from aqueous solutions. *Journal of the Electrochemical Society* **2006,** *153* (7), C483-C487.
3.19. Miles, R. E. H.; Rudic, S.; Orr-Ewing, A. J.; Reid, J. P., Sources of Error and Uncertainty in the Use of Cavity Ring Down Spectroscopy to Measure Aerosol Optical Properties. *Aerosol Science and Technology* **2011,** *45* (11), 1360-1375.
3.20. Kim, S. H.; Woo, K. S.; Liu, B. Y. H.; Zachariah, M. R., Method of measuring charge distribution of nanosized aerosols. *Journal of Colloid and Interface Science* **2005,** *282* (1), 46-57.
3.21. Schnaiter, M.; Gimmler, M.; Llamas, I.; Linke, C.; Jaeger, C.; Mutschke, H., Strong spectral dependence of light absorption by organic carbon particles formed by propane combustion. *Atmospheric Chemistry and Physics* **2006,** *6*, 2981-2990.
3.22. Seinfeld; Pandis, *Atmospheric Chemistry and Physics: From Air Pollution to Climate Change*. 1st edition ed.; J. Wiley: New York, 1998.
4.1. Lee, K. T.; Cho, J., Roles of nanosize in lithium reactive nanomaterials for lithium ion batteries. *Nano Today* **2011,** *6* (1), 28-41.
4.2. Li, H.; Shi, L. H.; Lu, W.; Huang, X. J.; Chen, L. Q., Studies on capacity loss and capacity fading of nanosized SnSb alloy anode for Li-ion batteries. *Journal of the Electrochemical Society* **2001,** *148* (8), A915-A922; Zhang, S. S.; Ding, M. S.; Xu, K.; Allen, J.; Jow, T. R., Understanding solid electrolyte interface film formation on graphite electrodes. *Electrochemical and Solid State Letters* **2001,** *4* (12), A206-A208; Li, H.; Shi, L. H.; Wang, Q.; Chen, L. Q.; Huang, X. J., Nano-alloy anode for lithium ion batteries. *Solid State Ionics* **2002,** *148* (3-4), 247-258; Doi, T.; Iriyama, Y.; Abe, T.; Ogumi, Z., Electrochemical insertion and extraction of lithium ion at uniform nanosized Li4/3Ti5/3O4 particles prepared by a spray pyrolysis method. *Chemistry of Materials* **2005,** *17* (6), 1580-1582.
4.3. Li, H.; Wang, Z. X.; Chen, L. Q.; Huang, X. J., Research on advanced materials for Li-ion batteries. *Advanced Materials* **2009,** *21* (45), 4593-4607.
4.4. Poizot, P.; Laruelle, S.; Grugeon, S.; Dupont, L.; Tarascon, J. M., Nano-sized transition-metaloxides as negative-electrode materials for lithium-ion batteries. *Nature* **2000,** *407* (6803), 496-499.

4.5. Li, H.; Balaya, P.; Maier, J., Li-storage via heterogeneous reaction in selected binary metal fluorides and oxides. *Journal of the Electrochemical Society* **2004,** *151* (11), A1878-A1885.
4.6. Li, H.; Richter, G.; Maier, J., Reversible formation and decomposition of LiF clusters using transition metal fluorides as precursors and their application in rechargeable Li batteries. *Advanced Materials* **2003,** *15* (9), 736-739; Debart, A.; Dupont, L.; Poizot, P.; Leriche, J. B.; Tarascon, J. M., A transmission electron microscopy study of the reactivity mechanism of tailor-made CuO particles toward lithium. *Journal of the Electrochemical Society* **2001,** *148* (11), A1266-A1274; Balaya, P.; Li, H.; Kienle, L.; Maier, J., Fully reversible homogeneous and heterogeneous Li storage in $RuO_2$ with high capacity. *Advanced Functional Materials* **2003,** *13* (8), 621-625.
4.7. Yu, X. Q.; He, Y.; Sun, J. P.; Tang, K.; Li, H.; Chen, L. Q.; Huang, X. J., Nanocrystalline MnO thin film anode for lithium ion batteries with low overpotential. *Electrochemistry Communications* **2009,** *11* (4), 791-794.
4.8. Zhong, K.; Xia, X.; Zhang, B.; Li, H.; Wang, Z.; Chen, L., MnO powder as anode active materials for lithium ion batteries. *Journal of Power Sources* **2010,** *195* (10), 3300-3308.
4.9. Liu, J.; Pan, Q., MnO/C Nanocomposites as high capacity anode materials for Li-ion batteries. *Electrochemical and Solid State Letters* **2010,** *13* (10), A139-A142.
4.10. Sun, B.; Chen, Z.; Kim, H.-S.; Ahn, H.; Wang, G., MnO/C core-shell nanorods as high capacity anode materials for lithium-ion batteries. *Journal of Power Sources* **2011,** *196* (6), 3346-3349.
4.11. Nayak, S.; Malik, S.; Indris, S.; Reedijk, J.; Powell, A. K., Pyrolysis of a three-dimensional Mn-II/Mn-III network to give a multifunctional porous manganese oxide material. *Chemistry-a European Journal* **2010,** *16* (4), 1158-1162.
4.12. Fang, X.; Lu, X.; Guo, X.; Mao, Y.; Hu, Y.-S.; Wang, J.; Wang, Z.; Wu, F.; Liu, H.; Chen, L., Electrode reactions of manganese oxides for secondary lithium batteries. *Electrochemistry Communications* **2010,** *12* (11), 1520-1523.
4.13. Toupin, M.; Brousse, T.; Belanger, D., Influence of microstucture on the charge storage properties of chemically synthesized manganese dioxide. *Chemistry of Materials* **2002,** *14* (9), 3946-3952; Wu, M. S.; Chiang, P. C. J.; Lee, J. T.; Lin, J. C., Synthesis of manganese oxide electrodes with interconnected nanowire structure as an anode material for rechargeable lithium ion batteries. *Journal of Physical Chemistry B* **2005,** *109* (49), 23279-23284; Wu, M. S.; Chiang, P. C. J., Electrochemically deposited nanowires of manganese oxide as an anode material for lithium-ion batteries. *Electrochemistry Communications* **2006,** *8* (3), 383-388; Li, B.; Rong, G.; Xie, Y.; Huang, L.; Feng, C., Low-temperature synthesis of alpha-$MnO_2$ hollow urchins and their application in rechargeable $Li^+$ batteries. *Inorganic Chemistry* **2006,** *45* (16), 6404-6410.
4.14. Xia, H.; Lai, M.; Lu, L., Nanoflaky $MnO_2$/carbon nanotube nanocomposites as anode materials for lithium-ion batteries. *Journal of Materials Chemistry* **2010,** *20* (33), 6896-6902.
4.15. Pasero, D.; Reeves, N.; West, A. R., Co-doped $Mn_3O_4$: a possible anode material for lithium batteries. *Journal of Power Sources* **2005,** *141* (1), 156-158; Fan, Q.;

Whittingham, M. S., Electrospun manganese oxide nanofibers as anodes for lithium-ion batteries. *Electrochemical and Solid State Letters* **2007,** *10* (3), A48-A51.
4.16. Wang, H.; Cui, L.-F.; Yang, Y.; Casalongue, H. S.; Robinson, J. T.; Liang, Y.; Cui, Y.; Dai, H., $Mn_3O_4$-graphene hybrid as a high-capacity anode material for lithium ion batteries. *Journal of the American Chemical Society* **2010,** *132* (40), 13978-13980.
4.17. Fan, J.; Wang, T.; Yu, C. Z.; Tu, B.; Jiang, Z. Y.; Zhao, D. Y., Ordered, nanostructured tin-based oxides/carbon composite as the negative-electrode material for lithium-ion batteries. *Advanced Materials* **2004,** *16* (16), 1432-; Cheng, F.; Tao, Z.; Liang, J.; Chen, J., Template-directed materials for rechargeable lithium-ion batteries. *Chemistry of Materials* **2008,** *20* (3), 667-681.
4.18. Reddy, A. L. M.; Shaijumon, M. M.; Gowda, S. R.; Ajayan, P. M., Coaxial $MnO_2$/carbon nanotube array electrodes for high-performance lithium batteries. *Nano Letters* **2009,** *9* (3), 1002-1006.
4.19. Ji, L.; Zhang, X., Manganese oxide nanoparticle-loaded porous carbon nanofibers as anode materials for high-performance lithium-ion batteries. *Electrochemistry Communications* **2009,** *11* (4), 795-798.
4.20. Delmer, O.; Balaya, P.; Kienle, L.; Maier, J., Enhanced potential of amorphous electrode materials: Case study of RuO2. *Advanced Materials* **2008,** *20* (3), 501-+.
4.21. Guo, H. J.; Li, X. H.; Zhang, X. M.; Wang, H. Q.; Wang, Z. X.; Peng, W. J., Diffusion coefficient of lithium in artificial graphite, mesocarbon microbeads, and disordered carbon. *New Carbon Materials* **2007,** *22* (1), 7-11.
4.22. Zhu, Y.; Wang, C., Strain accommodation and potential hysteresis of $LiFePO_4$ cathodes during lithium ion insertion/extraction. *Journal of Power Sources* **2011,** *196* (3), 1442-1448.
5.1. Kasavajjula, U.; Wang, C. S.; Appleby, A. J., Nano- and bulk-silicon-based insertion anodes for lithium-ion secondary cells. *Journal of Power Sources* **2007,** *163* (2), 1003-1039.
5.2. Si, Y. C.; Zhao, L.; Yu, Z. B.; Wang, W. K.; Qiu, J. Y.; Yang, Y. S., A novel amorphous $Fe_2V_4O_{13}$ as cathode material for lithium secondary batteries. *Materials Letters* **2012,** *72*, 145-147.
5.3. Marom, R.; Amalraj, S. F.; Leifer, N.; Jacob, D.; Aurbach, D., A review of advanced and practical lithium battery materials. *Journal of Materials Chemistry* **2011,** *21* (27), 9938-9954.
5.4. Li, H.; Richter, G.; Maier, J., Reversible formation and decomposition of LiF clusters using transition metal fluorides as precursors and their application in rechargeable Li batteries. *Advanced Materials* **2003,** *15* (9), 736-739; Badway, F.; Cosandey, F.; Pereira, N.; Amatucci, G. G., Carbon metal fluoride nanocomposites - High-capacity reversible metal fluoride conversion materials as rechargeable positive electrodes for Li batteries. *Journal of the Electrochemical Society* **2003,** *150* (10), A1318-A1327; Badway, F.; Pereira, N.; Cosandey, F.; Amatucci, G. G., Carbon-metal fluoride nanocomposites - Structure and electrochemistry of $FeF_3$ : C. *Journal of the Electrochemical Society* **2003,** *150* (9), A1209-A1218; Pereira, N.; Klein, L. C.; Amatucci, G. G., The electrochemistry of $Zn_3N_2$ and LiZnN - A lithium reaction mechanism for metal nitride electrodes. *Journal of the Electrochemical Society* **2002,** *149* (3), A262-A271; Silva, D. C. C.; Crosnier, O.; Ouvrard, G.; Greedan, J.; Safa-Sefat, A.; Nazar, L. F., Reversible lithium uptake by $FeP_2$. *Electrochemical and Solid*

*State Letters* **2003,** *6* (8), A162-A165; Wang, Y.; Fu, Z. W.; Yue, X. L.; Qin, Q. Z., Electrochemical reactivity mechanism of $Ni_3N$ with lithium. *Journal of the Electrochemical Society* **2004,** *151* (4), E162-E167.

5.5. Okamoto, H.; Sugiyama, Y.; Nakano, H., Synthesis and modification of silicon nanosheets and other silicon nanomaterials. *Chemistry-a European Journal* **2011,** *17* (36), 9864-9887.

5.6. Winter, M.; Besenhard, J. O., Electrochemical lithiation of tin and tin-based intermetallics and composites. *Electrochimica Acta* **1999,** *45* (1-2), 31-50.

5.7. Lee, K. T.; Jung, Y. S.; Oh, S. M., Synthesis of tin-encapsulated spherical hollow carbon for anode material in lithium secondary batteries. *Journal of the American Chemical Society* **2003,** *125* (19), 5652-5653; Kim, I. S.; Blomgren, G. E.; Kumta, P. N., Sn/C composite anodes for Li-ion batteries. *Electrochemical and Solid State Letters* **2004,** *7* (3), A44-A48; Zhang, W. M.; Hu, J. S.; Guo, Y. G.; Zheng, S. F.; Zhong, L. S.; Song, W. G.; Wan, L. J., Tin-nanoparticles encapsulated in elastic hollow carbon spheres for high-performance anode material in lithium-ion batteries. *Advanced Materials* **2008,** *20* (6), 1160-; Kim, M. G.; Sim, S.; Cho, J., Novel core-shell Sn-Cu anodes for lithium rechargeable batteries prepared by a redox-transmetalation reaction. *Advanced Materials* **2010,** *22* (45), 5154-.

5.8. Jung, Y. S.; Lee, K. T.; Ryu, J. H.; Im, D.; Oh, S. M., Sn-carbon core-shell powder for anode in lithium secondary batteries. *Journal of the Electrochemical Society* **2005,** *152* (7), A1452-A1457.

5.9. Derrien, G.; Hassoun, J.; Panero, S.; Scrosati, B., Nanostructured Sn-C composite as an advanced anode material in high-performance lithium-ion batteries. *Advanced Materials* **2007,** *19* (17), 2336-+; Hassoun, J.; Derrien, G.; Panero, S.; Scrosati, B., A nanostructured Sn-C composite lithium battery electrode with unique stability and high electrochemical performance. *Advanced Materials* **2008,** *20* (16), 3169-3175.

5.10. Yu, Y.; Gu, L.; Zhu, C. B.; van Aken, P. A.; Maier, J., Tin nanoparticles encapsulated in porous multichannel carbon microtubes: Preparation by single-nozzle electrospinning and application as anode material for high-performance Li-based batteries. *Journal of the American Chemical Society* **2009,** *131* (44), 15984-+.

5.11. Mao, O.; Dunlap, R. A.; Dahn, J. R., Mechanically alloyed Sn-Fe(-C) powders as anode materials for Li-ion batteries - I. The $Sn_2Fe$-C system. *Journal of the Electrochemical Society* **1999,** *146* (2), 405-413; Li, H.; Shi, L. H.; Lu, W.; Huang, X. J.; Chen, L. Q., Studies on capacity loss and capacity fading of nanosized SnSb alloy anode for Li-ion batteries. *Journal of the Electrochemical Society* **2001,** *148* (8), A915-A922; Courtney, I. A.; McKinnon, W. R.; Dahn, J. R., On the aggregation of tin in SnO composite glasses caused by the reversible reaction with lithium. *Journal of the Electrochemical Society* **1999,** *146* (1), 59-68.

5.12. Wang, Y.; Lee, J. Y.; Deivaraj, T. C., Tin nanoparticle loaded graphite anodes for Li-ion battery applications. *Journal of the Electrochemical Society* **2004,** *151* (11), A1804-A1809.

5.13. Li, H.; Shi, L. H.; Wang, Q.; Chen, L. Q.; Huang, X. J., Nano-alloy anode for lithium ion batteries. *Solid State Ionics* **2002,** *148* (3-4), 247-258.

5.14. Xu, Y. H.; Guo, J. C.; Wang, C. S., Sponge-like porous carbon/tin composite anode materials for lithium ion batteries. *Journal of Materials Chemistry* **2012,** *22* (19), 9562-9567.

5.15. Liu, Q.; Ma, X.; Zachariah, M. R., Combined on-line differential mobility and particle mass analysis for determination of size resolved particle density and microstructure evolution. *Microporous and Mesoporous Materials* **2012,** *153*, 210-216.
5.16. Ehara, K.; Hagwood, C.; Coakley, K. J., Novel method to classify aerosol particles according to their mass-to-charge ratio - Aerosol particle mass analyser. *Journal of Aerosol Science* **1996,** *27* (2), 217-234; Lall, A. A.; Ma, X. F.; Guha, S.; Mulholland, G. W.; Zachariah, M. R., Online nanoparticle nass neasurement by combined aerosol particle mass analyzer and differential mobility analyzer: Comparison of theory and measurements. *Aerosol Science and Technology* **2009,** *42* (11), 1075-1083.
5.17. Sunkara, B.; Zhan, J. J.; Kolesnichenko, I.; Wang, Y. Q.; He, J. B.; Holland, J. E.; McPherson, G. L.; John, V. T., Modifying metal nanoparticle placement on carbon supports using an aerosol-based process, with application to the environmental remediation of chlorinated hydrocarbons. *Langmuir* **2011,** *27* (12), 7854-7859.
5.18. Li, X. F.; Dhanabalan, A.; Gu, L.; Wang, C. L., Three-dimensional porous core-shell Sn@carbon composite anodes for high-performance lithium-ion battery applications. *Advanced Energy Materials* **2012,** *2* (2), 238-244.
6.1. Vollath, D., *Nanomaterials: An introduction to synthesis, properties and application*. Wiley-VCH: 2008.
6.2. Schartl, W., Current directions in core-shell nanoparticle design. *Nanoscale* **2010,** *2* (6), 829-843.
6.3. deJonge, H.; MittelmeijerHazeleger, M. C., Adsorption of $CO_2$ and $N_2$ on soil organic matter: Nature of porosity, surface area, and diffusion mechanisms. *Environmental Science & Technology* **1996,** *30* (2), 408-413.
6.4. R. M. Cornell, U. S., *The iron oxides: Structure, properties, reactions, occurrences, and uses*. Wiley-VCH: 2003.
6.5. Galarneau, A.; Desplantier, D.; Dutartre, R.; Di Renzo, F., Micelle-templated silicates as a test bed for methods of mesopore size evaluation. *Microporous and Mesoporous Materials* **1999,** *27* (2-3), 297-308.
6.6. Eren, H., Density measurement. Wiley Encyclopedia of Electrical and Electronics Engineering. 1999.
6.7. Hinds, W. C., *Aerosol technology: Properties, behavior, and measurement of airborne particles*. Wiley: 1999.
6.8. Kim, S. H.; Woo, K. S.; Liu, B. Y. H.; Zachariah, M. R., Method of measuring charge distribution of nanosized aerosols. *Journal of Colloid and Interface Science* **2005,** *282* (1), 46-57.
6.9. Ehara, K.; Hagwood, C.; Coakley, K. J., Novel method to classify aerosol particles according to their mass-to-charge ratio - Aerosol particle mass analyser. *Journal of Aerosol Science* **1996,** *27* (2), 217-234.
6.10. Ma, X.; Zachariah, M. R., Size-resolved kinetics of Zn nanocrystal hydrolysis for hydrogen generation. *International Journal of Hydrogen Energy* **2010,** *35* (6), 2268.
6.11. Ma, X. F.; Zachariah, M. R., Oxidation anisotropy and size-dependent reaction kinetics of zinc nanocrystals. *Journal of Physical Chemistry C* **2009,** *113* (33), 14644-14650; Zhou, L.; Rai, A.; Piekiel, N.; Ma, X. F.; Zachariah, M. R., Ion-mobility spectrometry of nickel nanoparticle oxidation kinetics: Application to energetic materials. *Journal of Physical Chemistry C* **2008,** *112* (42), 16209-16218.

6.12. Kim, S. H.; Mulholland, G. W.; Zachariah, M. R., Density measurement of size selected multiwalled carbon nanotubes by mobility-mass characterization. *Carbon* **2009,** *47* (5), 1297-1302.
6.13. Park, K.; Kittelson, D. B.; Zachariah, M. R.; McMurry, P. H., Measurement of inherent material density of nanoparticle agglomerates. *Journal of Nanoparticle Research* **2004,** *6* (2-3), 267-272.
6.14. Lall, A. A.; Ma, X. F.; Guha, S.; Mulholland, G. W.; Zachariah, M. R., Online nanoparticle mass measurement by combined aerosol particle mass analyzer and differential mobility analyzer: Comparison of theory and measurements. *Aerosol Science and Technology* **2009,** *42* (11), 1075-1083.
6.15. Tsai, D. H.; DelRio, F. W.; Keene, A. M.; Tyner, K. M.; MacCuspie, R. I.; Cho, T. J.; Zachariah, M. R.; Hackley, V. A., Adsorption and conformation of serum albumin protein on gold nanoparticles investigated using dimensional measurements and in situ spectroscopic methods. *Langmuir* **2011,** *27* (6), 2464-2477.
6.16. Prakash, A.; McCormick, A. V.; Zachariah, M. R., Tuning the reactivity of energetic nanoparticles by creation of a core-shell nanostructure. *Nano Letters* **2005,** *5* (7), 1357-1360.
6.17. Gadalla, A. M.; Yu, H. F., Thermal-decomposition of Fe(III) nitrate and its aerosol. *Journal of Materials Research* **1990,** *5* (6), 1233-1236.
6.18. Ma, L. Q.; Song, Z. L., Cellular structure control of aluminium foams during foaming process of aluminium melt. *Scripta Materialia* **1998,** *39* (11), 1523-1528.
6.19. Yu, H. F.; Liao, W. H., Evaporation of solution droplets in spray pyrolysis. *International Journal of Heat and Mass Transfer* **1998,** *41* (8-9), 993-1001.
7.1. Bharali, D. J.; Klejbor, I.; Stachowiak, E. K.; Dutta, P.; Roy, I.; Kaur, N.; Bergey, E. J.; Prasad, P. N.; Stachowiak, M. K., Organically modified silica nanoparticles: A nonviral vector for in vivo gene delivery and expression in the brain. *Proceedings of the National Academy of Sciences of the United States of America* **2005,** *102* (32), 11539-11544.
7.2. Wang, Y. J.; Price, A. D.; Caruso, F., Nanoporous colloids: Building blocks for a new generation of structured materials. *Journal of Materials Chemistry* **2009,** *19* (36), 6451-6464.
7.3. Capek, I., On inverse miniemulsion polymerization of conventional water-soluble monomers. *Advances in Colloid and Interface Science* **2010,** *156* (1-2), 35-61.
7.4. Huh, S.; Wiench, J. W.; Yoo, J. C.; Pruski, M.; Lin, V. S. Y., Organic functionalization and morphology control of mesoporous silicas via a co-condensation synthesis method. *Chemistry of Materials* **2003,** *15* (22), 4247-4256.
7.5. Yao, G.; Wang, L.; Wu, Y. R.; Smith, J.; Xu, J. S.; Zhao, W. J.; Lee, E. J.; Tan, W. H., FloDots: Luminescent nanoparticles. *Analytical and Bioanalytical Chemistry* **2006,** *385* (3), 518-524.
7.6. Michalet, X.; Pinaud, F. F.; Bentolila, L. A.; Tsay, J. M.; Doose, S.; Li, J. J.; Sundaresan, G.; Wu, A. M.; Gambhir, S. S.; Weiss, S., Quantum dots for live cells, in vivo imaging, and diagnostics. *Science* **2005,** *307* (5709), 538-544.
7.7. Shibata, S.; Taniguchi, T.; Yano, T.; Yamane, M., Formation of water-soluble dye-doped silica particles. *Journal of Sol-Gel Science and Technology* **1997,** *10* (3), 263-268.

7.8. Zhao, X. J.; Bagwe, R. P.; Tan, W. H., Development of organic-dye-doped silica nanoparticles in a reverse microemulsion. *Advanced Materials* **2004,** *16* (2), 173-+.
7.9. Vanblaaderen, A.; Vrij, A., Synthesis and characterization of colloidal dispersions of fluorescent, monodisperse silica spheres. *Langmuir* **1992,** *8* (12), 2921-2931.
7.10. Li, X. D.; Zhai, Q. Z.; Zou, M. Q., Optical properties of (nanometer MCM-41)-(malachite green) composite materials. *Applied Surface Science* **2010,** *257* (3), 1134-1140.
7.11. Xie, C. J.; Yin, D. G.; Li, J.; Zhang, L.; Liu, B. H.; Wu, M. H., Preparation of a novel type of fluorescein isothiocyanate doped fluorescent silica nanoparticles and its application as pH probe. *Chinese Journal of Analytical Chemistry* **2010,** *38* (4), 488-492.
7.12. Ma, D. L.; Kell, A. J.; Tan, S.; Jakubek, Z. J.; Simard, B., Photophysical properties of dye-doped silica nanoparticles bearing different types of dye-silica interactions. *Journal of Physical Chemistry C* **2009,** *113* (36), 15974-15981.
7.13. Gao, X. Q.; He, J.; Deng, L.; Cao, H. N., Synthesis and characterization of functionalized rhodamine B-doped silica nanoparticles. *Optical Materials* **2009,** *31* (11), 1715-1719.
7.14. Rocha, L. A.; Caiut, J. M. A.; Messaddeq, Y.; Ribeiro, S. J. L.; Martines, M. A. U.; Freiria, J. D.; Dexpert-Ghys, J.; Verelst, M., Non-leachable highly luminescent ordered mesoporous $SiO_2$ spherical particles. *Nanotechnology* **2010,** *21* (15).
7.15. Wang, Y.; Li, Z. H.; Zhong, W. Y.; Li, H.; Xu, D. K.; Chen, H. Y., Rhodamine B doped silica nanoparticle labels for protein microarray detection. *Science China-Chemistry* **2010,** *53* (4), 747-751; Stein, A.; Melde, B. J.; Schroden, R. C., Hybrid inorganic-organic mesoporous silicates - Nanoscopic reactors coming of age. *Advanced Materials* **2000,** *12* (19), 1403-1419; Tsyalkovsky, V.; Klep, V.; Ramaratnam, K.; Lupitskyy, R.; Minko, S.; Luzinov, I., Fluorescent reactive core-shell composite nanoparticles with a high surface concentration of epoxy functionalities. *Chemistry of Materials* **2008,** *20* (1), 317-325; Guli, M.; Chen, Y.; Li, X. T.; Zhu, G. S.; Qiu, S. L., Fluorescence of postgrafting Rhodamine B in the mesopores of rodlike SBA-15. *Journal of Luminescence* **2007,** *126* (2), 723-727.
7.16. Nandiyanto, A. B. D.; Kim, S. G.; Iskandar, F.; Okuyama, K., Synthesis of spherical mesoporous silica nanoparticles with nanometer-size controllable pores and outer diameters. *Microporous and Mesoporous Materials* **2009,** *120* (3), 447-453.
7.17. Thomassen, L. C. J.; Aerts, A.; Rabolli, V.; Lison, D.; Gonzalez, L.; Kirsch-Volders, M.; Napierska, D.; Hoet, P. H.; Kirschhock, C. E. A.; Martens, J. A., Synthesis and characterization of stable monodisperse silica nanoparticle sols for in vitro cytotoxicity testing. *Langmuir* **2010,** *26* (1), 328-335.
7.18. Lee, S. J.; Choi, M.-C.; Park, S. S.; Ha, C.-S., Synthesis and characterization of hybrid films of polyimide and silica hollow spheres. *Macromolecular Research* **2011,** *19* (6), 599-607.
7.19. Nakamura, K.; Yamanaka, K.; Shikata, T., Hybrid threadlike micelle formation between a surfactant and polymer in aqueous solution. *Langmuir* **2003,** *19* (21), 8654-8660.
7.20. He, Q.; Shi, J.; Cui, X.; Zhao, J.; Chen, Y.; Zhou, J., Rhodamine B-co-condensed spherical SBA-15 nanoparticles: Facile co-condensation synthesis and excellent fluorescence features. *Journal of Materials Chemistry* **2009,** *19* (21), 3395-3403.

7.21. Al-Shamiri, H. A. S.; Kana, M. T. H., Laser performance and photostability of Rhodamin B in solid host matrices. *Applied Physics B-Lasers and Optics* **2010,** *101* (1-2), 129-135.
7.22. Waters, J. C., Accuracy and precision in quantitative fluorescence microscopy. *Journal of Cell Biology* **2009,** *185* (7), 1135-1148.
7.23. Quemeneur, F.; Rinaudo, M.; Pepin-Donat, B., Influence of molecular weight and pH on adsorption of chitosan at the surface of large and giant vesicles. *Biomacromolecules* **2008,** *9* (1), 396-402.
7.24. Christensen, K.; Bose, H. S.; Harris, F. M.; Miller, W. L.; Bell, J. D., Binding of steroidogenic acute regulatory protein to synthetic membranes suggests an active molten globule. *Journal of Biological Chemistry* **2001,** *276* (20), 17044-17051.
7.25. Grasset, F.; Dorson, F.; Cordier, S.; Molard, Y.; Perrin, C.; Marie, A. M.; Sasaki, T.; Haneda, H.; Bando, Y.; Mortier, M., Water-in-oil microemulsion preparation and characterization of $Cs_2Mo_6X_{14}$ @$SiO_2$ phosphor nanoparticles based on transition metal clusters (X = Cl, Br, and I). *Advanced Materials* **2008,** *20* (1), 143-.
7.26. Nan, A. J.; Bai, X.; Son, S. J.; Lee, S. B.; Ghandehari, H., Cellular uptake and cytotoxicity of silica nanotubes. *Nano Letters* **2008,** *8* (8), 2150-2154.
8.1. Singh, D. P.; Ali, N., Synthesis of $TiO_2$ and CuO nanotubes and nanowires. *Science of Advanced Materials* 2010, *2* (3), 295-335.
8.2. Xiao, X. D.; Miao, L.; Xu, G.; Lu, L. M.; Su, Z. M.; Wang, N.; Tanemura, S., A facile process to prepare copper oxide thin films as solar selective absorbers. *Applied Surface Science* 2011, *257* (24), 10729-10736.
8.3. Pelinovsky, D.; Schneider, G., Justification of the coupled-mode approximation for a nonlinear elliptic problem with a periodic potential. *Applicable Analysis* 2007, *86* (8), 1017-1036.